THE UNIVERSITY *of* LIVERPOOL

Robust Inertia Emulation Control of Doubly-Fed Induction Generator based Wind Turbines Participating in Power System Frequency Support

Thesis submitted in accordance with the
requirements of the University of Liverpool
for the degree of Doctor of Philosophy

in

Electrical Engineering and Electronics

by

Lei Ba, MSc

July 2021

Robust Inertia Emulation Control of Doubly-Fed Induction Generator based Wind Turbines Participating in Power System Frequency Support

by

Lei Ba

Acknowledgements

I would like to give my sincere thank to my primary supervisor, Dr. L. Jiang, who gave me the opportunity to pursue a PhD degree in the University of Liverpool. Throughout the four years' study, his guidance and support enabled me to develop a deep understanding of my work. Without his consistent and illuminating instructions, my research work and my life could not proceed to this stage. The research skill, writing skill and presenting skill he taught me will benefit me throughout my life.

I also appreciate all of the members of smart grid control and renewable energy group, the University of Liverpool. Special thanks also go to my colleagues, Dr. C. Duan, Dr. Y. Du, Dr. K. Shi, Dr. R. Wang, Dr. Y. Wang for their support and friendship.

Besides, I would like to thank the University of Liverpool and the China Scholarship Council for funding my PhD study. My thanks also go to the Department of Electrical Engineering and Electronics at the University of Liverpool, for providing research facilities that made it possible for me to carry out this research.

Finally, I want to give my special thank to my husband Dr. Haotian Xu, for his invaluable support, understanding, patience, and love during my postgraduate life, and also to our family, for their encouragement and financial support during these years.

Abstract

Nowadays most wind power generators are required by system operators to have frequency support capability via designing a supplementary frequency support controller to emulate the inertia response of synchronous generators. However, such a design excites a new lightly damped oscillation mode and deteriorates the torsional oscillation mode of the wind turbine drive train. Moreover, the phase-locked loop, which is commonly used to measure the frequency at the point of common coupling, will participate and dominate the new lightly damped oscillation mode. Thus, when the wind turbine generators contribute to system frequency support, the impact of the phase-locked loop on the system stability needs to pay more attention.

In this thesis, a robust damping controller is designed based on H_∞ mixed-sensitivity robust control approach for a doubly-fed induction generator based wind turbine to mitigate system oscillation during frequency support and provide robust damping performance considering uncertain system operating points. The damping ratio of the new oscillation mode is used to evaluate the performance of the proposed damping controller. Compared to the residue method based conventional damping controller design, the robust damping controller can ensure the damping ratio of the new oscillation mode above 0.15 considering uncertainties.

A new robust H_∞ PD-type controller design approach is proposed to design an integrated inertia emulation controller. The robustness of the proposed approach is achieved based on H_∞ control technique to convert to a linear matrix inequality. Simultaneously, the regional pole placement objective is introduced as an additional linear matrix inequality to guarantee the damping performance. The designed integrated inertia emulation controller can simultaneously achieve robust frequency support performance and guaranteed damping performance, which avoids the de-

sign of an additional damping control loop. Comparing to a conventional inertia emulation controller, the design of the integrated inertia emulation controller can ensure a minimum 0.15 damping ratio of the new oscillation mode.

Furthermore, due to the frequency support requirements, the coupling effect between the drive train of wind turbines and electrical systems is increased which results in a poorly damped torsional oscillation mode. To ensure the safe operation of the wind turbine considering uncertainties and different external disturbances, a robust torsional oscillation damping controller is proposed. The proposed controller is designed based on H_∞ mixed-sensitivity robust control approach, where the robust damping performance against uncertainties can be formulated in the linear matrix inequality framework to place the closed-loop poles in a pre-defined region. Compared to a conventional torsional oscillation damping controller designed by the residue method, the robust damping performance on the deteriorated torsional oscillation mode can be ensured with the proposed controller, which is evidenced by a minimum 0.15 damping ratio of the torsional oscillation mode.

Moreover, the impact of phase-locked loop on the system stability during DFIG-WTs frequency support is also investigated. Once the phase-locked loop is used to measure the frequency, the new lightly damped oscillation is dominated by both the phase-locked loop and inertia emulation controller. Analysis results show that the weak power grid and large phase-locked loop parameters will deteriorate the system stability when DFIG-WTs participate in the system frequency support. A mixed H_2/H_∞ based robust damping controller is designed which can ensure the system stability against different phase-locked loop parameters and power grid strength. The minimum 0.15 damping ratio of the new oscillation mode is ensured and thus oscillation can be mitigated within 10s. Comparing to the single objective H_∞ based damping controller, the proposed damping controller can provide better transient performance and its damping performance is better for the weak power grid and large phase-locked loop parameters.

Declaration

The author hereby declares that this thesis is a record of work carried out in the Department of Electrical Engineering and Electronics at the University of Liverpool during the period from September 2017 to July 2021. The thesis is original in content except where otherwise indicated.

Contents

List of Figures

List of Tables

List of Abbreviations

AGC	Automatic Generation Control
CDC	Conventional Damping Controller
CIEC	Conventional Inertia Emulation Controller
CTODC	Conventional Torsional Oscillation Damping Controller
DFIG	Doubly-fed Induction Generator
FN	Frequency Nadir
GSC	Grid Side Converter
IEC	Inertia Emulation Controller
IIEC	Integrated Inertia Emulation Controller
LMI	Linear Matrix Inequality
MPPT	Maximum Power Point Tracking
PCC	Point of Common Coupling
PD	Proportional-Derivative
PLL	Phase-locked Loop
PI	Proportional-Integral
PSS	Power System Stabiliser
PV	Photovoltaic
RDC	Robust Damping Controller
ROCOF	Rate of Change of Frequency
RSC	Rotor Side Converter
RTODC	Robust Torsional Oscillation Damping Controller
SCR	Short-circuit Ratio
SG	Synchronous Generator
SMIB	Single Machine Infinity Bus
TOD	Torsional Oscillation Damper
TSO	Transmission System Operator
VC	Vector Control

VIC	Virtual Inertia Control
VSC	Voltage Source Converter
WT	Wind Turbine
WTG	Wind Turbine Generator

Chapter 1

Introduction

1.1 Power System with High Penetration Levels of Renewable Energy

Over the last two decades, considering the impact of fossil fuels on the environment and human health, renewable energies have experienced fast development and large integration in the modern power system. A growing number of governments have set policies which encourage companies to employ renewable energies to achieve sustainable goals [1]. In 2020, renewable energy achieved the highest share in the global electricity mix which accounted for an estimate of 29%, where more than 256 GW renewable energies have been added globally [1]. On the other hand, the costs of electricity generated by renewable energies, such as wind and solar, are reduced significantly in recent years. From 2009, the wind turbine cost has declined by almost one-third [12]. The global average cost of solar photovoltaics (PV) has dropped 85% since 2010, while the cost of onshore wind power has reduced by 56% [1]. These cost reductions make the electricity generated by renewable energies becoming more competitive and cost-effective than the gas, oil and coal fired power plants [13]. For China, European Union, Indian and the United States, it has been shown that the investment in the new wind and solar power plants is less than the gas fired power plants [1]. Based on the report of the International Renewable Energy Agency, doubling the renewable energy share by 2030 can reduce air pol-

lution and human health damage which can contribute to up to 4200 billion USD annual net savings [14]. The energy transition to these renewable energies can help the economic development and also support a cleaner and healthier future environment, where the trend of integrating high penetration levels of renewable energy in the power system will continue.

Over the past few years, the average growths of solar PV and wind power are 27% and 13%, respectively [15,16]. As shown in Fig.1.1, the annually new installed capacity of solar PV and wind power have been increased dramatically in 2020. 139 GW solar PV was added which accounted for more than half of the total renewable power capacity. Meanwhile, 93 GW of wind power was installed in the same time period, which contributes to around 39% of new installed renewable energy.

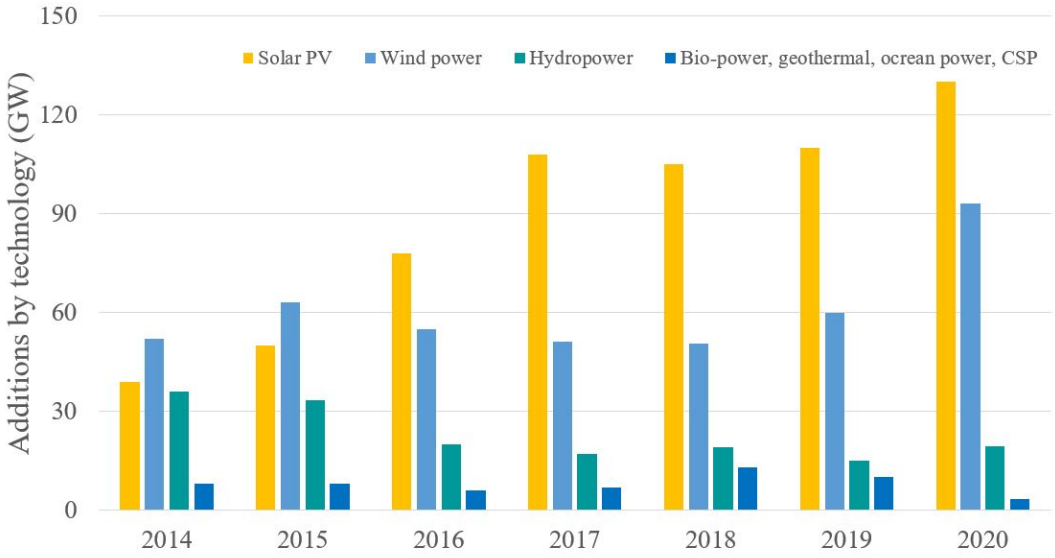

Figure 1.1: Annual additions of renewable power capacity between 2014 - 2020 [1]

Wind power, as one of the leading renewable energies, has been rapidly developed in recent years. The penetration levels of wind power have been increased significantly in modern power systems. As shown in Fig.1.2, the global cumulative capacity of wind power has been increased dramatically from 2001 to 2020. Based on the Renewable 2021 Global Status Report, more than 93 GW wind power has been installed globally in 2020, which has reached 743 GW total capacity [1]. Around 4.5% electricity generation was produced by wind power. China and the

United States have led the fastest growth of wind power installation in their record years. Wind power penetration levels of several countries are also relatively high, including Denmark (over 58%), Uruguay (40.4%), Ireland (38%), Germany(33%) and Greece (32%). In the United Kingdom, 41.6% of electricity generation was from renewable energies in Quarter 1 2021, where wind power contributes to up to 25.2% of total renewable energy generation [17].

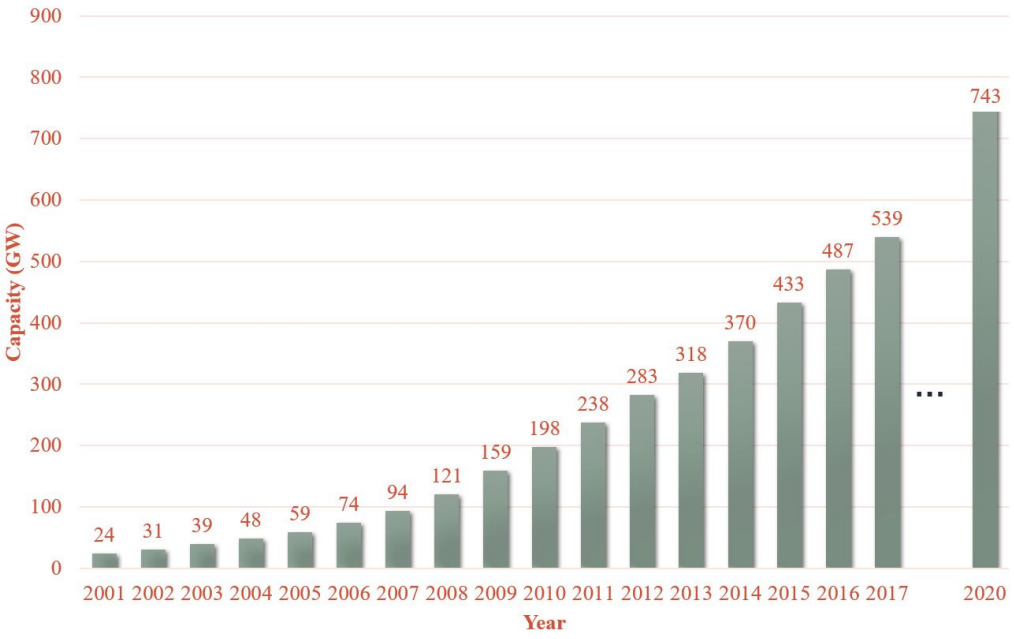

Figure 1.2: Global cumulative wind power capacity (GW) [2]

Nowadays, at least nine countries have achieved 20% electricity generated by wind and solar. The investment in wind power is still in rapid growth, where China and the United States lead the top 2 annual investments in 2020 [1]. It can be foreseen that the penetration levels of wind power will continue to rise and the interest in wind power is still increasing. Therefore, it is significant to research the power system with high penetration levels of wind power.

1.2 Power System Frequency Regulation

Frequency is a real-time variable in the power system which highly depends on the active power balance between power generation and load consumption [18]. To achieve a stable operation of a power system, system frequency should be regulated and stabilised at nearly a constant [4]. The change of load in a power system can be directly reflected by the frequency variation. Fig.1.3 shows the system frequency behaviour after a sudden load connection. During the load disturbance event, system frequency will drop instantaneously and it will change at a rate determined by the total system inertia. Following a frequency change, the power generators are required to provide active power support to the corresponding load change, which needs frequency control methods to enable these generators to response.

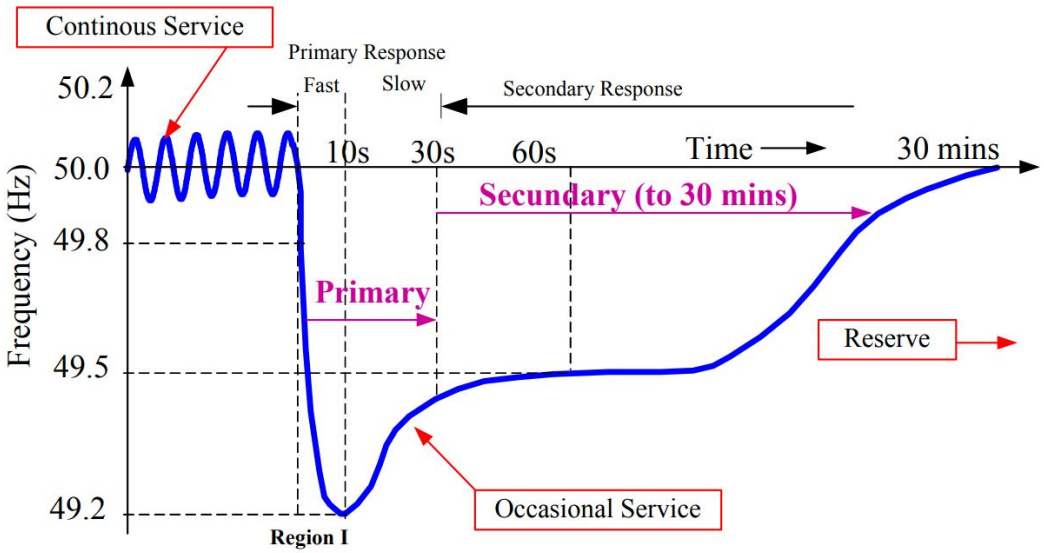

Figure 1.3: System frequency response with control in the UK [3]

1.2.1 Control of Frequency in Power System

The control of frequency is important as it can ensure the constant speed operation of the induction and synchronous motors in the system [4]. Maintaining the motors operating at the constant speed is especially significant to guarantee the

performance of generating units. This is due to the fact that the generating performance is highly determined by these auxiliary drives associated with the fuel, water and steam systems. The power system frequency is generally regulated by a hierarchical control process. Depending on the time and size of a frequency deviation, the frequency control can be divided into three levels, which are called the primary, secondary and tertiary and emergency frequency control levels [4, 19].

Primary frequency control

The power system frequency is firstly regulated by the automatic primary frequency control, where its action is normally operated within the first 30 seconds of a frequency event. As shown in Fig.1.4, a load disturbance is immediately reflected by the change of the generating units electrical power P_e. The mismatch between the mechanical power P_m and the electrical power P_e will cause the rotor speed variation. When the speed governor is absent, the system frequency response is provided by releasing the kinetic energy stored in the generating units which is highly dependent on the inertia constant H as shown in (1.2.1). For generating units like thermal and hydro power plants, a large amount of inertia can be contributed. Thus, the change of frequency can be effectively slowed and a longer time is allowed to respond and react to the load disturbance. By releasing kinetic energy stored in the rotating mass of generating unit, power imbalance can be compensated and system frequency can be arrested.

$$\Delta E = \Delta P_m - \Delta P_e = 2H\frac{d\Delta\omega_r}{dt} \tag{1.2.1}$$

In a power system, loads consist of different types of electrical devices. The resistive loads like lighting and heating loads cannot contribute to the frequency control as the electrical power is independent to the system frequency. For the motor loads like the fans and pumps, the change of frequency can be reflected by the change of motor speed and thus cause the change of electrical power [4]. The frequency-dependent characteristics of the motor loads are given as

$$\Delta P_e = \Delta P_L + D\Delta\omega_r \tag{1.2.2}$$

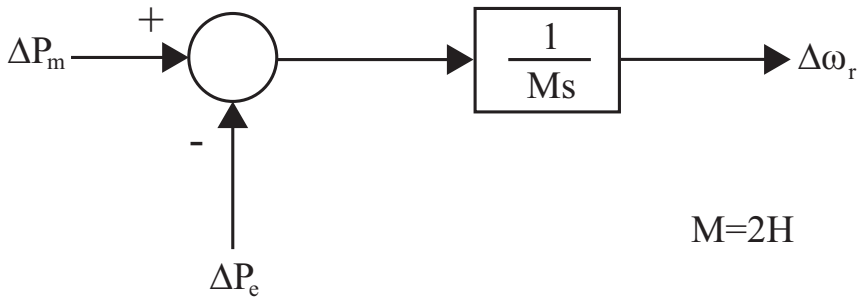

Figure 1.4: Block diagram of generator power respond to load change

where ΔP_L is the electrical power change from the resistive loads and $D\Delta\omega_r$ represents the electrical power change from the frequency-dependent loads. D is the load damping constant.

The load damping constant is used to describe the percent change of load resulting from a percent change of frequency. Typically, the value of D is chosen as 1% to 2%, where 2% represents the 1% change of frequency will cause a 2% change of load. After considering the damping load effect, the block diagram of Fig.1.4 is updated as shown in Fig.1.5.

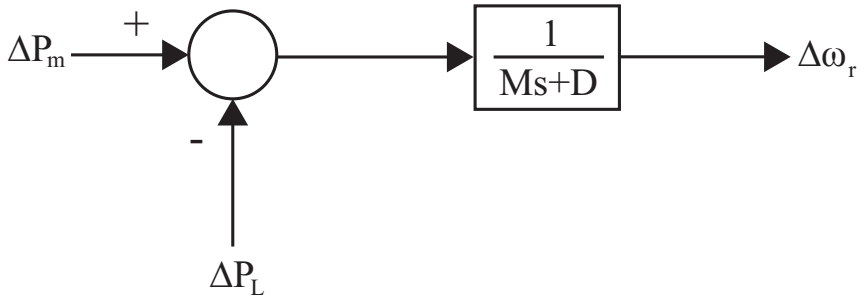

Figure 1.5: Block diagram of generator power respond to load change including motor loads damping

Generally, the governor of a generating unit is designed to restore the system frequency by controlling the rotor speed after inertia response. Fig.1.6 shows the schematic diagram of a steam or water turbine equipped with a governor, where the valve or gate position of the turbine is adjusted based on the rotor speed error.

When the multiple generators are participating in the system frequency control, the active power output needs to be shared between generators which is achieved

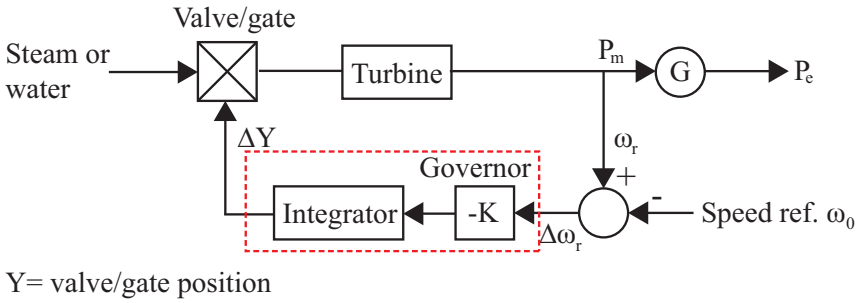

Figure 1.6: Schematic of a stream or water turbine with a governor [4]

by the speed regulation or the droop control as shown in Fig.1.7 [4]. The droop control gain R is the generating unit droop characteristic parameter, which is used to describe the relationship between the active power and system frequency. It is normally expressed in percent as shown in (1.2.3).

$$\begin{aligned} \text{Percent } R &= \frac{\text{percent speed or frequency change}}{\text{percent active power output change}} \times 100 \\ &= \left(\frac{\omega_{NL} - \omega_{FL}}{\omega_0} \right) \times 100 \end{aligned} \tag{1.2.3}$$

where ω_{NL} and ω_{FL} are the speed without load and at full load, respectively. ω_0 is the nominal speed. Because of the proportional droop control of governors, the system frequency may be settled in a value which is different to the nominal frequency [20]. In this case, it is necessary to deploy the secondary frequency control.

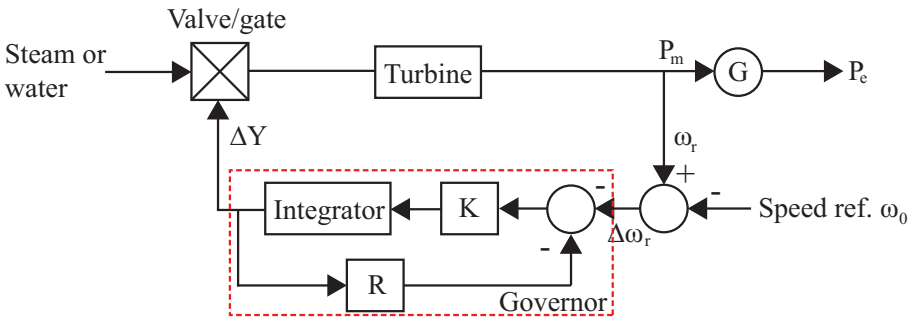

Figure 1.7: Schematic of a stream or water turbine with a governor having a droop characteristic [4]

Secondary frequency control

When the frequency drop is significant, a secondary frequency control will be activated to restore system frequency from 30 seconds to 15 minutes. The active power output from all generating units are already provided by the governors in the primary frequency control. To restore system frequency to its nominal value, additional control is provided which is the so-called load frequency control (LFC) or automatic generation control (AGC) through the available reserved power in the system. In an isolated power system, the AGC can be achieved by introducing an additional integral control signal acting on the load references of the governor as shown in Fig.1.8.

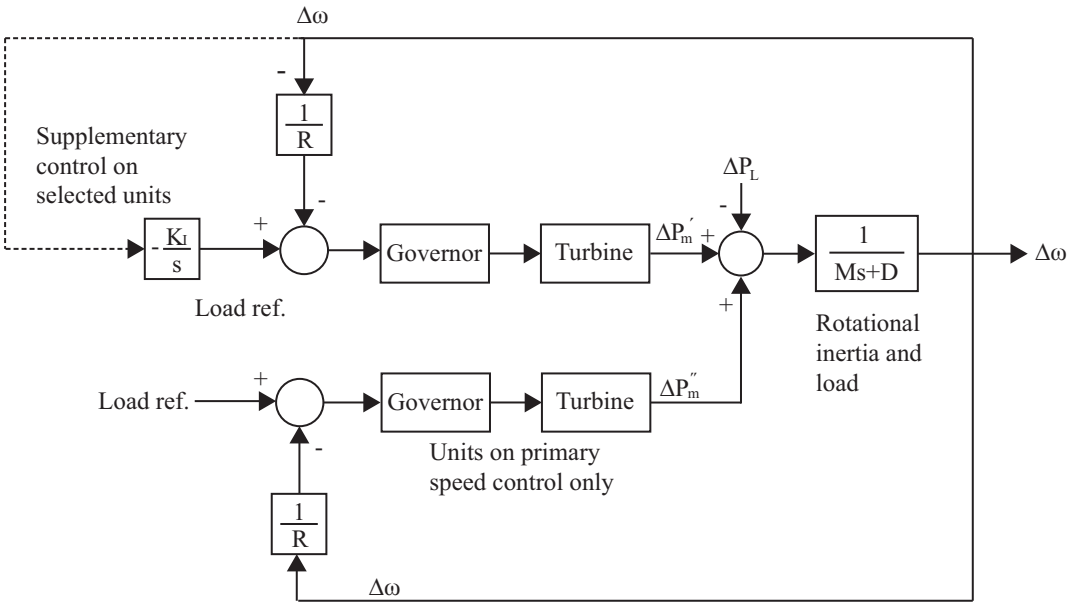

Figure 1.8: AGC with additional integral control signal [4]

For an interconnected power system, the system is partitioned into several controlled areas which are interconnected by transmission lines. During the AGC, system frequency deviation is obtained and partitioned to the control areas. The required active power to maintain system frequency within the acceptable limit is given by AGC to control the generating units in each area. Fig.1.9 shows the AGC applied in each control area for an interconnected power system. The common applied AGC technique is based on PI controller where the controller gains should be

properly tuned to ensure the desired frequency response [21].

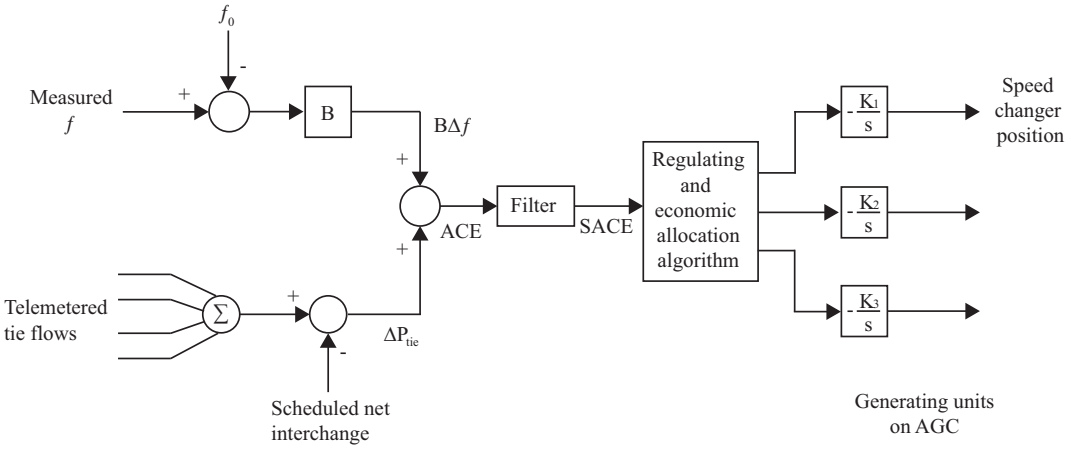

Figure 1.9: AGC of interconnected power system at each area [4]

Tertiary and emergency frequency control

When the power imbalance causes a large frequency drop and the secondary frequency control cannot compensate the frequency deviation, a tertiary frequency control which is the last level of frequency regulation will act to avoid the occurrence of the cascading system frequency drop and instability [20]. At this control stage, the transmission system operators will participate to use the available reserves provided by the connected generating units and reschedule operation requests to the frequency controls from different generating units to restore the frequency.

If the disturbance is serious, the extreme frequency decline can occur and it will cause cascaded system failures and even worse the whole system blackout. In this situation, if the generating units are not able to rapidly provide sufficient active power output, the frequency decline will be highly dependent on the frequency sensitive characteristics of loads [4]. In many cases, because of under-frequency protection relays of the existing generating units, the frequency decline may also trip these generators and thus lead to a further frequency drop. To prevent the spread frequency decline to the other areas, the emergency control must be activated which is achieved through the under-frequency load shedding program in the

affected area [22]. This control program is also helpful in the fast restoration of the affected loads [23].

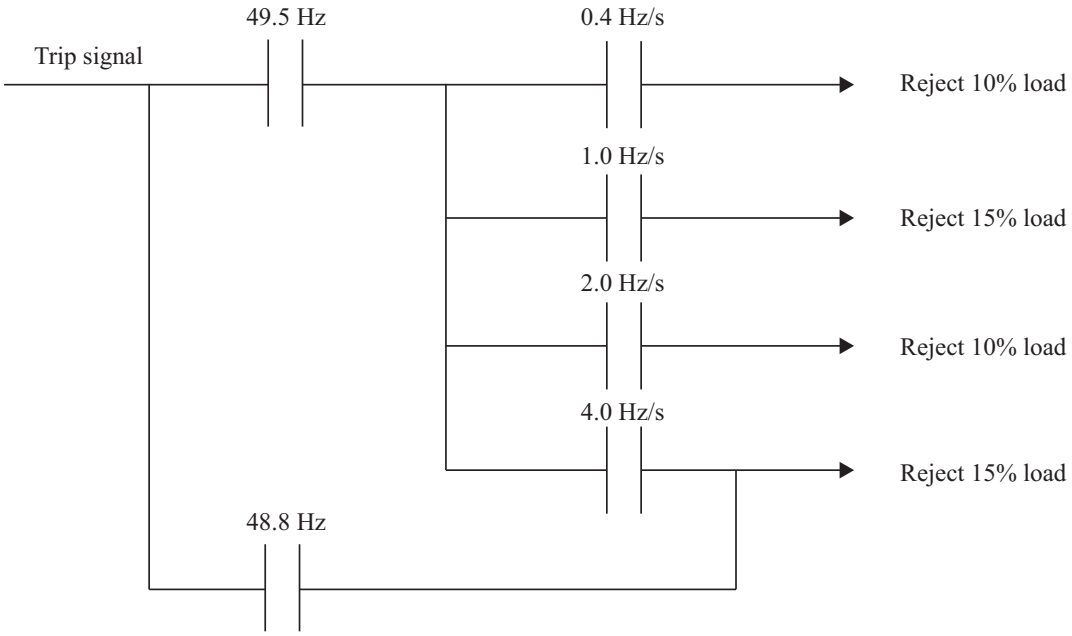

Figure 1.10: Tripping logic [4]

Fig.1.10 shows the tripping logic during the under-frequency protection procedure used in the Ontario Hydro. Both the frequency decline value and rate of change of frequency are considered in the protection procedure. Up to 50% of the total loads in the whole power system may be disconnected in this protection scheme. In National Grid Code OC6.6, when the system frequency is dropped below 49.5 Hz over a period of time, the under-frequency protection will be activated and disconnected unnecessary loads [5]. The under-frequency protection scheme includes nine stages. Based on the frequency threshold, up to 60% cumulative unnecessary loads will be tripped to avoid further system failure.

1.2.2 Challenges on Frequency Regulation with High Wind Power Penetration Levels

With the increased penetration levels of wind power in the power system, frequency regulation of the power system is facing great challenges and has attracted

a lot of attention of the system operators [24]. Thus, the impacts of high wind power penetration levels on the power system frequency regulation are necessary to be investigated, which include the issues associated with intermittent wind power generation, reduced system inertia and power system stability.

The first challenge is due to the intermittent wind power generation. Because of the stochastic nature of wind, wind power generation is intermittent and hard to predict, which increases the uncertainties on active power balance to restore system frequency. These uncontrollable wind power generation can also cause more serious and common system operating points shifting during power system operation. Thus, robust control on power system frequency regulation with high wind power penetration levels is necessary. When the penetration level of wind power is high, both the small signal and transient stability of the power system will be affected significantly [25]. Especially in a weak power grid, the fluctuation of wind power will cause serious voltage and frequency fluctuation [26]. In the traditional power system operation, synchronous generators (SGs) will change their generation levels as the system load variation to achieve the economics dispatch. For the case of high wind power penetration levels, a dispatchability value needs to be given to regulate the wind power to optimise the net benefits [27].

High wind power penetration levels can also cause the system inertia reduction and lead to fast frequency change and large frequency deviation [28]. Traditionally, SGs are used to support the system frequency following a contingency. The generation and load mismatch in a power system can cause the change of rotational speed of the SGs and thus brings a corresponding change of the system frequency [29]. The frequency support capability is significantly determined by the inertia of the SGs. Large inertia is desired for the frequency stability consideration as it can slow the rate of the change of frequency. For the variable speed wind turbines, the output power of these WTGs are decoupled from the power grid frequency by the power electronics to achieve the maximum power tracking based on the available wind speed. However, when a large amount of electricity is generated by wind power, the total system inertia is reduced significantly as the WTGs cannot react to the grid frequency change and thus contribute zero inertia to the power system. Hence, the

system operators have updated the grid code requirements and requested the WTGs to have the frequency support capability [5,6,30,31]. Supplementary frequency support controllers are designed and added at the active power control loop of WTGs to participate in the frequency regulation.

Finally, under the secure and stable power system operation consideration, the system frequency should be regulated during the normal and abnormal operation [24] and electromechanical oscillation of power system needs to be well damped [32]. When the WTG participates in the power system frequency regulation, the frequency support controller of WTG may affect the inter-area modes either in a positive or a negative aspect. The eigenvalue analysis and simulations are obtained in [33] which illustrated that the frequency support control of a WTG provided a positive influence on inter-area mode damping. [34] evaluated the impact of WTG frequency support controller on the damping of inter-area mode under different tie-line power in a classic 2-area system. It has been found that the damping performance of inter-area mode can be improved with the deployed frequency support controller. As reported in [35], considering the WTG with frequency support controller, the oscillation frequency is almost unchanged whereas the damping ratio is deteriorated. The influence of frequency support controller parameters are studied in [36]. It can be seen that an increased frequency support controller gain will improve the oscillation frequency and damping of the inter-area modes. While the time constant of the frequency support controller increases, the impact is adverse.

1.3 Wind Turbine Generators Participating in System Frequency Support

Due to the fast development of environmentally friendly renewable generation, the installation of renewable energies such as PV and wind has been largely grown in recent years. This results in the portion of the total power generation provided by renewable energy increased significantly [37]. Hence, the study on the modern power system with a high renewable energy penetration is necessary and the change on the frequency dynamic response is important.

In the conventional power system, SGs can react to grid frequency deviation as the rotor of the SG is directly coupled to the power grid frequency. When the SGs contribute to system frequency support, the kinetic energy stored in the rotor inertia can be released initially and the governor will take a response followed to react to change the mechanical power input [38]. This is normally called the slow frequency dynamics as the inertia behaviour is slow swing-type support in a grid frequency event.

Unlike SGs, renewable energies connect to the power grid through the inverters. Such inverter-based renewable energy resources provide zero inertia to the system as they are not electromagnetically coupled to the power grid. The control designs of renewable energies are to operate at their maximum power point tracking and thus are not able to response to frequency deviation naturally.

When a large amount of conventional SGs is displaced by the inverter-based renewable energies, the total power system inertia will be reduced significantly. This will cause insufficient frequency support capability which can lead to a faster rate of change of frequency (ROCOF) and a lower frequency nadir (FN) [39, 40]. It has been reported that during a frequency event, a large transient frequency drop due to a high renewable energy penetration may trigger unnecessary protection actions, even the system has sufficient capacity to reach its steady state operation [41]. Thus, the need for the frequency support provided by these renewable energies is highly desired.

To achieve a stable operation of the power system, it is important to use the potential frequency support capability of WTGs. For this purpose, several grid codes have been updated for the growing wind power penetration in the modern power system, where additional requirements on the WTGs to participate in system frequency regulation are added.

1.3.1 Grid Code Requirements of the United Kingdom

Comparing to the large European network, the frequency control becomes a severe challenge in the United Kingdom power grid because of its island situation. This is due to the limited power reserve available for frequency support. With the

increased penetration level of wind power in the power grid, a stricter grid code requirement on the frequency support capability is developed.

For both the offshore and onshore wind turbines with the capacity over 50MW, the United Kingdom grid code requires that they must be able to participate in system frequency support through varying their active power output. The active power output control can be achieved by two operation modes which are frequency sensitive mode and limited frequency sensitive mode [30].

For the limited frequency sensitive operation mode, the SGs are required to output the active power such that the system frequency is maintained between 49.5 Hz and 50.5 Hz, where the active power output of WTGs should be independent to the frequency change in this range. When the system frequency is between 47 Hz to 49.5 Hz, both the rated power below and above 50 MW wind power plants shall be able to act possibly based on the frequency drop, where the amount of active power decline should not exceed 5%.

As for the frequency sensitive operation mode, it includes the system ancillary services and commercial ancillary service for frequency control. The system ancillary services are compulsory services to support reactive power and grid frequency. The commercial ancillary services are the capability on fast start, black start and generator units tripping during system faults [30]. Thus, the wind power plants where their rated power are above 50MW must provide the system ancillary service in frequency sensitive operation mode based on system operators' instruction. In this situation, the wind power plants will no longer operate in the limited frequency sensitive mode.

The frequency sensitive operation mode mentioned is a general operation mode including the primary response, and/or secondary response and/or high frequency response [30]. The primary and secondary response is applied to the negative frequency deviation. Meanwhile, the high frequency response is suitable for the positive frequency deviation. When a frequency deviation occurs, the relevant frequency response will be activated automatically by the appropriate controller.

For the primary response, the generator unit increases its active power between 10s to 30s after the frequency deviation ramp detection. From 30s to 30mins, the

secondary response will be activated to increase the active power output. As for the high frequency response, the decrease in active power output is achieved within 10s after the detection on the frequency deviation ramp.

When the WTGs operate in the frequency sensitive mode, they will need to operate in the deloading mode rather than on the maximum power point tracking point, such that they are able to increase or decrease their power output based on the system frequency change. The minimum requirement on the power change of the WTG for a 0.5 Hz frequency deviation can be found in Fig.1.11. It shows that the active power change is determined by the actual loading of the WTG. The actual active power contributing to the frequency support should be at least the operating level provided. It should also be noted that the requirement on the active power change for other frequency deviation values can be determined accordingly as Fig.1.11. In

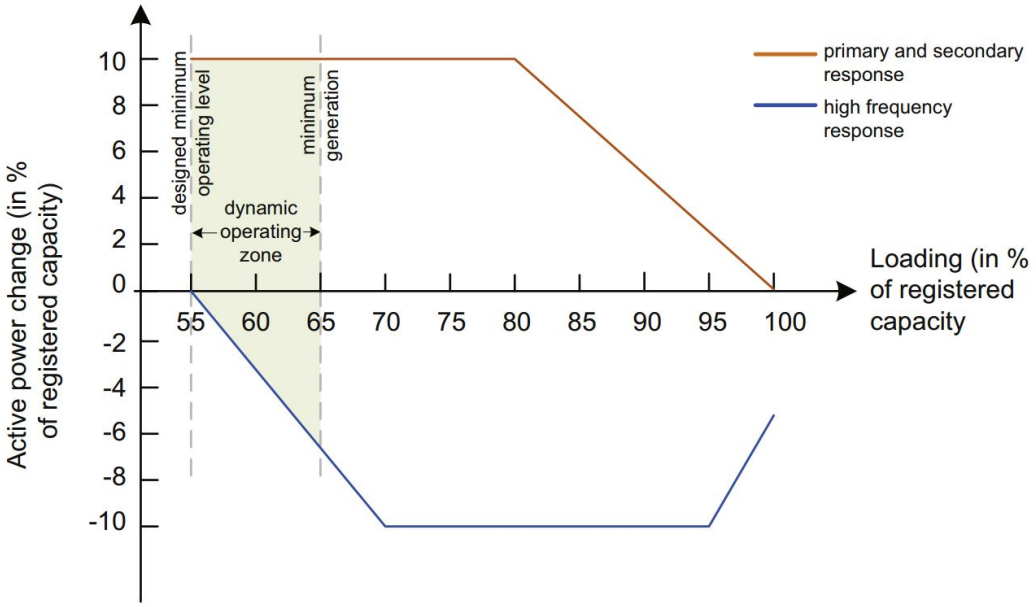

Figure 1.11: Minimum requirement on the WTG active power change during a 0.5 Hz frequency deviation given by the UK grid code [5]

Fig.1.11, the minimum generation and designed minimum operating levels are also given by the grid code. The WTG should remain to output at least 65% of its rated power. For the designed minimum operating level, it shows the bound where the WTG needs to react to the high frequency response. At the designed minimum op-

erating level, the generators are also required to provide high frequency response only when the frequency deviation is above 0.5 Hz. Moreover, the deadband of the controllers used in the frequency sensitive mode is given which should be up to ± 0.15 Hz.

1.3.2 Grid Code Requirements of Ireland

The grid code of Ireland has given a specific requirement for wind power plants on their frequency control capability, where the operating margin is used to describe the power reserve. This operating margin is the additional power output of wind power plants to ensure that the system frequency deviation is limited and properly correctly during a frequency drop event. This operating reserve should include the primary, secondary and tertiary operating reserve band 1 and 2. This reserve is available to support system frequency up to 20 mins following a frequency event. Thus, as required by the Irish grid code, the wind power plants need to have system frequency support capability and provide primary and secondary reserves.

The primary frequency reserve will last up to 30 seconds after a frequency deviation event. Only SGs with the rated power above 60MW are required to ensure their primary reserves when the frequency is varied between 48.8 Hz and 50.2 Hz. The wind power plants should provide frequency support based on the power and frequency curve shown in Fig.1.12, which is provided by the TSO of the Irish power grid. Automatic controllers are installed in the wind power plants to act to activate the power reserves. According to Fig.1.12, it can be seen that the wind power plants will operate below the available active power at the normal frequency operation. The active power output of the wind power plant is set as shown by line 'B' - 'C'. If the system frequency falls below the frequency set at point 'B', the wind power plant should provide the frequency support by ramping up its active power output. Its ramp rate should follow the power/frequency characteristic curve given by line 'B' - 'A'. For a frequency rise event where the frequency is above point 'C', the wind power plant should reduce its active power output followed the curve defined by line 'C' - 'D' - 'E'. When the system frequency is equal to or above the frequency at point 'D' - 'E', the wind power plant should not output active power. During a

frequency deviation event, the primary frequency support provided by wind power plants should be activated immediately when the frequency is out of the deadband without the participation from TSO.

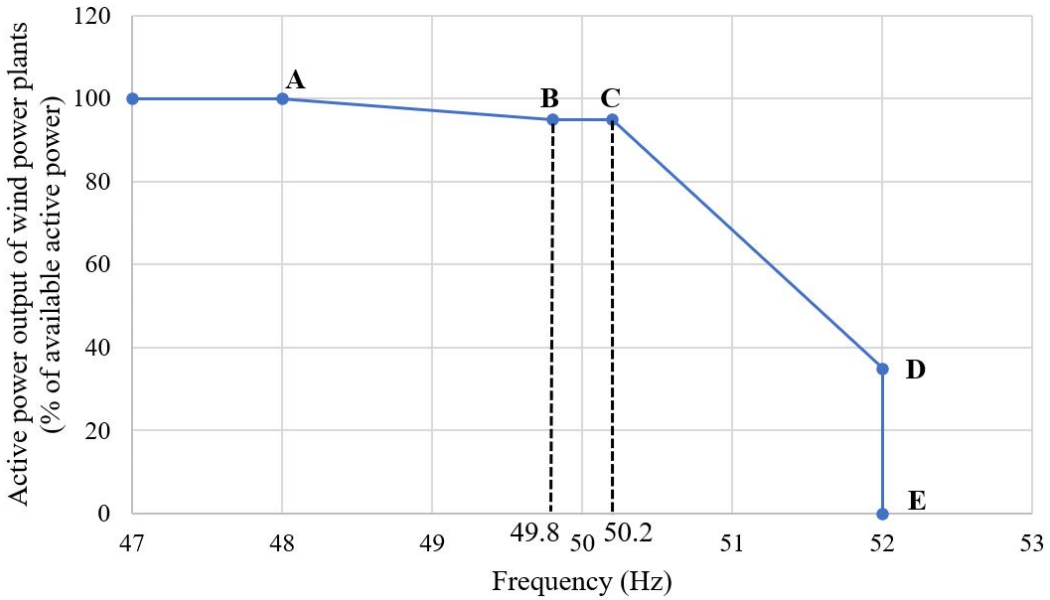

Figure 1.12: Droop response provided for wind power plants by the Irish grid code [6]

As for the secondary power reserve, it will contribute to the system frequency support from 5 seconds to 10 minutes following a frequency deviation event. Both automatic controllers and the TSO will be involved in deciding the secondary frequency support.

1.3.3 Grid Code Requirements of Hydro-Quebec

In 2005, the existing wind power generation integrated in Hydro-Quebec is 1500 MW and a planned 2000MW wind power generation will be added. A new grid code requirement is then given by Hydro-Quebec TransEnergie (HQT) to request the installed wind power generation with the frequency support capability, such that the system frequency stability can be maintained. The requirement indicates that the frequency support provided by wind power generation should only be activated during the major frequency deviation. Similar to the frequency support performance

provided by a SG with a 3.5s inertia constant, the WTG should be able to provide at least the same inertia response as a SG to support system frequency [42]. Moreover, the grid code requires that only the wind farms rated above 10MW must be equipped with a frequency control system to provide frequency support during a frequency deviation event in a short time period (less than 10 seconds) and the frequency control system should regulate frequency continuously [43, 44]. Simulation results are given and show that WTGs with inertia response can ensure frequency nadir is within its limit during a under frequency event and thus the automatic load shedding can be avoided [45].

In 2012, the HQT grid code is improved with detailed inertia emulation requirement on power contribution and the recovery phase [46]. In the revised grid code, the connected wind power plants are required to contribute to at least 6% of the rated power for inertia response. The duration of the inertia response should last at least 9s. In the recovery process, the maximum allowed power reduction of the wind power plant is 20% of the rated power. The recovery time for inertia emulation capability to be available again is 2 minutes [44].

1.4 Frequency Support Control Methods from Wind Turbine Generators

In general, the frequency support of WTGs can be provided in four stages, which are inertial emulation, primary frequency response, secondary frequency response and tertiary frequency response depending upon the time frame [7]. The widely studied frequency support approach provided by WTGs is achieved by adding an additional signal into the active power reference for the WTG to adjust the output power of the WTG to correspond to the power grid frequency variation.

1.4.1 Inertia Emulation Response

Following a sudden generation and load imbalance, the kinetic energy stored in the rotating mass of the wind turbine blades and generator rotor can be used to

support system frequency [7]. As shown in (1.4.1), the available kinetic energy ΔE which can be released for frequency support between t_0 to t_1 depends on the moment of inertia J, initial rotor speed ω_0 and rotor speed deviation $\Delta\omega = \omega_0 - \omega_1$.

$$\begin{aligned}\Delta E &= \int_{t_0}^{t_1} \Delta P_{in}(t)\mathrm{d}t = \frac{1}{2}J\left(\omega_0^2 - \omega_1^2\right) \\ &= \frac{1}{2}J\left(2\omega_0\Delta\omega - \Delta\omega^2\right)\end{aligned} \tag{1.4.1}$$

where ΔP_{in} is the power provided in inertial emulation control. Up to now, the inertial emulation control can be achieved in three ways which are natural inertia control, step-wise inertia control and virtual inertial control [7].

Natural inertial control

The natural inertial control provided by a WTG is achieved by changing its active power output during a frequency drop event. The active power output will be changed based on the real-time measurement of ROCOF or the frequency deviation or both, to emulate the inertia response of a SG in a power system [47–50]. The ROCOF dependent natural inertial control can be accomplished through one shot or continuous $\mathrm{d}f/\mathrm{d}t$ control approach [48, 51].

The one shot $\mathrm{d}f/\mathrm{d}t$ control is achieved using a pre-designed lookup table, where the desired active power output is decided by the measured $\mathrm{d}f/\mathrm{d}t$ value. In [51], when the active power of a wind power plant is below 1 pu while greater than 0.95 pu, a temporary rotor speed restoration will be used.

The continuous $\mathrm{d}f/\mathrm{d}t$ control strategy will use the real time ROCOF to output the desired active power during a frequency event. Similar to the frequency support behaviour of SGs, the power and torque provided by the WTG during a frequency contingency can be expressed by the following.

$$\Delta P_{in} = K_{in}\omega_s\frac{\mathrm{d}\omega_\mathrm{s}}{\mathrm{d}t} \tag{1.4.2}$$

$$\Delta\tau_{in} = K_{in}\frac{\mathrm{d}\omega_\mathrm{s}}{\mathrm{d}t} \tag{1.4.3}$$

where K_{in} is the inertia controller gain, ω_s is the synchronous speed in per-unit. ΔP_{in} is the power obtained from the stored kinetic energy in the WTG rotor. Nor-

mally, the $\mathrm{d}\omega_{\mathrm{s}}/\mathrm{d}t$ in (1.4.2) and (1.4.3) can be changed to $\mathrm{d}f/\mathrm{d}t$, such that the inertia response of WTG depends on the ROCOF directly. According to the swing equations of the SGs, the K_{in} can be chosen to equal to the twice of inertia constant H of WTG [52, 53]. The block diagram of the continuous $\mathrm{d}f/\mathrm{d}t$ controller is given in Fig.1.13. By increasing the K_{in} and relaxing the power rate rate limit, the natu-

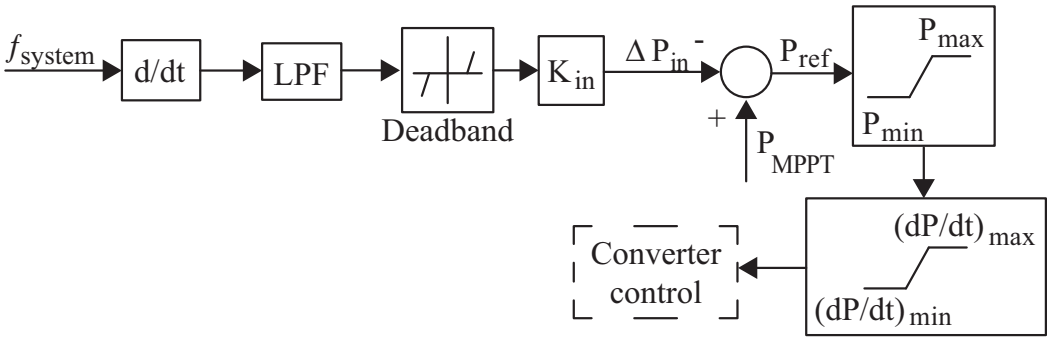

Figure 1.13: Block diagram of a continuous $\mathrm{d}f/\mathrm{d}t$ control approach

ral inertia response performance can be improved [54]. When the measured $\mathrm{d}f/\mathrm{d}t$ is used in the inertia response, a low pass filter (LPF) is normally added after the derivative block to reduce the effect of the noise during measurement [7].

Two types of frequency deviation based natural inertial response are commonly used as given in [49, 50]. According to the droop control gain, the frequency deviation based natural inertial response can be classified as a fixed-droop and variable-droop control. The power provided by the droop control is expressed as:

$$\Delta P_{in} = \left(-\frac{1}{R_{dr}}\right)\Delta f \tag{1.4.4}$$

where R_{dr} is the droop coefficient. The block diagrams of a fixed-droop and variable-droop control are given in Fig.1.14 and 1.15, respectively. For the variable-droop control approach presented in Fig.1.15, the droop coefficient is varied based on the ROCOF and the steady state rotor speed ω_0, such that the natural inertia response can be improved by using an optimal controller gain to improve the frequency nadir and avoid over-deceleration of the WTG. Moreover, a high-pass filter (HPF) is used to avoid the unnecessary droop response after the fault is cleared, such that the WTG can return to its MPPT operation [50, 55].

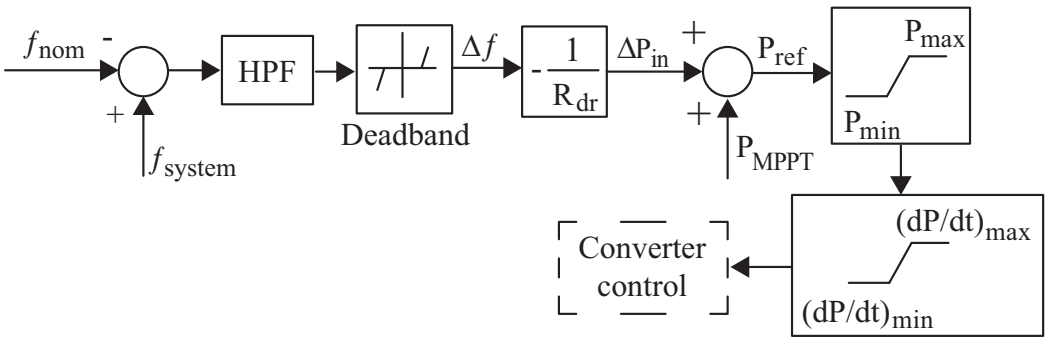

Figure 1.14: Block diagram of a fixed droop control approach

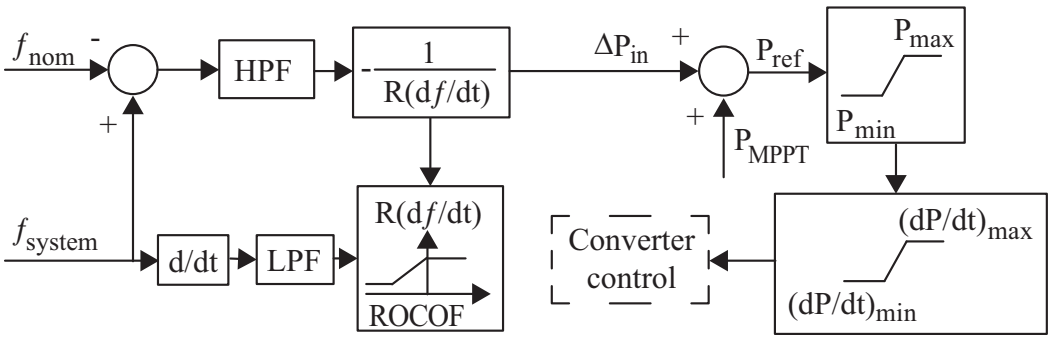

Figure 1.15: Block diagram of a variable droop control approach

According to the above discussion, it can be concluded that a larger K_{in} can mitigate the ROCOF during a frequency event, where the frequency nadir is unaffected. In contrast, a larger $\frac{1}{R_{dr}}$ can help on improving the frequency nadir. Hence, a combination of the $\mathrm{d}f/\mathrm{d}t$ control and droop control is preferred in the natural inertia response, where the control objective on the ROCOF mitigation and frequency nadir improvement can be accomplished and also the secondary frequency drop can be avoided [49, 50].

Step-wise inertia control

The step-wise inertia control is achieved to provide a constant active power output following a frequency event. As a type of inertia control, the output is obtained by releasing the kinetic energy stored in the WTG and it can last up to ten seconds under different wind speed operations [56–60]. Comparing to the natural inertia control, inertia control output power can be determined differently by using the desired amount and duration. Meanwhile, the inertia response provided by the step-wise inertia control is faster and more reliable as the real time frequency does not need to be measured to determine the output power. It has been found that the frequency nadir can be improved significantly after a frequency event and also a smooth recovery of kinetic energy can be achieved [47]. The performance of a step-wise inertia control can be affected by several factors, which includes the wind speed, inertia constants of WTG, output power of inertia response, time duration and also ramp rate limit [7].

One step-wise inertia control approach is designed by modifying the reference rotor speed of the WTG to ensure a constant inertia response power output during a frequency event. Thus, the constant inertia response power can be calculated using (1.4.5).

$$P_{\text{in}}\, t = \frac{1}{2} J \omega_{r0}^2 - \frac{1}{2} J \omega_{rt}^2 \tag{1.4.5}$$

where t is the time duration of inertia response, ω_{r0} is the initial rotor speed and ω_{rt} is the rotor speed at time t. Using (1.4.5), the reference rotor speed can be obtained

as:

$$\omega_{ref} = \omega_{rt} = \sqrt{\omega_{r0}^2 - 2\frac{P_{in}}{J}t} \tag{1.4.6}$$

As shown in Fig.1.16, the block diagram of a step-wise inertia control is provided, where the reference rotor speed ω_{ref} is achieved using (1.4.6).

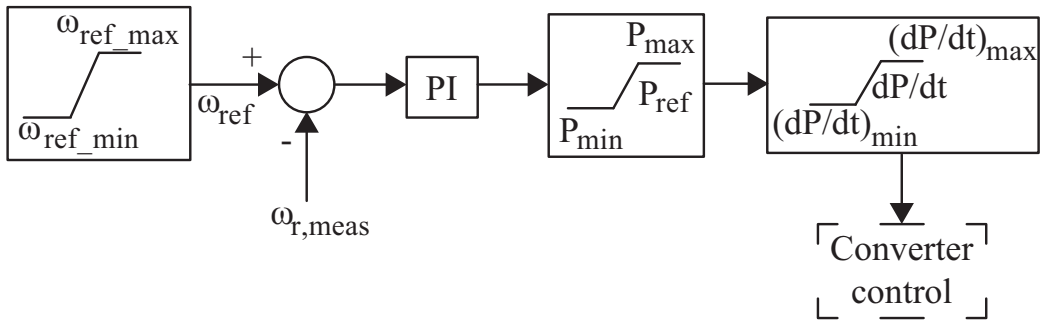

Figure 1.16: Block diagram of a step-wise inertia control based on ω_r [7]

Another step-wise inertia control is achieved by temporarily overproducing the active power of a variable speed wind turbine, where a temporary power ΔP_{op} was added on P_{MPPT} [8]. In the study, a 0.2 pu active power can be overproduced and it can last at least 10 seconds. The block diagram of the step-wise inertia control based on temporary overproduction is illustrated in Fig.1.17, where the reference power P_{ref} can be a constant or a variable value based on the strategy selected in the overproduction period.

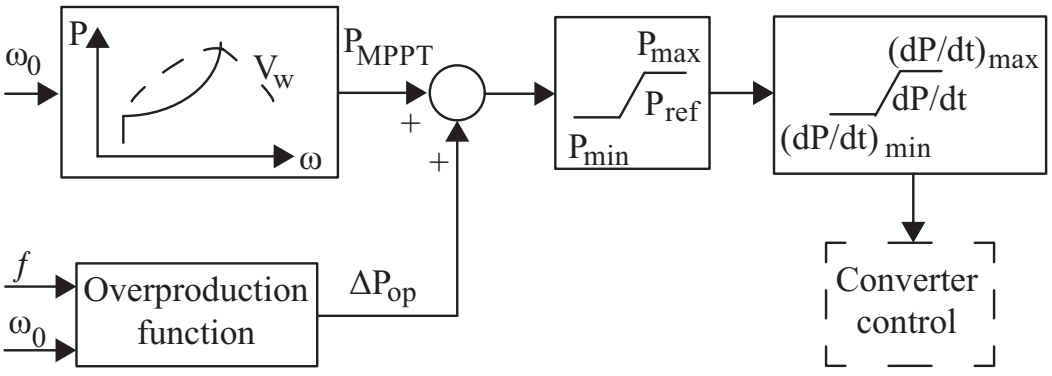

Figure 1.17: Block diagram of a step-wise inertia control based on temporary overproduction [8]

In the inertia response process, the overproduction period will be terminated once a minimum rotor speed ω_{min} is reached. After the overproduction period, the electrical power of WTG will be less than the available mechanical power by the amount defined as under-production power ΔP_{up}. Due to this situation, the rotor speed of the WTG will be able to return to its MPPT based on the current wind speed. When ΔP_{up} is increased, the under-production period can be shortened such that the rotor speed of the WTG can be recovered faster. However, if a larger ΔP_{up} is set, a secondary frequency drop may be more serious. Hence, based on deloaded operation, an improved primary frequency response through temporary overproduction of active power is proposed in [61], such that the secondary frequency drop can be avoided and the frequency deviation can be minimised. In [59–62], two other approaches are proposed for DFIGs and PMSGs to add the incremental active power on the basis of the MPPT power and torque curve, which can help rotor speed of WTG return to its pre-event value when temporary overproduction period ends.

Virtual inertia control

In the recent research, a novel inertia control strategy, which is called as virtual inertia control (VIC), is proposed to use the hidden inertia of wind turbine blades to achieve fast frequency support [7]. One approach is proposed to change the active power output on the basis of the system frequency deviation. In order to provide fast frequency support using this approach, the operating point of a WTG will be shifted from a MPPT curve to a VIC power curve to compensate power imbalance during a frequency event. Equation (1.4.7) defines the coefficient K_{VIC} of the VIC curve and is used to smoothly recover the rotor speed to the desired MPPT operation point [9]. The lower and upper limit of the VIC power curve can be obtained using $K_{VIC_{min}}$ and $K_{VIC_{max}}$ to ensure the stable operation of the variable speed wind turbine under time-varying wind speed conditions.

$$K_{VIC} = \frac{\omega_{r0}^3}{(\omega_{r0} + 2\pi\lambda\Delta f)^3} k_{opt} \tag{1.4.7}$$

As shown in (1.4.7), K_{VIC} is a function of the frequency deviation Δf. λ is the virtual inertia coefficient, which is defined as the ratio of the change of rotor

and grid angular speed during a frequency event, $\lambda = \Delta\omega_r/\Delta\omega_s$. k_{opt} is the MPPT curve coefficient. ω_{r0} is the initial rotor speed. Note that the kinetic energy released of a variable speed wind turbine during the rotor speed changing from ω_{r0} to ω_{r1} is equivalent to the kinetic energy released of a SG from ω_{s0} to ω_{s1}. The block diagram of VIC is given in Fig.1.18. A washout filter is added to eliminate the dc component of frequency error in the steady-state [9].

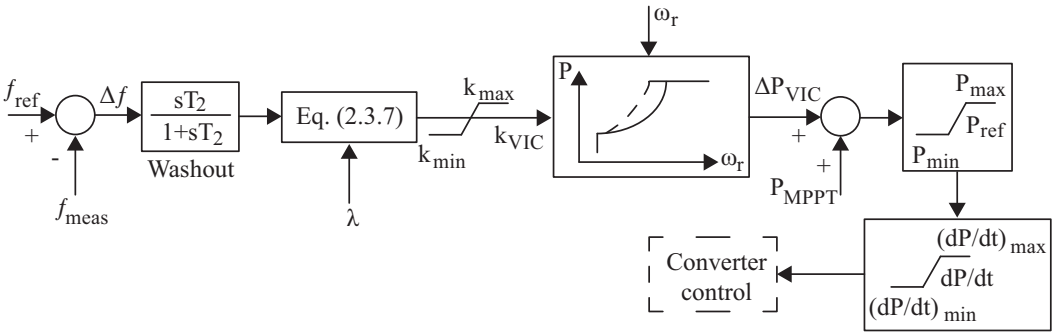

Figure 1.18: Block diagram of a virtual inertia control [9]

For the design of VIC coefficient, several approaches are proposed and described in [57,63–65]. In [57], an optimised controller is designed for WTG VIC to enhance the frequency support capability in a diesel generator dominated power system. The linear quadratic regulator approach is used to design the optimal VIC coefficient K_{VIC}. In [63], a variable virtual inertia controller is designed and implemented to enhance the frequency support capability of WTG at the start of the frequency contingency. As shown in (1.4.8), the controller inertia coefficient is changed following a linear decreasing function, such that the maximum power is provided at the start of the frequency support and the coefficient equals to zero when minimum rotor speed is reached.

$$H_{synt}\left(\omega_r\right) = H_{\max}\left[1 + \frac{\omega_r - \omega_{r0}}{\omega_{r0} - \omega_{r,\min}}\right] \tag{1.4.8}$$

[64] proposes a variable proportional coefficient VIC scheme to reduce the impact of WTG frequency support on grid frequency dynamics. The variable coefficient $K_{VIC} = 1 + k_{sup}\Delta f$ is adaptively regulated based on the frequency deviation, where k_{sup} is a constant. Two virtual inertia controller tuning approaches are proposed in [65], which are called as the worst case and optimal tuning approaches.

Using the worst case approach, the virtual inertia controller gains are set based on the minimum WTG rotor speed. With the optimal tuning approach, the controller gains are optimised considering the minimum rotor speed, maximum WTG output power and the maximum allowed change rate of the output power simultaneously.

Comparing the inertia response provided by the natural inertia control and VIC, it can be found that a real time measurement of the system frequency is needed for both control approaches. Meanwhile, the inertia response performs on the MPPT operation [7]. However, the major difference is that the secondary frequency drop can be eliminated in the VIC due to the K_{VIC} defined in (1.4.7).

The comparative simulation results of the above three inertia controls were provided in [7]. It can be concluded that the VIC showed the best performance as it can achieve the smallest ROCOF and the highest frequency nadir. The ROCOF was also mitigated with step-wise inertia control. However, the secondary frequency drop is obvious because of the rotor speed recovery. In contrast, the other two inertia controls could eliminate this issue.

In addition to the above three classic inertia controls, an alternative approach is proposed in [66] for DFIG to contribute to the inertia response by directly changing the phase-locked loop parameters. Moreover, a novel virtual synchronous control is presented in [67], where the DFIG provided the inertia response to a weak grid. Without the requirement on the conventional phase-locked loop (PLL) to synchronise to the grid, the DFIG can directly synchronise to the grid through active power control with virtual synchronous control approach. In this way, the DFIG can naturally support system frequency using inertia response similar to the conventional SGs and the system frequency stability can be improved.

1.4.2 Primary Frequency Response

Traditionally, wind turbines operate under the MPPT point to extract the maximum power from wind. However, in order to contribute to the primary, secondary and tertiary frequency response, the WTGs will be operated under the so-called suboptimal mode through the deloading control. In case of a frequency disturbance event, the WTGs are always able to support a certain amount of active power by

using the available power reserve.

Normally, the power reserve can be obtained through three approaches, which are 'Balanced' control, 'Delta' control and 'Fixed reserve' control. Balanced control sets a constant percentage of the rated power as the reserve [53]. A fixed proportion of the maximum available active power is reserved in the delta control [68–70]. When a fixed reserve control is used, the reserve achieved will be a fixed amount of the active power [71]. The mathematical expressions of reference power for the above three control approaches are given as follows:

1. Balanced control

$$P_{ref} = \begin{cases} P_{de} & P_{de} \leq P_{MPPT} \\ P_{MPPT} & P_{de} > P_{MPPT} \end{cases} \tag{1.4.9}$$
$$P_{de} = [0, \ldots, P_{Rated}]$$

2. Delta control

$$P_{ref} = \begin{cases} (1 - K_{Reserve})\, P_{MPPT} & P_{MPPT} \leq P_{Rated} \\ (1 - K_{Reserve})\, P_{Rated} & P_{MPPT} > P_{Rated} \end{cases} \tag{1.4.10}$$
$$K_{\text{Reserve}} = [0, \ldots, 1]$$

3. Fixed reserve control

$$P_{ref} = \begin{cases} 0 & P_{MPPT} \leq \Delta P_{Reserve} \\ P_{MPPT} - \Delta P_{Reserve} & P_{MPPT} \leq P_{Rated} \\ P_{Rated} - \Delta P_{Reserve} & P_{MPPT} \geq P_{Rated} \end{cases} \tag{1.4.11}$$
$$\Delta P_{Reserve} = [0, \ldots, \Delta P_{\max}]$$

where P_{ref} is the active power reference of the WTG; P_{MPPT} is the maximum wind power; P_{Rated} is the rated power of the WTG; $K_{Reserve}$ is the fixed coefficient of available maximum active power; $\Delta P_{Reserve}$ is the fixed active power used as spinning reserve; $\Delta P_{\max}$ is the maximum active power reserve.

Comparing the three reserve control approaches, it can be found that the delta and fixed reserve achieve higher energy efficiency than the balance. This is because they provide the long-term power reserve and less wind power curtailment. In [72],

it has been reported that the offshore wind farms can provide 5% of their rated power as the spinning reserve and they can sustain this reserve for up to 89% event duration time under variable wind speed operations. However, with the balanced control approach, the time-varying wind power output can be smoothed, such that the impact of uncertainties caused by intermittent wind power in the power system operation can be effectively reduced [48,69,73–75]. It should be noted that accurate wind speed measurement and the upper limit of the WTG rotor speed will affect the power reserve margin [54, 74]. The research in [76] proposed a dynamic reserve allocation approach where the total required power reserve of a wind farm will be separated and given based on the current wind speed of individual wind turbine. In [7], the power reserve provided by the balance ($P_{de} = 0.8$), delta($K_{Reserve} = 0.2$), fixed reserve ($\Delta P_{Reserve} = 0.2$) under different wind speed is compared. It can be found that the balanced control approach will only provide a constant power reserve when the active power of the WTG is above 0.8 pu. When the active power is below 0.8 pu, the WTG will operate at MPPT mode. For the delta control approach, its power reserve is increased with the rise of wind speeds. When the wind speed reaches the rated wind speed (12m/s), the power reserve will be maintained at a constant value, 0.2 pu. Finally, the fixed reserve control approach will be ensured as 0.2 pu of the rated wind power under a wide wind speed operation range.

Rotor speed control based deloading approach

As shown in Fig.1.19, the rotor speed control based deloading approach can be achieved by shifting the operating point of the wind turbine left or right of its MPPT operating point while the rotor speed will be maintained below its upper limit. The active power of WTG can be changed between P_{de} and P_{max} using the rotor speed between $\omega_{r,de}$ and ω_{max} [48, 56]. In [7], the reference power of a deloading WTG with a given rotor speed can be calculated using a linear equation as shown in (1.4.12) or a pre-defined look-up table [74].

$$P_{ref} = P_{de} + (P_{max} - P_{de}) \left(\frac{\omega_{r,de} - \omega_{r,meas}}{\omega_{r,de} - \omega_{r,max}} \right) \tag{1.4.12}$$

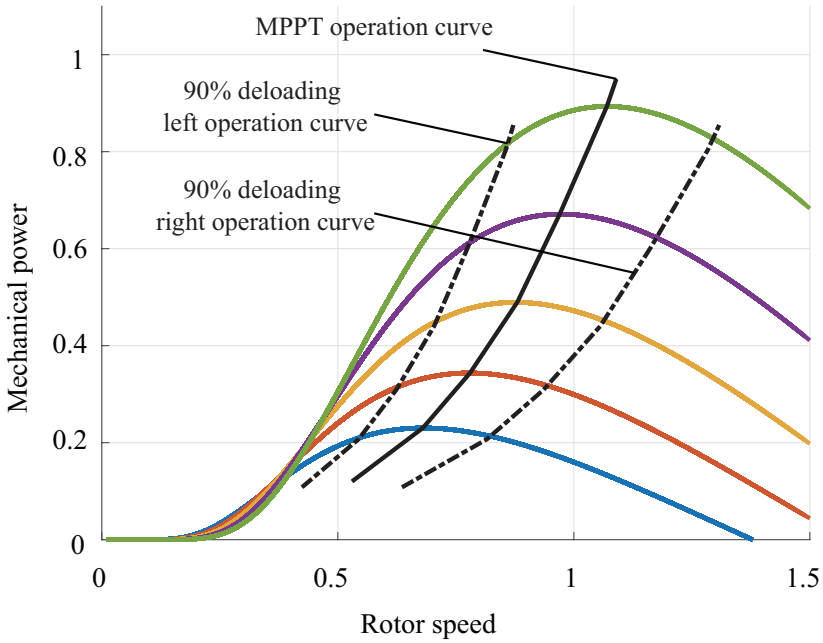

Figure 1.19: 90% WTG deloading operation curve

where P_{max} is the maximum power; P_{de} is the deloading power; $\omega_{r,de}$ is the rotor speed which can achieve P_{de}; $\omega_{r,meas}$ is the measured rotor speed and $\omega_{r,max}$ is the maximum rotor speed which can obtain P_{max}.

In Fig.1.19, the 90% deloading left operation curve is less preferred as it will cause instability issues, where the wind turbine is easy to stall during a under-frequency event. Therefore, the wind turbine will be operated at the 90% deloading right operation curve, such that the wind turbine can provide a stable frequency support in the whole wind speed operation range [48]. Another advantage of using the right operating curve is that the WTG is capable of providing the frequency response through a combination of reserved active power and stored kinetic energy. This is because the rotor speed can be decreased from the deloading operation curve to its MPPT curve. Moreover, it can also reduce the tear and wear losses of pitch angle actuation comparing to the pitch angle control based deloading approach, where the power reserve is obtained by pitch angle controller alone.

To ensure the rotor speed is below its allowed maximum value ω_{max} during the medium and high wind speed operations, the deloading control objectives are de-

signed specifically for the different wind speed operations and the secure operation constraints are set. For the low wind speed operation, only the rotor speed control is needed for the deloading. The combination control of rotor speed and pitch angle will be used in the medium speed operation. During the high wind speed operation, a modified pitch angle control is designed to achieve the deloading operation [48, 55, 56].

Pitch angle control based deloading approach

In general, the pitch angle control of a wind turbine is to prevent the overloading of the generator and converters and also overspeeding of the rotor [77]. In order to participate in the system frequency regulation, the original pitch angle control strategy has to be modified. An initial pitch angle β_0 will be set to ensure a certain amount of the power reserve for the primary frequency response purpose. Considering the servo time constant of the pitch angle controller, the speed of the pitch angle control based deloading approach is much slower than the rotor speed control based deloading approach, where the rotor speed control is achieved through fast power converter control [7].

Primary frequency control

Primary frequency response is normally activated when a frequency deviation exceeds a scheduled value through automatic governor response [7]. In the traditional power system, this response is provided by the governor droop control of a SG, where the output power of the governor is controlled by the frequency deviation and droop controller parameters [37, 53, 76, 78–80]. Similar to the SG, when the frequency deviation exceeds the allowed threshold, the primary frequency support of the WTG is normally activated at a few tens of seconds and it can last for up to 15 minutes [79]. As the frequency support at the primary frequency control stage is activated after the inertia response and before the secondary frequency control, it is very important for primary frequency control to achieve steady state frequency deviation mitigation and ensure zero steady state frequency deviation [7].

Different to the inertia response, the primary response requires the WTG to operate under deloading condition to ensure that a sufficient amount of power reserve is available in corresponding to a frequency event. The capabilities of WTG primary frequency response are mainly evaluated from four aspects, which are delay time, ramp rate, magnitude and response speed [81].

Based on the conventional governor droop response of primary frequency control, the droop control of the WTG adjusts its active power corresponding to the frequency deviation through the power converter control. During a frequency event, the active power output of WTG will be increased or decreased to react to the grid frequency deviation. The relationship between the active power output of a droop control and the frequency deviation is given in (1.4.13).

$$\Delta P_{dr} = K_{dr}\left(f - f_{ref}\right) \tag{1.4.13}$$

where f_{ref} is the reference frequency. The droop control gain is defined as the inverse of speed droop constant R which is shown in (1.4.14).

$$R = \frac{\Delta f}{\Delta P_{dr}} = -\frac{1}{K_{dr}} \tag{1.4.14}$$

According to the grid code [5, 6], the speed droop constant is normally chosen between 3% and 5% for a SG. It has been reported in [69] that a large K_{dr} can mitigate the steady-state frequency deviation without an obvious impact on the system small signal stability.

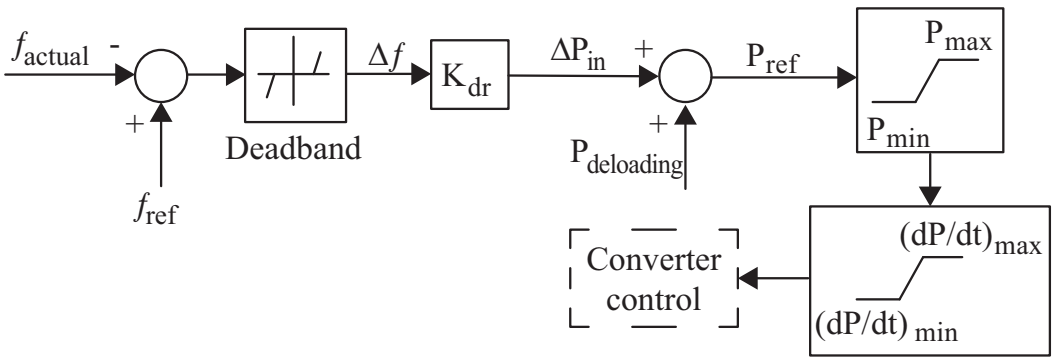

Figure 1.20: Block diagram of a droop response

Fig.1.20 shows the block diagram of the droop response, where the droop response performance is determined by droop slopes, deadband and power ramp rate. These parameters should be carefully chosen to ensure the power output of the droop response is within the available power reserve margin [71, 82–84]. By properly selecting the deadband of the droop response, it can prevent frequent droop controller activation to small frequency deviation [85]. In addition, according to the system operational requirements, both symmetrical and asymmetrical droop can be used in the system frequency response.

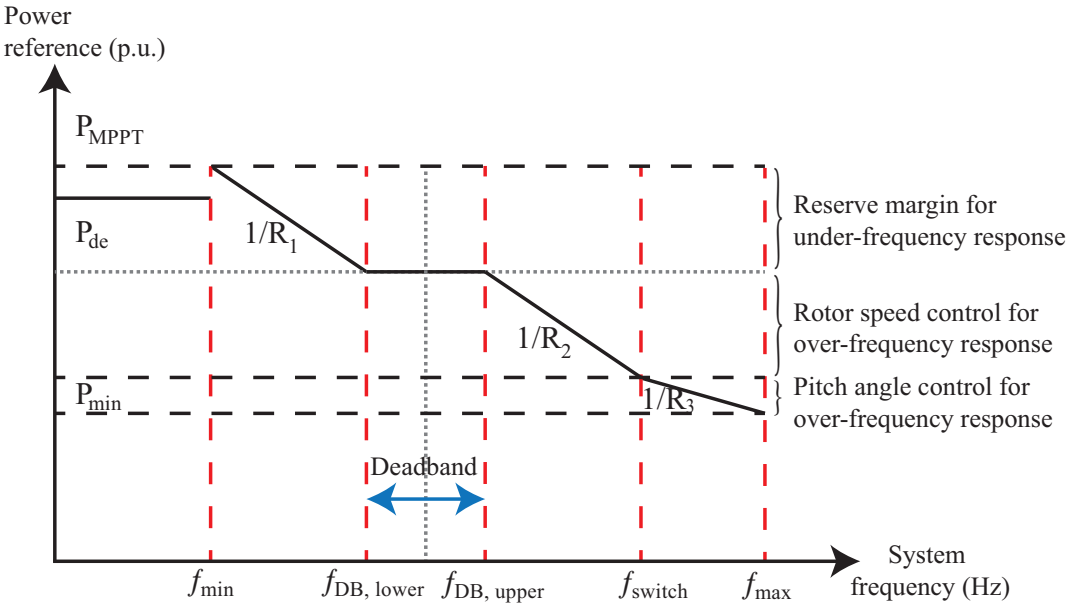

Figure 1.21: Frequency and power characteristics of a droop response

The characteristics between system frequency and power reference is set as shown in Fig.1.21. The active power reference is obtained using (1.4.15).

$$P_{ref} = \begin{cases} P_{MPPT} & f \leq f_{\min} \\ P_{de} + (1/R_1)\,\Delta f & f_{\min} < f \leq f_{DB,lower} \\ P_{de} & f_{DB,lower} \leq f \leq f_{DB,upper} \\ P_{de} - (1/R_2)\,\Delta f & f_{DB,upper} < f \leq f_{switch} \\ P_{de} - (1/R_3)\,\Delta f & f_{switch} < f \leq f_{max} \end{cases} \tag{1.4.15}$$

where $f_{DB,lower}$ and $f_{DB,upper}$ define the lower and upper deadband limit; f_{switch} is the frequency to switch from rotor speed control to pitch angle control. For the

system frequency drops below $f_{DB,lower}$, the active power of WTG will be controlled to increase until its output power reaches the P_{MPPT} for the current wind speed. If the system frequency is above $f_{DB,upper}$, the active power of WTG will be decreased by accelerating the rotor. When the system frequency is above f_{switch}, the rotor speed of WTG reaches its maximum value. At this time, the pitch angle control will be enabled to limit the active power with a higher pitch angle β, where the rotor speed is maintained at its maximum value. It should be noted that the value of R_3 is mainly depends on the pitch angle variation range [86].

According to the droop control parameters, the existing droop control approach can be divided as the static droop and dynamic droop control. The static droop control provides the droop control similar to the governor droop control of a SG, where the droop control gain K_{dr} is a constant and the slope of droop curve is fixed [7]. The active power output of a WTG depends on the frequency deviation. It can be found that the static droop control approach can successfully arrest the frequency nadir and mitigate the steady state frequency deviation [47, 54, 87–92].

The dynamic droop control approach will adjust the K_{dr} and deadband for the droop control curve based on the ROCOF, deloading level or the real-time wind speed [7]. With this control approach, a trade-off between the frequency response performance and the impacts on the structural loading is ensured. [93] shows that the dynamic droop control approach can provide an improved primary frequency response performance without the heavy impact on the mechanical components of the wind turbine, such as the shaft and its tower. Comparing to the static droop control approach, the dynamic droop control approach can also achieve the better frequency nadir and the frequency recovery process. In addition, the required strong frequency response at low wind speed is enhanced as the static droop control approach can only provide a limited active power output as its reserve is insufficient.

An improved frequency response can be achieved by a real time-varying droop coefficient as well. In [85], it has been reported that a small droop coefficient of a static droop control approach will lead to WTG instability, whereas a large coefficient can cause system oscillation during the rotor speed recovery stage. With the dynamic droop control approach, the shared active power within a wind farm can be

optimised. The individual WTG can have a specific active power output requirement for frequency support based on the reserved power considering the real time wind speed faced. [74] adopts a similar control strategy where a variable droop control approach was proposed. The droop control coefficients of the wind turbines were optimised based on the experienced wind speeds. This was because the available power reserve was determined by the wind speeds. The overall frequency performance was improved comparing to the static droop control approach and a more smoothed steady state frequency was also achieved.

1.4.3 Secondary Frequency Response

Secondary frequency response can be activated at tens of seconds and till several minutes after a frequency event [79]. It can take part in the normal operating conditions and also the emergency frequency events [53, 76]. According to the load change which causes a frequency deviation, the required power output signals will be sent to each participating WTs by TSOs to provide frequency support. Thus, the secondary frequency will normally take several minutes to react [94]. Fig.1.22 shows the schematic diagram of a wind power plant participating in system secondary frequency response. The set point for each WT will be determined mainly based on participation factors, which are calculated using an optimisation approach considering the ramp rates, available reserves, the transmission line power flow limits and generator costs [95].

The secondary frequency control strategies proposed in [48, 53, 96] were based on the mechanical power reserve obtained using pitch angle control of WTs. Another control strategy of the secondary frequency response was proposed in [97] which is achieved by using the mechanical power reserve achieved through the rotor speed regulation.

1.4.4 Tertiary Frequency Response

After the secondary frequency response, the tertiary frequency control will participate and it takes the longest time to make the decision which can be from several

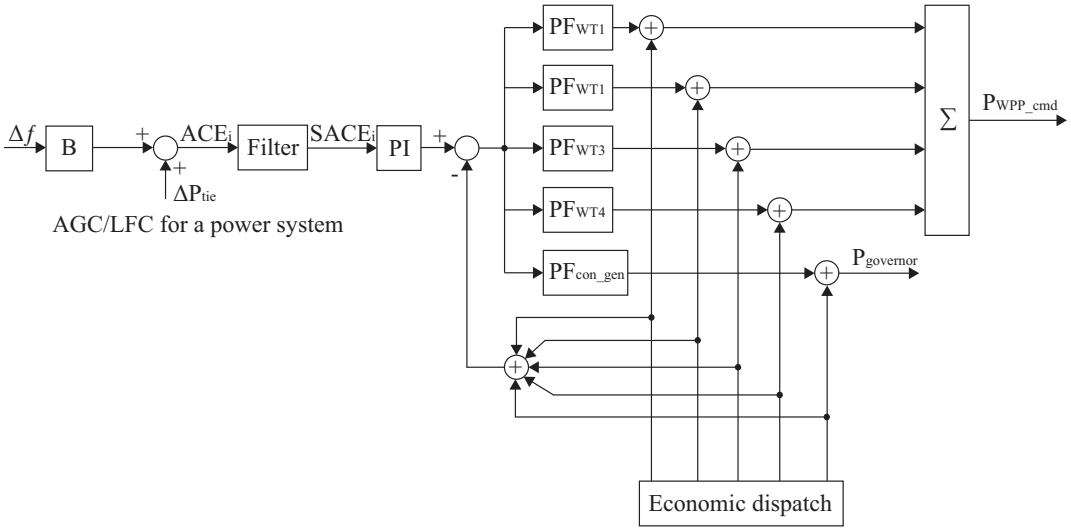

Figure 1.22: Schematic diagram of a secondary frequency control [7]

minutes to hours [98]. After the consideration of the whole system economic dispatch, optimal power flow and the power reserve and restoration of the wind power generators, the tertiary frequency control signal is provided by the TSO. The active power output references for SGs and WTGs are set based on the TSO instructions. Considering the tertiary frequency control, the electricity markets are normally in two types which are an intraday real-time market where economic dispatch is updated by minutes and a day-ahead market where the economic dispatch is determined under the daily economics [7].

1.4.5 Control Methodologies for Improving Frequency Support Performance

Gains of the inertia response (IR) and droop (DR) control loops are usually set up based on the grid code requirements. Inappropriate selection of IR and DR control loop gains will lead to insufficient frequency support performance and will also affect system stability. Considering sufficient kinetic energy can be released by DFIG, if the IR control loop gain is large, frequency nadir (FN) can be improved while avoiding the over-deceleration of DFIG. However, over-voltages or stall may occur. On the contrary, a small IR control loop gain can avoid over-deceleration,

whereas the contribution on improving the FN is limited [99]. A novel idea to calculate IR control loop gain was proposed from the perspectives of avoiding wind turbines from stalling in [48]. The IR control loop gain was calculated through the worst-case analysis. A linear gain DR control loop was proposed to approximate the DR control loop with the nonlinear droop gain to be feasibly implemented in the dynamic equivalent model of the wind farm [100]. Approaches have been proposed to tune suitable frequency support controller gains for improving the frequency support performance of DFIG-WTs. Based on the releasable kinetic energy from WTs, the IR and DR control loop gains were adjusted by the rotor speed of DFIG in [101]. A time-variable droop characteristic was proposed for WTGs to support frequency and avoid frequency instability in [102]. Chau et al. [103] proposed a novel control strategy which use frequency deviation of local SGs with different weighting to improve the system primary frequency response and enhance low frequency oscillation. The DR control loop gain was designed by using particle swarm optimisation approach to achieve better frequency support performance under different system parameters [104].

Robust Control

Horowitz was the first who formulated a clear robust feedback control problem in 1963. The research indicated that model uncertainty was the main factor which can determine the performance of feedback controller and the robust controller was then designed based on the root-locus and frequency support approaches for the models with uncertain parameters [105]. Then in the early 1970s, many researchers noticed that optimal control theory cannot ensure feedback control performance in the presence of differences between the models and reality [106]. At this point, more attention was paid to robust control and the evolution of control theory research was shifted from optimisation to robustness.

Robust control is to design the controller which is able to guarantee system stability and meet the design performance specifications considering the modelling errors and random external disturbances [107]. In other words, the designed controller using robust control approach should ensure its control performance is below

a predefined norm in the presence of uncertainties. Normally, the design performance specifications can be the stability, control effort optimisation and disturbance rejection, etc [10].

The robust control design approach includes the Linear Quadratic (LQ), Linear Quadratic Gaussian (LQG), H_2 and H_∞ control techniques. Among the robust control approach, H_∞ based robust control approach is the most popular. H_∞ robust control approach formulates the control objectives based on the weighting functions in the frequency domain [108]. The robust stability and robust performance are achieved through H_∞ norm minimisation of the cost function for the closed-loop system. In contrast to H_∞, LQ and H_2 control are purely designed based on the time domain performance specifications. The LQG control approach is more effective for random noise rejections [109].

In [110–114], H_∞ based controllers were designed to ensure robust stability in a power system. The mixed-sensitivity H_∞ based controllers then developed to concern control performance expressed by multiple closed-loop transfer functions [10, 115, 116]. Regional pole placement constraints are considered in conjunction with mixed-sensitivity H_∞ control objective to guarantee satisfactory damping performance [10, 116, 117]. As the H_∞ control approach considers the several control specifications through weighted functions into a single objective problem in the frequency domain, its performance is inadequate for the realistic applications [107]. Thus, the robust control design is improved by combining various control approaches and formulating a multi-objective synthesis control problem. As discussed, H_2 control approach can achieve the control objectives on the transient behaviours and the noises can be measured by H_2 norm (LQR terms) effectively. The mixed H_2/H_∞ control problem in conjunction with regional pole placement is formulated, where the H_2 performance can ensure the system transient behaviours in time domain and H_∞ performance can guarantee robustness against model uncertainties. In [107, 118–121], mixed H_2/H_∞ robust control approach was used to design the robust wide-area damping controller.

With the robust control approach, the designed controller can provide superior performance on dealing with model uncertainties and random external disturbances,

such that a guaranteed performance can be ensured over wide operating points. This is especially desired where the power system is penetrated by high levels of wind power generation. Obviously, the robust control approach can ensure guaranteed performance at the cost of conservatism. However, it can still improve the controller performance over the classical design approach and is a preferred approach for the complex designs [122].

1.5 Motivations and Objectives

1.5.1 Motivations

With the increasing penetration of wind power in the power system, the system inertia is reduced significantly as the WTGs are connected to the power grid through inverters and provide zero inertia. To ensure the secure and stable operation of the system, the WTGs are required by the system operators to contribute to the frequency support. However, the supplementary frequency support controllers of WTGs deteriorate the system stability which needs to be fully analysed and controlled. Motivated by this, this thesis investigates the impact of the DFIG-WT with frequency support capabilities on the new oscillation mode introduced by the frequency support controllers and the torsional oscillation mode of the wind turbine drive train. Moreover, when the PLL is used to measure the grid frequency, the effect of the PLL on the new oscillation mode is also researched. Uncertainties, resulting from parameters, system operating points and external disturbances, are unavoidable of a power system with DFIG-WTs participating in the frequency support and thus affect the frequency support performance and system stability. Hence, this thesis proposes the controllers for the DFIG-WTs which can ensure satisfactory frequency support performance and system stability considering uncertainties.

Introduced New Oscillation Mode

When the DFIG-WT participates in system frequency support, it has been found that a new lightly damped oscillation mode will be introduced in the system which

will deteriorate system stability [35, 123]. Modal analysis indicates that this new oscillation is mainly dominated by the inertia emulation controller. The oscillation frequency of the new mode is between 0.5 and 2 Hz, which is in the power system low frequency oscillation range [38]. If the inertia control loop gain K_{in} is increased, the oscillation frequency and damping of the new mode will be decreased. System instability will occur for a large K_{in}, where the damping is negative. For an increasing droop control loop gain K_{dr}, the oscillation frequency will be increased whereas the damping is firstly increased and then decreased [35].

To avoid the impact of the DFIG-WT frequency support capability on the system stability, damping controllers were designed to improve the damping ratio of the introduced new oscillation mode. Conventionally, residue approach is used to design the damping controller [35]. As the residue approach is designed at one system operating point, the satisfactory damping performance can only be ensured at one specific condition. When uncertainties exist in the parameters, system operating points and external disturbances, the damping performance on the introduced new oscillation mode may be deteriorated and the system stability cannot be maintained. Hence, the introduced new oscillation mode is worth to be considered when there are uncertainties of DFIG-WT participating in frequency support.

Wind Turbine Torsional Oscillation Mode

In addition to the new oscillation mode, the frequency support controller of the DFIG-WT will also affect the torsional oscillation mode of WTs. When the DFIG-WT contributes to system frequency support, the mechanical system of the wind turbine and the electrical system are strongly coupled because of the frequency support controller [124]. The oscillation in the grid frequency will be transmitted easily to the wind turbine drive train and lead to the torsional oscillation, where the damping becomes deteriorated. Hence, the mechanism of the WTG frequency support controller on torsional oscillation mode damping has been studied thoroughly [125, 126].

Recent researches proposed damping controllers to mitigate the impact of frequency support controllers on the torsional oscillation mode of the WT. One possi-

ble approach is to control the energy stored in the DC-link capacitor of the WTGs to damp the torsional mode [87, 125]. In [35], the damping controller was designed based on the residue method. A band-pass filter was used to extract the torsional oscillation. The generator electromagnetic torque was adjusted to compensate the torsional oscillation, where it was implemented at the current control at the rotor side converter control. Similar to [35], the damping controller was improved by an adjustable band-pass filter [124]. Another kind of torsional mode mitigation added the damping controller in the droop controller [127]. As the controllers are designed for a specific frequency of torsional oscillation, the damping performance may be deteriorated under the effect of parameter uncertainties, time-varying system operating points and random external disturbances. Thus, it will lead to a poorly damped torsional oscillation mode and cause damage on the mechanical components of the wind turbine drive train. Obviously, when the uncertainties exist in the DFIG-WT contributing to system frequency support, the research on the torsional oscillation mode is important and needs to be considered.

In this thesis, to ensure the stability of both the power system and wind turbine during DFIG-WTs participating in frequency support, the impact of frequency support controller on the introduced new oscillation mode and wind turbine torsional oscillation mode is worth to be studied. This motivates the robust controllers design to ensure robust frequency support performance and satisfactory stability when there are uncertainties resulting from parameters, time-varying operating points and external disturbances.

1.5.2 Objectives

Considering the uncertainties from parameters, time-varying system operating points and random external disturbances, the objectives of this thesis are to design the controllers such that DFIG-WTs can achieve robust inertia emulation frequency support performance without affecting the stability of system and wind turbine drive train. More detailed objectives of this thesis are as follows:

- With the additional control loops, the DFIG-WT can be configured to have

the frequency support capability. However, a new poorly damped oscillation mode which is dominated by the additional frequency support control loops is excited and results in deteriorated system stability. Hence, a robust damping controller is designed to achieve robust damping performance on the new oscillation mode considering the uncertainties in the power system with DFIG-WTs participating in frequency support.

- Although the robust damping controller can damp the new excited oscillation mode well, the introduction of a supplementary damping controller will increase the complexity of the DFIG-WTs frequency support, which brings the idea of an integrated frequency support control loop. The robust frequency support performance can be considered in the design stage of control, such that a poorly damped oscillation mode is not excited and the stability can be ensured during frequency support.

- When the grid frequency and wind turbine is direct coupled by the additional frequency support control loops, the impact on the torsional oscillation of the wind turbine drive train cannot be neglected. Such poorly damped oscillation will cause the damage on the mechanical components of the drive train and consequently a reduced lifetime of the drive train. To suppress the poorly damped torsional oscillation under parameter uncertainties of wind turbine inertia and different wind speed, a robust damping controller is preferred to be designed and added to the wind turbine to ensure the robust stability of the wind turbine drive train.

- Moreover, as the PLL can be used to obtain the frequency at the point of common coupling for DFIG-WT contributing to frequency support, a poorly damped oscillation mode is found which is dominated by both PLL and the frequency support control loops. Therefore, robust damping controllers are designed to maintain robust system stability considering the impact of PLL parameters uncertainties and power grid strength variation.

1.6 Main Contributions

This thesis is based on the research work conducted on the robust inertia emulation control of DFIG-WTs participating in the system frequency support. With the additional frequency support control loop of the DFIG-WT, a poorly damped oscillation mode is introduced and the torsional oscillation mode of wind turbine is deteriorated. Moreover, the introduced new oscillation mode will be dominated by both PLL and inertia emulation controller when PLL is used to obtain the frequency. In order to ensure the frequency support performance with satisfactory damping performance on the oscillation mode, robust controllers are designed and equipped in the DFIG-WTs, where the control performance is robust against parameter uncertainties, time-varying operating points and random external disturbances. The main contributions include:

- The H_∞ mixed-sensitivity control approach is firstly proposed in designing a robust damping controller (RDC) to ensure robust stability of DFIG-WTs participating in system frequency support. A RDC is designed based on the H_∞ mixed-sensitivity control approach for the DFIG-WTs to provide robust damping performance on the new poorly damped oscillation mode introduced by the inertia emulation controller (IEC). Both small signal stability analysis and simulation results are obtained to show the robust damping performance against time-varying system operating points than the residue approach based conventional damping controller (CDC) in a single-machine infinity bus (SMIB) system, a two-area four-machine (4M11B) system and a New England New York 68-bus (16M68B) system.

- To avoid additional RDC design, an integrated inertia emulation controller (IIEC) is proposed for DFIG-WTs to simultaneously provide robust frequency support performance and satisfactory damping performance. A robust PD-type controller design approach is firstly proposed to design IIEC. The robust PD-type controller design approach is based on a H_∞ control theory with additional linear matrix inequality constraint on pole placement. Both small signal stability analysis and simulation results are obtained to show the robust-

ness of the designed IIEC than the conventional inertia emulation controller (CIEC) in a SMIB system, a 4M11B system and a 16M68B system. The performance of the IIEC and the CIEC plus RDC is also compared and the IIEC can achieve robust frequency support performance and satisfactory damping performance simultaneously as the CIEC plus RDC.

- In addition to the new excited poorly damped oscillation mode introduced by an IEC, it is found that IEC will deteriorate the WT torsional oscillation mode. On the basis of the DFIG-WT with a RDC, a robust torsional oscillation damping controller (RTODC) is then proposed to mitigate the impact of WT torsional oscillation. The output selection of WT RTODC is firstly achieved by calculating the geometric controllability, where it shows that the reactive power control loop has superior damping performance than the active power control loop on suppressing the torsional oscillation. Then, a RTODC is proposed and designed using H_∞ mixed-sensitivity control approach to ensure the robust wind turbine drive train stability during DFIG-WT participating in system frequency support. The robust damping performance is verified through small signal stability analysis and simulation results under parameter and system operating point uncertainties and compared to the residue approach based conventional torsional oscillation damping controller (CTODC) in a 4M11B system and a 16M68B system.

- When PLL is used to obtain frequency, the new oscillation mode will be affected by both PLL and IEC. A mixed H_2/H_∞ based robust damping controller is firstly designed for DFIG-WT with PLL participating in system frequency support, which can ensure robust damping ratio of the new oscillation dominated by both PLL and IEC. A detailed study on the impact of PLL on DFIG-WTs participating in system frequency support is firstly investigated. Analysis shows that once the PLL is used to obtain the point of common coupling frequency, an oscillation mode which is dominated by both PLL and IEC is found. The effect of power grid strength and PLL parameters on the oscillation mode is studied, where a weak grid strength and large PLL param-

eters deteriorate the system stability. A mixed H_2/H_∞ based robust damping controller and a H_∞ mixed-sensitivity based robust damping controller are designed to damp the new oscillation mode. Small signal stability analysis and simulation results are obtained and show that both robust damping controllers can ensure robust stability under different PLL parameters and power grid strength in a 4M11B system and a 16M68B system, where the mixed H_2/H_∞ based robust damping controller has better transient performance.

Fig.1.23 shows the Block diagram of the connections between Chapters. The controllers proposed in Chapter 2, 3 and 5 are based on the new oscillation mode excited by the DFIG-WTs with IEC participating in system frequency support. On the basis of the control strategy proposed in Chapter 2, an integrated IEC is proposed in Chapter 3 which is designed based on a novel robust PD-type controller design approach proposed. When the PLL is considered in measuring the frequency during DFIG-WT contributing to system frequency support, the impact of PLL on DFIG-WT participating in system frequency support is firstly investigated in Chapter 5. A mixed H_2/H_∞ based robust damping controller is then designed in this chapter to ensure robust damping performance on the PLL and IEC dominated oscillation mode considering uncertainties. In addition to the new oscillation mode, Chapter 4 investigated the impact of IEC on the torsional oscillation mode of WT drive train during frequency support. RTODC is proposed and designed to ensure robust damping performance on the torsional oscillation based on H_∞ mixed-sensitivity control approach as Chapter 2.

Publication list

1. Lei Ba, Wei Yao, Pingliang Zeng, Lin Jiang, Integrated Inertia Emulation Controller of DFIG-Based Wind Turbine with Guaranteed Damping Performance: A Robust Approach, *IEEE Transactions on Power Systems*, 2021. (Revised and under the 2^{nd} review)

2. Lei Ba, Lin Jiang, Robust Torsional Oscillation Damping Controller of DFIG-Based Wind Turbine with Frequency Response Capability, 2021 (Due to sub-

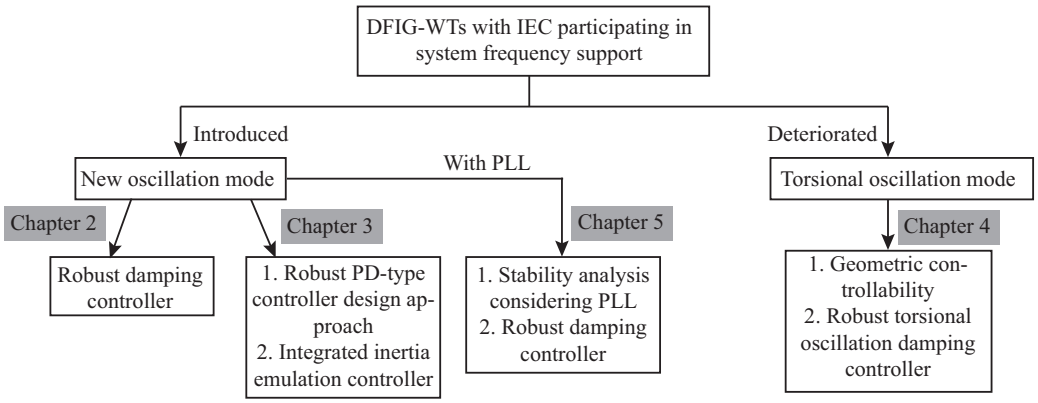

Figure 1.23: Block diagram of the connections between Chapters

mit to *IET Renewable Power Generation*)

3. Lei Ba, Wei Yao, Lin Jiang, Robust Damping Controller for DFIG-Based Wind Turbine with Frequency Response, *2019 IEEE Sustainable Power and Energy Conference (iSPEC)*, 2019.

1.7 Thesis Outline

The rest of the thesis is organised as follows:

- In Chapter 2, the model and control of the DFIG-WT are firstly presented. The supplementary frequency support controller of the DFIG-WT contributing to system frequency support is given. The proposed H_∞ mixed-sensitivity based RDC design is illustrated which is able to provide robust damping performance on the new oscillation mode introduced by the IEC. The robust damping performance of a RDC is evaluated on the DFIG-WTs participating in the system frequency support in a SMIB system, a 4M11B system and a 16M68B system. Both small signal stability analysis and simulation results are obtained and compared to the DFIG-WTs equipped with CDC.

- Chapter 3 proposes and designs an IIEC, such that the designed controller can provide the robust frequency support performance with satisfactory damp-

ing performance. Thus, the need of an additional damping controller can be avoided. A robust PD-type controller design approach is proposed to design IIEC which is formulated based on H_∞ control approach cooperating with the regional pole placement requirement. The performance of the IIEC is verified in a SMIB system, a 4M11B system and a 16M68B system. Both small signal stability and simulation results are obtained to verify the performance of the proposed IIEC in comparison to the CIEC and CIEC plus RDC.

- Chapter 4 analyses the impact of the IEC on the wind turbine drive train torsional oscillation, it has been found that the additional IEC will deteriorate the torsional oscillation mode which will lead to the damage on the mechanical components. Geometric controllability is calculated in the selection of the controller output. The RTODC is designed based on H_∞ mixed-sensitivity control approach to ensure robust stability of wind turbine drive train during frequency support. Cooperating with the RDC proposed in Chapter 2, the RTODC can provide robust damping performance on the torsional oscillation mode while the introduced new oscillation mode is simultaneously damped by RDC. The performance of the RDC+RTODC is verified in a 4M11B system and a 16M68B system. Both small signal stability and simulation results are provided to test the robust damping performance on the torsional oscillation mode in comparison to the CIEC and CIEC plus CDC+CTODC.

- Chapter 5 investigates the impact of the PLL on the system stability of DFIG-WT participating in frequency support. With the frequency measured by the PLL, the new oscillation mode will be affected by both the PLL and IEC. A mixed H_2/H_∞ based robust control approach is used to design a robust damping controller to provide the robust damping performance against different power grid strength and PLL parameters. The mixed-sensitivity H_∞ control approach based robust damping controller is also designed and compared. Case studies are conducted in a 4M11B system and a 16M68B system. Both small signal stability and simulation results are provided to verify the performance of the superior robust damping performance of H_2/H_∞ based

robust damping controller on the poorly damped oscillation mode than the H_∞ based robust damping controller.

- Chapter 6 is the conclusion of this thesis. The work presented in thesis is summarised and the future research perspectives are discussed.

Chapter 2

Robust Damping Controller for DFIG-based Wind Turbine Participating in the System Frequency Support

2.1 Introduction

Wind power, as a rapidly developed renewable energy, has been widely integrated in power systems nowadays [128, 129]. Due to high penetration level of these wind power in power system, system frequency support capability is significantly affected as the variable speed wind turbines are connected to the power grid through power converters which makes them cannot contribute to frequency changes like traditional power plants. In order to improve system frequency support capability, system operators require the wind power plants to participate in frequency support [30]. For instance, wind power plants are given specific requirement for power reservation during grid frequency deviation in the UK and Ireland grid codes [5, 6].

Doubly Fed Induction Generator (DFIG), as the most common generator for variable speed wind turbine, has been widely deployed in wind power generation [11]. Unlike the synchronous generators, the rotor of DFIG is decoupled from grid

through the back-to-back converter. When a large amount of power generated by DFIG is connected to grid, system effective inertia will be reduced as DFIG cannot contribute to frequency support. Due to the lack of frequency support capability, IECs are designed for DFIG-WT to support system frequency. When a frequency deviation occurred in the system, the IEC will provide auxiliary power to support system frequency.

Many researches have designed IEC for DFIG-WT to support power system frequency [82,130]. A hybrid modulated active damping control scheme for mitigating power oscillations caused by IEC was proposed in [35]. To achieve better frequency support performance for DFIG-WTs, some studies are focusing on IEC gain optimisation [48, 99, 100, 103, 104]. Throughout the literature reviews, most researches are focusing on frequency support gain optimisation for a better frequency support performance during DFIG-WT participating in system frequency support. However, the impact of an IEC on system stability is not researched in most references. Although [35] and [103] proposed active power controllers adding at the rotor side converter (RSC) of DFIG-WT to improve the power system low frequency oscillation caused by an IEC, these controllers are CDCs, which are limited to be designed at one system operating point. When the system operating point changes, a CDC will not be able to provide sufficient damping. Therefore, a RDC is desired to be designed to provide robust damping performance under different system operating points. Comparing to the other robust controllers designed by using LQ and H_2 method, the H_∞ control method can achieve its control performance by flexibly choosing its weighting functions in frequency domain [118]. Although the performance of a RDC has been proven in damping the inter-area oscillation of a power system under time-varying system operating points [10, 107, 131], the design of a RDC for WTGs participating in system frequency support has not been investigated in the existing researches.

In this chapter, a RDC is proposed and designed for DFIG-WTs participating in system frequency support based on H_∞ mixed-sensitivity control approach using LMIs with regional pole placements [10, 118], which can provide sufficient damping support during system oscillation and its damping performance is robust under

different system operating points. A CDC design is also provided for comparison. The robust damping performance of the proposed damping controller is verified by both small signal stability analysis and simulation results when the DFIG-WTs contribute to the frequency support in a SMIB system, a 4M11B system and a 16M68B system.

This chapter is organised as follows. Section 2.2 shows the model and control of DFIG-WT connected to a power grid. Section 2.3 introduces the frequency response controller. Section 2.4 presents the proposed RDC design. Section 2.5 shows the small signal stability analysis results, simulation results and discussion. Finally, a conclusion is made in Section 2.6.

2.2 Model and Control of DFIG based Wind Turbine Connected to a Grid

Fig.2.1 shows the diagram of the DFIG-WT connected to a power grid, where the stator of DFIG is connected to the grid directly and the rotor is connected through back-to-back converters [132]. The converter which is connected to the rotor of DFIG is called the RSC while the grid side converter (GSC) is connected to the grid. For the DFIG-WT, a gearbox is used between the turbine shaft and rotor of DFIG which can increase the generator speed to the desired level, such that the mechanical power captured by the wind turbine can be converted to the electrical power [133].

2.2.1 Wind Turbine Model

The mechanical power captured by wind turbine can be expressed as (2.2.1):

$$P_m = \frac{1}{2}\rho\pi R^2 C_p(\lambda,\beta)V_w^3 \tag{2.2.1}$$

where ρ, R, C_p and V_w are the air density, wind turbine radius, power coefficient and the wind speed, respectively. The power utilisation coefficient C_p is determined by

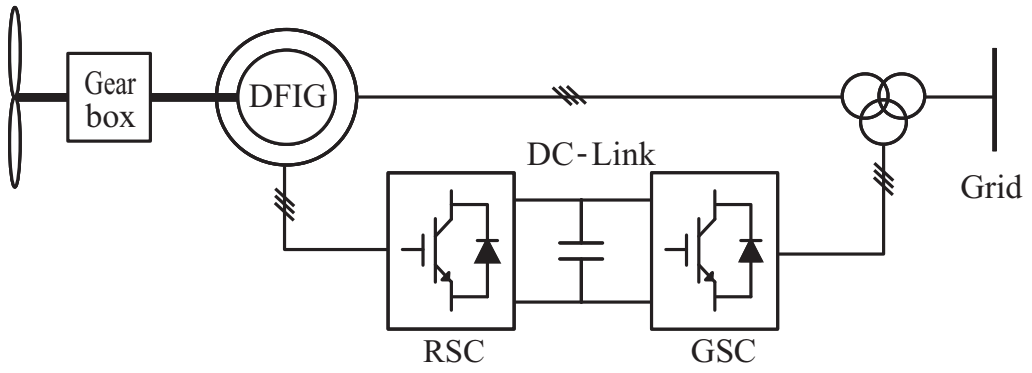

Figure 2.1: Diagram of DFIG based Wind Turbine Connected to a Grid

blade tip speed ratio λ and blade pitch angle β as shown in (2.2.2).

$$C_p = 0.5176\left(\frac{116}{\lambda_i} - 0.4\beta - 5\right)e^{-\frac{21}{\lambda_i}} + 0.0068\lambda \tag{2.2.2}$$

$$\frac{1}{\lambda_i} = \frac{1}{\lambda + 0.08\beta} - \frac{0.035}{\beta^3 + 1} \tag{2.2.3}$$

where the blade tip speed ratio is calculated by (2.2.4).

$$\lambda = \frac{\omega_r R}{V_w} \tag{2.2.4}$$

The maximum captured power by the wind turbine is achieved at maximum C_p where the blade tip speed ratio is optimum and pitch angle equals zero. For the wind turbine operating below rated wind speed, the rotor speed should be adjusted according to variable wind speed such that the optimal λ and maximum C_p can be ensured. With the rotor speed, the maximum captured power from wind can be obtained by using the optimum power-speed characteristic curve [134]. For the speed smaller than the lower limit and larger than the rated speed, the power will be set to its minimal value and rated value.

2.2.2 DFIG Model

The DFIG is modelled with generator convention in dq reference frame. The voltage equations in per unit (pu) of the DFIG in dq frame are given as [135, 136]:

$$\begin{cases} v_{sd} = R_s i_{sd} + \frac{1}{\omega_b}\dot{\phi_{sd}} - \omega_s \phi_{sq} \\ v_{sq} = R_s i_{sq} + \frac{1}{\omega_b}\dot{\phi_{sq}} + \omega_s \phi_{sd} \\ v_{rd} = R_r i_{rd} + \frac{1}{\omega_b}\dot{\phi_{rd}} - (\omega_s - \omega_r)\phi_{rq} \\ v_{rq} = R_r i_{rq} + \frac{1}{\omega_b}\dot{\phi_{rq}} + (\omega_s - \omega_r)\phi_{rd} \end{cases} \tag{2.2.5}$$

where v_{sd}, v_{sq}, v_{rd} and v_{rq} are the stator and rotor voltages in dq axis. i_{sd}, i_{sq}, i_{rd} and i_{rq} stator and rotor currents in dq axis. ϕ_{sd}, ϕ_{sq}, ϕ_{rd} and ϕ_{rq} are the stator and rotor flux linkages in dq axis. L_s, L_s and L_m are the stator, rotor and magnetising inductance. R_s and R_r are the stator and rotor resistance. ω_b is the base angular speed. ω_s and ω_r are the rotating speed of the reference frame and rotor speed.

The stator and the rotor flux linkage variables can be expressed as:

$$\begin{cases} \phi_{sd} = L_s i_{sd} + L_m i_{rd} \\ \phi_{sq} = L_s i_{sq} + L_m i_{rq} \\ \phi_{rd} = L_s i_{rd} + L_m i_{sd} \\ \phi_{rq} = L_r i_{rq} + L_m i_{sq} \end{cases} \tag{2.2.6}$$

The electromagnetic torque is obtained as:

$$T_e = \frac{L_m}{L_s}\left(\phi_{sq} i_{rd} - \phi_{sd} i_{rq}\right) \tag{2.2.7}$$

and the stator active and reactive power are obtained as:

$$\begin{cases} P_s = v_{sd} i_{sd} + v_{sq} i_{sq} \\ Q_s = v_{sq} i_{sd} - v_{sd} i_{sq} \end{cases} \tag{2.2.8}$$

2.2.3 Control of DFIG

Stator Voltage Oriented Vector Control

In stator voltage oriented vector control, the rotating reference frame will be aligned to the $d-$axis stator voltage while the $q-$axis stator voltage equals to zero,

which can be expressed as $v_{sd} = V_s$ and $v_{sq} = 0$. Ignoring the stator flux dynamics and neglecting the small stator resistances, (2.2.5) can be rewritten as:

$$\begin{cases} v_{sd} = V_s \approx -\omega_s \phi_{sq} \\ v_{sq} = 0 \approx \omega_s \phi_{sd} = 0 \end{cases} \tag{2.2.9}$$

$$\begin{cases} \phi_{sd} \approx 0 \\ \phi_{sq} = \phi_s \approx -\frac{V_s}{\omega_s} \end{cases} \tag{2.2.10}$$

Thus, the relationship between the currents and stator fluxes described in (2.2.6) can be written as:

$$\begin{cases} 0 = L_s i_{sd} + L_m i_{rd} \\ \phi_s = L_s i_{sq} + L_m i_{rq} \end{cases} \tag{2.2.11}$$

Using (2.2.11), the stator currents can be expressed by rotor currents as:

$$\begin{cases} i_{sd} = -\frac{L_m}{L_s} i_{rd} \\ i_{sq} = -\frac{V_s}{\omega_s L_s} - \frac{L_m}{L_s} i_{rq} \end{cases} \tag{2.2.12}$$

According to (2.2.9) and (2.2.12), the stator active power and reactive power in stator voltage oriented vector control can be derived as:

$$\begin{cases} P_s = -\frac{L_m}{L_s} V_s i_{rd} \\ Q_s = \frac{V_s^2}{\omega_s L_s} + \frac{L_m}{L_s} V_s i_{rq} \end{cases} \tag{2.2.13}$$

The electromagnetic torque (2.2.7), can also be obtained as:

$$T_e = -\frac{L_m}{L_s} \frac{V_s}{\omega_s} i_{rd} \tag{2.2.14}$$

According to (2.2.13) and (2.2.14), it can be found that P_s and T_e is proportional to the i_{rd} while Q_s is proportional to i_{rq}. Hence, the control of the stator active and reactive power is decoupled and can be achieved by regulating i_{rd} and i_{rq}, respectively.

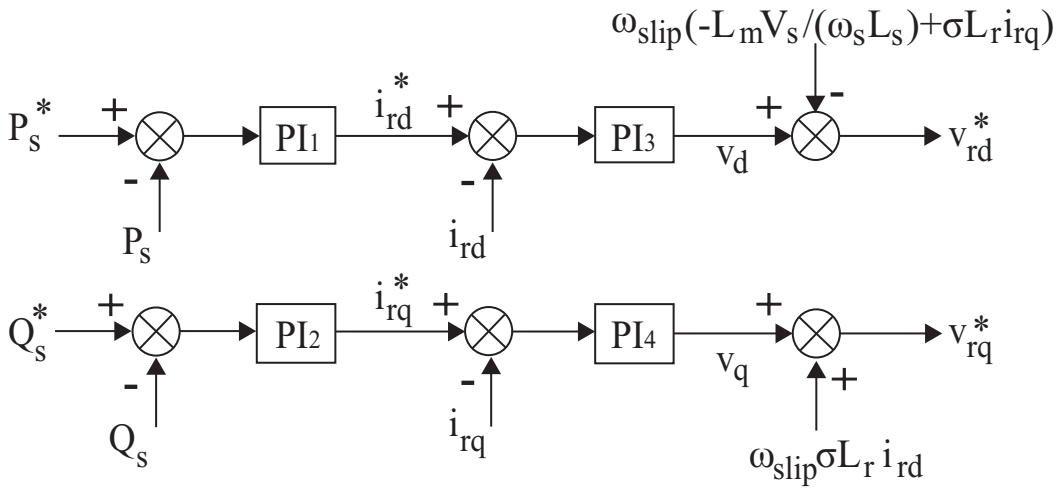

Figure 2.2: RSC control loops

Rotor Side Converter control

Fig.2.2 shows the block diagram of RSC control loops. The control objective of RSC is to regulate the active power and reactive power of DFIG, which is achieved by the outer control loops. The inner control loops are designed to ensure the actual rotor currents can follow the rotor current references which are provided by the outer power control loops. The decoupled control of d and q axis is achieved by using the vector control. From (2.2.6) and (2.2.10), the rotor flux linkages can be derived as:

$$\begin{cases} \phi_{rd} = \sigma L_r i_{rd} \\ \phi_{rq} = -\frac{L_m}{\omega_s L_s} V_s + \sigma L_r i_{rq} \end{cases} \tag{2.2.15}$$

where $\sigma = 1 - L_m^2/(L_s L_r)$ is the leakage coefficient. Substituting rotor flux linkages in (2.2.15) to (2.2.5) yields

$$\begin{cases} v_{rd} = R_r i_{rd} + \frac{\sigma L_r}{\omega_b} \frac{\mathrm{d}i_{rd}}{\mathrm{d}t} - \omega_{slip} \left(-\frac{L_m}{\omega_s L_s} V_s + \sigma L_r i_{rq} \right) \\ v_{rq} = R_r i_{rq} + \frac{\sigma L_r}{\omega_b} \frac{\mathrm{d}i_{rq}}{\mathrm{d}t} + \omega_{slip} \sigma L_r i_{rd} \end{cases} \tag{2.2.16}$$

where $\omega_{slip} = \omega_s - \omega_r$ is defined as the slip speed.

Defining v_d and v_q as auxiliary control inputs, the voltage outputs of the RSC,

v_{rd}^* and v_{rq}^*, can then be expressed as:

$$\begin{cases} v_{rd}^* = v_d - \omega_{slip}\left(-\frac{L_m}{\omega_s L_s}V_s + \sigma L_r i_{rq}\right) \\ v_{rq}^* = v_q + \omega_{slip}\sigma L_r i_{rd} \end{cases} \tag{2.2.17}$$

By comparing (2.2.16) and (2.2.17), it can be found that

$$\begin{cases} v_d = R_r i_{rd} + \frac{\sigma L_r}{\omega_b}\frac{\mathrm{d}i_{rd}}{\mathrm{d}t} \\ v_q = R_r i_{rq} + \frac{\sigma L_r}{\omega_b}\frac{\mathrm{d}i_{rq}}{\mathrm{d}t} \end{cases} \tag{2.2.18}$$

Then, PI controllers can be used to regulate the $d-$ and $q-$ axis rotor currents, which are given as:

$$\begin{cases} v_d = K_{pd}(i_{rd}^* - i_{rd}) + K_{id}\int(i_{rd}^* - i_{rd})\mathrm{d}t \\ v_q = K_{pq}(i_{rq}^* - i_{rq}) + K_{iq}\int(i_{rq}^* - i_{rq})\mathrm{d}t \end{cases} \tag{2.2.19}$$

where K_{pd} and K_{id} are the proportional gain and the integral gain of the PI controller 3; K_{pq} and K_{iq} are the proportional gain and the integral gain of the PI controller 4.

Similarly, the PI controllers which are used to regulate the active power and reactive power are designed as:

$$\begin{cases} i_{rd}^* = K_{PP}(P_s^* - P_s) + K_{IP}\int(P_s^* - P_s)\mathrm{d}t \\ i_{rq}^* = K_{PQ}(Q_s^* - Q_s) + K_{IQ}\int(Q_s^* - Q_s)\mathrm{d}t \end{cases} \tag{2.2.20}$$

where K_{PP} and K_{IP} are the proportional gain and the integral gain of the PI controller 1; K_{PQ} and K_{IQ} are the proportional gain and the integral gain of the PI controller 2.

Grid Side Converter Control

Fig.2.3 shows the block diagram of GSC control loops. The control objective of a grid side converter is to regulate the DC-link voltage which is achieved by the outer DC voltage control loop and inner current control loops. Based on the grid voltage oriented vector control, the voltage outputs of GSC can be expressed as:

$$\begin{cases} v_{gd}^* = -R_g i_{gd} - \frac{L_g}{\omega_b}\frac{\mathrm{d}i_{gd}}{\mathrm{d}t} + \omega_s L_g i_{gq} + u_{gd} \\ v_{gq}^* = -R_g i_{gq} - \frac{L_g}{\omega_b}\frac{\mathrm{d}i_{gq}}{\mathrm{d}t} - \omega_s L_g i_{gd} \end{cases} \tag{2.2.21}$$

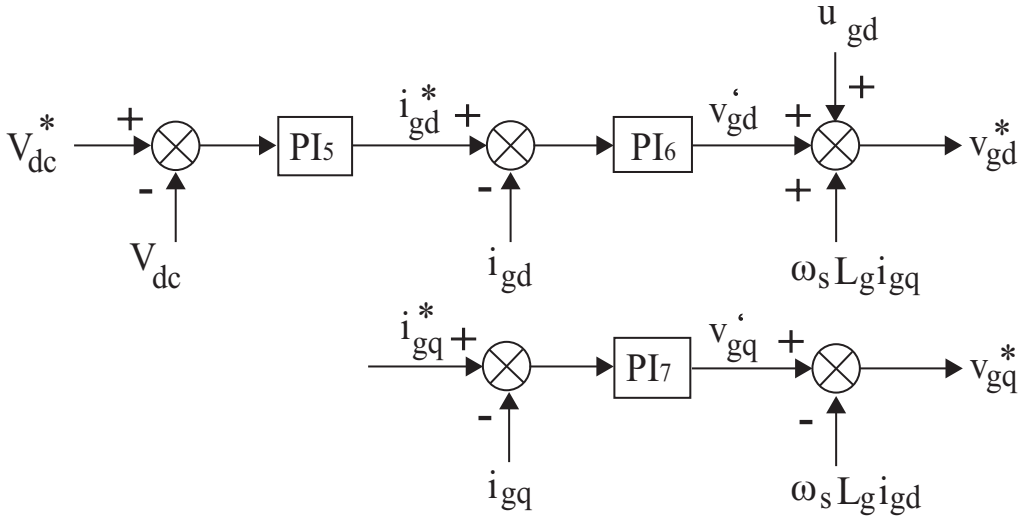

Figure 2.3: GSC control loops

where v_{gd} and v_{gq} are the voltages of GSC in dq axis. u_{gd} is the grid voltage at d-axis. i_{gd} and i_{gq} are the currents in dq axis. L_g is the inductance of GSC. R_g is the resistance.

Defining $v_{gd}^{'}$ and $v_{gq}^{'}$ as auxiliary control inputs, the voltage outputs of the GSC, v_{gd}^{*} and v_{gq}^{*}, can then be expressed as:

$$\begin{cases} v_{gd}^{*} = v_{gd}^{'} + \omega_s L_g i_{gq} + u_{gd} \\ v_{rq}^{*} = v_{gq}^{'} - \omega_s L_g i_{gd} \end{cases} \tag{2.2.22}$$

By comparing (2.2.21) and (2.2.22), it can be found that

$$\begin{cases} v_{gd}^{'} = -R_g i_{gd} - \frac{L_g}{\omega_b}\frac{\mathrm{d}i_{gd}}{\mathrm{d}t} \\ v_{gq}^{'} = -R_g i_{gq} - \frac{L_g}{\omega_b}\frac{\mathrm{d}i_{gq}}{\mathrm{d}t} \end{cases} \tag{2.2.23}$$

Then, PI controllers can be used to regulate the $d-$ and $q-$ axis of GSC currents, which are given as:

$$\begin{cases} v_{gd}^{*} = K_{pgd}(i_{gd}^{*} - i_{gd}) + K_{igd}\int(i_{gd}^{*} - i_{gd})\mathrm{d}t \\ v_{gq}^{*} = K_{pgq}(i_{gq}^{*} - i_{gq}) + K_{igq}\int(i_{gq}^{*} - i_{gq})\mathrm{d}t \end{cases} \tag{2.2.24}$$

where K_{pgd} and K_{igd} are the proportional gain and the integral gain of the PI controller 6; K_{pgq} and K_{igq} are the proportional gain and the integral gain of the PI controller 7.

Similarly, the PI controller which is used to regulate the DC-link voltage is designed as:

$$i_{gd}^{*} = K_{PV}(V_{dc}^{*} - V_{dc}) + K_{IV}\int (V_{dc}^{*} - V_{dc})\mathrm{d}t \tag{2.2.25}$$

where V_{dc} is the DC-link voltage, where K_{PV} and K_{IV} are the proportional gain and the integral gain of the PI controller 5.

2.3 Frequency Support Provided by Wind Turbine Generators

The frequency support is achieved based on the inertia emulation control which includes an inertia response control loop and a droop control loop. The block diagram of the IEC is given in Fig.2.4.

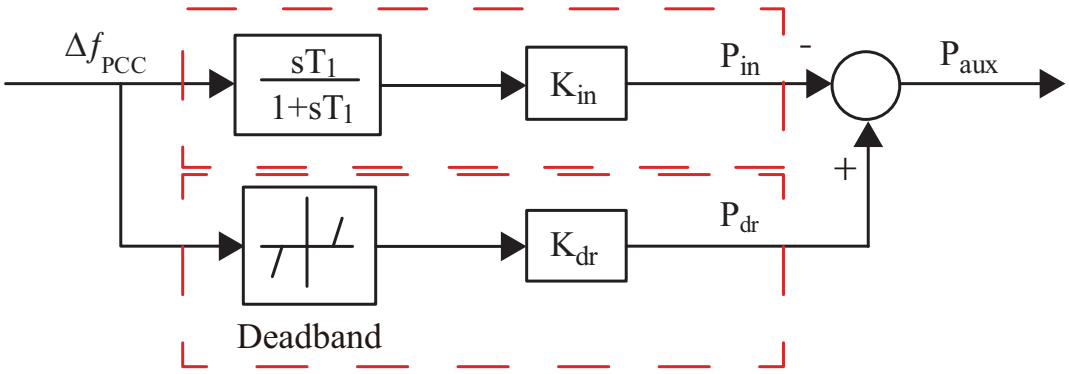

Figure 2.4: Block diagram of the IEC

2.3.1 Inertia Response Control Loop

The inertia response (IR) control loop of the IEC is shown in the upper part of Fig.2.4. This control loop is designed to emulate IR of a synchronous generator through differentiating the frequency deviation, which can limit the rate of frequency change when the power generated and load consumption is not balanced [82]. Therefore, in order to support the frequency, the output of the IR loop should be subtracted from the auxiliary power P_{aux} as Fig.2.4. Equations (2.3.1) and (2.3.2)

are used to express the working principle of an IR control control loop, which is similar to the swing equation of synchronous generators [123].

$$P_{in} = K_{in} \times \frac{\mathrm{d}\Delta\omega_s}{\mathrm{d}t} \tag{2.3.1}$$

$$P_{in} = K_{in} \times \frac{\mathrm{d}\Delta f_{PCC}}{\mathrm{d}t} \tag{2.3.2}$$

where P_{in} is the supplementary active power provided by the IR control loop, $\Delta\omega_s$ and Δf_{PCC} are the synchronous generator speed deviation and frequency deviation at the PCC of wind turbine generator connection. K_{in} is the IR control loop gain. Considering the real application, a high pass filter is chosen to replace the direct differentiator d/dt [89].

The most appropriate inertia gain can be obtained using the stored kinetic energy in the wind turbine which can be released during system FR [48], which is expressed as (2.3.3).

$$\Delta E_k = \int \Delta P_{IR} dt = \frac{K_{in}}{2} \int d{\omega_s}^2 \tag{2.3.3}$$

Then, the most appropriate gain for IR control loop can be calculated as (2.3.4), where H is the wind turbine inertia.

$$K_{in} = 1.85H \tag{2.3.4}$$

2.3.2 Droop Control Loop

The droop (DR) control loop of the IEC is shown in the lower part of Fig.2.4. The control objective is to improve the FN when frequency deviation exceeds the deadband [48]. The expression of a droop control loop is described by (2.3.5). As shown in (2.3.5), it can be seen that P_{dr} is proportional to the frequency deviation at PCC. The performance of droop control loop is dependent on K_{dr}.

$$P_{dr} = \frac{f_{nom} - f_{PCC}}{R} = K_{dr} \times \Delta f_{PCC} \tag{2.3.5}$$

where K_{dr} is the droop control loop gain, which equals to $\frac{1}{R}$. R is the wind turbine droop characteristic parameter. In order to optimise the droop control performance, K_{dr} can be a linear time-variant gain which can achieve the same droop control

performance as the quadratic droop gain [100]. The linear time-variant droop gain can be calculated by using

$$K_{droop}(\omega_r) = A_{linear} \times \omega_r + B_{linear} \tag{2.3.6}$$

where $A_{linear} = 28.5714$ and $B_{linear} = -17.1428$.

The supplementary power reference obtained by both IR and DR control loops is added and expressed as P_{aux}. P_{aux} will be augmented to the power reference obtained by maximum power point tracking (MPPT) as a new reference power for the active power control of power converter.

Fig.2.5 shows the diagram of the DFIG-WT with frequency support capability connected to a power grid. The proposed RDC will provide additional damping power added to the active power control loop. P_s^* will be used as the new active power reference in the rotor side converter control of RSC.

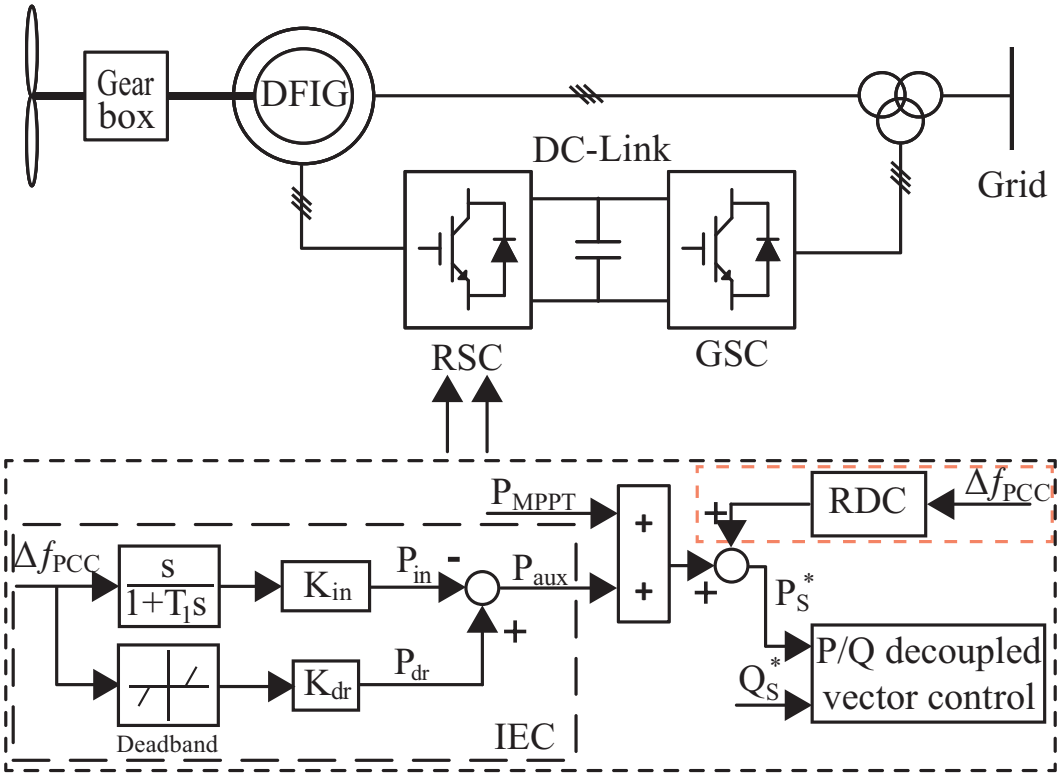

Figure 2.5: DFIG-WT equipped with the IEC and robust damping controller

2.3.3 Small Signal Stability Analysis of the DFIG-WT with IEC

Table 2.1: New excited oscillation modes of DFIG with IEC

Installed system	Eigenvalues	f (Hz)	ζ
SMIB	$-0.2281 \pm 6.7048i$	1.0671	0.034
4M11B	$-0.3619 \pm 7.5317i$	1.1987	0.048
16M68B	$-0.1551 \pm 4.9844i$	0.7933	0.0311

Through the small signal stability analysis of DFIG-WT with IEC equipped in a SMIB system, a 4M11B system and a 16M68B system at different wind speeds, it can be found that the worst case is occurred when the wind turbine is operated at rated wind speed. For simplicity, the worst-case small signal stability analysis results are provided here. Table2.1 shows that a new oscillation mode is excited for the DFIG-WT with IEC equipped in different types of power systems. As seen in Table2.1, the new excited oscillation mode has very poor damping ratio. Analysing participation factors of the new excited mode, it can be found that state variables of the IEC dominate the new excited mode as shown in Fig.2.6. Therefore, in order to mitigate system oscillation of DFIG-WT with IEC under different system operating points, a RDC is needed to be designed, which is introduced in the next section.

2.4 Proposed Robust Damping Controller Design

Among the robust control techniques, H_∞ based robust control technique is the most popular approach due to its freedom in achieving control objectives through frequency domain based weighting functions. The standard H_∞ mixed-sensitivity formulation can achieve the output disturbance rejection and control effort optimisation simultaneously [10].

2.4.1 Proposed Robust Damping Controller

H_∞ mixed-sensitivity control method is achieved by minimising the H_∞ norm of a certain closed-loop transfer function considering uncertainties using LMIs, where

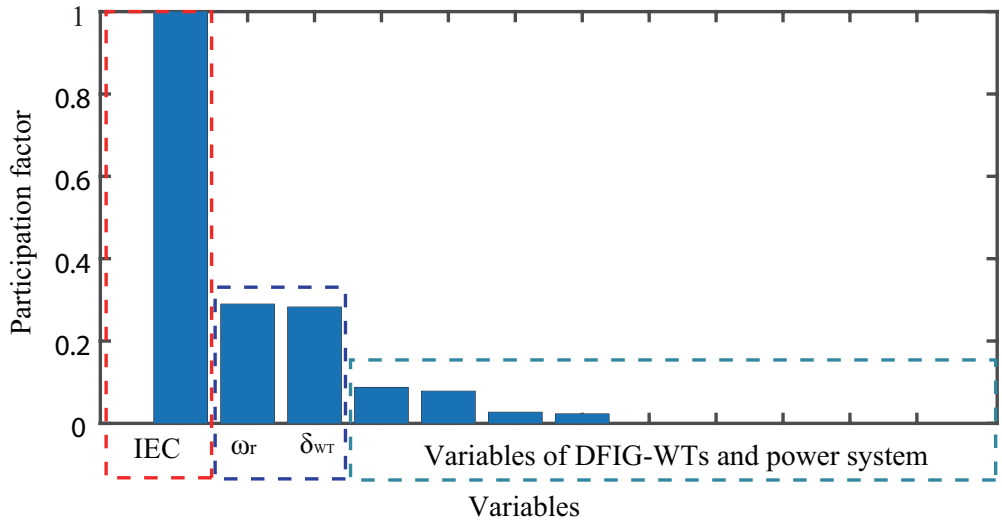

Figure 2.6: The participation factor of the states in the new excited oscillation mode

the H_∞ norm can measure the worst-case of system gain [118]. Suppose a linear system has the transfer function described by $G(s)$, the definition of the H_∞ norm is given as (2.4.1) [107].

$$\|G(s)\|_\infty = \sup_{u(t)\neq 0} \frac{\|y(t)\|_2}{\|u(t)\|_2} \tag{2.4.1}$$

where the $y(t)$ and $u(t)$ are the input and output of the linear system. A stable linear system should have the H_∞ norm as (2.4.2).

$$\|G(j\omega)\|_\infty = \sup_{\omega} |G(j\omega)| \tag{2.4.2}$$

This value will be the peak value of the magnitude value in the Bode plot.

In this chapter, H_∞ mixed-sensitivity design formulation is expected to achieve output disturbance and optimise control effort simultaneously [10]. It can be described as minimising the H_∞ norm of sensitivity function S, which represents the transfer function between the disturbance input and measured output. In addition, the control effort optimisation can be achieved by minimising $\|KS\|_\infty$. Since the output disturbance is normally occurred at low frequencies and control action is required at high frequencies. Appropriate weighting functions can be selected to achieve two minimisation problems over the whole frequency range.

Fig.2.7 shows the diagram for the H_∞ mixed-sensitivity damping controller design configuration. The input and output of RDC are selected as the PCC frequency deviation and supplementary damping active power provided by DFIG-WT, respectively. d is the disturbance input. z_1 and z_2 are the outputs to be regulated, which represents the impact of disturbance on system output Δf_{PCC} and control effort, respectively. Weighting functions $W_1(s)$ and $W_2(s)$ are selected as a low pass filter and a high pass filter, respectively. $W_1(s)$ is chosen for output disturbance rejection. $W_2(s)$ can be selected to reduce the control effort at high frequencies [10]. Equation (2.4.3) shows the weighting function chosen for designing the robust damping controller.

$$W_1(s) = \frac{15}{s+15}, W_2(s) = \frac{8s}{s+80} \tag{2.4.3}$$

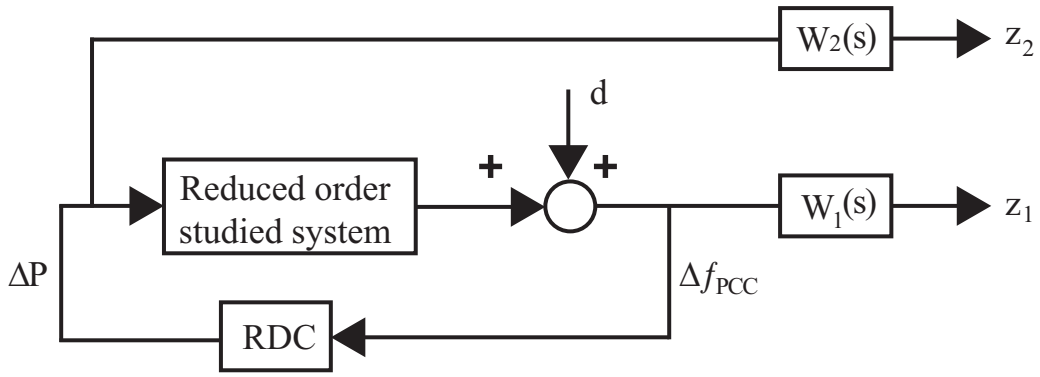

Figure 2.7: H_∞ Mixed-sensitivity damping controller configuration

In addition, the regional pole placement requirement is also added to ensure the damping performance of the designed robust damping controller. This is achieved by placing the closed-loop system poles in the desired region. In this chapter, a minimum 0.15 damping ratio is set such that the oscillation can be mitigated within 12-15s, where a conic sector is used to describe the interested pole region [10].

The full order of DFIG-WT connected to a SMIB system is 17th order. Large calculation time will be required and complex controller will be designed if the plant order is high. In addition, only few states contain the interested system characteristics. Hence, the Schur method was used for model truncation [137]. According

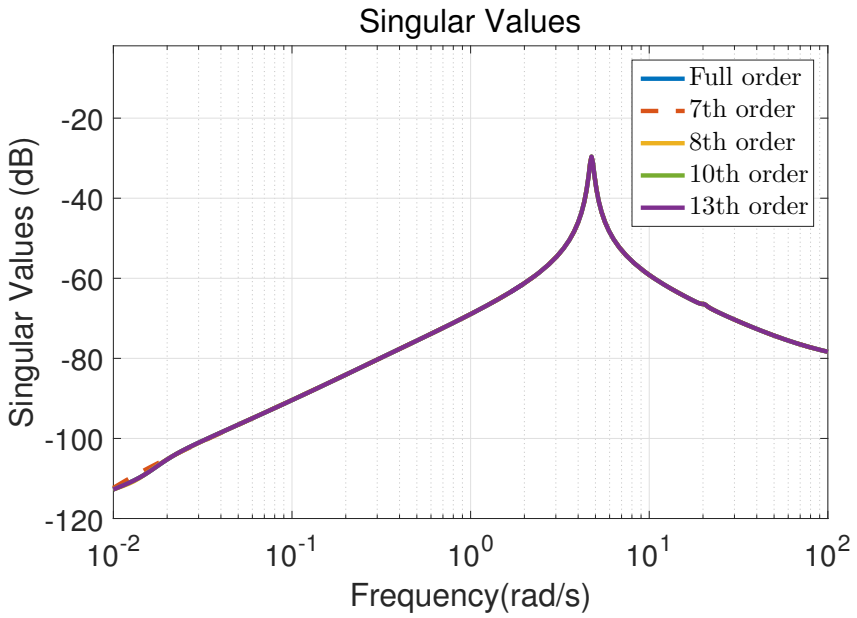

Figure 2.8: Frequency responses of the full order and reduced order systems

to the frequency responses of the full order and reduced order systems at different order shown in Fig.2.8, it can be found that the system order for more than 8th order can maintain the similar frequency response as the full order system in the interested frequency range between 0.01 Hz and 100 Hz. Hence, an 8th order reduced model is selected to design the controller. The transfer function of the 8th order reduced model is shown in the following equations.

$$H_{system}(s) = \frac{N(s)}{D(s)} \tag{2.4.4}$$

$$\begin{aligned} N(s) = &- 8.5287 \times 10^{-5}s^8 - 0.0088s^7 - 0.0641s^6 \\ &- 3.5872s^5 - 6.4373s^4 - 1.268s^3 - 0.0122s^2 \\ &- 2.3071 \times 10^{-4}s + 6.0208 \times 10^{-8} \end{aligned} \tag{2.4.5}$$

$$\begin{aligned} D(s) = &s^8 + 3.8106s^7 + 437.6901s^6 + 1.0399 \times 10^3 s^5 \\ &+ 9.7706 \times 10^3 s^4 + 1.9363 \times 10^4 s^3 \\ &+ 4.3192 \times 10^3 s^2 + 53.2105s + 0.8958 \end{aligned} \tag{2.4.6}$$

Using the reduced order model and selected weighting functions, the linearised model considering the effect of weighting function can be obtained. Since the sys-

tem order of the reduced order system model considering the weighting function became 10th-order, the current model can be further truncated to a 4th-order. The robust controller can be calculated using *hinfmix* function in MATLAB LMI Control Toolbox. The transfer function of the designed RDC is given in (2.4.7)-(2.4.9). The block diagram of the proposed RDC is shown in Fig.2.9.

$$H_{robust}(s) = \frac{N_c(s)}{D_c(s)} \tag{2.4.7}$$

$$\begin{aligned} N_c(s) =& 1.1449 \times 10^8 s^3 + 9.9789 \times 10^9 s^2 \\ &+ 4.4635 \times 10^9 s + 1.9263 \times 10^8 \end{aligned} \tag{2.4.8}$$

$$\begin{aligned} D_c(s) =& s^4 + 1.7811 \times 10^6 s^3 + 9.0086 \times 10^7 s^2 \\ &+ 4.7058 \times 10^6 s + 1.6973 \times 10^4 \end{aligned} \tag{2.4.9}$$

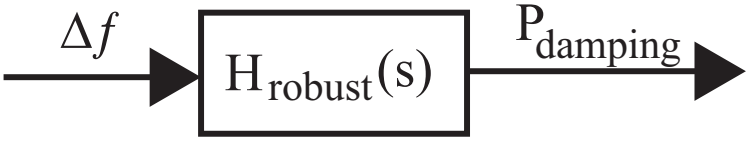

Figure 2.9: Block diagram of a robust damping controller

The design approach of the proposed RDC to ensure satisfactory damping performance when DFIG-WTs participates in system frequency support is summarised by the following steps.

1. Obtain a detailed nonlinear model of power system with DFIG-WTs and build up the model in MATLAB/Simulink.

2. Linearise the nonlinear model at one system operating point by using the Linear Analysis in Control System Toolbox of MATLAB.

3. Carry out model deduction via Schur balanced model reduction approach, and build the closed-loop system model as shown in Fig.2.7.

4. Reduce the closed-loop system model using the Schur balanced model reduction approach, and design the proposed RDC via $hinfmix$ function provided by LMI Control Toolbox in MATLAB.

5. Small signal stability analysis is carried out to verify the satisfactory damping performance on the new excited oscillation mode of the proposed RDC in a linear model given in Step (2).

6. Validate the effectiveness of the proposed RDC via simulation study on the nonlinear detailed model obtained in Step (1).

2.4.2 Conventional Damping Controller

A damping controller was conventionally designed by using the residue method. Residue method uses a feedback transfer function to change the eigenvalues of the system. The damping of a system oscillation mode will be increased by moving the real part of the mode to the left [138]. The residue of eigenvalue λ_i can be expressed in (2.4.10).

$$H_{jk}(s) = \sum_{i=1}^{n} \frac{r_{ijk}}{s - \lambda_i} \tag{2.4.10}$$

where H_{jk} is the transfer function from input j to output k, the residue is obtained by (2.4.11),

$$r_{ijk} = C_j v_i w_i B_k \tag{2.4.11}$$

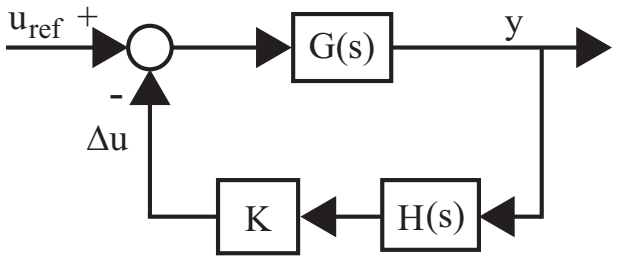

Figure 2.10: Block diagram of a gain closed-loop system

If the transfer function of controller $\phi(s, K)$ has a constant gain K for a single input/output system as shown in Fig.2.10, the sensitivity analysis on eigenvalue is given as [139]:

$$\frac{\partial \lambda_i}{\partial K} = r_{ijk} \frac{\partial \phi(s, K)}{\partial K} \tag{2.4.12}$$

Substituting $\phi(s, K) = KH(s)$ to (2.4.12) and assuming K is small, it gives

$$\frac{\Delta\lambda_i}{\Delta K} = r_{ijk}H\left(\lambda_i\right) \tag{2.4.13}$$

At the initial operating point where $\Delta K = K$, (2.4.13) can be written as:

$$\Delta\lambda_i = r_{ijk}KH\left(\lambda_i\right) \tag{2.4.14}$$

It can be found that a higher residue can move the associated eigenvalue more efficiently.

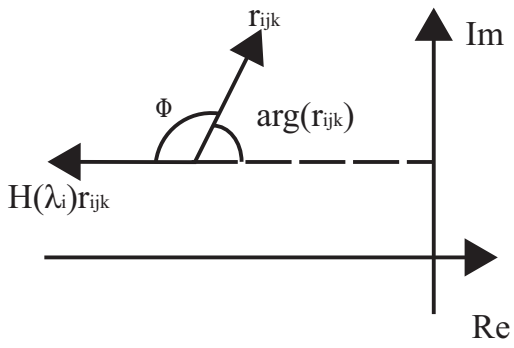

Figure 2.11: Eigenvalue displacement for phase compensation

The conventional damping controller is designed for a specific oscillation mode to improve the damping of this mode without changing the oscillation frequency. As shown in Fig.2.11, the direction of correct displacement is achieved by correctly choosing $arg(r_{ijk})$ to make the displacement of eigenvalue moving to the left along the real axis. Using the phase of the residue, the lead-lag parameters of the conventional damping controller can be obtained to move the eigenvalue in the desired direction. The controller gain is selected properly to achieve the desired damping effect without affecting the oscillation frequency. Equations (2.4.15)-(2.4.18) are used to calculate the parameters for lead-lag filters in the conventional damping controller, where m is selected as 2 for a second-order damping controller.

$$\phi = 180^\circ - angle(r_{ijk}) \tag{2.4.15}$$

$$\alpha = \frac{1 - sin(\frac{\phi}{m})}{1 + sin(\frac{\phi}{m})} \tag{2.4.16}$$

$$T_1 = \frac{1}{\omega_i \sqrt{\alpha}} \tag{2.4.17}$$

$$T_2 = \alpha T_1 \tag{2.4.18}$$

For the DFIG-WT model with IEC, the input and output of the controller are selected using observability as PCC frequency deviation and damping active power added to the RSC active power control loop. The feedback transfer function of the conventional damping controller can be expressed as equation (2.4.19). The block diagram of the conventional damping controller is shown in Fig.2.12.

$$H_{con}(s) = K \frac{T_w}{1 + T_w s} (\frac{1 + T_1 s}{1 + T_2 s})^2 \tag{2.4.19}$$

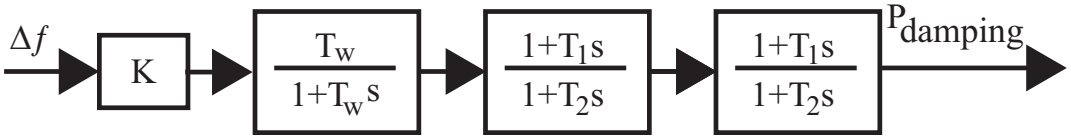

Figure 2.12: Block diagram of a conventional damping controller

The compensation constants T_1 and T_2 are calculated using equation (2.4.15)-(2.4.18) which are $T_1 = 0.1048s$ and $T_2 = 0.0811s$. The gain K is set as 10. The time constant T_w is set as 10 s. Based on the design of a damping controller using the residue method, the limitation of residue method is found which is that it was designed based on the system linearisation results at one operating point. Hence, when the system operating point changes, such as the connected power grid changing from a strong grid to a weak power grid, the CDC will not be able to provide sufficient phase compensation for the new system operating point. Therefore, a RDC is desired for a power system integrated with renewable energy and designed for handling uncertainties while maintaining stability.

2.5 Performance Evaluation

2.5.1 A Single Machine Infinity Bus System

The performance evaluation of a simple SMIB system is effective in understanding the damping performance provided by RDC. After the performance verification in a SMIB system, it will be helpful to validate the damping performance of a RDC in complex power systems [4].

Small signal stability analysis

Table2.2 and 2.3 show the new excited oscillation mode of the DFIG-WT connected to a strong and a weak power grid with a conventional and the proposed robust damping controller. Comparing the small signal stability analysis results in Table2.1 for a SMIB system to Table2.2 and 2.3, it can be found that adding a damping controller can improve the damping ratio of the IEC dominated oscillation mode for both a strong and weak grid connection.

Table 2.2: New excited oscillation mode of the DFIG-WT connecting to a strong power grid

Controller type	Eigenvalues	f (Hz)	ζ
Conventional	$-1.2327 \pm 10.5733i$	1.6828	0.1158
Robust	$-2.0311 \pm 10.4609i$	1.6649	0.1906

Comparing the small signal stability analysis results in Table2.2 to 2.3, it can be found that the damping performance of the new excited oscillation mode is robust against power grid strength when a RDC is equipped. However, the damping ratio for different power grid strength of the DFIG-WT using a CDC cannot be ensured. When the DFIG-WT is connected to a strong power grid, the damping ratio is high as shown in Table2.2 whereas the damping ratio of the new excited oscillation mode is low for a weak grid connection as given in Table2.3.

Table 2.3: New excited oscillation mode of the DFIG-WT connecting to a weak power grid

Controller type	Eigenvalues	f (Hz)	ζ
Conventional	$-0.3177 \pm 6.6671i$	1.0611	0.0476
Robust	$-1.1543 \pm 6.6149i$	1.0528	0.1719

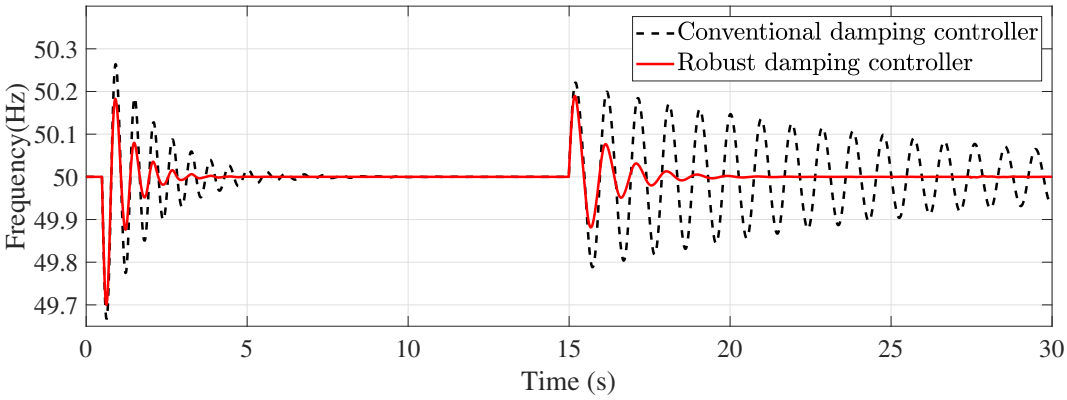

Figure 2.13: System frequency response with grid strength change

Simulation results

Fig.2.13 shows the simulation results of system frequency response during power grid strength variation. The power grid strength is changed from a weak grid to a strong grid at 0.5 second and the grid strength is changed back to a weak grid at 15 seconds. According to the simulation results shown in Fig.2.13, it can be found that the damping performance of the proposed robust damping controller is robust in regardless of the power grid strength change. The oscillation is mitigated within 5 seconds. However, the damping performance of conventional damping controller for the case of changing the power grid strength from a strong grid to a weak grid at 15 seconds cannot meet the oscillation settling time requirement. The oscillation takes more than 15 seconds to be mitigated, whereas the oscillation for the case of changing the power grid strength from a weak grid to a strong grid at 0.5 second can be mitigated within 10 seconds. The simulation results obtained is consistent to the small signal stability results shown in Table2.2 and 2.3.

2.5.2 A Two-area Four-machine System

Fig.2.14 shows the single line diagram for integrating the DFIG-WTs in a 4M11B power system. A 4M11B system is one of the benchmark models used to study the different types of oscillations that will occur in a typical interconnected power system [4]. The generators, loads and line impedance parameters are set as [4], which are provided in Appendix A. The synchronous generators G1-G4 are installed with PSS to damp the system inter-area oscillation mode. Comparing to the classic 4M11B system provided in [4], the DFIG-WTs are connected to the system at bus 8 through a long transmission line, which will be supposed to connect wind farm to a weak grid, the short circuit ratio at point 12 is less than 3. The nominal operating point is selected as 480 MW tie-line power flow between two areas. The output power of wind farm equals to 504 MW for 15% wind power penetration level.

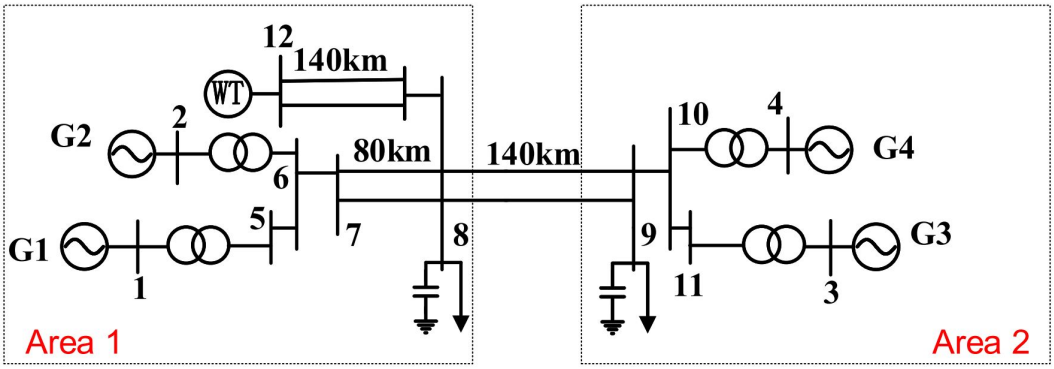

Figure 2.14: A 4M11B system with DFIG-based wind power system

Small signal stability analysis

The small signal stability analysis results comparing the damping performance of conventional and robust damping controller in a 4M11B system with different tie-line power flows between two areas are given in Table2.4. Comparing the results shown in Table2.4, it can be found that the robust damping controller can always provide the sufficient damping performance when the tie-line power flows are changed. A minimum 0.15 damping ratio of the new excited mode can be main-

tained by using the proposed robust damping controller, whereas the damping performance using a conventional damping controller cannot meet the damping ratio requirement.

Table 2.4: New excited modes of the 4M11B system for different tie-line power flow between Area I and II

Controller type	$P_{Tie-line}$ (MW)	Eigenvalues	f (Hz)	ζ
Conventional	200	$-0.5419 \pm 7.8238i$	1.2452	0.0691
	300	$-0.4973 \pm 7.6818i$	1.2226	0.0646
	480	$-0.4381 \pm 7.4889i$	1.1919	0.0584
	600	$-0.3488 \pm 7.1836i$	1.1433	0.0485
Robust	200	$-1.2929 \pm 7.6850i$	1.2231	0.1659
	300	$-1.2398 \pm 7.5423i$	1.2004	0.1622
	480	$-1.1679 \pm 7.3513i$	1.17	0.1568
	600	$-1.0742 \pm 7.0560i$	1.123	0.1505

In addition, the small signal stability analysis results of new excited mode for high DFIG penetration levels are given in Table2.5, where a high wind power penetration level means that more than 10% load consumption is provided by wind power [140]. Comparing the damping ratio of the new excited mode for using a conventional and a robust damping controller, it can be concluded that the damping performance of the proposed damping controller is robust for different wind power penetration levels. A minimum 0.15 damping ratio of new excited mode can also be ensured for different wind power penetration levels. However, the damping performance of the conventional damping controller is varied when the DFIG penetration level changed.

Simulation results

The simulation results for the DFIG-WTs connected to a 4M11B system are provided for investigating the robustness of the proposed damping controller during power system variation. The nominal operating condition for the DFIG-WTs con-

Table 2.5: New excited modes of the 4M11B system for different DFIG penetration level

Controller type	DFIG penetration level	Eigenvalues	f (Hz)	ζ
Conventional	15%	$-0.4381 \pm 7.4889i$	1.1919	0.0584
	20%	$-0.4154 \pm 6.6017i$	1.0507	0.0628
	25%	$-0.4447 \pm 5.5977i$	0.8909	0.0792
	30%	$-0.5463 \pm 4.5270i$	0.7205	0.1198
	35%	$-0.5983 \pm 4.9204i$	0.7831	0.1237
Robust	15%	$-1.1679 \pm 7.3513i$	1.17	0.1569
	20%	$-1.0547 \pm 6.5069i$	1.0356	0.16
	25%	$-0.9660 \pm 5.5292i$	0.88	0.1721
	30%	$-0.8173 \pm 4.5635i$	0.7263	0.1763
	35%	$-1.0365 \pm 4.8814i$	0.7769	0.2077

nected to a 4M11B system is at 480 MW power flow between two areas and 15% wind power penetration level. A three-phase short circuit fault at node 9 is added at 0.5s and cleared at 0.6s. Fig.2.15 shows the simulation results of system frequency for nominal operating condition. The power flow between two areas is 480 MW for Fig.2.15. According to the simulation results in Fig.2.15, it can be found that the robust damping controller provide better damping performance comparing to a conventional damping controller. Frequency oscillation can be mitigated within 6 seconds when the proposed robust damping controller is used. However, the conventional damping controller takes more than 20 seconds to mitigate the oscillation.

Fig.2.16 shows the simulation results of system frequency for 600MW power flow between two areas with a conventional damping controller and with a robust damping controller. The system operating point is changed by increasing the power flow between two areas from 480MW to 600MW. As shown in Fig.2.16, the oscillation can still be mitigated within 6 seconds by using a robust damping controller. This proves that the proposed damping controller can provide better damping performance than the conventional damping controller when the system operating point is

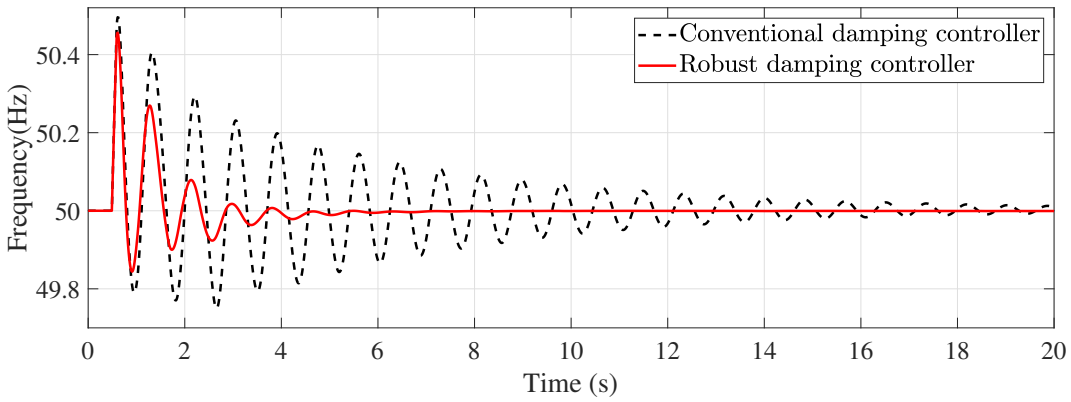

Figure 2.15: System frequency response for 480MW power flow and 15% wind penetration level in a 4M11B system

changed in a 4M11B system. In addition, the damping performance of the proposed controller is robust during power flow variation as the time for oscillation mitigation is almost unchanged for different power flow. The simulation results in Fig.2.15 and Fig.2.16 are consistent with the small signal stability results provided in Table2.4.

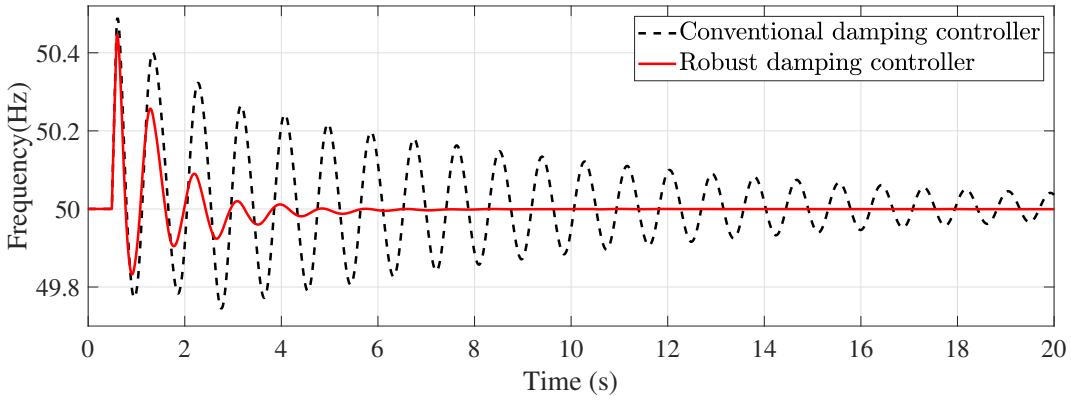

Figure 2.16: System frequency response for 600MW power flow in a 4M11B system

The wind power penetration level is calculated by using the total wind power generation and the total load consumption, which can be expressed by the total wind power generation as a percentage of total load consumption. A high wind power penetration level means that more than 10% load consumption is provided by wind power [140]. In this chapter, the simulation results of 15% and 30% wind power penetration levels are selected for comparing the damping performance in oscillation mitigation during system operating point variation. Since the nominal

operating condition is for 15% DFIG penetration levels in a 4M11B system, the system frequency response is already given in Fig.2.15. Based on Fig.2.15, it can be concluded that the robust damping controller in a 15% DFIG penetration level can provide sufficient damping when the system operating point is changed by different wind power penetration levels. Frequency oscillation is mitigated within 6 seconds for using a robust damping controller. However, the conventional damping controller takes more than 20 seconds to be mitigated.

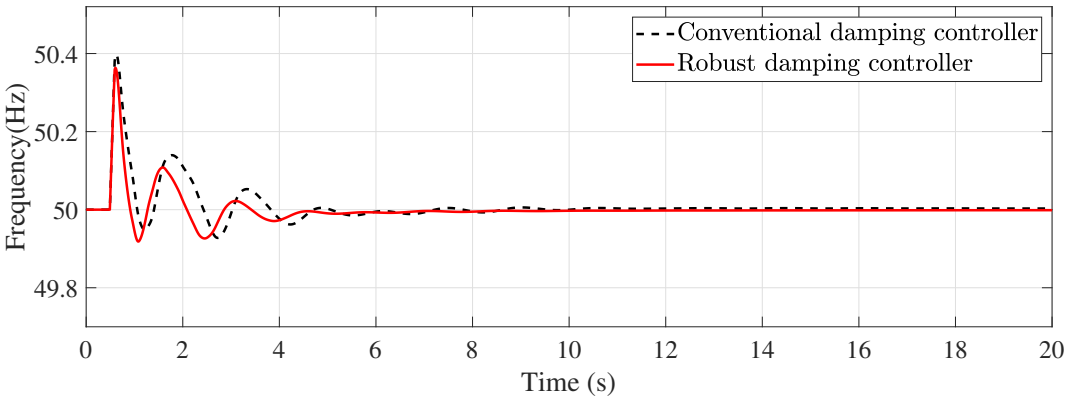

Figure 2.17: System frequency response for 30% wind penetration levels in a 4M11B system

Fig.2.17 shows the system frequency response with 30% DFIG penetration levels. Results in Fig.2.17 indicate that the proposed robust damping controller can maintain high robust damping performance in regardless of wind power penetration level variation. Comparing the results in Fig.2.15 and Fig.2.17, it can be concluded that the robust damping controller can always provide sufficient damping performance during DFIG-WT frequency support even when the system structure changed with different wind power penetration levels. It can also be observed that the damping performance of using a conventional damping controller is significantly improved. This is because more wind power can contribute to system frequency response. However, the proposed robust damping controller can still provide better damping performance than a conventional damping controller even in a high wind power penetration level. In addition, the frequency deviation for using proposed robust damping controller is less comparing to using a conventional damping controller. The small signal stability analysis results shown in Table2.5 are verified by

system frequency response shown in Fig.2.15 and 2.17.

2.5.3 A New England New York 68-Bus System

The performance of the proposed robust damping controller is also verified when the DFIG-WTs participating in the frequency response of a 16M68B system. A 16M68B system is a more complex power system model where its performance is more similar to a real power system [131]. Fig.2.18 shows the single line diagram of a 16M68B system, which is a 16-machine 5-area power system. It describes the reduced-order model of the New England and New York interconnected power system [116]. The first nine SGs denoted by G1 - G9 represents the generation of the New England Test System which is shown in Area I. The SGs G10 - G13 are the generation of the New York power system which is set as Area II. The other three SGs are the representation of the generation of three connected neighbourhoods of the New York Power system. The DFIG-WTs are located in Area II at a new bus 69 and connected to the bus 31 of the 16M68B system through a long transmission line where the short circuit ratio is calculated as 3. Similar to the 4M11B system, the SGs G1-G16 are all equipped with a PSS to provide the sufficient damping to the local and inter-area oscillation modes. The parameters of detailed bus data, line data and generator data can be found in [10, 141], which are also given in Appendix B.

Small signal stability analysis results

Small signal stability analysis results under different tie-line power flow between Area I and II are given in Table2.6. By comparing the damping performance of the proposed robust damping controller to the conventional damping controller, it can be found that the robust damping performance is ensured under different tie-line power flow between two areas when the robust damping controller is used. The damping ratio of the new excited mode is above 0.15 as designed, such that the oscillation can be damped with 12-15s. However, when the conventional damping controller was used, the damping performance of the new excited mode cannot meet the system

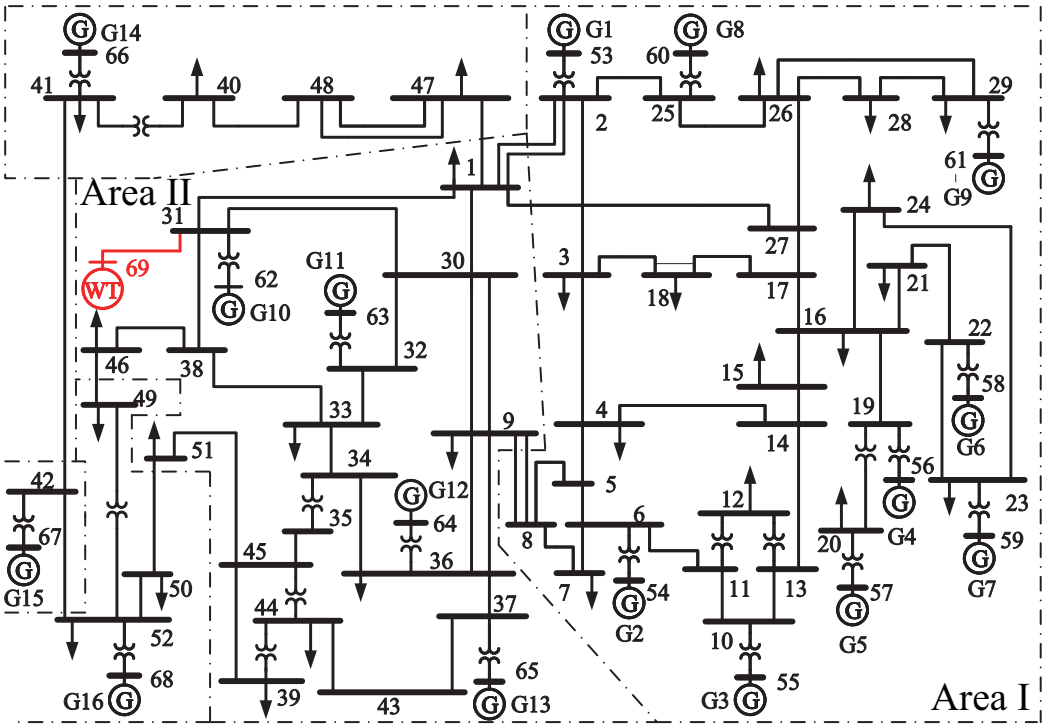

Figure 2.18: A 16M68B system with DFIG-WTs

stability requirement.

Table 2.6: New excited modes of the 16M68B system for different tie-line power flow between Area I and II

Controller type	$P_{Tie-line}$ (MW)	Eigenvalues	f (Hz)	ζ
Conventional	100	$-0.4058 \pm 5.1517i$	0.8199	0.0785
	300	$-0.4051 \pm 5.1276i$	0.8161	0.0788
	500	$-0.4034 \pm 5.0884i$	0.8098	0.0790
	700	$-0.4000 \pm 5.0300i$	0.8005	0.0793
	900	$-0.3934 \pm 4.9500i$	0.7878	0.0790
Robust	100	$-0.8009 \pm 5.1882i$	0.8257	0.1526
	300	$-0.7992 \pm 5.1653i$	0.8221	0.1529
	500	$-0.7955 \pm 5.1279i$	0.8161	0.1533
	700	$-0.7892 \pm 5.0702i$	0.8072	0.1537
	900	$-0.8273 \pm 4.1024i$	0.7949	0.1543

Simulation results

Time domain simulation results are also provided to verify the small signal stability analysis results and the robustness of the proposed damping controller in a 16M68B system. To verify the damping performance, a load disturbance is added

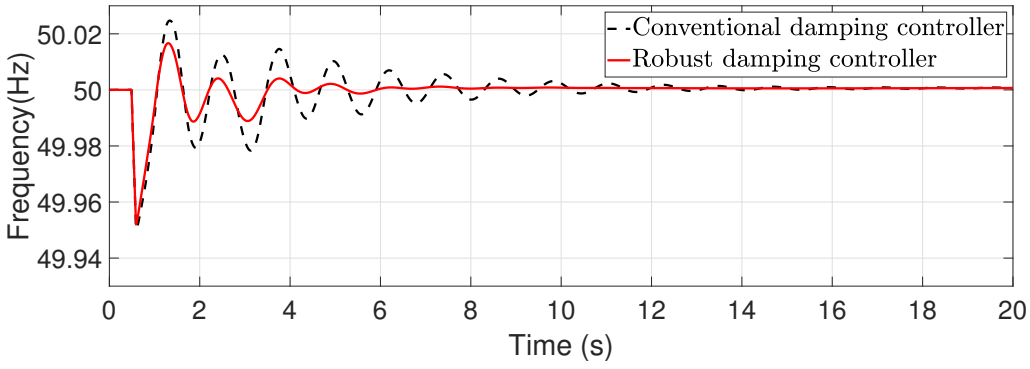

Figure 2.19: System frequency response for 100MW power flow between Area I and II in a 16M68B system

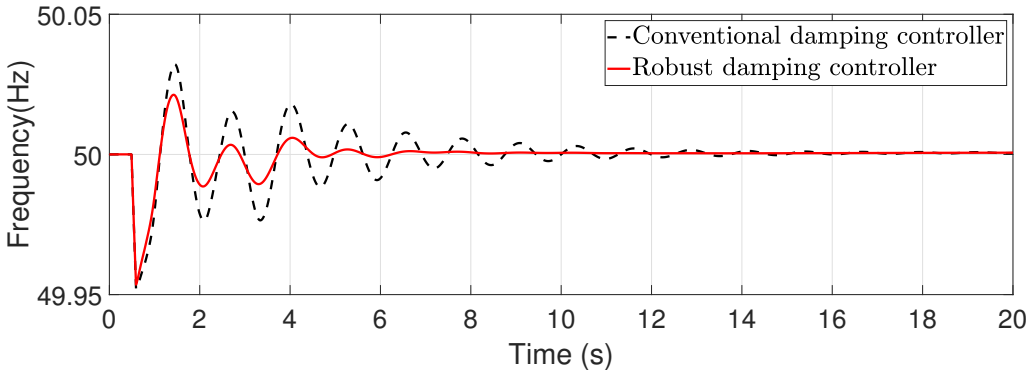

Figure 2.20: System frequency response for 900MW power flow between Area I and II in a 16M68B system

at 0.5s at bus 1. Fig.2.19 and Fig.2.20 show the simulation results for the 100MW and 900MW tie-line power flow between Area I and II, respectively. Comparing the simulation results, the proposed robust damping controller can ensure that the oscillation is mitigated with 10 seconds. Moreover, its damping performance is robust against different tie-line power flow between two areas. In contrast, the damping performance of the conventional damping controller is poor for different tie-line power flow.

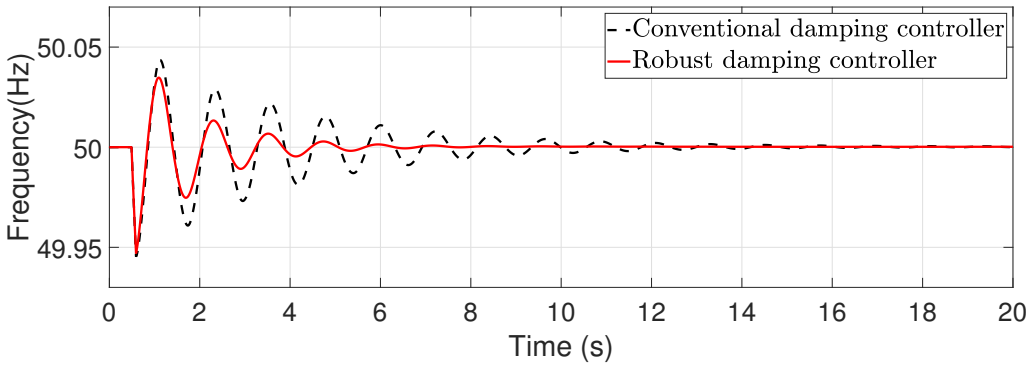

Figure 2.21: System frequency response for 100MW power flow between Area I and II under a new fault at bus 47 in a 16M68B system

Moreover, the robustness of the proposed damping controller is verified under an uncertain external disturbance. The fault was changed to bus 47 which was added at 0.5s. Fig.2.21 and 2.22 show the simulation results of system frequency under a new fault. By comparing the simulation results between Fig.2.19 and 2.21, it can be

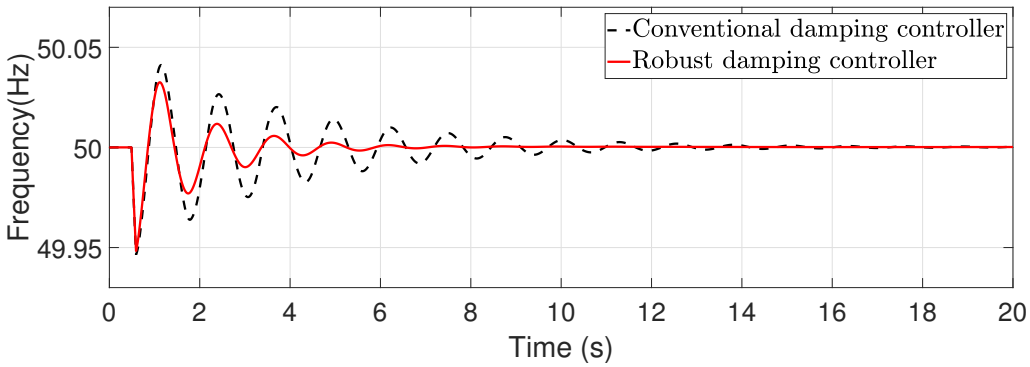

Figure 2.22: System frequency response for 900MW power flow between Area I and II under a new fault at bus 47 in a 16M68B system

seen that the proposed robust damping controller can also achieve robust damping performance for a uncertain disturbance. The comparison between the simulation results given in Fig.2.20 and 2.22 can also verify that the proposed robust damping controller can provide the robust damping performance of a new fault under a 900MW power flow between Area I and II.

Throughout the damping controller design process for improving the damping performance of the DFIG-WT in participating system frequency support, the conventional damping controller cannot provide sufficient damping when the system operating conditions change. As for the robust damping controller, it was designed considering the system uncertainties and hence it can provide robust damping performance under different uncertainties, such as power grid strength change, power system structure change, power flow between two areas change, wind power penetration level change and also uncertain external disturbance in this chapter. Hence, based on the small signal stability analysis results and simulation results achieved, it can be verified that the proposed robust damping controller can provide robust damping performance to mitigate the power oscillation caused by IEC in regardless of system uncertainties.

2.6 Conclusion

In conclusion, as the grid codes required, widely employed DFIG-WTs are required by system operators to participate system frequency support when the grid frequency deviation occurs. Modelling the IEC in the DFIG-WT was achieved at first. After that, the small signal stability analysis results were obtained to show that the IEC of a DFIG-WT will introduce a poorly damped oscillation mode in the system which deteriorates the system stability. Considering the uncertain system operating points, a robust damping controller is desired and modelled to maintain system stability during DFIG-WT participating in system frequency support and provide robust damping performance. The proposed robust damping controller was designed based on H_∞ mixed-sensitivity robust control method using LMIs. The regional pole place control objective is added to ensure that the damping performance of the new excited oscillation mode. In order to verify the robustness of proposed damping controller, a conventional damping controller based on residue method was also designed. Case studies for connecting the DFIG-WT to a SMIB system considering power grid strength change, a 4M11B system with different power flow between the two areas and wind power penetration levels and a 16M68B system with different power flow and uncertain external disturbance were obtained and the robustness of the proposed damping controller was verified.

Although the proposed RDC can successfully ensure robust damping performance on the poorly damped oscillation mode introduced by the IEC, the additional damping controller design will add complexity to DFIG-WT participating in system frequency support. Thus, to avoid the design of an additional RDC, an integrated IEC is proposed and designed in Chapter 3, which can simultaneously achieve the frequency support performance under uncertainties and guarantee the damping performance.

Chapter 3

Integrated Inertia Emulation Controller of DFIG-Based Wind Turbine with Guaranteed Damping Performance: A Robust Approach

3.1 Introduction

Wind power has been widely exploited as one of the leading renewable energy sources in nowadays power systems [129]. With the increased displacement of conventional synchronous generators (SGs) by those wind turbine generators (WTGs), inertia of the whole power grid will be reduced due to the decoupled dynamics of the WTG's rotor and the grid frequency, and introduce challenges on frequency stability and frequency deviation [142]. To deal with those challenges, most grid codes have introduced that demand WTGs to participate in system frequency support and maintain system frequency stability [5,6,30,31]. As the typical value of WTG rotor inertia is similar to the inertia of the SG, WTG is capable of providing frequency support by designing appropriate frequency support controller to emulate inertia response of SG [82].

According to different time scales, WTGs participating in system frequency

support includes short-term inertia emulation control via temporarily releasing the stored kinetic energy (KE) in WTGs during the initial stage of a frequency disturbance [64, 99, 143, 144], or long-term power reserve control [53, 94, 97, 98] via releasing the reserved power from the deloaded WTGs to respond dispatch command from the automatic generation control scheme [7, 101]. As the long-term frequency support is not effective at the start of a frequency contingency, the interests of this chapter only focus on short-term frequency support methods provided by the WTGs.

The short-term inertia emulation controller (IEC) is usually designed to include auxiliary inertia response (IR) control loop [63, 64], or a droop (DR) control loop [102], or both IR and DR loops [65, 101, 145]. As the performance of those IECs heavily depends upon those control loop gains [47], numerous researches are proposed to tune those gains to improve the performance of the IEC. Based on the operation experience of synchronous generators, the ranges of those gains are provided as the guidance in the grid codes [30, 42]. It has been illustrated in [50] that appropriate tuned IEC gains can enhance the system frequency dynamic response. In [63, 64], the time-varying IEC with IR control loop only was proposed to prevent large frequency drop. [102] used a time-varying DR gain of IEC to avoid a large frequency excursion. Both IR and DR control loops are tuned to improve the frequency nadir, based on a rotor speed under a pre-disturbance condition [101], a time-varying rotor speed [145], respectively; or via an optimisation approach considering constraints such as the minimum rotor speed, the maximum WTG power output and the rate of change of power output [65]. In [48], the inertia control is designed from the perspectives of avoiding wind turbine stalling and the IR control loop gain is set through the worst-case analysis. Considering sufficient kinetic energy can be released by DFIG, if the IR control loop gain is large, frequency nadir (FN) can be improved while avoiding the over-deceleration of DFIG. However, over-voltages or stall may occur. On the contrary, a small IR control loop gain is proposed to avoid over-deceleration, whereas the contribution on improving the FN is limited [99]. However, most of above studies focus on the improvement of a better transient response and ensure key indexes of the frequency variable (nadir and the rate of change of frequency (ROCOF)) not exceeding their operation limits,

while the stability of closed-loop system including the WT and the IEC has not been considered at the design stage.

The impact of the proposed IEC on the the stability of the power system equipped with DFIG-WTs has been investigated [35, 123]. As the IR loop of the IEC introduces a new oscillation mode, inappropriate gains of the IEC may result in a lightly damped oscillation mode to deteriorate the system stability during frequency support [35]. An additional damping loop has been designed to damp the newly excited and poorly damped oscillation mode, via conventional residue method [35], or robust damping controller (RDC) based on H_∞ mixed-sensitivity approach [123]. Although those additional damping loops can effectively suppress the newly introduced oscillation mode, the design and introduction of additional damping control loops further increase the complexity of the DFIG-WTs controller. On the other hand, the impact of inertia control parameters (proportional constant and time constant) of the IEC in the WT on electromechanical oscillation damping (EOD) of synchronous generator in power system has been investigated [36]. In [103], a novel DFIG based power system stabiliser (DFIG-PSS) control structure has been proposed to simultaneously improve the primary frequency response and low-frequency oscillation damping (LFOD) of a DFIG-integrated complex power system, via designing a PSS in the rotor-side converter (RSC) with the utilisation of tie-line power deviation signal to enhance the primary frequency response, and the improvement of LFOD by using frequency deviation signals of the local SGs. However, the poor damping performance of the newly excited oscillation mode by the IEC was not addressed in those researches.

Advanced control approaches have been employed for designing the IECs, such as nonlinear control [146] and nonlinear model predictive control [147]. An adaptive feedback linearization controller is designed based on the nonlinear model of WTGs to fully consider the nonlinear dynamic and an adaptive parameter estimation algorithm to mitigate the impact of parameter variations [146]. In [147], a new nonlinear model predictive control scheme is proposed to achieve dynamically optimal frequency support of wind farm and stability of individual WTGs, considering the nonlinear dynamic of each WTG and local wind speed conditions. It adopts a

three layers structure, in which the total wind farm power reference for frequency support is determined in the top-layer based on moving horizon estimation and linear model predictive control. The performance of model predictive control relies on the accuracy of the model of the wind farm and WTGs. In fact, there are multiple uncertainties existing in the power system with DFIG-WTs, such as parameters and model uncertainties, and external disturbances. The design of IEC without considering these uncertainties will degrade the frequency support performance and system stability. Robust control approaches have been adopted to tackle those uncertainties in the design of damping control for power system with DFIG-WTs [148, 149]. However, based on our best knowledge, the impact of those uncertainties and the impact of IEC on the system stability have not been considered at the design stage of the IEC. Therefore, it is highly desired to design an IEC for the DFIG-WTs which can achieve robust frequency support performance against uncertainties and simultaneously ensuring stability.

A new approach is proposed in this chapter to design a robust PD-type controller. The robustness of the proposed approach is achieved based on H_∞ control technique to convert the H_∞ constraint to a linear matrix inequality (LMI). Simultaneously, the regional pole placement objective is introduced as an additional LMI to guarantee damping performance. The proposed integrated inertia emulation controller (IIEC) can simultaneously achieve robust frequency support performance and guaranteed damping performance, which avoiding the design of an additional damping control loop in [35, 123]. Moreover, it can achieve robust frequency support performance against time-varying operation points, parameter and model uncertainties and external disturbance with guaranteed damping performance. Performance of the proposed IIEC is verified via small-signal stability analysis and simulation tests on a SMIB system, a 4M11B system and a 16M68B power system and compared with conventional inertia emulation controller (CIEC), and CIEC with RDC.

The remainder of this chapter is organised as follows. The CIEC for DFIG-WTs participating in system frequency support is presented in Section 3.2. Section 3.3 describes the proposed robust PD-type controller design approach. In Section 3.4, the design of IIEC for DFIG-WT participating in system frequency support is given.

Performance of the proposed IIEC is verified on case studies in Section 3.5. Section 3.6 concludes this chapter.

3.2 Conventional Inertia Emulation Controller

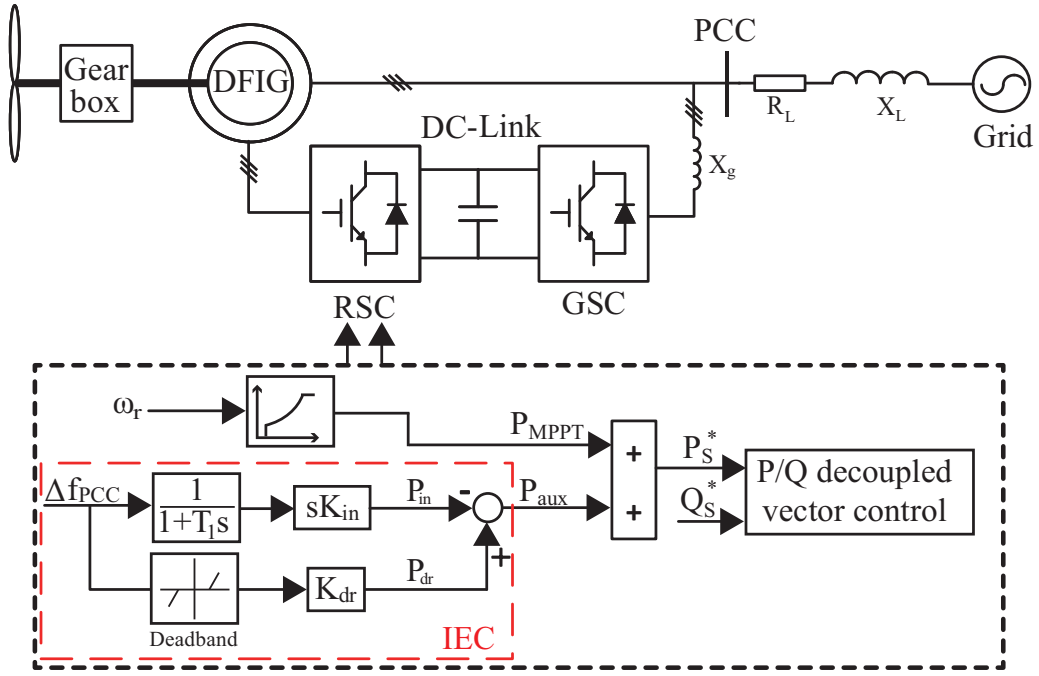

Figure 3.1: Auxiliary IEC added at rotor side converter control of DFIG-WTs

As shown in Fig.3.1, to participate in the system frequency support, auxiliary IEC was designed and augmented at the active power control loop of the DFIG-WT RSC control loop [34, 82]. The input of the IEC is the frequency deviation. The output of IEC P_{aux} is auxiliary power generated during frequency support period which is achieved by releasing the kinetic energy stored in the rotating mass of DFIG-WT [143]. The upper path of the IEC is the IR control loop to limit the rate of change of frequency [96, 150]. The lower path of the IEC is the DR control loop to improve the FN after the frequency deviation occurred. The auxiliary power provided by IR and DR control loop is given as:

$$P_{in} = K_{in}\frac{\mathrm{d}}{\mathrm{d}t}\Delta f_{PCC} \tag{3.2.1}$$

$$P_{dr} = K_{dr}\Delta f_{PCC} \tag{3.2.2}$$

where K_{in} and K_{dr} are the IR gains and DR gains, P_{in} and P_{dr} are the supplementary power, Δf_{PCC} is the frequency deviation at the point of common coupling (PCC).

The supplementary power obtained by both loops will be added to the power reference for maximum power point tracking (MPPT) as the new reference power P_s^* for the RSC active power control loop, as given in Fig.3.1. As shown in (3.2.1) and (3.2.2), the IEC is a Proportional-Differential (PD) type controller and its performance is depended upon the gains K_{in} and K_{dr}.

As pointed out in [35, 123], a new lightly damped oscillation mode will be introduced when the DFIG-WT participates in system frequency support which will deteriorate system stability. An additional conventional damping control loop is designed to suppress this mode in [35] and a robust damping control loop is proposed and designed in [123]. To avoid the design of an additional damping controller to maintain system stability during frequency support, an integrated inertia emulation controller with guaranteed damping performance so as to simultaneously provide frequency support is desired. The next section will illustrate the proposed design approach of the PD-type based IEC in this chapter.

3.3 Proposed Robust PD-type Controller Design Approach

This section introduces a robust PD-type controller approach using H_∞ control technique to minimise the effect of disturbance on the regulated output, combined with the regional pole placement objective to ensure the sufficient system damping performance.

3.3.1 Linear System Model with Disturbance

Considering a linear system with external disturbance d as

$$\begin{cases} \dot{x} = Ax + Bu + Fd \\ y = Cx \\ z_1 = C_z x \end{cases} \tag{3.3.1}$$

where x represents the state variable of the system. The input is u and the output is y. A is the state matrix, B is the input matrix and C is the output matrix, F is the disturbance input gain matrix, C_z is the regulated output matrix and z_1 is a regulated output .

Design a PD-type controller:

$$u = [K_P y - K_D \frac{d}{dt} y] = K_P C x - K_D C \frac{d}{dt} x \tag{3.3.2}$$

where the K_D and K_P are gains which need to be designed in the following section; then the closed-loop system of (3.3.1) with the PD-type controller (3.3.2) can be obtained as [151]:

$$\begin{cases} E\dot{x} = \bar{A}x + Fd \\ z_1 = C_z x \end{cases} \tag{3.3.3}$$

where $E = I + BK_DC$ and $\bar{A} = (A + BK_PC)$.The closed-loop system shown in equation (3.3.3) can be solved by regarding as a singular system where $E = I + BK_DC$ is required to be invertible for analysing the stability of the above system. Fig.3.2 shows the closed-loop system with a PD-type controller, where the parameter and model uncertainties are considered as part of and included in the external disturbance d.

The control objective of the robust approach is to design a PD-type controller under H_∞ performance specification where the closed-loop system stability can be ensured and the effect of the disturbance d on the regulated output z_1 is minimised as:

$$\left\| \frac{z_1}{d} \right\|_\infty < \gamma \tag{3.3.4}$$

where γ is the robust performance index and $\gamma > 0$. $\|.\|_\infty$ represents the ∞-norm. Moreover, to ensure the satisfactory damping performance of the closed-loop system via pole placement.

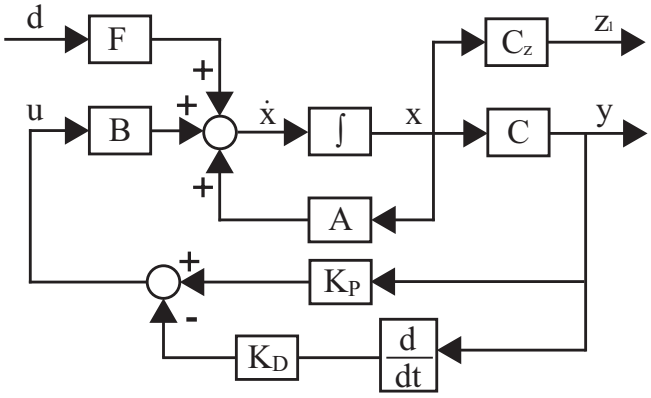

Figure 3.2: Linear system with a PD-type controller considering uncertainties

3.3.2 Robust PD-type Controller Design Approach

For the closed-loop system given in (3.3.3), the Lyapunov function is designed as:

$$V = (Ex)^T P_\infty Ex \tag{3.3.5}$$

The derivative of (3.3.5) is expressed as:

$$\begin{aligned} \dot{V} &= (E\dot{x})^T P_\infty Ex + (Ex)^T P_\infty E\dot{x} \\ &= [\bar{A}x + Fd]^T P_\infty Ex + [Ex]^T P_\infty [\bar{A}x + Fd] \end{aligned} \tag{3.3.6}$$

Based on Lyapunov stability theorem and considering the effect of disturbance, the system (3.3.3) is stable, that is, $\dot{V} < 0$ if the inequality (3.3.7) is satisfied [152].

$$\dot{V} + z_1^T z_1 - \gamma^2 d^T d < 0 \tag{3.3.7}$$

Substituting (3.3.6) in (3.3.7), we have:

$$\begin{aligned} &[\bar{A}x + Fd]^T P_\infty Ex + [Ex]^T P_\infty [\bar{A}x + Fd] + z_1^T z_1 - \gamma^2 d^T d \\ &= x^T [\bar{A}^T P_\infty E + E^T P_\infty \bar{A} + C_z^T C_z] x + d^T F^T P_\infty Ex \\ &+ x^T E^T P_\infty Fd - \gamma^2 d^T d < 0 \end{aligned} \tag{3.3.8}$$

and which can be rewritten (3.3.8) in matrix form as:

$$\begin{bmatrix} x \\ d \end{bmatrix}^T \begin{bmatrix} \Phi & M \\ N & -\gamma^2 I \end{bmatrix} \begin{bmatrix} x \\ d \end{bmatrix} < 0 \tag{3.3.9}$$

where $\Phi = \bar{A}^T P_\infty E + E^T P_\infty \bar{A} + C_z^T C_z$, $M = E^T P_\infty F$ and $N = F^T P_\infty E$. In order to solve the inequality in (3.3.7), $\Phi < 0$ should hold [152]. Applying the Schur complement on $\Phi < 0$ and transferring it to a LMI for the calculation by defining the new matrix V_1 and V_2, Φ is written as:

$$\Phi = \begin{bmatrix} \Phi(1,1) & C^T V_2^T & C^T V_1^T \\ V_2 C & -P_\infty & 0 \\ V_1 C & 0 & -P_\infty \end{bmatrix} < 0 \tag{3.3.10}$$

where

$$\begin{aligned} \Phi(1,1) =& A^T P_\infty + C^T V_1^T + A^T V_2 C \\ &+ P_\infty A + C^T V_2^T A + V_1 C + C_z^T C_z \end{aligned} \tag{3.3.11}$$

$$V_1 = P_\infty B K_P \tag{3.3.12}$$

$$V_2 = P_\infty B K_D \tag{3.3.13}$$

Then, substituting Φ in (3.3.9), (3.3.9) is described in the LMI format as:

$$\begin{bmatrix} x \\ d \end{bmatrix}^T \Xi \begin{bmatrix} x \\ d \end{bmatrix} < 0 \tag{3.3.14}$$

where

$$\Xi = \begin{bmatrix} \Phi(1,1) & C^T V_2^T & C^T V_1^T & M_1 \\ V_2 C & -P_\infty & 0 & 0 \\ V_1 C & 0 & -P_\infty & 0 \\ N_1 & 0 & 0 & -\gamma^2 I \end{bmatrix} \tag{3.3.15}$$

$$M_1 = P_\infty F + C^T V_2^T F \tag{3.3.16}$$

$$N_1 = F^T P_\infty + F^T V_2 C \tag{3.3.17}$$

Moreover, to ensure satisfactory damping performance, the closed-loop system poles should be placed in the desired region $\mathcal{D}$ in the left-half plane [10, 153], as shown in Fig.3.3. The LMI regions can be defined by convex subsets $\mathcal{D}$ if there exists symmetric matrices $\alpha = [\alpha_{kl}] \in \boldsymbol{R}^{m \times m}$ and $\beta = [\beta_{kl}] \in \boldsymbol{R}^{m \times m}$ [10,153,154], such that,

$$\mathcal{D} = \{ z \in \boldsymbol{C} : \quad f_{\mathcal{D}}(z) < 0 \} \tag{3.3.18}$$

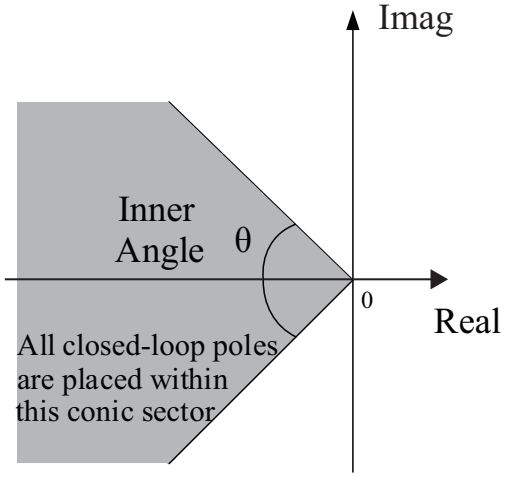

Figure 3.3: Closed-loop system pole region $\mathcal{D}$ [10]

with

$$f_{\mathcal{D}}(z) := \alpha + z\beta + \bar{z}\beta^T = [\alpha_{kl} + \beta_{kl}z + \beta_{lk}\bar{z}]_{1\leq k,l\leq m} \tag{3.3.19}$$

If a dynamical system is described by $\dot{x} = Ax$, it is called $\mathcal{D}$ stable if all poles of this system lies in the $\mathcal{D}$. In other words, the matrix A is $\mathcal{D}$-stable if and only if there exists a symmetric matrix $P_{\mathcal{D}}$ such that

$$M_{\mathcal{D}}(A, P_{\mathcal{D}}) < 0, P_{\mathcal{D}} > 0 \tag{3.3.20}$$

where $M_{\mathcal{D}}(A, P_{\mathcal{D}}) := \alpha \otimes P_{\mathcal{D}} + \beta \otimes (AP_{\mathcal{D}}) + \beta^T \otimes (AP_{\mathcal{D}})^T$ and $\otimes$ denotes the Kronecker production of matrices [153].

The LMI region $\mathcal{D}$ can be chosen as symmetric regions with respect to the real axis in the complex plane, such as disks, horizontal strips, conic sectors, circles and etc. Furthermore, it can also be defined as the intersection of the above regions. From Theorem (2) in [153], the matrix A has its poles in the region if and only if there exists a positive definite symmetric matrix $P_{\mathcal{D}}$, such that equation (3.3.21) is satisfied.

$$\begin{pmatrix} \sin\theta\left(A^T P_{\mathcal{D}} + P_{\mathcal{D}}^T A\right) & \cos\theta\left(A^T P_{\mathcal{D}} - P_{\mathcal{D}}^T A\right) \\ \cos\theta\left(P_{\mathcal{D}}^T A - A^T P_{\mathcal{D}}\right) & \sin\theta\left(A^T P_{\mathcal{D}} + P_{\mathcal{D}}^T A\right) \end{pmatrix} < 0 \tag{3.3.21}$$

In this chapter, the interested pole region $\mathcal{D}$ is selected as a conic sector, where the apex is at the origin and inner angle equals to 2θ, which is the Sector $(\mathcal{S}(0, 0, \theta))$.

Then, for the closed-loop system (3.3.3), the system has its poles in the desired conic sector if and only if there exists a positive definite symmetric matrix $P_{\mathcal{D}}$, such that (3.3.22) is satisfied [10].

$$\begin{pmatrix} \sin\theta\,(z+\bar{z}) & \cos\theta\,(z-\bar{z}) \\ \cos\theta\,(\bar{z}-z) & \sin\theta\,(z+\bar{z}) \end{pmatrix} < 0 \tag{3.3.22}$$

where $z = \bar{A}^T P_{\mathcal{D}} E$ and $\bar{z} = E^T P_{\mathcal{D}} \bar{A}$. Using the same method for deriving a LMI for (3.3.10), (3.3.22) is rewritten as,

$$\begin{pmatrix} \sin\theta L_1 & \cos\theta L_2 \\ \cos\theta L_3 & \sin\theta L_1 \end{pmatrix} < 0 \tag{3.3.23}$$

where

$$L_1 = \begin{bmatrix} L_1(1,1) & C^T S_2^T & C^T S_1^T \\ S_2 C & -P_{\mathcal{D}} & 0 \\ S_1 C & 0 & -P_{\mathcal{D}} \end{bmatrix} \tag{3.3.24}$$

and $L_1(1,1) = A^T P_{\mathcal{D}} + C^T S_1^T + A^T S_2 C + P_{\mathcal{D}} A + C^T S_2^T A + S_1 C$, $L_2 = A^T P_{\mathcal{D}} + C^T S_1^T + A^T S_2 C - P_{\mathcal{D}} A - C^T S_2^T A - S_1 C$, $L_3 = P_{\mathcal{D}} A + C^T S_2^T A + S_1 C - A^T P_{\mathcal{D}} - C^T S_1^T - A^T S_2 C$. S_1 and S_2 are defined as $S_1 = P_{\mathcal{D}} B K_P$ and $S_2 = P_{\mathcal{D}} B K_P$.

Based on the aforementioned discussion, the design of a robust PD-type controller for a linear system can be summarised as the following theorem.

Theorem 1. *Consider a given closed-loop system (3.3.3) and a prescribe γ, if there exists a common solution $P = P_{\mathcal{D}} = P_\infty > 0$, such that (3.3.14) and (3.3.23) hold. Then, the closed-loop system (3.3.3) is stable with γ against disturbance d, and closed-loop poles located in the desired region $\mathcal{D}$. Moreover, the desired robust PD-type controller gains are given by:*

$$K_P = (PB)^+ V_1 \tag{3.3.25}$$

$$K_D = (PB)^+ V_2 \tag{3.3.26}$$

where X^+ denotes the generalised inverse of X.

3.4 Design of Integrated Inertia Emulation Controller

This section firstly presents the design of an IIEC for the DFIG-WTs participating in system frequency support. Then, the steps of the design of IIEC is summarised.

Considering the nonlinear DFIG-WT model provided in Section 2.2 connected to a power grid, the whole system is linearised at the equilibrium operating point. The input u is chosen as P_{aux} and the output y is frequency deviation Δf. Then, the linearised system with uncertainties can be expressed as (3.3.1), where $x = [x_{DFIG}, x_g]^T$ are the state variables of the DFIG-WT and power grid. d is the external disturbance. z_1 is the regulated output.

For a DFIG-WT integrated in a large power system model, the order of the linearised system model is relatively high. However, only little number of the system states contribute to the selected input-output connection [155]. Thus, a reduced linearised system model will be used in the controller design, where the Schur balanced truncation model reduction approach is selected to truncate the order of the studied system [137]. According to the frequency response of the full order and the reduced order system, the reduced order is selected by choosing the reduced-order system which has the similar Hankel singular value as full-order system in the interested frequency range for the studied oscillation mode.

Then, using the Theorem 1 and the YALMIP Toolbox in MATLAB, the IIEC gains K_{dr} and K_{in} which can ensure H_∞ control stability and regional pole placements simultaneously can be calculated and achieved.

The design approach of the proposed IIEC for DFIG-WTs participating in system frequency support can be summarised by the following steps.

1. Obtain a detailed nonlinear model of power system with DFIG-WTs and build up the model in MATLAB/Simulink.

2. Linearize the nonlinear model at one system operating point as shown in (3.3.1) by using the Linear Analysis in Control System Toolbox of MATLAB.

3. Carry out model deduction via Schur balanced model reduction approach,

and obtain the closed-loop system model (3.3.3) with the PD-type frequency support controller (3.3.2).

4. Design the IIEC based on Theorem 1, and solve the LMIs in Theorem 1 via YALMIP Toolbox in MATLAB. Moreover, the obtained IIEC gains are checked to remain within the reasonable range according to the grid code.

5. Small signal stability analysis is carried out to verify the satisfactory damping performance of the introduced oscillation mode of the proposed IIEC in a linear model given in Step (2).

6. Validate the effectiveness of the proposed IIEC via simulation study on the nonlinear detailed model obtained in Step (1).

Comparing to the RDC designed in Chapter 2, the designed IIEC can achieve the satisfactory damping performance on the introduced oscillation mode as the RDC while maintaining robust frequency support performance. This is because system stability is considered in the design stage of IIEC. Thus, additional RDC design can be avoided and the application of the DFIG-WT contributing to system frequency support can be simplified.

3.5 Performance Evaluation

3.5.1 A Single Machine Infinity Bus System

The SMIB system chosen for controller performance evaluation in this section is the same as the one used in Section 2.5.1. Both small signal stability analysis and simulation results are obtained to verify the proposed IIEC in a SMIB system.

Small Signal Stability Analysis

Using the steps provided in Section 3.4, the IIEC gains for DFIG-WTs connecting to a SMIB system are $K_{dr} = 9.2097$ and $K_{in} = 2.5542$. With the droop slope R given by system operators [30, 42], the value of the DR control loop gain can be

calculated by $K_{dr} = 1/R$ and should be in the range between 8.33 to 50. Thus, it can be seen that the obtained DR control loop gain is reasonable.

Table 3.1: New excited oscillation modes of DFIG with CIEC

Grid strength	Eigenvalues	f (Hz)	ζ
Strong grid	$-0.1798 \pm 4.7566i$	0.7570	0.0378
Weak gird	$0.0702 \pm 3.9866i$	0.6345	-0.0176

By analysing small signal stability analysis results of a DFIG-WT with a CIEC in a SMIB system under different wind speeds, the system stability was the worst under the rated wind speed operation, i.e. 12 m/s. Therefore, the worst-case small signal stability analysis result is provided in this chapter. Table3.1 only shows oscillation frequency (f) and damping ratio (ζ) of the new introduced oscillation mode of the DFIG-WT with the CIEC under strong and weak grid connections. It can be concluded that the damping ratio of the introduced oscillation mode of the DFIG-WT with the CIEC is low and its value reduces when the power grid strength deteriorates. Under a weak grid connection, the introduced oscillation mode will have a negative damping ratio, which will lead to the system instability during frequency support.

Due to the impact of the frequency support provided by DFIG-WTs on the turbine torsional oscillation mode, a torsional oscillation damper (TOD) proposed in [35] was added to avoid the damage on turbine shaft by providing satisfactory damping performance on torsional oscillation mode. Table3.2 shows small signal stability analysis results of the torsional oscillation mode for the cases without TOD and IEC, with TOD and CIEC, with TOD and IIEC. According to the small signal stability analysis results, it can be found that the torsional oscillation mode can be successfully damped by TOD. Thus, the effect of IEC on turbine shaft can be mitigated. In addition to analysing the small signal stability of the CIEC and proposed IIEC, the small signal stability analysis results of DFIG-WTs with a CIEC plus RDC proposed in [123] are also included for comparison. Table3.3 shows the oscillation frequency and damping ratio of introduced oscillation mode dominated by CIEC, CIEC plus RDC and the proposed IIEC when DFIG-WT is connected to differ-

ent power grid strengths. The damping ratio of the introduced oscillation mode of DFIG-WT equipped with the IIEC indicates that the proposed IIEC can ensure satisfactory damping performance when DFIG-WTs is connected to different power grid strength. It also shows that the design requirement on the damping ratio is satisfied when the system operating point change is caused by power grid strength variation. However, the introduced oscillation mode of using a CIEC for DFIG-WT connecting to a weak power grid has a negative damping ratio which will cause the system instability. By comparing the damping ratio of the oscillation mode dominated by a CIEC plus RDC to the proposed IIEC, it can be found that both controllers can achieve the sufficient damping performance which indicates that the proposed IIEC can ensure the satisfactory damping performance as using a CIEC plus RDC. Thus, the design of an additional RDC can be avoided.

Table 3.2: Turbine torsional oscillation mode

Controller type	Eigenvalue	f(Hz)	ζ
Without TOD and IEC	$-1.5074 \pm 20.1361i$	3.2048	0.0746
Without TOD and with CIEC	$-0.7416 \pm 20.2537i$	3.2235	0.0366
Without TOD and with IIEC	$-0.6898 \pm 20.28i$	3.2277	0.034
With TOD and CIEC	$-1.6230 \pm 20.1759i$	3.2111	0.0802
With TOD and IIEC	$-3.0257 \pm 19.9645i$	3.1774	0.15

Table 3.3: Introduced oscillation mode for different power grid strength

Grid strength	Controller type	Eigenvalues	f (Hz)	ζ
Strong grid	CIEC	$-0.1798 \pm 4.7566i$	0.7570	0.0378
	CIEC plus RDC	$-0.6236 \pm 4.6086i$	0.7335	0.1341
	IIEC	$-1.4655 \pm 9.0513i$	1.4406	0.1598
Weak grid	CIEC	$0.0702 \pm 3.9866i$	0.6345	-0.0176
	CIEC plus RDC	$-0.6015 \pm 3.9640i$	0.6309	0.1500
	IIEC	$-1.3094 \pm 6.9805i$	1.1110	0.1844

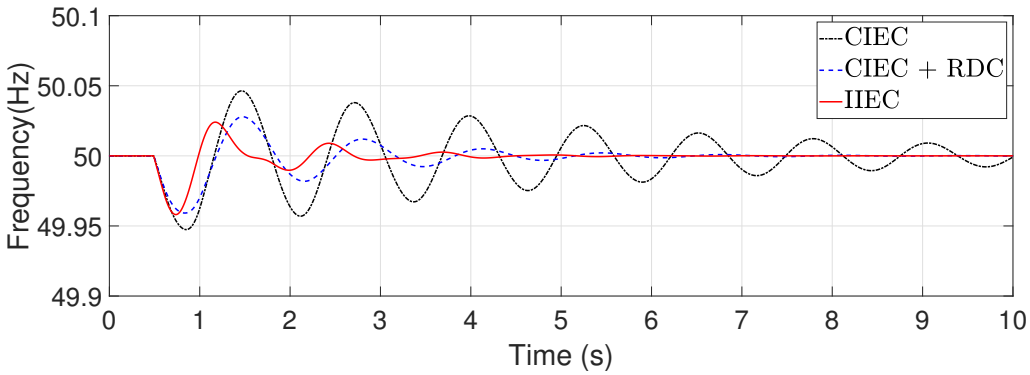

Figure 3.4: Frequency response of a DFIG-WT under strong power grid connection

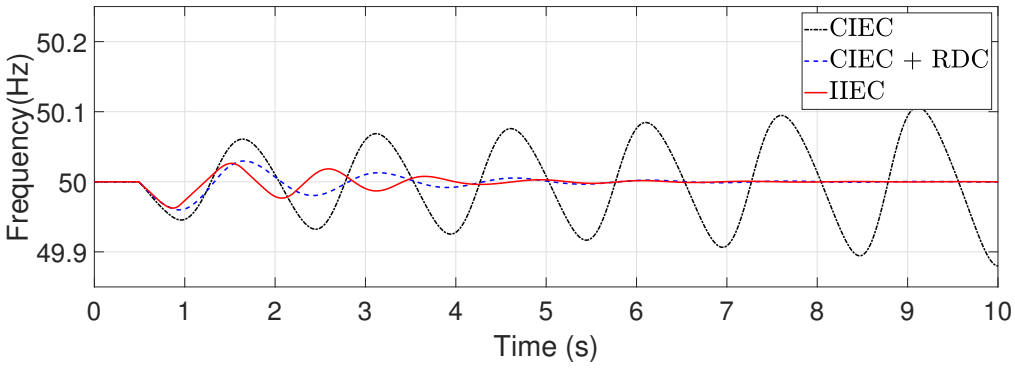

Figure 3.5: Frequency response of a DFIG-WT under a weak power grid connection

Simulation Results

After satisfactory damping performance verification of the introduced oscillation mode via small signal stability analysis results, simulation results are also obtained to test the frequency support performance of the proposed IIEC. The DFIG-WT was connected to a SMIB system and a sudden load disturbance was added at 0.5s. Fig.3.4 and Fig.3.5 show the frequency response under different power grid strength. By comparing the simulation results presented in Fig.3.4 and Fig.3.5, it indicates that the CIEC will deteriorate the system stability and lead system instability when the DFIG-WT is under a weak power grid connection. The frequency response and the damping performance of the CIEC were varied for different system operating points. However, the DFIG-WT equipped with CIEC plus RDC and the IIEC can support system frequency and the oscillation can be mitigated within 7 seconds for both grid strength. The frequency response of using the IIEC was robust against different power grid strength. Therefore, the proposed IIEC for DFIG-WT can provide robust frequency support performance without introducing poorly damped oscillation mode in the system and thus avoiding the use of an additional RDC. FN, as a frequency support performance evaluation index [156], is also included to show the frequency support performance. The comparison of FN for DFIG-WT equipped with different IEC under strong and weak grid strength is provided in Table3.4. It can be found that the frequency deviation by using CIEC plus RDC and IIEC can achieve similar frequency support performance under power grid strength variation. Moreover, the damping performance of frequency shown in Fig.3.4 and Fig.3.5 are consistent to the small signal stability results achieved in Table3.3.

3.5.2 A Two-area Four-machine System

The DFIG-WTs with the proposed IIEC are also connected to a classic 4M11B system provided in [4] to verify its performance, which is the same as Section 2.5.2. The single line diagram of the studied 4M11B with the DFIG-WTs connecting to node 8 is given in Fig.3.6, where DFIG-WTs are added at a new node 12. A 140 km transmission line is used between node 8 and 12 for DFIG-WTs integration. Based

Table 3.4: Frequency support performance comparison of a DFIG-WT under a different power grid strength connection

Grid strength	Controller type	FN (Hz)
Strong grid	CIEC	49.947
	CIEC plus RDC	49.959
	IIEC	49.958
Weak grid	CIEC	-
	CIEC plus RDC	49.960
	IIEC	49.962

on the calculation, the short circuit ratio (SCR) at node 12 equals to 3. Thus, the connection between the DFIG-WTs and 4M11B system is weak. The parameters of four generators and loads of 4M11B system are provided in the Appendix A. Other parameters, such as line impedance, are set as [4]. Power system stabilisers (PSS) are installed at G1-G4 to maintain satisfactory damping ratio of the system inter-area oscillation mode. The nominal 4M11B system operating point is set as 400 MW power flow from node 8 to 9. The power generated by the DFIG-WTs is 504 MW which is 15% wind penetration level in the system. By using the proposed approach provided in Section 3.4, the IIEC gains for DFIG-WTs connecting to a 4M11B system are calculated as $K_{dr} = 9.9435$ and $K_{in} = 4.9579$.

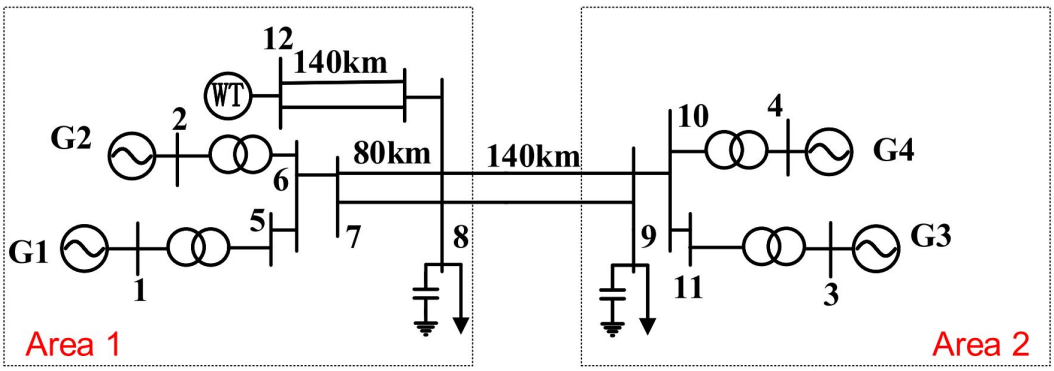

Figure 3.6: 4M11B system with DFIG-WTs integration

Small Signal Stability Analysis

The small signal stability analysis results of the introduced oscillation mode dominated by a CIEC, a CIEC plus RDC and an IIEC for DFIG-WTs participating in 4M11B system frequency support under tie-line power variation are provided in Table3.5. Comparing the small signal stability analysis results, both the CIEC

Table 3.5: New excited mode for different tie-line power flow

Controller type	$P_{Tie-line}$(MW)	Eigenvalues	f (Hz)	ζ
CIEC	300	$-0.3368 \pm 7.2885i$	1.1600	0.0462
	400	$-0.2986 \pm 7.1499i$	1.1379	0.0417
	500	$-0.2435 \pm 6.9406i$	1.1046	0.0351
CIEC plus RDC	300	$-1.1276 \pm 7.1181i$	1.1329	0.1565
	400	$-1.0223 \pm 6.7923i$	1.0810	0.1488
	500	$-1.0242 \pm 6.7979i$	1.0819	0.1490
IIEC	300	$-2.8233 \pm 14.7379i$	2.3456	0.1881
	400	$-2.6604 \pm 14.4804i$	2.3046	0.1807
	500	$-2.4256 \pm 14.1026i$	2.2445	0.1695

plus RDC and IIEC will not introduce the low frequency poorly damped oscillation in the system under tie-line power flows variations. However, the damping ratio of introduced oscillation mode dominated by CIEC is low which will cause low frequency oscillation. By comparing the damping ratio of the DFIG-WTs with a CIEC plus RDC to the IIEC, the proposed IIEC can achieve a similar damping performance as the CIEC plus RDC. Hence, the system damping performance can be ensured by only adding an IIEC to avoid further design and application of a RDC.

Similarly, the small signal stability analysis results regarding the introduced oscillation mode of applying a CIEC, a CIEC plus RDC and an IIEC for DFIG-WTs participating in a 4M11B system frequency support with different DFIG-WTs penetration levels are given in Table3.6. Based on the damping ratio of introduced oscillation mode in Table3.6, it indicates that the proposed IIEC and the CIEC plus RDC can provide satisfactory damping performance under different DFIG-WTs penetration levels as the design requirement. However, the DFIG-WTs with a CIEC in-

troduces a poorly damped low frequency oscillation mode and its damping ratio is different while the DFIG-WTs penetration levels change.

Table 3.6: Introduced oscillation mode under different DFIG-WTs penetration level

Controller type	Penetration level	Eigenvalues	f (Hz)	ζ
CIEC	15%	$-0.2986 \pm 7.1499i$	1.1379	0.0417
	20%	$-0.3139 \pm 6.3386i$	1.0088	0.0495
	25%	$-0.3552 \pm 5.3085i$	0.8449	0.0668
CIEC plus RDC	15%	$-1.0824 \pm 6.9874i$	1.1121	0.1531
	20%	$-1.0044 \pm 6.2229i$	0.9904	0.1593
	25%	$-0.8848 \pm 5.2443i$	0.8346	0.1664
IIEC	15%	$-2.6604 \pm 14.4804i$	2.3046	0.1807
	20%	$-1.9069 \pm 12.3500i$	1.9656	0.1526
	25%	$-1.0154 \pm 9.7275i$	1.5482	0.1038

Simulation Results

In order to further verify the effectiveness of the proposed IIEC in a 4M11B system, the time-domain simulation results are also obtained under tie-line power flow variation and change in DFIG-WTs penetration levels in the system. A 15% load disturbance at node 8 was added at 0.5s. Fig.3.7 shows the frequency response of DFIG-WTs with a CIEC, a CIEC plus RDC and an IIEC in a 4M11B system under nominal operating point. According to the simulation results, the IIEC can provide better frequency support performance comparing to the CIEC and its damping performance is almost the same as the DFIG-WTs equipped with CIEC plus additional RDC, which means no lightly damped oscillation mode will be introduced.

The frequency response of 500MW tie-line power flow is also provided for comparison as shown in Fig.3.8. Comparing the simulation results in Fig.3.7 and Fig.3.8, the proposed IIEC can provide robust frequency support performance under different tie-line power flow. However, the CIEC will introduce poorly damped oscillation mode during frequency support for both tie-line power flow. Such frequency oscillation will cause large frequency deviation and a low FN. The frequency support

performance index for 400MW and 500MW tie-line power flow was also provided in Table3.7 and 3.8. By comparing FN, the proposed IIEC achieves robust frequency support performance under tie-line power variation. Moreover, the damping performance of frequency shown in Fig.3.7 and Fig.3.8 verified the small signal stability results achieved in Table3.5.

Similar to the small signal stability analysis results, the frequency response under different DFIG-WTs penetration levels in a 4M11B system is also achieved and shown in Fig.3.7 and Fig.3.9. The robustness of the proposed IIEC is verified by 15% and 25% DFIG-WTs penetration levels. According to the simulation results, the proposed IIEC can achieve robust frequency support performance when the DFIG-WTs penetration levels change from 15% to 25%. However, the damping of DFIG-WT with a CIEC is still low, which can be seen that oscillation takes more than 10s to be settled. Moreover, a large frequency deviation can still be observed with CIEC in Fig.3.9 for 25% DFIG-WTs penetration level, which also cause a lower FN. Considering the damping performance of the proposed IIEC and the CIEC plus RDC, the system damping is similar for both controllers. As for the frequency support performance shown in Fig.3.7 and Fig.3.9, the proposed IIEC can provide robust frequency support performance considering the variations of DFIG-WTs penetration levels in the system. Table3.9 provides the frequency support performance index for 25% wind power penetration level. Comparing the FN given in Table3.7 and 3.9, it can also verify that the proposed IIEC can achieve the robust frequency support performance. Moreover, the damping performance of frequency shown in Fig.3.7 and Fig.3.9 are still in accordance with the small signal stability results obtained in Table3.6.

Table 3.7: Frequency support performance comparison under nominal operating point in a 4M11B system.

Controller type	FN (Hz)
CIEC	49.8614
CIEC plus RDC	49.8924
IIEC	49.898

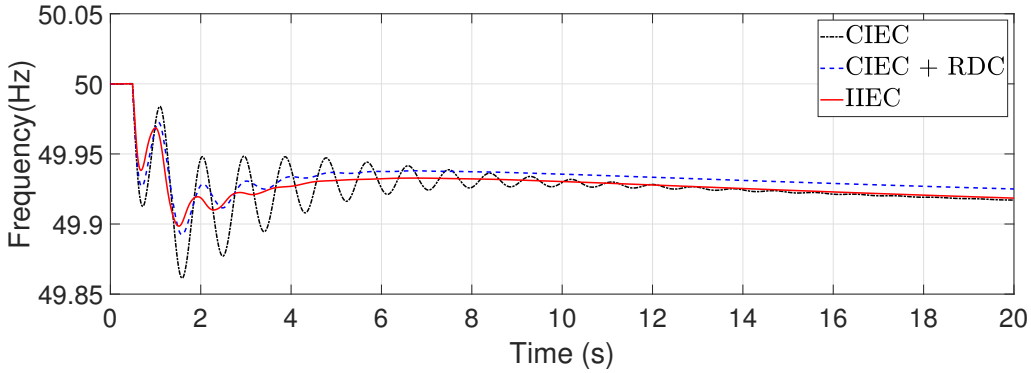

Figure 3.7: Frequency response under nominal operating point in a 4M11B system.

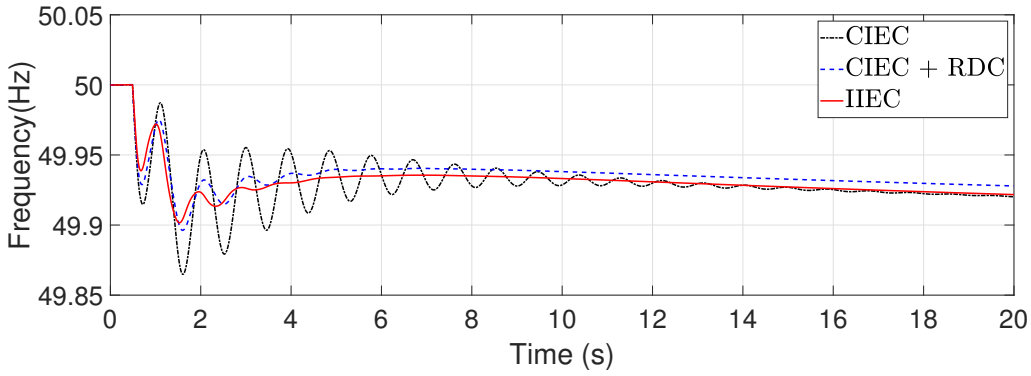

Figure 3.8: Frequency responses under 500MW tie-line power flow in a 4M11B system.

Table 3.8: Frequency support performance comparison under 500MW tie-line power flow in a 4M11B system.

Controller type	FN (Hz)
CIEC	49.8649
CIEC plus RDC	49.8962
IIEC	49.9

Table 3.9: Frequency support performance comparison under 25% DFIG-WTs penetration level in a 4M11B system.

Controller type	FN (Hz)
CIEC	49.8293
CIEC plus RDC	49.88
IIEC	49.875

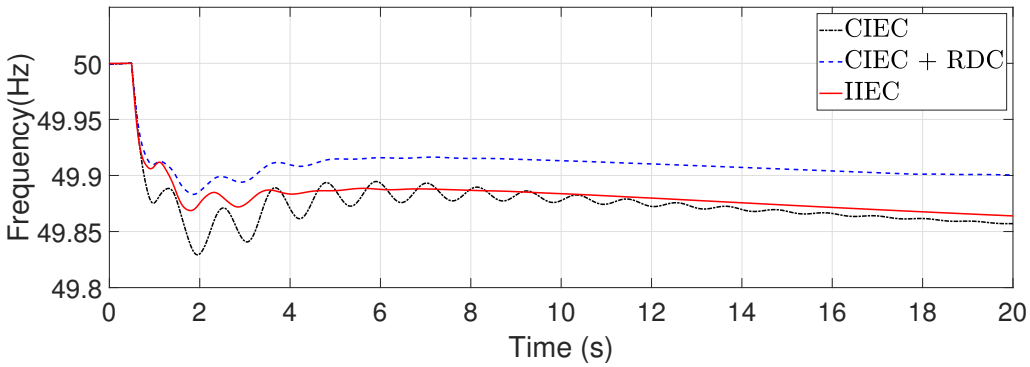

Figure 3.9: Frequency response under 25% DFIG-WTs penetration level in a 4M11B system.

3.5.3 A New England New York 68-Bus System

In order to test the robustness performance of the proposed IIEC in a more complicated power system, the DFIG-WTs are connected to a 16M68B system as Section 2.5.3. The single line diagram of a modified 16M68B system with the DFIG-WTs connected at a new node 69 is shown in Fig.3.10. The DFIG-WTs are connected to node 31 of the 16M68B system which are highlighted in red color. The parameters of detailed bus data, line data and generator data are given in Appendix B.

Small Signal Stability Analysis

Table3.10 shows the small signal stability analysis results of 16M68B system with DFIG-WTs integration under different tie-line power flow between Area I and II. The small signal stability analysis results for using different frequency support controller are included and compared. According to the small signal stability results, it can be found that the new excited oscillation mode by CIEC is poor-damped under different tie-line power flow. Thus, the oscillation will take more than 10 seconds to settle. The damping ratio of the new excited oscillation mode by using additional RDC and proposed IIEC are all above 0.15 where the oscillation can be mitigated within 12-15s.

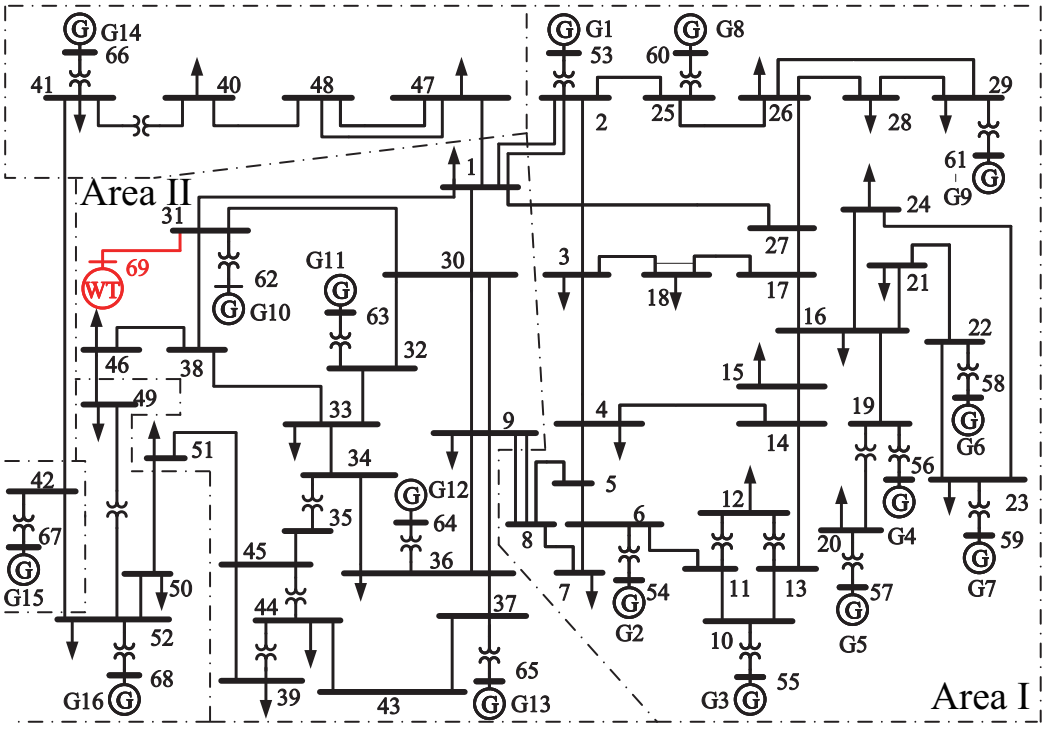

Figure 3.10: 16M68B system with DFIG-WTs integration

Table 3.10: New excited mode for different tie-line power flow

Controller type	$P_{Tie-line}$(MW)	Eigenvalues	f (Hz)	ζ
CIEC	100	$-0.1634 \pm 5.6647i$	0.9016	0.0288
	500	$-0.1556 \pm 5.5736i$	0.8871	0.0279
	900	$-0.141 \pm 5.4143i$	0.8617	0.0260
CIEC plus RDC	100	$-1.0576 \pm 5.6337i$	0.8966	0.1845
	500	$-1.0485 \pm 5.5461i$	0.8827	0.1858
	900	$-1.0317 \pm 5.3918i$	0.8581	0.1879
IIEC	100	$-2.8754 \pm 11.9577i$	1.9031	0.2338
	500	$-2.8649 \pm 11.9054i$	1.8948	0.234
	900	$-2.8412 \pm 11.8136i$	1.8802	0.2338

Simulation Results

In addition to the small signal stability analysis results, simulation results are also obtained to evaluate the performance of the proposed IIEC in a 16M68B system. Fig.3.11 and 3.12 show the simulation results for 16M68B system with DFIG-WTs integration under 100MW and 900MW power flow between Area I and II. At 0.5s, a 150MW load disturbance at bus 1 was added. According to the simulation results, it can be seen that the DFIG-WTs with IIEC can provide robust frequency support performance under tie-line power flow variation between the system. Thus, designing additional RDC can be avoid to provide robust frequency support performance while maintain satisfactory damping performance of the new excited oscillation mode. The frequency support performance index for 100MW and 900MW tie-line power flow was also provided in Table3.11 and 3.12. By comparing FN, the proposed IIEC achieves robust frequency support performance under tie-line power variation in a 16M68B system. Moreover, the damping performance of frequency shown in Fig.3.11 and Fig.3.12 verified the small signal stability results achieved in Table3.10.

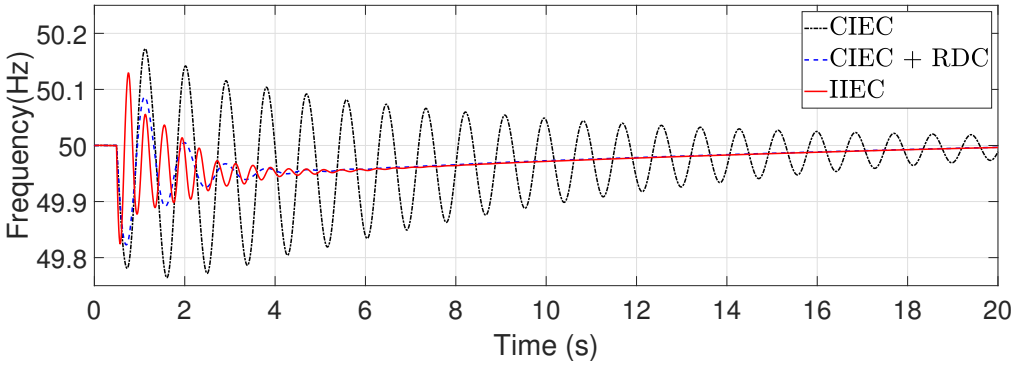

Figure 3.11: Frequency responses under 100MW Area I and II power flow in a 16M68B system

Moreover, the robustness of the proposed IIEC is also verified by changing the considered disturbance. A load disturbance was added at bus 47 at 1 second. The simulation results for the new disturbance are shown in Fig.3.13. By comparing the simulation results in two different disturbances, it can be found that the proposed

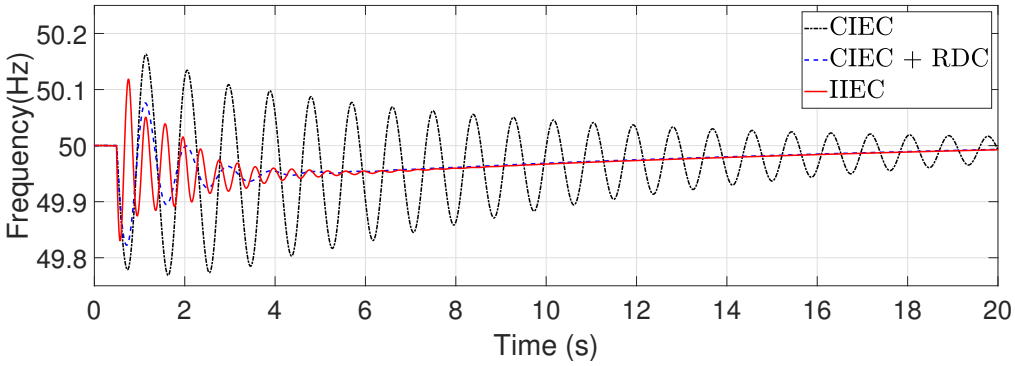

Figure 3.12: Frequency responses under 900MW area I and II power flow in a 16M68B system

Table 3.11: Frequency support performance comparison under 100MW power flow between Area I and II in a 16M68B system.

Controller type	FN (Hz)
CIEC	49.7643
CIEC plus RDC	49.8228
IIEC	49.8246

Table 3.12: Frequency support performance comparison under 900MW power flow between Area I and II in a 16M68B system.

Controller type	FN (Hz)
CIEC	49.7687
CIEC plus RDC	49.8224
IIEC	49.8303

IIEC can ensure robust frequency support performance under different fault disturbance. The oscillation can be mitigated within 10s as the design requirement. The frequency support performance index for different load disturbances was also provided in Table3.11 and 3.13. By comparing FN, the proposed IIEC achieves robust frequency support performance under different disturbance in a 16M68B system.

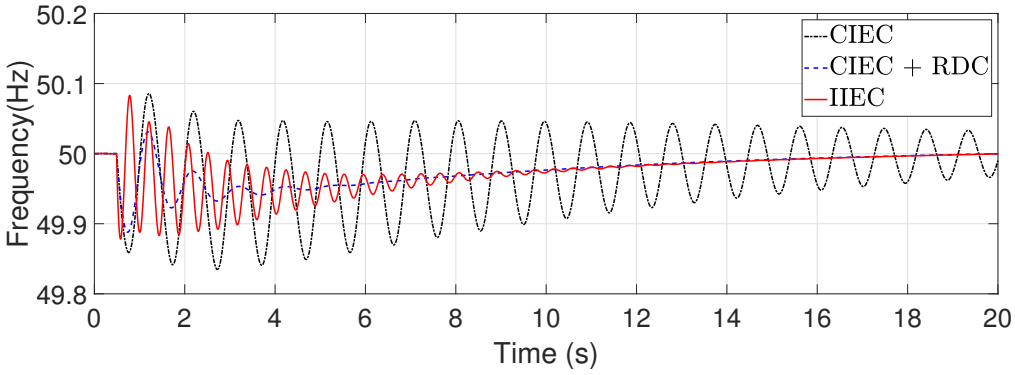

Figure 3.13: Frequency responses for a load disturbance at bus 47 in a 16M68B system

Table 3.13: Frequency support performance comparison under a load disturbance at bus 47 in a 16M68B system.

Controller type	FN (Hz)
CIEC	49.8348
CIEC plus RDC	49.8879
IIEC	49.878

Based on the small signal stability results and time-domain simulation results presented above, the proposed IIEC shows the capability of providing robust frequency support performance when the system operating point changes. Moreover, the new introduced oscillation mode has sufficient damping ratio, which indicates that the system damping can be mitigated within 10s. However, the new introduced oscillation mode by CIEC is poorly damped in the system and it will introduce challenges to system stability. Comparing the approach for adding a RDC to improve the system damping when the CIEC is used, the proposed IIEC can provide similar damping performance. This can help maintain system frequency by using

DFIG-WTs without designing an additional damping controller to the system and the practical implementation of DFIG-WTs participating in the system frequency support can be simplified.

3.6 Conclusion

This chapter proposes a novel IIEC design approach for DFIG-WTs participating in system frequency support which can achieve robust frequency support performance and satisfactory damping performance simultaneously. A theorem is proposed which can design the frequency support controller with robust frequency support performance by H_∞ synthesis. To ensure the satisfactory damping performance, the regional pole placement control objective is added and cooperates with the robust frequency support controller to design the proposed IIEC which can provide both robust frequency support performance and satisfactory damping performance. Case studies are achieved by connecting the DFIG-WTs with IIEC to a SMIB system, a 4M11B system and a 16M68B system. Both small signal stability analysis and time-domain simulation are carried out to show the effectiveness of the proposed IIEC. With the proposed IIEC, the DFIG-WTs can provide robust frequency support performance comparing to the CIEC and CIEC plus RDC. Moreover, the damping ratio of new introduced oscillation mode is above 0.15 as the design requirement as RDC, such that system oscillation can be mitigated within 10s as system operation required. Hence, additional damping controller design can be avoided and the DFIG-WTs participating in the system frequency regulation can be simplified.

Chapter 4

Robust Torsional Damping Controller for DFIG-based Wind Turbine Participating in the System Frequency Support

4.1 Introduction

Due to the fast development of wind power generation for environmental consideration, the penetration level of wind power has been increased significantly in the modern power system. With such fast-growing wind power, it will lead to less system inertia for system frequency support [142, 157, 158]. System operators have proposed grid codes requirements on the wind power participating in system frequency support [5, 6, 30, 31, 159, 160]. Additional control loops, namely inertia response and droop response, are designed for wind turbine generators to response to system frequency dynamics during a disturbance. With additional control loops, the interaction between the mechanical system of WT and the electrical system is unavoidable [124]. Such interaction will affect the drive train dynamics of WT. Thus, it may lead to the WT torsional oscillation and even worse effect may cause the damage on the drive train components of WTs [126]. For example, the gearbox,

which is one of the components of the drive train, has been reported in [161] that the actual gearbox of a WT needs to be replaced every six to eight years where the expected lifetime is advised to be 20 years.

The torsional oscillation, which can also be referred to as torsional vibration, is the oscillation that occurred on the drive train of WT. Due to the torsional deformations caused by the mechanical torque adding on the drive train, mechanical stress occurs. The torsional oscillation will be generated by torsional deformations and it is a measure of mechanical stress [162]. Such oscillation will cause drive train shaft vibration, decrease the shaft lifetime and will even worse lead to shaft damage. Moreover, the torsional oscillation in the drive train will be converted to the electrical power oscillation. This oscillation will interact with power system oscillation mode and cause resonance, which is unfavourable for the power system stability [92, 163].

Several studies on torsional oscillation damping controller design have been investigated in [92, 162, 164, 165]. In [162], an oscillation damping controller was proposed to reduce or remove the unwanted torsional oscillations using generator torque. A five-mass drive train model was studied, which provide detailed studies on the multiple torsional oscillations of the drive train. Band-pass filters were designed to extract the specific oscillation frequency to damp. However, the damping performance of the band-pass filter based torsional damping controller was compromised considering uncertainties and retuning of the band-pass filter was needed [92]. A model-based torsional oscillation damper was then proposed to avoid retuning, such that the torsional oscillation damping performance can be ensured subjected to uncertainties. The proposed model-based damper was designed by using a discrete-time Kalman filter to generate the desired compensated torque for damping the torsional oscillation under parameter uncertainties. In [164], it has been found that the above torsional damping controller induced additional oscillation at another frequency during the damping at the torsional oscillation. Thus, a so-called virtual inertia controller, was proposed to prevent torsional oscillation through adding virtual inertia based on generator torque. With the proposed virtual inertia controller, the drive train oscillation frequency can be temporarily switched and thus prevent

resonance in the WT drive train. Comparing to the virtual inertia based damping approach, a faster damping performance can be achieved using the nonlinear method based on sliding mode control theory proposed in [165] to mitigate the torsional oscillation. The aforementioned literature has successfully mitigated the effect of the torsional oscillation on the drive train of a variable speed wind turbine. However, all of them did not consider the torsional oscillation of the drive train when the WT participates in system frequency support.

For the torsional oscillation considering the impact of wind turbine generators contributing to frequency support, the literature which addressed this issue is shown in [35,87,124–127]. [125,126] studied the mechanism of the impact of wind turbine generators contributing to system frequency support on WT torsional oscillation in details. The concern of wind turbine generators with frequency support on WT drive train torsional oscillation has been raised. The recent works on damping the torsional oscillation are mainly implemented through controlling the dc-link capacitor energy and generator torque. In [87,125], the proposed damping control strategies are based on the dc-link capacitor of the converter. Reference [87] proposed to utilise the energy stored in the dc-link capacitor of wind turbine generators to mitigate the effect of the IEC on the drive train of wind generator. [125] compared the performance of a conventional dc-link bandwidth tuning method and active damping method on reducing the mechanical stress caused by IEC. To overcome the impacts of these methods on turbine maximum power point tracking (MPPT) performance, a new filter method was proposed based on modification the dc-link reference voltage. The authors in [35,124] designed the controller with a band pass filter to extract the oscillation and adjust the generator electromagnetic torque by changing the current reference at the rotor side converter control. Using the residue method, the torsional oscillation damper (TOD) was designed in [35] to mitigate the effect of an IEC on torsional oscillation mode. An adaptive damping controller was proposed to damp the torsional oscillation mode in [124]. Another recent research proposed a resonance damper by the modification on the droop controller of the wind turbine generator [127]. The damper is designed based on the pole-zero cancellation method to reduce the resonance and avoid the fatigue damage on the WT drive train. In all

of the existing literature, the torsional oscillation damper design did not consider the theoretical analysis on the active and reactive power control approach selection to ensure the most effective control loop. Hence, detailed controllability analysis will be investigated in this chapter. Although [124] use an adaptive damping controller to enhance the torsional damping performance under various operating conditions, the design of torsional oscillation damper included the band-pass filter which needed to be adaptively retuned under different operating conditions. To overcome this disadvantage, a robust torsional oscillation damping controller is desired to be designed to achieve robust torsional oscillation mitigation performance considering model mismatch, parameter uncertainties and different external disturbances which may happen in the DFIG-WT participating in the system frequency support.

This chapter proposes a robust torsional oscillation damping controller (RTODC) to ensure robust damping performance of WT torsional oscillation when the DFIG-WT participates in system frequency support. The proposed RTODC can provide robust damping performance for torsional oscillation mode simultaneously with the DFIG-WT equipped with a robust damping controller (RDC) for the new oscillation mode excited by the DFIG-WT IEC. Small signal stability results and simulation results are provide to verify the robustness on a 4-machine 11-bus (4M11B) system and a New England New York 68-bus (16M68B) power system. The main contributions of this chapter are:

1) The proposed RTODC is designed based on the reactive power control of the DFIG-WT, where the geometric controllability is calculated to show that the reactive power control loop has superior damping performance than the active power control loop on mitigating the torsional oscillation.

2) A RTODC based on H_∞ mixed-sensitivity approach is proposed to provide guaranteed damping performance on the torsional oscillation mode of the drive train of DFIG-WT participating in system frequency support where the impact of DFIG-WT with frequency support capability on the torsional oscillation can be mitigated.

3) The RDC presented in [123] is improved by considering the effect of torsional

oscillation mode in its design. The designed robust torsional damping controller can work simultaneously with the RDC, such that the robust damping performance of the torsional oscillation mode and the new excited oscillation mode can be ensured against parameter uncertainties, time-varying operation points and external disturbances.

The rest of this Chapter is organised as follows. Section 4.2 shows the studied two-mass wind turbine model and the effect of the DFIG-WT with an IEC on torsional oscillation mode of drive train. The proposed RTODC design is given in Section 4.3. The case study of a 4M11B system with DFIG-WTs is obtained and given in Section 4.4. Section 4.5 shows the case study of a 16M68B system with DFIG-WTs. Finally, a conclusion is drawn in Section 4.6.

4.2 Torsional Oscillation of a Wind Turbine Drive Train

This section firstly presents the two mass drive train model of DFIG-WT. Then, the effect of an IEC on WT torsional oscillation mode is illustrated.

4.2.1 Drive Train Model

As the wind turbine and generator shaft has different softness, a two-mass drive train model is usually chosen to study the dynamics of the drive train of DFIG-WT. Fig.4.1 shows the representation of a two-mass drive train model of a WT. A low speed shaft and wind turbine are modelled in one mass and the high speed shaft and generator is modelled as another mass. The dynamics of the two-mass drive train model can be described as (4.2.1)-(4.2.3):

$$\frac{\mathrm{d}\omega_t}{\mathrm{d}t} = \frac{T_t - K_s\theta_s - D_m(\omega_t - \omega_r)}{2H_t} \tag{4.2.1}$$

$$\frac{\mathrm{d}\omega_r}{\mathrm{d}t} = \frac{T_e + K_s\theta_s + D_m(\omega_t - \omega_r)}{2H_g} \tag{4.2.2}$$

$$\frac{\mathrm{d}\theta_s}{\mathrm{d}t} = \omega_b(\omega_t - \omega_r) \tag{4.2.3}$$

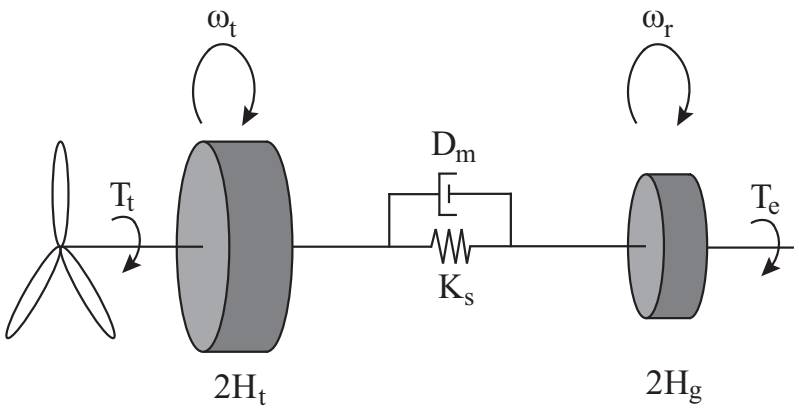

Figure 4.1: Two-mass wind turbine drive train

where ω_t, ω_r and ω_b are turbine angular speed, generator angular speed and base angular speed. θ_s is the shaft twist angle. H_t and H_g are the turbine and generator inertia constants. T_m and T_e are turbine mechanical torque and generator electrical torque. D_m is the mutual damping coefficient.

4.2.2 Effect of an IEC on torsional oscillation mode of a DFIG-WT

Table 4.1: Torsional Oscillation modes of the 4M11B system

Case	Eigenvalues	f (Hz)	ζ
Without IEC	$-0.1429 \pm 19.6301i$	3.1242	0.01
With IEC	$0.6457 \pm 19.6814i$	3.1324	-0.0328

Table4.1 shows the small signal stability analysis results of the torsional oscillation of the wind turbine without and with an IEC. According to the damping ratio of the torsional oscillation mode, it can be found that torsional oscillation mode of DFIG-WT with supplementary frequency support capability will be deteriorated.

Simulation results are also provided to show the effect of an IEC on the WT torsional oscillation mode. As shown in Fig.4.2, the rotor speed of a DFIG-WT is hardly changed during a frequency disturbance when the DFIG-WT does not partic-

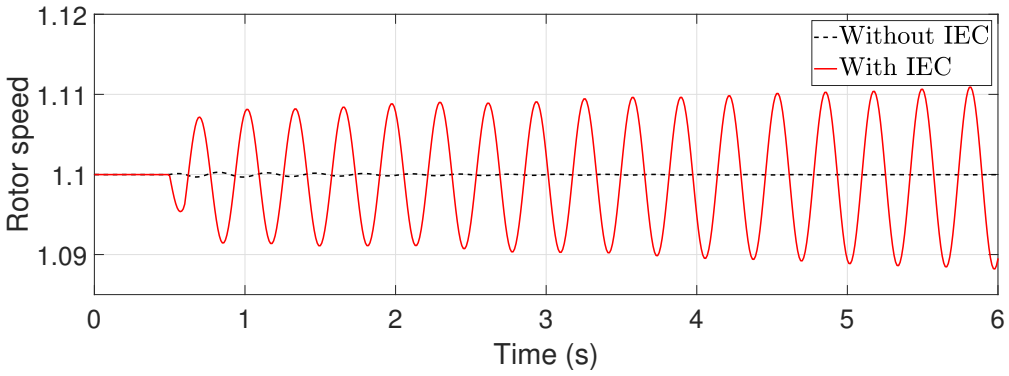

Figure 4.2: Drive-train speed of DFIG-WT

ipate in system frequency support. However, when additional IECs are equipped in the DFIG-WT, a poorly damped oscillation is observed. Both small signal stability analysis and simulation results illustrate that the torsional oscillation mode of the WT will be deteriorated when the wind turbine generator contributes to system frequency support. Thus, it is necessary to design a damping controller to effectively suppress the oscillation on the shaft damping of DFIG-WT. Considering the real application, model mismatch, uncertain parameters and the time-varying operating points are inevitable. Hence, it is desired to design a robust torsional oscillation damping controller to ensure satisfactory damping performance of torsional oscillation mode under different operating conditions.

4.3 H_∞ Mixed-sensitivity Robust Torsional Damping Controller Design

This section firstly introduces the controllability analysis on the selection of the output signals for the torsional damping controller. After that, the robust torsional oscillation damping controller design approach is provided.

4.3.1 Geometric controllability

In order to properly select the output signals for the design of torsional damping controller, the geometric approach is used where better performance can be observed using the controllability calculated via geometric approach [166]. The geometric measures of controllability m_{ci} for a mode 'i' is given as follows [167]:

$$m_{ci}(k) = \cos\left(\theta\left(l_i, b_k\right)\right) = \frac{\left|b_k^T l_i\right|}{||l_i||||b_k||} \tag{4.3.1}$$

where b_k represents the kth column of the input matrix B, l_i is the ith left eigenvector. The acute angle between b_k and l_i is described by $\cos\left(\theta\left(f_i, l_k\right)\right)$. $|f|$ and $||f||$ are the modulus and Euclidien norm of f [166].

Since the torsional damping controller is normally aggregated at the active power or reactive power control loop of the DFIG rotor side converter control, the geometric controllability when selecting these two control loops as the system input will be studied and compared. Using (4.3.1), the geometric controllability for different inputs of system can be calculated as shown in Table4.2, where P_{damp} and Q_{damp} represent the system input at active and reactive power control loop, respectively. According to the calculated controllability, it can be found that the controllability of using Q_{damp} has relatively higher geometric controllability than P_{damp}. Thus, the torsional oscillation mode can be well damped by selecting Q_{damp} as the input of system and as the output of the torsional oscillation damping controller.

Table 4.2: Geometric Controllability of different inputs

Input Vector	Geometric Controllability
P_{damp}	0.0117
Q_{damp}	0.3876

4.3.2 H_∞ Based Robust Torsional Oscillation Damping Controller Design

Fig.4.3 shows the configuration for achieving the H_∞ mixed-sensitivity robust control design, where the mixed-sensitivity control function is to mitigate the effect

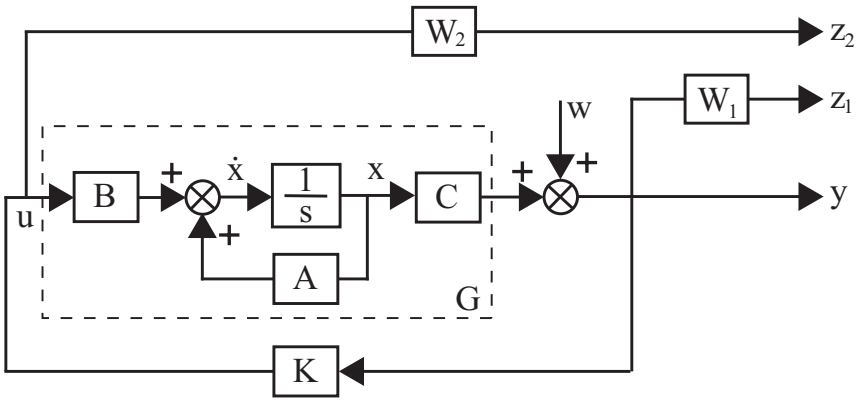

Figure 4.3: H_∞ mixed-sensitivity Design configuration

of disturbance on the output and optimise the control effort in a limited bandwidth [10]. G is the open-loop system model considering the effect of RDC but excluding the proposed torsional oscillation damping controller, where A, B and C are the system matrices. K is the controller to be designed.

In the H_∞ mixed-sensitivity robust control approach, the output disturbance rejection control objective is achieved by minimising H_∞ norm of the closed-loop transfer function S between the disturbance input w and output y, which is represented by the sensitivity function $S = (I - GK)^{-1}$. Meanwhile, the control effort optimisation is ensured by minimising the H_∞ norm of KS. In order to achieve the two control objectives simultaneously, the weighting functions are appropriately selected, where a low-pass filter is used for output disturbance rejection at low frequency range and a high-pass filter is used to optimise the control at high frequency range [10]. Thus, the control objectives are summarised and given in (4.3.2).

$$\min_{K\in\mathbb{S}} \left\| \begin{bmatrix} W_1 S \\ W_2 K S \end{bmatrix} \right\|_\infty < \gamma \tag{4.3.2}$$

where γ is the H_∞ performance index. The design configuration given in Fig.4.3

can be written as:

$$\begin{cases} \dot{x} = Ax + B_1 w + B_2 u \\ z = C_1 x + D_{11} w + D_{12} u \\ y = C_2 x + D_{21} w \end{cases} \tag{4.3.3}$$

where x is the state variables of the system, u and y are input and output of system. z is given as $z = \begin{bmatrix} z_1 & z_2 \end{bmatrix}^T$.

The state-space representation of the controller can be expressed as (4.3.4):

$$\begin{aligned} \dot{x_c} &= A_c x_c + B_c y \\ u &= C_c x_c + D_c y \end{aligned} \tag{4.3.4}$$

Then, the transfer function of closed-loop system between w and z can be obtained,

$$F_{zw} = \begin{bmatrix} W_1 S \\ W_2 K S \end{bmatrix} = D_s + C_s (sI - A_s)^{-1} B_s \tag{4.3.5}$$

where

$$\begin{aligned} A_s &= \begin{bmatrix} A + B_2 D_c C_2 & B_2 C_c \\ B_c C_2 & A_c \end{bmatrix} \\ B_s &= \begin{bmatrix} B_1 + B_2 D_c D_{21} \\ B_c D_{21} \end{bmatrix} \\ C_s &= \begin{bmatrix} C_1 + D_{12} D_c C_2 & D_{12} C_c \end{bmatrix} \\ D_s &= D_{11} + D_{12} D_c D_{21} \end{aligned} \tag{4.3.6}$$

Based on Lyapunov stability theorem and Schur's formula [168], the robust controller can be designed to find the a symmetric matrix $P_\infty > 0$ such that the inequality (4.3.7) is satisfied with $\|F_{zw}\|_\infty < \gamma$, where $\gamma > 0$.

$$\begin{pmatrix} P_\infty A_s + A_s^T P_\infty & B_s & P_\infty C_s^T \\ B_s^T & -\gamma I & D_s^T \\ C_s P_\infty & D_s & -\gamma I \end{pmatrix} < 0 \tag{4.3.7}$$

Moreover, additional requirement on the placement of closed-loop system poles is added to cooperate with the guaranteed robustness. If a positive definite symmet-

ric matrix $P_{\mathcal{D}}$ exists, such that (4.3.8) is satisfied [10],

$$\begin{pmatrix} \sin\theta\left(A_s P_{\mathcal{D}} + P_{\mathcal{D}} A_s^T\right) & \cos\theta\left(A_s P_{\mathcal{D}} - P_{\mathcal{D}} A_s^T\right) \\ \cos\theta\left(P_{\mathcal{D}} A_s^T - A_s P_{\mathcal{D}}\right) & \sin\theta\left(P_{\mathcal{D}} A_s^T + A_s P_{\mathcal{D}}\right) \end{pmatrix} < 0 \tag{4.3.8}$$

Then, it can be concluded that the closed-loop system poles can be placed in the desired region defined by $\mathcal{D}$. Considering the inequalities in (4.3.7) and (4.3.8), if there exist a matrix P, such that a common solution $P = P_{\mathcal{D}} = P_\infty > 0$ can be found. The designed controller K has a guaranteed robustness $\|F_{zw}\|_\infty < \gamma$ with required regional pole placement.

Using the above design approach, the RTODC can be designed where the input of RTODC is selected as the rotor speed deviation $\Delta\omega_r$ to damp the oscillation in the drive train of WT. The output of RTODC is selected using geometric controllability given in Section 4.3.1 as Q_{damp}. The detailed design approach of RTODC can be summarised as follows:

1. Obtain a detailed nonlinear model of power system with DFIG-WTs and build up the model in MATLAB/Simulink.

2. The RDC proposed in Chapter 2 is designed and equipped in DFIG-WTs to mitigate the impact of poorly damped oscillation mode introduced by IEC.

3. Linearise the nonlinear model at one system operating point by using the Linear Analysis in Control System Toolbox of MATLAB, where Q_{damp} is set as the open-loop input and $\Delta\omega_r$ as open-loop output in linearisation.

4. Carry out model deduction via Schur balanced model reduction approach, and build up the controller design configuration as shown in Fig.4.3.

5. Design the RTODC using $'hinfmix'$ function provided by LMI Toolbox in MATLAB, where the interested region for the closed-loop system poles is set by using $'lmireg'$ function.

6. Small signal stability analysis is carried out to verify the satisfactory damping performance of the torsional oscillation mode of the proposed RTODC in a linear model given in Step 2.

7. Validate the effectiveness of the proposed RTODC via simulation study on the nonlinear detailed model obtained in Step 1.

Note that controller designed by using $'hinfmix'$ will have the order of the reduced order plus the order of the weighting functions. It will be a quite high order to implement in practice [116]. Thus, the Schur balanced reduction approach can also be used to reduced the order of the designed RTODC. The reduced-order of designed controller will be selected based on the unchanged frequency response to the full order.

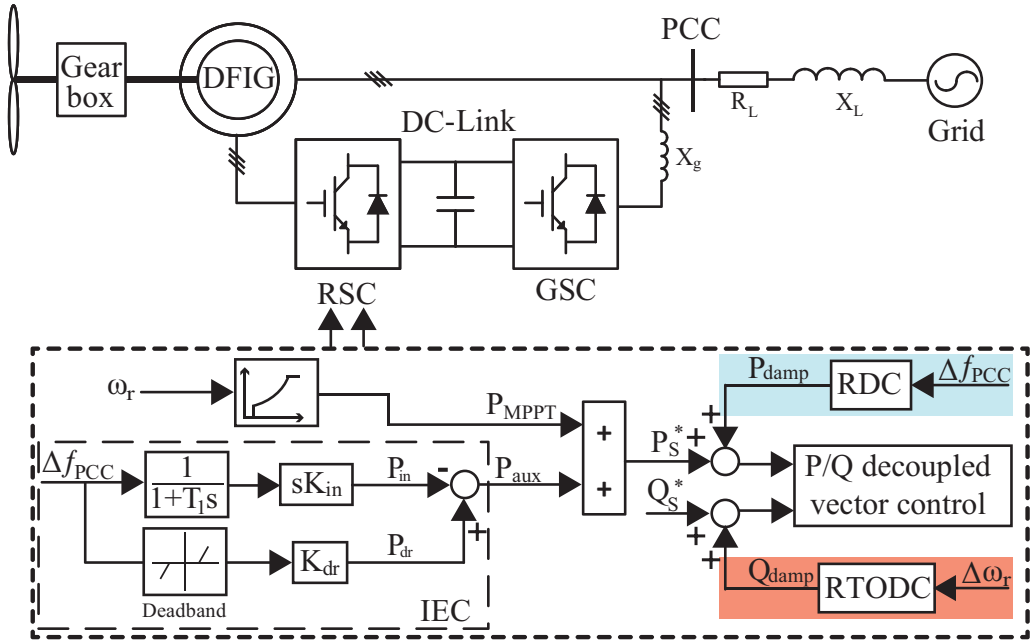

Figure 4.4: DFIG-WT equipped with a RDC and a RTODC

As shown in Fig.4.4, the RDC proposed in Chapter 2 is already designed and added at the active power control loop of DFIG-WT to provide guaranteed damping performance on the new oscillation mode excited by an IEC. The RTODC is designed based on the model of DFIG-WT with a RDC. It will be added at the reactive power control loop in the rotor side converter control of DFIG-WT to mitigate the effect of torsional oscillation mode. As the active and reactive power control of DFIG-WT is decoupled, the RDC and RTODC can ensure robust damping performance on the new oscillation mode and torsional oscillation mode, respectively.

The difference between controllers designed in this chapter and previous chapters is discussed from two points of view. Firstly, by comparing to the controllers designed in previous chapters in terms of the control purpose, the RTODC proposed in this chapter is designed for damping the deteriorated torsional oscillation mode of the WT drive train due to an IEC, whereas the RDC in Chapter 2 and the IIEC in Chapter 3 are designed to mitigate the impact of the oscillation mode introduced by an IEC. Secondly, comparing design approaches between these controllers, the RDC designed in Chapter 2 and the RTODC designed in this chapter are based on the H_∞ mixed-sensitivity robust damping controller design approach. The IIEC designed in Chapter 3 is based on the novel robust PD-type controller approach proposed in Chapter 3.

4.4 Case Study I - Two-area Four-machine System

To verify the robustness of the proposed RTODC on damping torsional oscillation of DFIG-WT participating in system frequency support, a 4M11B system is chosen as the first case study as Section 2.5.2. Fig.4.5 shows the single line diagram of a 4M11B system with DFIG-WTs connecting at bus 8 [4]. A new bus 12 is added for the point of the DFIG-WTs connection. The parameters of this system can be found in Appendix A.

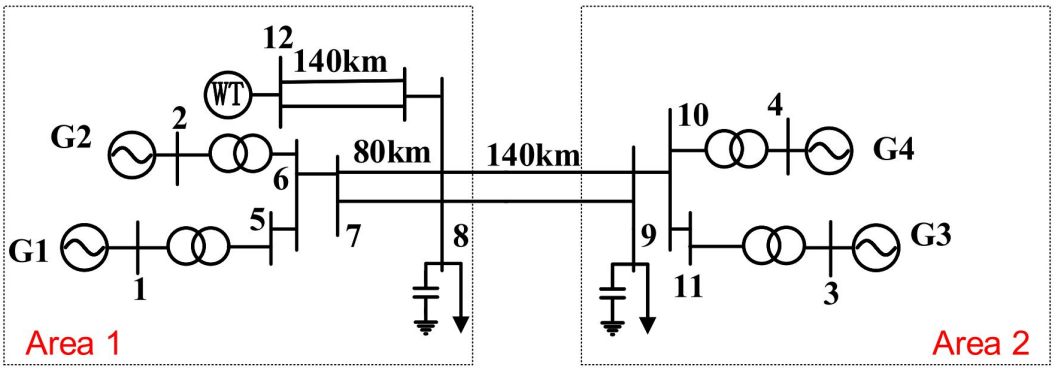

Figure 4.5: 4M11B system with DFIG-WTs participating in system frequency support

4.4.1 Controller Design

The full order of a 4M11B system with DFIG-WTs is a 69th order model. Since the controller design using such a high order will increase the calculation time and most of the states are not relevant to the interested torsional oscillation, Schur balanced truncation model reduction approach is used to truncate the order of the studied system [137]. Fig.4.6 shows the frequency response of the full order and reduced order of a 4M11B system with DFIG-WTs. It can be seen that the 15th reduced order achieved the similar frequency response as the full-order system. Thus, a reduced 15th order system model is used to design the controller.

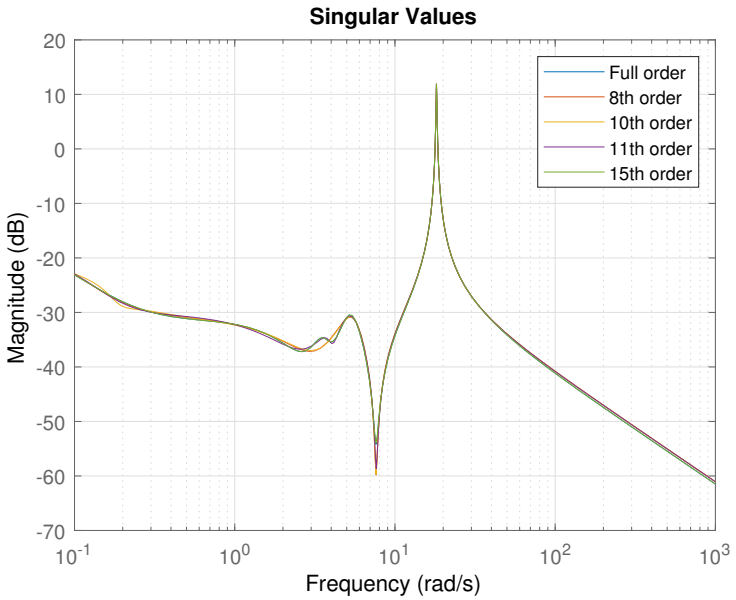

Figure 4.6: Frequency response of a 4M11B system with full order and reduced order

In order to achieve the output disturbance rejection and control effort optimisation simultaneously, appropriate weighting functions are chosen for designing the RTODC and are given in (4.4.1).

$$W_1(s) = \frac{50}{s+50}, W_2(s) = \frac{9s}{s+200} \tag{4.4.1}$$

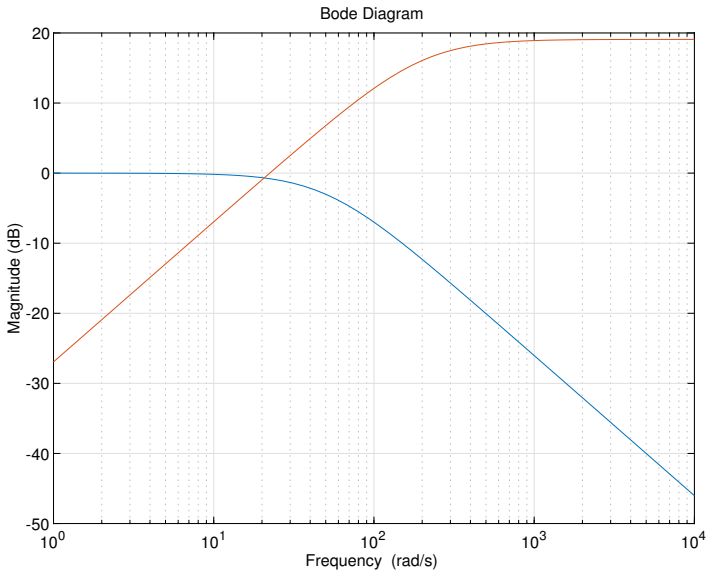

Figure 4.7: Frequency response of W_1 and W_2

By using the RTODC design approach provided in Section 4.3.2, the RTODC for damping the torsional mode of DFIG-WTs participating in the system frequency support in a 4M11B system is designed which is given in (4.4.2) - (4.4.4).

$$H_{RTODC}(s) = \frac{N_t(s)}{D_t(s)} \tag{4.4.2}$$

$$\begin{aligned} N_t(s) =& 3.4692 \times 10^8 s^5 + 6.7621 \times 10^{10} s^4 + 2.53 \times 10^{11} s^3 \\ &+ 4.1395 \times 10^{11} s^2 + 2.5827 \times 10^{11} s + 2.5579 \times 10^{10} \end{aligned} \tag{4.4.3}$$

$$\begin{aligned} D_t(s) =& s^6 + 6.2724 \times 10^8 s^5 + 1.2818 \times 10^{10} s^4 + 2.5926 \times 10^{11} s^3 \\ &+ 1.2524 \times 10^{11} s^2 + 1.4542 \times 10^9 s - 1.1965 \times 10^9 \end{aligned} \tag{4.4.4}$$

In order to show the robustness of the proposed RTODC, the conventional torsional damping controller is also designed by using residue method provided in [138]. The transfer function of the CTODC can be expressed by (4.4.5).

$$H_{CTODC}(s) = K \frac{T_w}{1 + T_w s} \left(\frac{1 + T_1 s}{1 + T_2 s}\right)^2 \tag{4.4.5}$$

where the compensation constants T_1 and T_2 equal to 0.0481 s and 0.0472 s, respectively. K is set to 1.9949. The wash-out filter time constant T_w is 10 s.

4.4.2 Performance Evaluation

Small signal stability analysis results

Table4.3 shows the small signal stability analysis results of the torsional oscillation mode of a 4M11B system with DFIG-WTs under different inertia constants. The small signal stability analysis results of DFIG-WTs with a CIEC and CIEC plus CDC+CTODC are also provided for comparison. Based on Table4.3, it can be found that torsional oscillation will cause system instability when the CIEC is used. The damping performance of using CIEC plus CDC+CTODC is poor and varied against different inertia constants. By equipping a CTODC, the damping ratio of the torsional oscillation mode can be improved. However, when the inertia constant increases, the damping performance of the CTODC is reduced. As for the CIEC plus RDC+RTODC, the damping ratio of the torsional oscillation mode is ensured as the design against different inertia constants. Thus, the torsional oscillation can be well damped and the effect of the IEC on wind turbine oscillation can be minimised under different turbine inertia constants. Moreover, Table4.4 shows the damping performance of the new excited oscillation mode by a CIEC, it can be seen that the proposed RTODC can work well with RDC, where the robust damping performance of the new excited oscillation mode can be achieved simultaneously.

Small signal stability analysis results under different DFIG-WT operating points are obtained by changing the wind speed of DFIG-WT. As shown in Table4.5, it can be found that when the wind speed is varied, the damping performance of the proposed RTODC is still robust. However, the damping performance of the CTODC is varied for different wind speed. The damping ratio of the new excited oscillation mode is given in Table4.6. It can also be verified that the proposed RTODC will not affect the robust damping performance on the new excited oscillation mode by RDC. Both RTODC and RDC can provide robust damping performance for torsional oscillation mode and the new excited oscillation mode accordingly under different wind speed. This is because the output of RDC is applied to the outer active power control loop of RSC and the output of RTODC is augmented at the reactive power control loop of RSC. For the vector control of the DFIG RSC, the control of active

Table 4.3: Torsional oscillation mode against different inertia constants in a 4M11B system

Controller type	H_g (s)	Eigenvalues	f (Hz)	ζ
CIEC	0.45	$0.6717 \pm 20.9701i$	3.3375	-0.0320
	0.52	$0.6457 \pm 19.6814i$	3.1324	-0.0328
	0.65	$0.6070 \pm 17.8881i$	2.8470	-0.0339
CIEC plus CDC+CTODC	0.45	$-0.5210 \pm 20.8968i$	3.3258	0.0249
	0.52	$-0.3721 \pm 19.6165i$	3.1221	0.0190
	0.65	$-0.1869 \pm 17.8355i$	2.8386	0.0105
CIEC plus RDC+RTODC	0.45	$-3.9464 \pm 22.0499i$	3.5094	0.1762
	0.52	$-6.4281 \pm 19.9748i$	3.1791	0.3063
	0.65	$-7.9589 \pm 19.7531i$	3.1438	0.3737

Table 4.4: New excited oscillation mode against different inertia constants in a 4M11B system

Controller type	H_g (s)	Eigenvalues	f (Hz)	ζ
CIEC	0.45	$-0.3490 \pm 5.2054i$	0.8285	0.0669
	0.52	$-0.3493 \pm 5.2054i$	0.8285	0.0669
	0.65	$-0.3497 \pm 5.2053i$	0.8284	0.0670
CIEC plus CDC+CTODC	0.45	$-0.5836 \pm 5.1748i$	0.8236	0.1121
	0.52	$-0.5835 \pm 5.1748i$	0.8236	0.1121
	0.65	$-0.5834 \pm 5.1747i$	0.8236	0.1120
CIEC plus RDC+RTODC	0.45	$-0.8307 \pm 5.1278i$	0.8161	0.1599
	0.52	$-0.8308 \pm 5.1280i$	0.8161	0.1599
	0.65	$-0.8311 \pm 5.1283i$	0.8162	0.1600

and reactive power is decoupled.

Table 4.5: Torsional oscillation mode against different wind speed in a 4M11B system

Controller type	V_w (m/s)	Eigenvalues	f (Hz)	ζ
CIEC	9	$0.4150 \pm 19.6630i$	3.1295	-0.0211
	11	$0.6542 \pm 19.6859i$	3.1331	-0.0332
	15	$0.2718 \pm 19.4434i$	3.0945	-0.0140
CIEC plus CDC+CTODC	9	$-0.6288 \pm 19.6317i$	3.1245	0.0320
	11	$-0.3293 \pm 19.6328i$	3.1247	0.0168
	15	$-0.7641 \pm 19.3698i$	3.0828	0.0394
CIEC plus RDC+RTODC	9	$-5.8100 \pm 20.0346i$	3.1886	0.2785
	11	$-6.3739 \pm 20.3929i$	3.2456	0.2983
	15	$-6.4048 \pm 20.6230i$	3.2822	0.2966

Table 4.6: New excited oscillation mode against different wind speed in a 4M11B system

Controller type	V_w (m/s)	Eigenvalues	f (Hz)	ζ
CIEC	9	$-0.1338 \pm 5.4050i$	0.8602	0.0247
	11	$-0.3057 \pm 5.5474i$	0.8829	0.0550
	15	$-0.3687 \pm 5.1025i$	0.8121	0.0721
CIEC plus CDC+CTODC	9	$-0.4658 \pm 5.2149i$	0.8300	0.0890
	11	$-0.5835 \pm 5.1748i$	0.8236	0.1121
	15	$-0.5938 \pm 5.0897i$	0.8100	0.1159
CIEC plus RDC+RTODC	9	$-0.7718 \pm 5.1643i$	0.8219	0.15
	11	$-0.8004 \pm 4.8044i$	0.7646	0.1643
	15	$-0.8231 \pm 5.0523i$	0.8041	0.1608

Simulation Results

Since the torsional oscillation mode is dominated by the rotor speed, the simulation results of rotor speed ω_r are provided to show the torsional oscillation mode. A load disturbance was added at 0.5s at the bus 9 of the 4M11B system and it was cleared after 0.1 s. Fig.4.8 and Fig.4.9 show the simulation results of ω_r under 0.45s and 0.65s generator inertia constant, respectively. By comparing the simulation results in Fig.4.8 and Fig.4.9, it can be found that the proposed RTODC can provide robust damping performance on the torsional oscillation mode against different turbine inertia. However, the damping performance of CTODC is deteriorated for a larger H_g. The simulation results shown in Fig.4.8 and Fig.4.9 are consistent to the small signal stability analysis results presented in Table4.3.

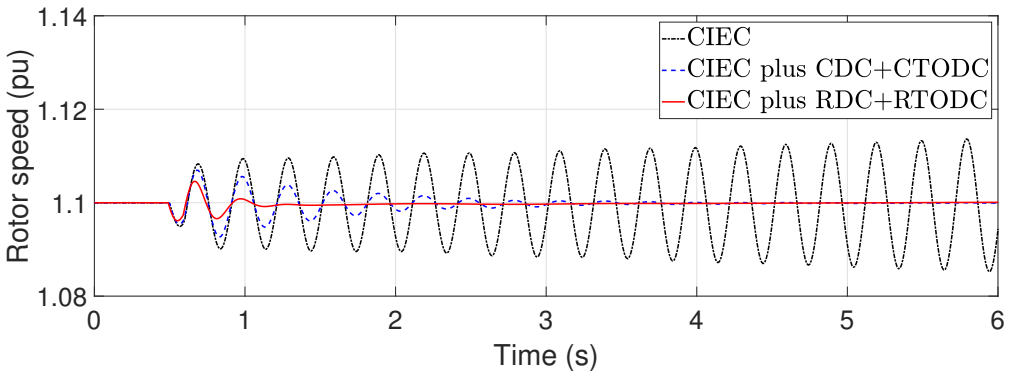

Figure 4.8: Rotor speed of a DFIG-WT for $H_g = 0.45s$ in a 4M11B system

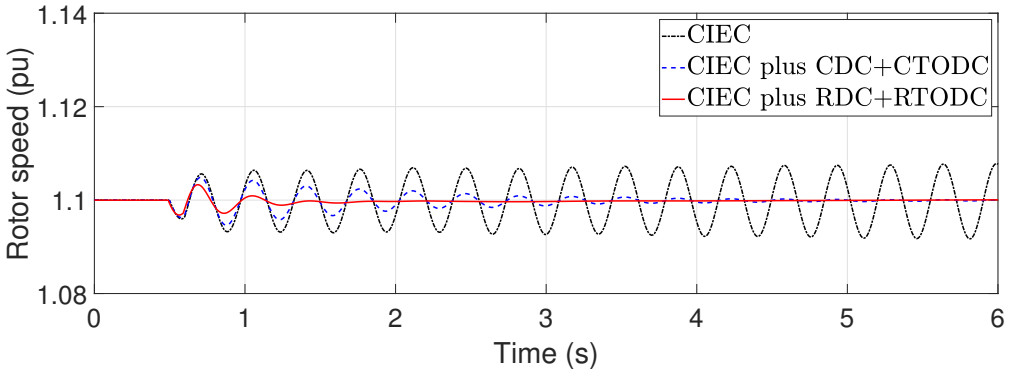

Figure 4.9: Rotor speed of a DFIG-WT for $H_g = 0.65s$ in a 4M11B system

Fig.4.10 and Fig.4.11 show the simulation results of rotor speed under $9m/s$ and $15m/s$ wind speed. According to the simulation results, it can also be concluded that the RTODC can provide robust damping performance on the torsional oscillation as the oscillation can be mitigated within 0.7s for both wind speed operation. However, the damping performance of the CTODC is varied. The simulation results shown in Fig.4.10 and Fig.4.11 are consistent to the small signal stability analysis results obtained and shown in Table4.5.

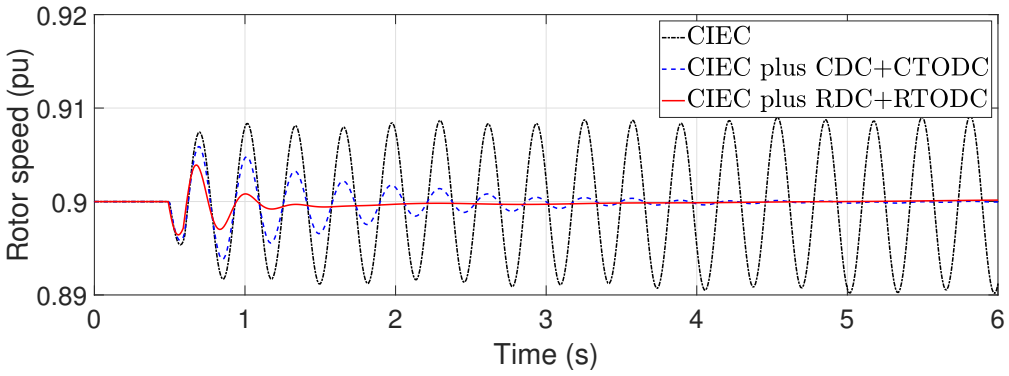

Figure 4.10: Rotor speed of a DFIG-WT for $V_w = 9m/s$ in a 4M11B system

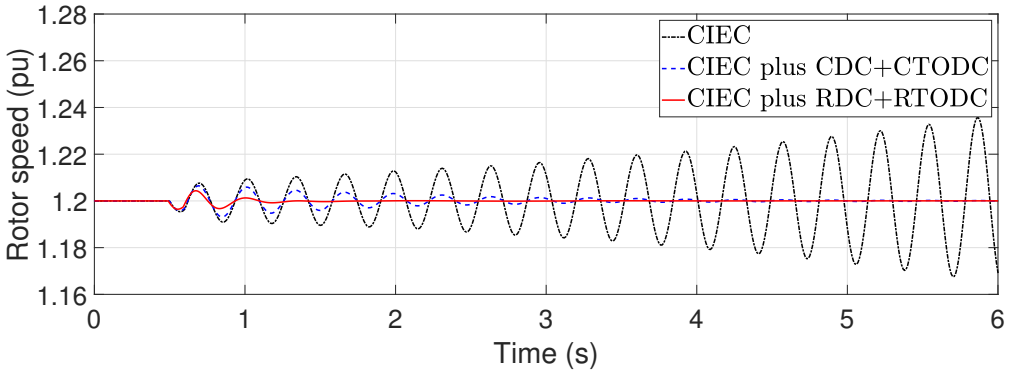

Figure 4.11: Rotor speed of a DFIG-WT for $V_w = 15m/s$ in a 4M11B system

The robustness of the proposed RTODC is also verified under a different disturbance, where a new load disturbance was added at load connected at bus 8 of the 4M11B system at 0.5s and it was cleared after 0.1s. Fig.4.12 and Fig.4.13 show the simulation results of the ω_r under a fault at bus 9 and bus 8. By comparing

the simulation results, it can be found that the proposed RTODC can provide robust damping performance on the torsional oscillation mode when the disturbance is changed. The oscillation on the rotor speed of a DFIG-WT can be mitigated before 1.5 s. However, the damping performance of torsional oscillation mode with a CTODC is varied under different disturbance.

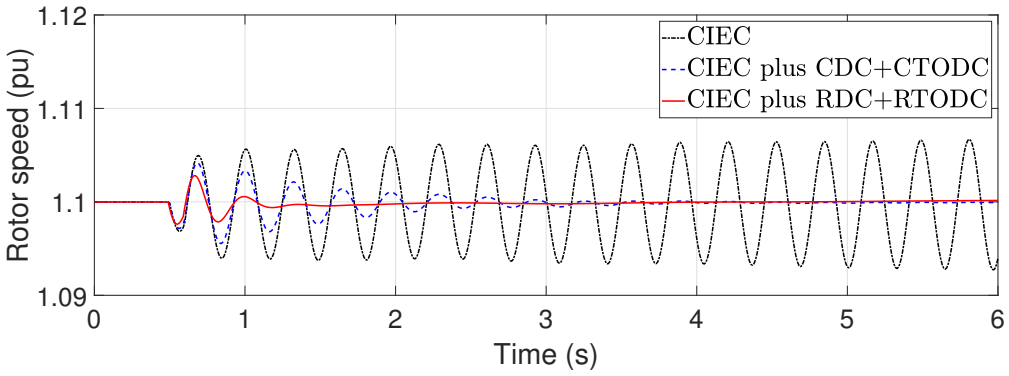

Figure 4.12: Rotor speed of a DFIG-WT for a fault at node 9 in a 4M11B system

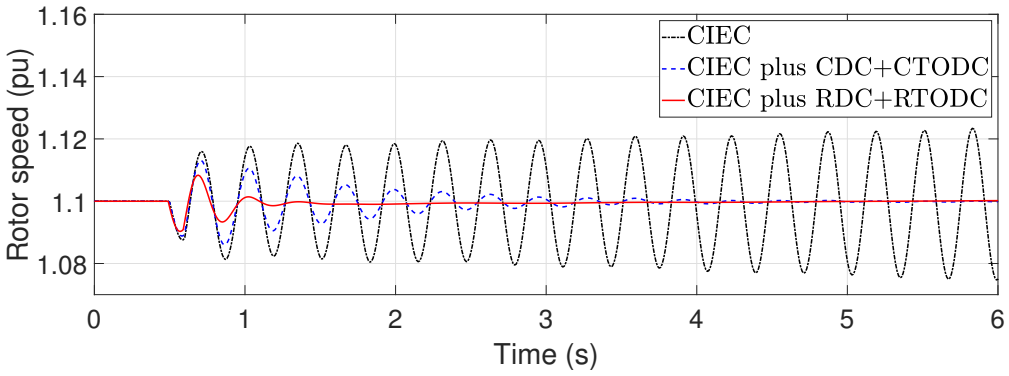

Figure 4.13: Rotor speed of a DFIG-WT for a fault at node 8 in a 4M11B system

4.5 Case Study II - New England New York 68-Bus System

To further investigate the robustness of the proposed RTODC in a more complex power system, the DFIG-WTs contributing to the frequency support in a 16M68B

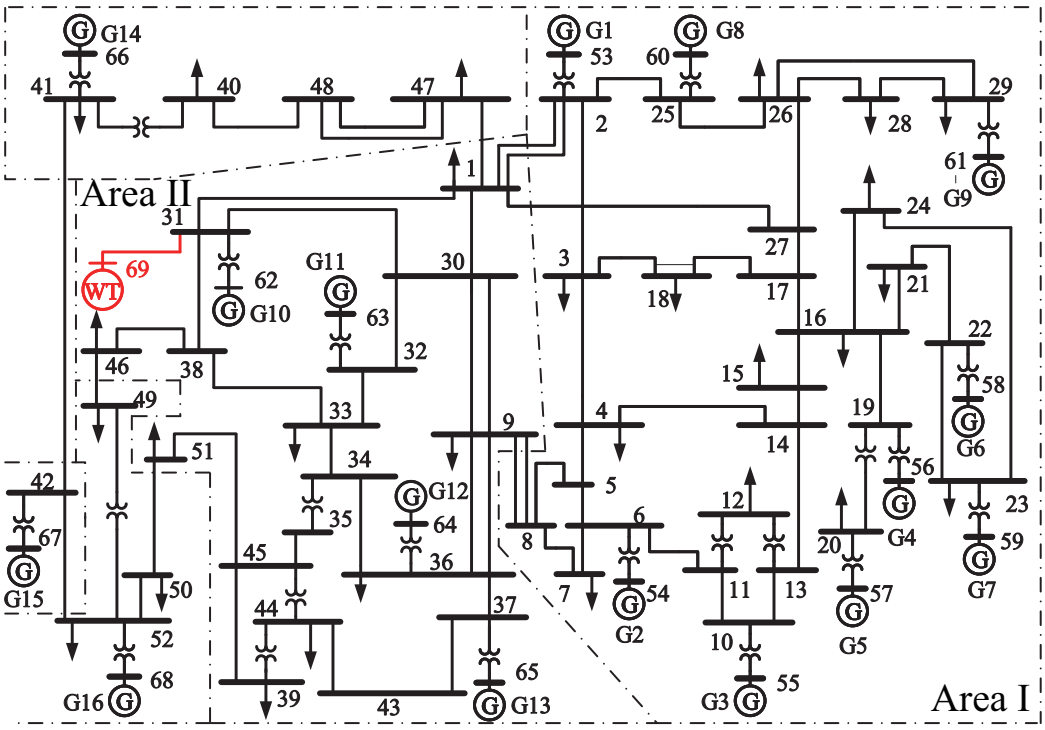

Figure 4.14: New England 68-bus system with DFIG-WTs participating in system frequency support [10]

system is provided in this section, which is the same as the one given in Section 2.5.3. Fig.4.14 shows the single line diagram of a 16M68B system with DFIG-WTs connected at bus 31. The parameters of detailed bus data, line data and generator data are given in Appendix B.

4.5.1 Controller Design

Since the full-order of a 16M68B system with DFIG-WTs is 220th order, Schur balanced truncation model reduction approach is used to reduced the system order to 11th order to design the controller. By using the approach proposed in Section 4.3.2, the RTODC for DFIG-WTs participating in the system frequency support in a 16M68B system is designed and given in (4.5.1) - (4.5.3).

$$H_{RTODC1}(s) = \frac{N_{t1}(s)}{D_{t1}(s)} \tag{4.5.1}$$

$$\begin{aligned} N_{t1}(s) =& 1.0657 \times 10^{7} s^{6} + 2.0577 \times 10^{9} s^{5} - 1.6733 \times 10^{10} s^{4} \\ & - 6.1575 \times 10^{9} s^{3} - 4.2617 \times 10^{8} s^{2} - 2.9887 \times 10^{5} s \\ & - 1.4316 \times 10^{-8} \end{aligned} \tag{4.5.2}$$

$$\begin{aligned} D_{t1}(s) =& s^{7} + 4.3181 \times 10^{6} s^{6} + 1.5483 \times 10^{8} s^{5} + 5.4851 \times 10^{8} s^{4} \\ & + 1.1564 \times 10^{9} s^{3} + 1.0201 \times 10^{8} s^{2} + 2.4314 \times 10^{4} s \\ & + 1.0804 \times 10^{-9} \end{aligned} \tag{4.5.3}$$

In order to compare the robustness of the proposed RTODC, the conventional torsional damping controller is also designed by using residue method provided in [138]. The transfer function of the CTODC can be expressed by (4.5.4).

$$H_{CTODC}(s) = K \frac{T_w}{1 + T_w s} \left(\frac{1 + T_1 s}{1 + T_2 s}\right)^2 \tag{4.5.4}$$

where the compensation constants T_1 and T_2 equal to 0.051 s and 0.0466 s, respectively. K is set to 2. The wash-out filter time constant T_w is 10 s.

4.5.2 Performance Evaluation

Small signal stability analysis results

Table4.7 and 4.8 show the small signal stability analysis results of a New England New York 68-bus system with DFIG-WTs participating in system frequency support under variable DFIG inertia constant H_g. The robustness of the proposed RTODC is verified by setting H_g as 0.45s, 0.52s and 0.65s. In addition to the small signal stability analysis results of DFIG-WT with a RTODC, the small signal stability analysis results of the DFIG-WT without additional damping controller and with a CTODC are also provided for comparison. The torsional oscillation mode is given in Table4.7 and the new oscillation mode excited by IEC is presented in Table4.8. By comparing the damping ratio of torsional oscillation mode given in Table4.7, it can be found that the torsional oscillation mode will be unstable if only the CIEC is used. The damping ratio of the torsional oscillation mode is improved with CIEC plus CDC+CTODC comparing to the CIEC only. However, the damping performance of CTODC is still poorly damped. When the proposed RTODC is used, a minimum 0.15 damping ratio is ensured for different inertia constants H_g as design requirement. Thus, the robust damping performance of torsional oscillation mode can be achieved and the effect of an IEC on WT shaft can be mitigated under variable wind turbine generator inertia. In addition to the small signal stability analysis results of the torsional oscillation mode, the small signal stability analysis results of the new introduced oscillation mode are also provided to ensure that the proposed RTODC will not affect the robust damping performance of the new introduced oscillation mode provided by RDC. As shown in Table4.8, satisfactory damping performance of the new introduced oscillation mode is achieved when RDC is equipped.

Table4.9 and 4.10 show the small signal stability analysis results of the torsional oscillation mode and new excited oscillation under different wind speed in a 16M68B system. By comparing the results shown in Table4.9, it can be seen that the proposed RTODC can still provide satisfactory damping performance against different wind speed. However, the damping performance is varied for different

Table 4.7: Torsional oscillation mode against different inertia constants in a 16M68B system

Controller type	H_g (s)	Eigenvalues	f (Hz)	ζ
CIEC	0.45	$0.5469 \pm 21.278i$	3.3865	-0.0257
	0.52	$0.5326 \pm 19.9442i$	3.1742	-0.0267
	0.65	$0.5149 \pm 18.092i$	2.8794	-0.0284
CIEC plus CDC+CTODC	0.45	$-0.3943 \pm 21.1603i$	3.3678	0.0186
	0.52	$-0.2713 \pm 19.8421i$	3.158	0.0137
	0.65	$-0.1138 \pm 18.011i$	2.8665	0.0063
CIEC plus RDC+RTODC	0.45	$-8.3277 \pm 21.2397i$	3.3804	0.365
	0.52	$-7.3149 \pm 18.8051i$	2.9929	0.3625
	0.65	$-5.2955 \pm 15.9083i$	2.5319	0.3158

Table 4.8: New excited oscillation mode against different inertia constants in a 16M68B system

Controller type	H_g (s)	Eigenvalues	f (Hz)	ζ
CIEC	0.45	$-0.1823 \pm 5.7328i$	0.9124	0.0318
	0.52	$-0.1824 \pm 5.7328i$	0.9124	0.0318
	0.65	$-0.1824 \pm 5.7327i$	0.9124	0.0318
CIEC plus CDC+CTODC	0.45	$-0.2881 \pm 5.7035i$	0.9077	0.0505
	0.52	$-0.288 \pm 5.7035i$	0.9077	0.0504
	0.65	$-0.2877 \pm 5.7035i$	0.9077	0.0504
CIEC plus RDC+RTODC	0.45	$-1.1529 \pm 5.3992i$	0.8593	0.2088
	0.52	$-1.2753 \pm 4.801i$	0.7641	0.2567
	0.65	$-1.2736 \pm 4.7849i$	0.7615	0.2572

wind speed operation when a CTODC is used. Moreover, the damping ratio of the new excited mode given in Table4.10 shows that the robust damping performance provided by RDC can be ensured under different wind speed operation. The proposed RTODC can work perfectly with the RDC.

Table 4.9: Torsional oscillation mode against different wind speed in a 16M68B system

Controller type	V_w (m/s)	Eigenvalues	f (Hz)	ζ
CIEC	9	$0.4211 \pm 19.7690i$	3.1463	-0.0213
	11	$0.6081 \pm 19.8729i$	3.1629	-0.0306
	15	$0.1989 \pm 19.7091i$	3.1368	-0.0101
CIEC plus CDC+CTODC	9	$-0.0563 \pm 19.6798i$	3.1321	0.0029
	11	$-0.0623 \pm 19.7756i$	3.1474	0.0032
	15	$-0.6159 \pm 19.6206i$	3.1227	0.0314
CIEC plus RDC+RTODC	9	$-3.2225 \pm 18.7630i$	2.9862	0.1693
	11	$-5.1921 \pm 18.5942i$	2.9594	0.2689
	15	$-8.0290 \pm 19.0683i$	3.0348	0.3881

Table 4.10: New excited oscillation mode against different wind speed in a 16M68B system

Controller type	V_w (m/s)	Eigenvalues	f (Hz)	ζ
CIEC	9	$-0.5543 \pm 6.0694i$	0.9660	0.0910
	11	$-0.3780 \pm 6.0028i$	0.9554	0.0628
	15	$-0.1916 \pm 5.7319i$	0.9123	0.0334
CIEC plus CDC+CTODC	9	$-0.6438 \pm 6.0409i$	0.9614	0.1060
	11	$-0.4749 \pm 5.9744i$	0.9509	0.0792
	15	$-0.3002 \pm 5.7081i$	0.9085	0.0525
CIEC plus RDC+RTODC	9	$-1.8073 \pm 5.6539i$	0.8999	0.3045
	11	$-1.6998 \pm 5.3032i$	0.8440	0.3052
	15	$-1.5582 \pm 4.6945i$	0.7472	0.3150

Simulation Results

Fig.4.15 and Fig.4.16 show the simulation results of rotor speed against different DFIG-WT generator inertia in a 16M68B system. Comparing the simulation results in Fig.4.15 and Fig.4.16, it can be found that the torsional oscillation mode can be well damped when the DFIG-WT is equipped with a RTODC and its damping performance is robust considering the uncertainties of the generator inertia. However, the damping performance of the CTODC is deteriorated when H_g increases. In addition, the simulation results verified the small signal stability analysis results provided in Table4.7.

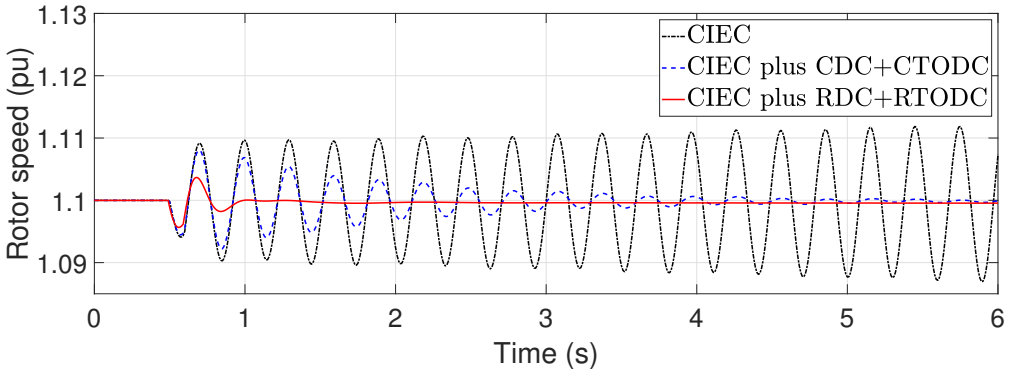

Figure 4.15: Rotor speed of a DFIG-WT for $H_g = 0.45s$ in a 16M68B system

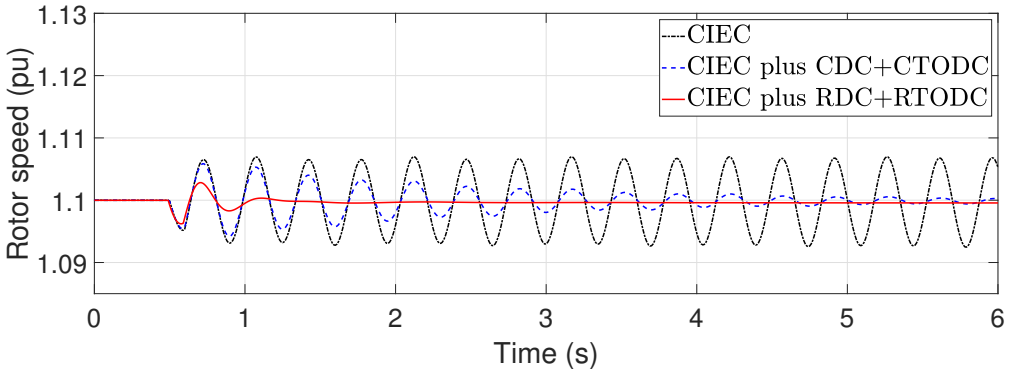

Figure 4.16: Rotor speed of a DFIG-WT for $H_g = 0.65s$ in a 16M68B system

Fig.4.17 and Fig.4.18 shows the simulation results of the rotor speed of DFIG-WT in a 16M68B system under different operating conditions which is achieved

by varying the wind speed. By comparing the simulation results in Fig.4.17 and Fig.4.18, it can be found that the damping performance of the RTODC is robust against different wind speed, whereas the damping performance of the CTODC is varied for different wind speed. The simulation results are also consistent to the small signal stability analysis results obtained in Table4.9.

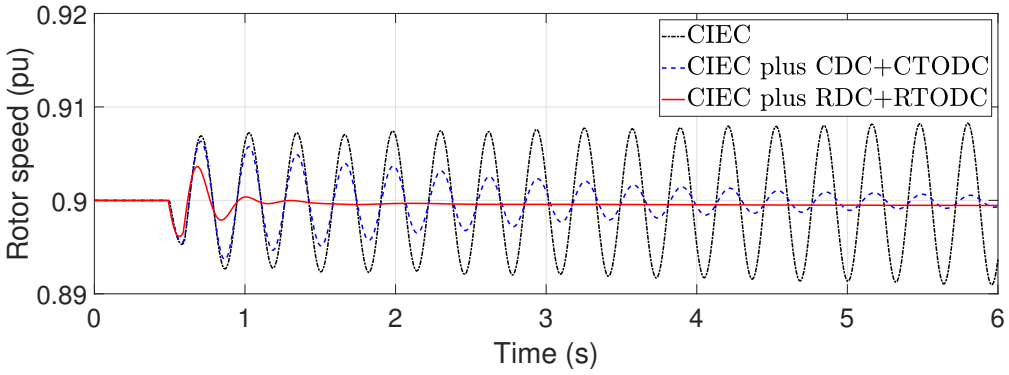

Figure 4.17: Rotor speed of a DFIG-WT for $V_w = 9m/s$ in a 16M68B system

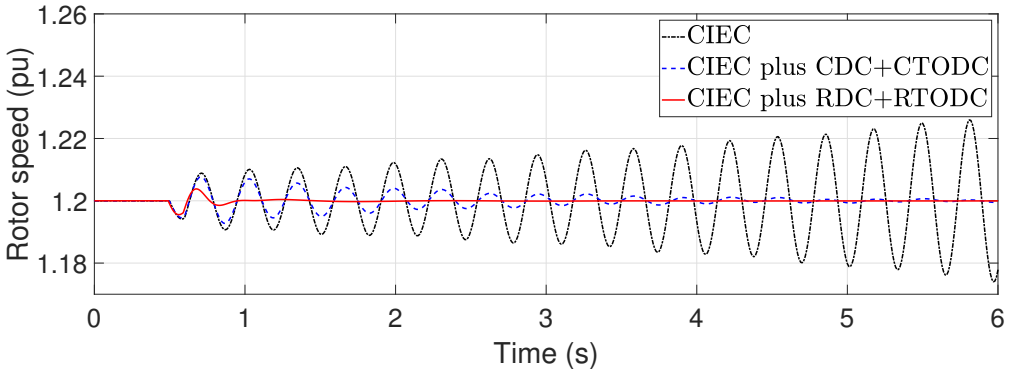

Figure 4.18: Rotor speed of a DFIG-WT for $V_w = 15m/s$ in a 16M68B system

In order to show the robustness of the RTODC under different external disturbances, another fault was added at bus 3 in the 16M68B system as shown in Fig.4.14. Fig.4.19 and Fig.4.20 show the simulation results of rotor speed under a load disturbance added at different bus in a 16M68B system. By comparing the simulation results in Fig.4.19 and Fig.4.20, it can be found that RTODC can still ensure robust damping performance under different external disturbance. However, the damping

performance of the CTODC is poor when a load disturbance is added at bus 47.

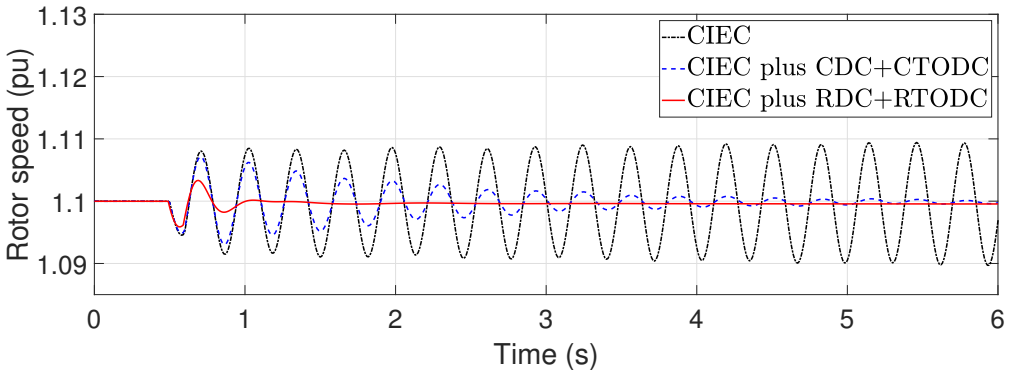

Figure 4.19: Rotor speed of a DFIG-WT for a fault at bus 47 in a 16M68B system

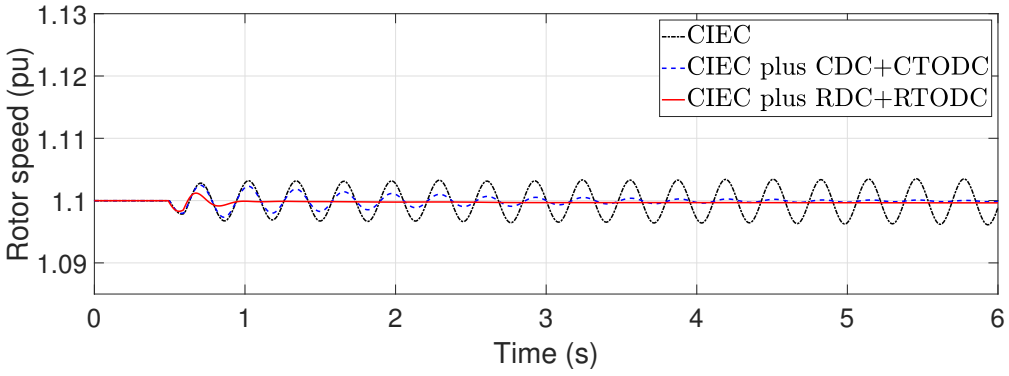

Figure 4.20: Rotor speed of a DFIG-WT for a fault at bus 3 in a 16M68B system

4.6 Conclusion

In conclusion, this chapter proposes a RTODC to damp the deteriorated torsional oscillation by the DFIG-WT providing system frequency support, while the damping performance provided by RDC on the new oscillation mode is unaffected. The geometric controllability is used to show that the reactive power control loop can achieve superior damping performance on torsional oscillation mode mitigation than the active power control loop. H_∞ mixed-sensitivity robust control approach is used to design the RTODC, where the output disturbance rejection and control

effort optimisation can be achieved simultaneously with ensured damping performance. Two case studies were achieved based on a 4M11B system and a 16M68B system with DFIG-WTs contributing to system frequency support. The robustness of the proposed RTODC was tested under parameter uncertainties, time-varying system operating points and also different external disturbances. Small signal stability analysis results of torsional oscillation mode show that the minimum 0.15 damping ratio is achieved considering uncertainties. In addition, the small signal stability analysis results of the new excited oscillation mode are also provided and it can verify that the proposed RTODC can work perfectly with the RDC. Simulation results verify the robust damping performance on torsional oscillation mode of the proposed RTODC comparing to the CIEC and CIEC with CDC+CTODC, which are also consistent to the obtained small signal stability analysis results.

Chapter 5

PLL-Synchronised DFIG-WT with Frequency Support Capability Connected to Weak Power Grids

5.1 Introduction

Due to the abundant availability of renewable resources in nature, increasing amount of renewable energies are integrated into the power grid [128]. Wind energy, as one of renewable energies, has been developed rapidly and widely integrated in the grid nowadays. The current installation of wind power generation has already achieved 743 GW global cumulative wind power capacity in 2020 [1]. However, the potential good wind power locations are far away from the main power grid, which requests a long transmission line for the wind turbine generators to be integrated into the grid [169]. High line impedance will exist between the point of common coupling (PCC) of a wind turbine generator and the infinite power grid [170]. In this situation, the wind turbine generator can be regarded as attaching to a weak power grid. The interaction between the wind turbine generator and the weak power grid, via impedance interaction, may cause oscillation. These undesirable oscillations may even lead to instability of the whole power system with integrated wind power generation. In October 2009, subsynchronous oscillation was first found in

the DFIG based wind power system connected to a series-compensated power system in Texas, USA [11, 171]. The subsynchronous oscillation accident caused a large amount of wind turbine tripped off and crowbar circuit breakdown. This kind of subsynchronous oscillation was also found in Hebei, China in 2010 and Xinjiang, China in 2015 [11]. Thus, it develops the concerns on the possible stability issues of connecting the wind turbine generators to a weak power grid.

Doubly-fed induction generator (DFIG), as a popular generator for variable speed wind turbine, has been widely deployed in wind power generation [11]. The advantages of using DFIG in wind power generation includes a wider rotor speed, mechanical stress reduction and power capture optimisation [172]. In a DFIG system based wind power system, the stator is directly connected to the power grid through high impedance transmission lines. Hence, the voltage and frequency at PCC of a DFIG system can be easily affected by the power grid disturbance, which will cause undesirable dynamics to DFIG control loops and may lead small signal instability of the DFIG based wind power system [170] [173]. Under this consideration, it is worth to analyse the stability of DFIG-WT connected to a weak power grid.

A phase-locked loop (PLL) is designed to estimate the frequency and phase angle of grid voltage and is a basic and fundamental component of the vector control. The frequency measured by the PLL control loop is used for the wind turbine generator participating in power system frequency support. If the power grid is relatively strong, i.e. the impedance is very small and such that the voltage and frequency of PCC are equivalent to infinite bus, PLL will work perfectly in a strong grid and PLL dynamics are often ignored [174]. However, when DFIG-WT is connected to a weak power grid, the impact of PLL dynamics are more obvious which cannot be neglected. Especially, if larger proportional and integral parameters are used in the PLL of DFIG-WT connected to a weak power grid, oscillation is likely to occur due to a narrower phase margin [175]. Based on the above explanations, PLL needs to be included in the DFIG-WT contributing to system frequency support and its impact on the system stability needs to be studied when DFIG-WT is connected to the power system via a long transmission line.

In [176], the dynamics of the PLL control loop under a weak grid connection

are studied and it can be found that the PLL will make errors on the estimated angle during the GSC instability of the wind turbine generator, which will lead to incorrect active and reactive current control. [177] shows that the PLL parameters have a great impact on VSC-HVDC stability when the ac grid strength is low. The small signal stability analysis study on an enhanced model of DFIG based wind farm connecting to a weak power system is presented in [174]. The impact of PLL parameters and power grid strength is studied and it is found that large PLL parameters and weak power grid strength will cause reduced damping ratio of the PLL oscillation mode [121]. However, the studied DFIG-WTs are not considered with frequency support capability where the impact of PLL measured frequency on DFIG-WT frequency support is neglected.

On the other hand, uncertainties of model, parameters and random external disturbances are the other factors that affect the system stability of DFIG-WT participating in system frequency support. The common robust control approaches mainly achieve on a single objective where the control requirements are considered simultaneously through weighted functions. In the real application, the single H_∞ synthesis cannot guarantee the performance when the noise exists in the measurement signal and the disturbance is random. This is because the noise and disturbance are more effectively measured by the H_2 norm. For this consideration, the control approach which can mix the H_2 and H_∞ design objective is highly desired to achieve more flexible and accurate design requirements of the closed-loop system performance [122]. In the multi-objective synthesis control approach, the robust performance in the existence of the model uncertainties can be provided by H_∞ synthesis, which mainly focus on the frequency-domain performance. For H_2 control synthesis, the system transient behaviours can be guaranteed by using the H_2 norm. Moreover, additional regional pole placement can be imposed to ensure the satisfactory damping performance of the closed-loop system poles.

Motivated by the impact of PLL parameters and power grid strength on system stability of a DFIG-WT system, different PLL parameters and power grid strength on the system stability of a DFIG-WT contributing to system frequency support is investigated in this Chapter. Once the PLL is used to measure the PCC frequency,

the new lightly damped oscillation mode is dominated by both PLL and IEC. To ensure system robust stability under power grid strength variation and different PLL parameters, a mixed output feedback control based damping controller is proposed. Both small signal stability analysis and simulation results are obtained to evaluate the robust damping performance. Case studies of DFIG-WTs participating in a 4M11B system and a 16M68B system frequency support are carried out.

The main contributions of this chapter include:

- Eigenvalue analysis is obtained to investigate the impact of power grid strength and PLL parameters on DFIG-WT contributing to system frequency support.
- The mixed output feedback control based damping controller is designed based on H_2/H_∞ synthesis, where the H_2 control can better suppress random disturbances and H_∞ control can provide robustness against model uncertainties.
- The H_∞ mixed-sensitivity based damping controller is also designed and compared with a mixed H_2/H_∞ based damping controller.

5.2 Problem Formulation

5.2.1 DFIG-WT Connected to A Weak Power Grid

Fig.5.1 shows a single line diagram of DFIG-WT connected to a power grid. It consists of a WT, DFIG, RSC, GSC, transmission line and a SMIB system. The wind turbine is connected to the DFIG through the gearbox. The stator of the DFIG is connected to the power grid directly. In addition, the rotor of DFIG is also connected to the grid through a RSC, a DC-link capacitor and a GSC. Detailed modelling of DFIG-WT has been given in Chapter 2. Thus, only the weak grid is discussed in detail. The long transmission line is used to model the weak power grid where the line impedance is determined by $Z_{line} = R_L + jX_L$. The power grid strength is commonly described using the short circuit ratio (SCR) which is defined as the ratio of the short circuit capacity at the point of connection to the power rating of the wind turbine generator at that point of connection [178]. According to this definition, the

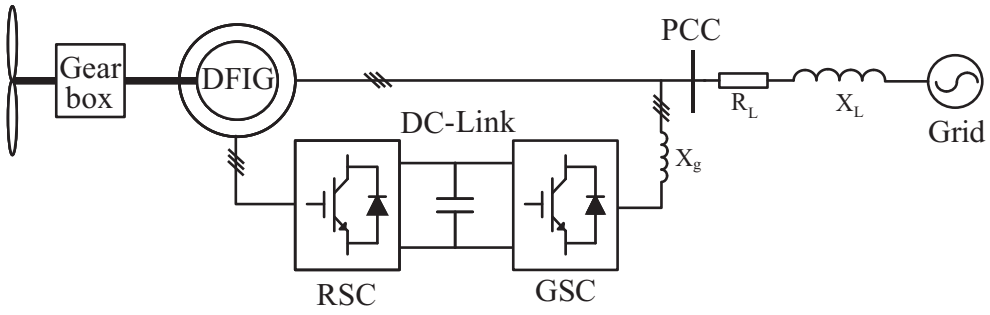

Figure 5.1: DFIG connected to a SMIB system through a transmission line $Z_{line} = R_L + jX_L$ [11]

SCR is shown in (5.2.1).

$$SCR = \frac{S_{SC}}{P_{rated}} \tag{5.2.1}$$

where S_{SC} is the short circuit capacity at the point of connection and P_{rated} represents the rated power of the wind turbine generator connected at this point. If the rated power of wind turbine generator is assumed to be the base power for per unit calculation. Then, the SCR in (5.2.1) can be rewritten as (5.2.2),

$$SCR = \frac{1}{Z_{line}} \tag{5.2.2}$$

where Z_{line} is the equivalent impedance of transmission system at the point of connection [178]. When the SCR is larger than 3, it will be considered as a strong grid. The weak power grid is defined when the SCR is less than 3 [179].

5.2.2 PLL Model

PLL is used to measure the phase angle of the grid voltage at the PCC. The schematic diagram of a PI-based PLL in a synchronous reference frame is shown in Fig.5.2, where K_{P-pll} and K_{I-pll} are the proportional and integral gains of the PLL. If $v_{sq} = 0$ holds, the d-axis of the dq frame is aligned to the stator voltage for a stator voltage based vector control approach, i.e. $v_{sd} = U_s$ and $v_{sq} = 0$. PLL will successfully track the phase angle of the grid voltage. Moreover, the frequency of measured grid voltage can also be obtained using ω_{pll}, which can help DFIG-WT to contribute to system frequency support.

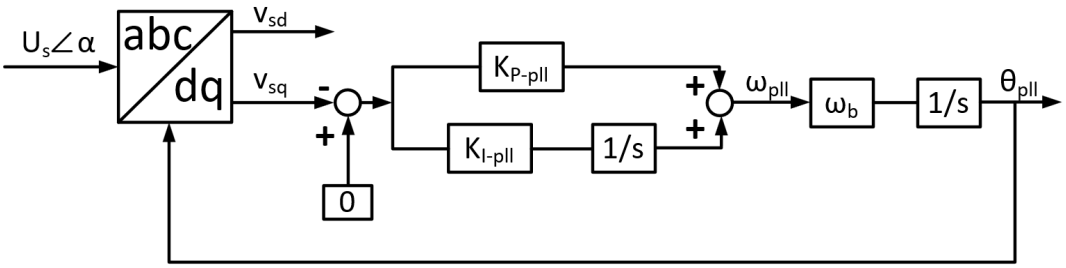

Figure 5.2: Phase-locked loop model

The dynamics of PLL can be described by (5.2.3), (5.2.4) and (5.2.5).

$$x_{pll} = \frac{1}{s}(v_{sq-ref} - v_{sq}) \tag{5.2.3}$$

$$\omega_{pll} = K_{P-pll}(v_{sq-ref} - v_{sq}) + K_{I-pll}x_{pll} \tag{5.2.4}$$

$$\theta_{pll} = \frac{\omega_b}{s}\omega_{pll} \tag{5.2.5}$$

where ω_b is the synchronous reference rotating speed.

5.2.3 Impact of PLL on DFIG-WTs with Frequency Support Capability

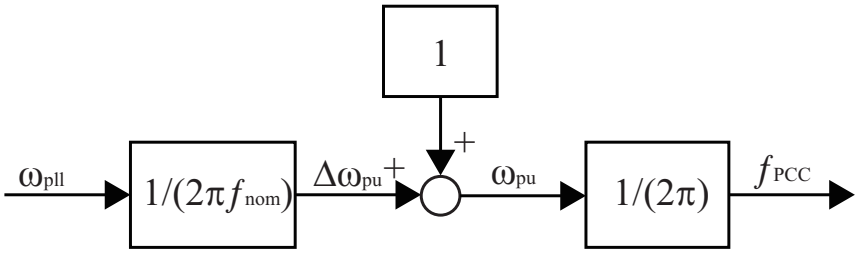

Figure 5.3: Block diagram of calculating f_{PCC}

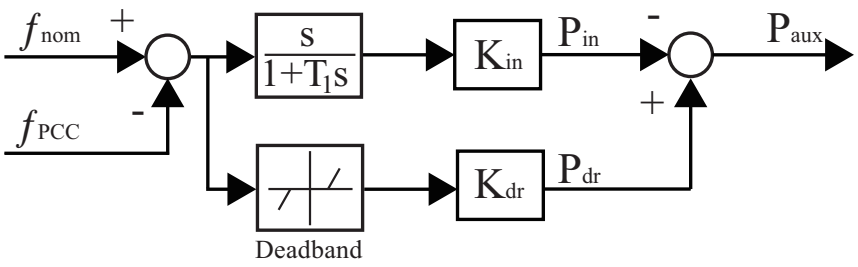

Figure 5.4: Block diagram of the IEC

As shown in Fig.5.3, the frequency at PCC can be obtained by using the PLL. The measured frequency f_{PCC} will be used as the input of the IEC as shown in Fig.5.4. Thus, the impact of PLL on the DFIG-WT contributing to system frequency support is needed to be investigated, especially during the weak grid and large PLL parameters. As pointed in [121], a weak grid strength or a large PLL controller gain will lead to the reduction of the PLL dominated oscillation mode damping ratio. Considering the effect of the IEC, a similar effect can be expected which motivates the design of a robust damping controller to ensure system stability. The mixed H_2/H_∞ output feedback control approach is used to design the controller where both the robustness against model uncertainties and improved system transient behaviour can be achieved simultaneously.

5.3 Robust Damping Controller Design: Mixed H_2/H_∞ Control Approach based on LMI Techniques

The mixed H_2/H_∞ control approach enables to mix the design from H_2 and H_∞ performance with regional pole placement, where the H_∞ performance can ensure the robustness against model uncertainties and H_2 performance is more helpful on dealing the stochastic impacts, such as noises and external disturbance [122]. The additional pole placement constraints are also added to ensure the minimum damping ratio of the closed-loop system poles.

5.3.1 Multi-Objective Synthesis of H_2/H_∞ Control

Fig.5.5 shows the block diagram of a mixed H_2/H_∞ based robust damping controller design, where G represents the open loop system model, K is the controller to be designed. d is the external disturbance. The output z_∞ is for H_∞ performance and z_2 is for H_2 performance. W_1 is a low-pass filter for output disturbance rejection measured by the H_2 channel. W_2 is a high-pass filter or it can be a small constant to optimise the control effort in the H_2 channel. W_3 is a high-pass filter to ensure robust performance against model uncertainties which is achieved in the H_∞ channel.

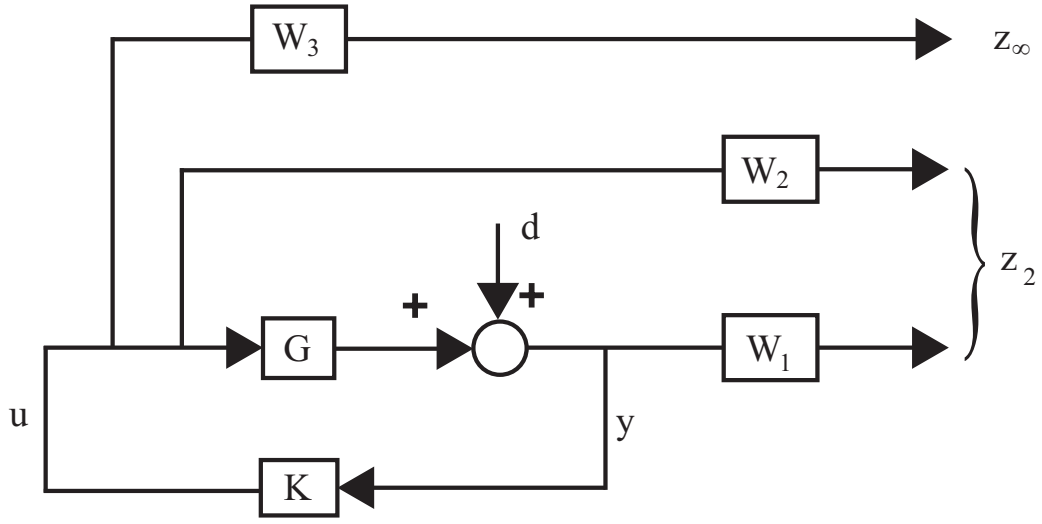

Figure 5.5: Block diagram of a mixed H_2/H_∞ output feedback control design

The H_2/H_∞ control design presented in Fig.5.5 can be considered as a multi-objective synthesis control problem to design a output feedback controller $u = Ky$, such that:

- The H_∞ norm of the transfer function from d to z_∞ should satisfy $\|T_{dz_\infty}\|_\infty < \gamma_0$, where γ_0 is a predefined positive value.
- The H_2 norm of the transfer function from d to z_2 should satisfy $\|T_{dz_2}\|_2 < v_0$, where v_0 is a predefined positive value.

- A trade-off criterion given in (5.3.1) needs to be minimised.

$$a \left\| T_{dz_\infty} \right\|_\infty^2 + b \left\| T_{dz_2} \right\|_2^2 \tag{5.3.1}$$

- The closed-loop system poles need to be placed in a defined LMI region $\mathcal{D}$.

Considering the open-loop system G as

$$\begin{cases} \dot{x} &= Ax + B_1 d + B_2 u \\ z_\infty &= C_\infty x + D_{\infty 1} d + D_{\infty 2} u \\ z_2 &= C_2 x + D_{21} d + D_{22} u \\ y &= C_y x + D_y d \end{cases} \tag{5.3.2}$$

The designed controller is given by:

$$\begin{cases} \dot{x_k} &= A_k x_k + B_k y \\ u &= C_k x_k + D_k y \end{cases} \tag{5.3.3}$$

Then, the closed-loop system can be obtained as:

$$\begin{cases} \dot{x_{cl}} &= A_{cl} x_{cl} + B_{cl} d \\ z_\infty &= C_{cl\infty} x_{cl} + D_{cl\infty} d \\ z_2 &= C_{cl2} x_{cl} + D_{cl2} d \end{cases} \tag{5.3.4}$$

The H_∞ performance can be maintained if there exists a positive-definite symmetric matrix P_∞, such that (5.3.5) is satisfied.

$$\begin{pmatrix} A_{cl} P_\infty + P_\infty A_{cl}^T & B_{cl} & P_\infty C_{cl\infty}^T \\ B_{cl}^T & -I & D_{cl\infty}^T \\ C_{cl\infty} P_\infty & D_{cl\infty} & -\gamma_0^2 I \end{pmatrix} < 0 \tag{5.3.5}$$

The H_2 performance can be maintained if there exists a positive-definite symmetric matrices P_2 and Q, such that (5.3.6) - (5.3.8) are satisfied.

$$\begin{pmatrix} A_{cl} P_2 + P_2 A_{cl}^T & B_{cl} \\ B_{cl}^T & -I \end{pmatrix} < 0 \tag{5.3.6}$$

$$\begin{pmatrix} Q & C_{cl2} P_2 \\ P_2 C_{cl2}^T & P_2 \end{pmatrix} > 0 \tag{5.3.7}$$

$$\mathrm{Trace}(Q) < v_0^2 \tag{5.3.8}$$

5.3.2 LMI Regions for Pole Placement

The regional pole placement can be achieved by placing the closed-loop poles in the predefined LMI regions. The LMI regions can be defined by convex subsets $\mathcal{D}$ if there exists symmetric matrices $\alpha = [\alpha_{kl}] \in \boldsymbol{R}^{m\times m}$ and $\beta = [\beta_{kl}] \in \boldsymbol{R}^{m\times m}$ [10, 153, 154], such that,

$$\mathcal{D} = \{z \in \boldsymbol{C} : \quad f_{\mathcal{D}}(z) < 0\} \tag{5.3.9}$$

with

$$f_{\mathcal{D}}(z) := \alpha + z\beta + \bar{z}\beta^T = [\alpha_{kl} + \beta_{kl}z + \beta_{lk}\bar{z}]_{1\leq k,l\leq m} \tag{5.3.10}$$

For the dynamical system described by (5.3.4), it is called $\mathcal{D}$ stable if all poles of this system lies in the $\mathcal{D}$. In other words, the matrix A_{cl} is $\mathcal{D}$-stable if and only if there exists a symmetric matrix $P_{\mathcal{D}}$ such that

$$M_{\mathcal{D}}(A_{cl}, P_{\mathcal{D}}) < 0, P_{\mathcal{D}} > 0 \tag{5.3.11}$$

where $M_{\mathcal{D}}(A_{cl}, P_{\mathcal{D}}) := \alpha \otimes P_{\mathcal{D}} + \beta \otimes (A_{cl}P_{\mathcal{D}}) + \beta^T \otimes (A_{cl}P_{\mathcal{D}})^T$ and $\otimes$ denotes the Kronecker production of matrices [153].

The LMI region $\mathcal{D}$ can be chosen as symmetric regions with respect to the real axis in the complex plane, such as disks, horizontal strips, conic sectors, circles and etc. Furthermore, it can also be defined as the intersection of the above regions. For a typical LMI region to ensure a minimum damping ratio, it can be a conic sector as shown in Fig.3.3, where the inner angle equals to 2θ. From Theorem (2) in [153], the matrix A_{cl} has its poles in the region if and only if there exists a positive-definite symmetric matrix $P_{\mathcal{D}}$, such that (5.3.12) is satisfied.

$$\begin{pmatrix} \sin\theta\left(A_{cl}^T P_{\mathcal{D}} + P_{\mathcal{D}}^T A_{cl}\right) & \cos\theta\left(A_{cl}^T P_{\mathcal{D}} - P_{\mathcal{D}}^T A_{cl}\right) \\ \cos\theta\left(P_{\mathcal{D}}^T A_{cl} - A_{cl}^T P_{\mathcal{D}}\right) & \sin\theta\left(A_{cl}^T P_{\mathcal{D}} + P_{\mathcal{D}}^T A_{cl}\right) \end{pmatrix} < 0 \tag{5.3.12}$$

Therefore, in order to consider the mixed H_2/H_∞ control objectives imposed with the pole placement constraints simultaneously, the convexity can be enforced by finding a common solution P, such that,

$$P = P_\infty = P_2 = P_{\mathcal{D}} > 0 \tag{5.3.13}$$

Then, the designed controller K based on a mixed H_2/H_∞ approach can be obtained.

5.3.3 Summary of Mixed H_2/H_∞ Output Feedback Control Approach

The design approach of the proposed damping controller can be summarised by the following steps.

1. Obtain a detailed nonlinear model of power system with PLL-synchronised DFIG-WTs and build up the model in MATLAB/Simulink.

2. Linearise the nonlinear model at one system operating point by using the Linear Analysis in Control System Toolbox of MATLAB, where Q_{com} is set as the open-loop input and $\Delta\theta_{pll}$ as open-loop output in linearisation.

3. Carry out model deduction via Schur balanced model reduction approach to obtain an acceptable order of system for controller design.

4. Design the H_2/H_∞ output feedback control based robust damping controller. The H_∞ performance is to ensure the robust performance against model uncertainties, while the H_2 performance is evaluated by considering the random disturbances.

5. Small signal stability analysis is carried out to verify the satisfactory damping performance of the proposed H_2/H_∞ output feedback control based robust damping controller in a linear model given in Step (2).

6. Validate the effectiveness of the proposed controller via simulation study on the nonlinear detailed model obtained in Step (1).

Fig.5.6 shows the block diagram of the implementation of the designed mixed H_2/H_∞ robust damping controller in the DFIG-WT, where $H_{K_m}(s)$ represents the transfer function of the designed controller.

The difference between the controllers designed in this chapter and previous chapters is compared in terms of control objectives, inputs, outputs and controller design approaches. For the control objectives, the controller designed in this chapter is used to ensure damping performance on new oscillation mode dominated by both

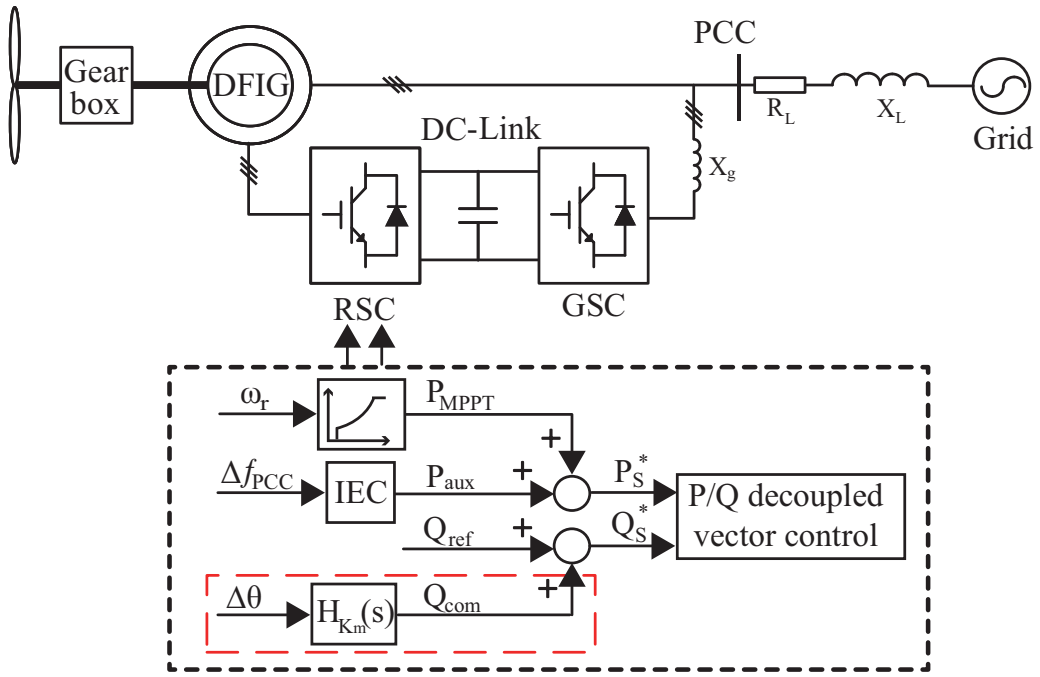

Figure 5.6: Block diagram of DFIG-WTs with a mixed H_2/H_∞ based robust damping controller

a PLL and an IEC, whereas the controllers designed in Chapter 2 and 3 are for the new oscillation mode dominated by an IEC only. In addition, the RTODC designed in Chapter 4 is for the torsional oscillation of the WT drive train deteriorated by the IEC. For the inputs and outputs of the controllers, the control input of the controller designed in this chapter is phase angle deviation $\Delta\theta$ measured by a PLL and the output is the reactive power compensation added at the reactive power control loop of a DFIG-WT RSC. The control input of the RDC designed in Chapter 2 is the frequency deviation Δf and the output is the active power compensation added at the active power control loop of a DFIG-WT RSC. The IIEC designed in Chapter 3 is an integrated controller and its input and output are the same as an IEC, which are the frequency deviation Δf and auxiliary power provided for frequency support respectively. The input and output of the RTODC designed in Chapter 4 are the DFIG rotor speed ω_r and damping power added at the reactive power control loop of a DFIG-WT RSC. As for the controller design approaches, the controller designed in this chapter is based on a mixed H_2/H_∞ output feedback control approach. Both

H_2 and H_∞ performance are considered in this design approach, such that robust damping performance against model uncertainties and random disturbances can be ensured simultaneously. The RDC designed in Chapter 2 and the RTODC designed in Chapter 4 are based on H_∞ mixed-sensitivity control approach, where the robust damping performance against model uncertainties is achieved and also the control effort is optimised. The IIEC designed in Chapter 3 is based on a novel robust PD-type controller design approach proposed in Chapter 3 which can ensure robust frequency support performance and satisfactory damping performance simultaneously.

5.4 Case Study I - Two-area Four-machine System

To illustrate the performance of the proposed H_2/H_∞ output feedback control based robust damping controller approach, a case study is firstly carried out on a 4M11B system, which is the same as the one discussed in Section 2.5.2. As shown in Fig.5.7, the DFIG-WTs are added at a new bus 12 and connected to bus 8 of the 4M11B system. The power grid strength is determined by the line impedance between the bus 8 and 12. Under the normal operating condition, the power flow between Area 1 and Area 2 is 400 MW. G1 - G4 are all equipped with PSS to damp the local and inter area oscillation modes of the system. The system parameters are given in Appendix A.

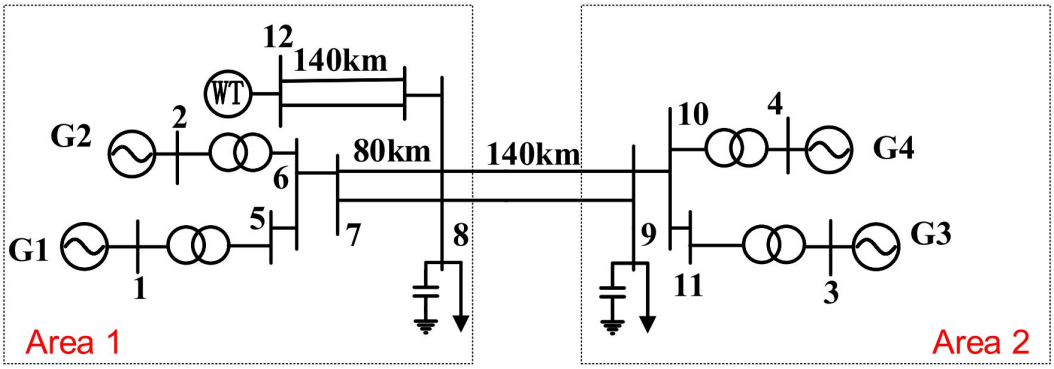

Figure 5.7: 4M11B system with DFIG-WTs participating in system frequency support

Through the small signal stability analysis under different wind speed operations, it can be found that the worst case is during the rated speed operation, where the wind speed is 12 m/s and the rotor speed is 1.2 p.u.. Hence, the case study is achieved under the 12m/s wind speed operation of DFIG-WT.

5.4.1 Stability Analysis

Table5.1 shows the small signal stability analysis results when the DFIG is connected to a 4M11B system through a long transmission line without frequency support capability. It can be seen that there is a poorly damped oscillation mode 2, which is dominated by the PLL.

Table 5.1: Oscillation modes of a 4M11B system with DFIG-WTs

No.	Eigenvalues	f(Hz)	ζ	Dominated states
1	$-30.027 \pm 294.45i$	46.8634	0.1014	Stator voltage
2	$-0.0508 \pm 72.7914i$	11.5851	0.0007	PLL
3	$-1.1307 \pm 17.8303i$	2.8378	0.0633	DFIG Mechanical
4	$-2.3115 \pm 7.2432i$	1.1528	0.3040	G1, G2
5	$-2.1604 \pm 6.8128i$	1.0843	0.3023	G3, G4
6	$-0.5979 \pm 3.3282i$	0.5297	0.1768	G1, G2, G3, G4

Table5.2 shows the small signal stability analysis results when the DFIG-WT equipped with frequency support capability. By comparing the results in Table5.1 and Table5.2, it can be found that the dominated states of oscillation mode 2 become both PLL and IEC. The oscillation frequency of the mode 2 is decreased and it is still poorly damped. In addition, the oscillation frequency of the stator voltage dominated oscillation mode 1 is increased after DFIG-WT equipped with an IEC, whereas its damping ratio is almost unchanged. The mechanical oscillation mode of the DFIG-WT is deteriorated after DFIG-WT contributing to system frequency support which is consistent to the problem discussed in Chapter 4. It can also be noted that the local oscillation mode 4 and 5 and the inter-area oscillation mode 6 are not affected after adding the IEC due to the satisfactory damping support provided

by PSS. Based on the aforementioned discussion, it is important to study the effect of PLL on system stability when the DFIG-WT contribute to frequency support, especially for the concerns on different power grid strength and PLL parameters.

Table 5.2: Oscillation modes of a 4M11B system with DFIG-WTs participating in system frequency support

No.	Eigenvalues	f(Hz)	ζ	Dominated states
1	$-32.024 \pm 316.09i$	50.3077	0.1008	Stator voltage
2	$-0.1075 \pm 12.0394i$	1.9161	0.0089	PLL, IEC
3	$-0.3564 \pm 18.2042i$	2.8973	0.0196	DFIG Mechanical
4	$-2.314 \pm 7.2442i$	1.153	0.3043	G1, G2
5	$-2.1533 \pm 6.8042i$	1.0829	0.3017	G3, G4
6	$-0.5986 \pm 3.3296i$	0.5299	0.1769	G1, G2, G3, G4

To analyse the effect of PLL and IEC on system stability, only the interested oscillation mode 2 in Table5.2, which is dominated by both PLL and IEC, is discussed in the following.

Impact of grid strength

Table5.3 shows the small signal stability analysis results of the oscillation mode 2 when the DFIG-WTs contribute to system frequency support under different power grid strength. By increasing the line impedance Z_{line} from $0.0093 + j0.093$ to $0.0315 + j0.315$, the SCR is changed from 5 to 1.4, which represents the power grid strength is varied from strong to weak. By comparing the results given in Table5.3, it can be found that the oscillation frequency of mode 2 is decreased when the SCR is decreased. Meanwhile, the damping ratio is also decreased for the drop of SCR. When the power grid strength is very weak, where SCR=1.4, the oscillation mode 2 becomes very poorly damped. It can be summarised that the stability of the DFIG-WT participating in system frequency support can be greatly affected by the grid strength where the damping ratio of the PLL and IEC dominated oscillation will reduce with the decreasing power grid strength.

Table 5.3: Oscillation mode 2 of a 4M11B system with DFIG-WTs participating in system frequency support under different grid strength

SCR	Eigenvalues	f(Hz)	ζ
5	$-1.6087 \pm 11.1966i$	1.7820	0.0950
4	$-0.9220 \pm 10.6054i$	1.6879	0.0866
3.07	$-0.6845 \pm 9.8515i$	1.5679	0.0693
2.1	$-0.4327 \pm 8.5987i$	1.3685	0.0503
1.4	$-0.1923 \pm 7.1876i$	1.1439	0.0267

Impact of PLL parameters

The PLL parameters, which are K_{P-pll} and K_{I-pll}, are normally set through trial and error approach. However, the time consumed on tuning parameters using this approach is tedious. Moreover, considering the uncertain generator parameters and operating conditions and also the nonlinearity in the inverter, PLL parameters will need to be changed to ensure its guaranteed performance [180]. Hence, the small signal stability analysis results under different PLL parameters are obtained to show the impact of PLL parameters on the system stability of DFIG-WT participating in system frequency support. Table5.4 shows the small signal stability analysis results of a 4M11B system with DFIG-WTs under different K_{P-pll}. It can be found that when the K_{P-pll} increases from 15 to 35, the oscillation frequency of mode 2 increases, whereas the damping ratio decreases. Hence, it can be concluded that PLL parameters can also affect the system stability of DFIG-WT participating in system frequency support. The damping ratio of the PLL and IEC dominated oscillation mode reduces with the increase of PLL parameters. Large PLL parameters will deteriorate system stability.

Based on the aforementioned finding, it can be concluded that both weak power grid and large PLL parameters will deteriorate system stability when the DFIG-WTs contributing to system frequency support. Thus, to ensure system stability of DFIG-WTs with frequency support capabilities against different parameters and system operating points, a robust damping controller is highly desired to ensure satisfactory damping performance of the PLL and IEC dominated oscillation mode.

Table 5.4: Oscillation mode 2 of a 4M11B system with DFIG-WTs participating in system frequency support under different K_{P-pll}

(K_{P-pll},K_{I-pll})	Eigenvalues	f(Hz)	ζ
(15,100)	$-0.4946 \pm 6.1954i$	0.9860	0.0796
(20,100)	$-0.4962 \pm 6.5087i$	1.0359	0.0760
(25,100)	$-0.4196 \pm 6.7826i$	1.0795	0.0617
(30,100)	$-0.3099 \pm 7.0048i$	1.1149	0.0442
(35,100)	$-0.1923 \pm 7.1876i$	1.1439	0.0267

5.4.2 Controller Design

Using the design approach provided in Section 5.3, a mixed H_2/H_∞ output feedback control based robust damping controller is designed in this section and added to the DFIG-WTs to ensure the system stability during frequency support under uncertainties. As the controller is designed to damp based on PLL dynamics, the input of the controller is the phase angle difference at the PCC and the output will be added at the Q-loop of the RSC of DFIG. The output signal of the damping controller is selected using the geometric measures of controllability as [167]. The full order of a 4M11B system with DFIG-WTs is 68, which will cause a longer time to solve the LMIs. Moreover, not all of states contains the characteristics of the studied system for controller design. Hence, the Schur balanced model reduction approach is used to reduce the system to a low order. The frequency response of a full order and reduced order of system is shown in Fig.5.8. It can be found that a 10th reduced order model can maintain the system performance in the interested frequency range, which is used in the robust damping controller design.

The interested LMI region for the robust damping controller is a conic sector with apex at the origin and inner angle 2θ. As the acceptable system operation should assure that oscillations can be mitigated in 10s [10], it can then be described as a minimum damping ratio $\zeta_{min} = cos^{-1}\frac{\theta}{2} = 0.15$ for the system closed-loop poles. The weighting functions are given as follows:

$$W_1(s) = \frac{30}{s+30}, W_2(s) = \frac{0.01s}{s+30}, W_2(s) = \frac{5s}{s+60} \tag{5.4.1}$$

The '$hinfmix$' function which is provided by the LMI Control Toolbox of

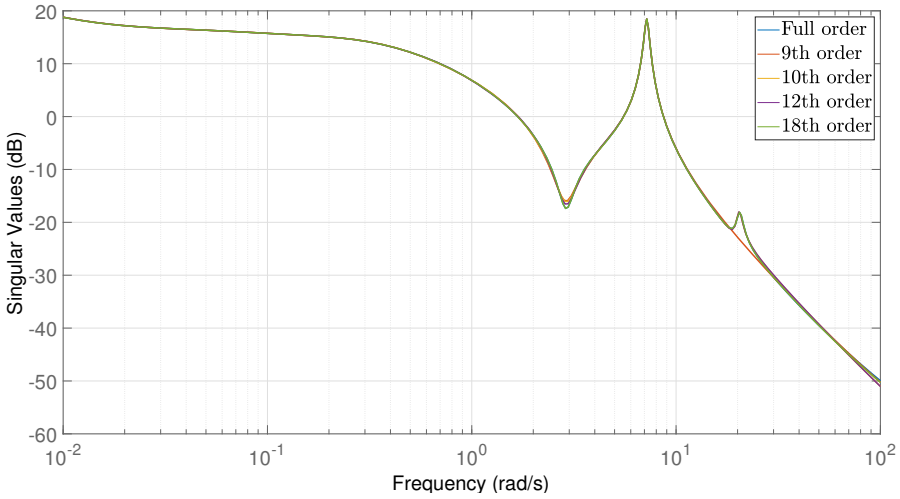

Figure 5.8: Singular values of the full order and reduced order of a 4M11B system with DFIG-WTs model

MATLAB was used to obtain the robust damping controller. The order of the designed controller was further reduced to a 9th order using the Schur balanced model reduction approach again. The designed mixed H_2/H_∞ based robust damping controller, which can be denoted as K_m for simplicity, is given as follows:

$$H_{K_m}(s) = \frac{N_m(s)}{D_m(s)} \tag{5.4.2}$$

$$\begin{aligned} N_m(s) =& 6.6924 \times 10^5 s^8 + 1.5977 \times 10^8 s^7 + 3.8309 \times 10^9 s^6 \\ & - 4.4172 \times 10^{10} s^5 - 8.8590 \times 10^{10} s^4 - 5.3943 \times 10^{10} s^3 \\ & + 4.1145 \times 10^{10} s^2 + 1.1470 \times 10^{10} s + 5.8053 \times 10^7 \end{aligned} \tag{5.4.3}$$

$$\begin{aligned} D_m(s) =& s^9 + 3.0958 \times 10^6 s^8 + 7.0106 \times 10^8 s^7 + 1.1151 \times 10^{10} s^6 \\ & + 9.4637 \times 10^{10} s^5 + 2.0756 \times 10^{11} s^4 + 4.8414 \times 10^{11} s^3 \\ & + 4.0558 \times 10^{11} s^2 + 5.8754 \times 10^{10} s + 4.6179 \times 10^8 \end{aligned} \tag{5.4.4}$$

Similarly, a robust damping controller based on H_∞ mixed-sensitivity approach can be designed, where the weighting functions are chosen as,

$$W_1(s) = \frac{30}{s+30}, W_2(s) = \frac{5s}{s+80} \tag{5.4.5}$$

The designed controller which is denoted as K_i is given as follows:

$$H_{K_i}(s) = \frac{N_i(s)}{D_i(s)} \tag{5.4.6}$$

$$\begin{aligned} N_i(s) =& 1.363 \times 10^7 s^8 + 1.4492 \times 10^9 s^7 + 4.3196 \times 10^9 s^6 \\ &+ 2.1019 \times 10^{10} s^5 + 3.8381 \times 10^{10} s^4 + 2.2446 \times 10^{10} s^3 \\ &+ 3.3962 \times 10^9 s^2 + 1.6362 \times 10^8 s + 1.4729 \times 10^6 \end{aligned} \tag{5.4.7}$$

$$\begin{aligned} D_i(s) =& s^9 + 1.7859 \times 10^7 s^8 + 1.2231 \times 10^9 s^7 + 1.4813 \times 10^{10} s^6 \\ &+ 5.3638 \times 10^{10} s^5 + 1.3286 \times 10^{11} s^4 + 6.0975 \times 10^{10} s^3 \\ &+ 9.7674 \times 10^9 s^2 + 5.5747 \times 10^8 s + 5.7008 \times 10^6 \end{aligned} \tag{5.4.8}$$

5.4.3 Performance Evaluation

Small signal stability analysis results

Table5.5 shows the small signal stability analysis results under different power grid strength when the K_m is used. By comparing the results obtained, it can be found that the K_m can maintain the designed damping ratio of the oscillation mode 2 against different power grid strengths.

Table 5.5: Oscillation mode 2 of a 4M11B system with DFIG-WTs equipped H_2/H_∞ based robust damping controller participating in system frequency support under different grid strength

SCR	Eigenvalues	f(Hz)	ζ
5	$-1.8218 \pm 11.8435i$	1.8850	0.1520
4	$-1.7946 \pm 11.2507i$	1.7906	0.1575
3.07	$-1.7368 \pm 10.4715i$	1.6666	0.1636
2.1	$-1.9176 \pm 9.1537i$	1.4569	0.2050
1.4	$-2.8242 \pm 7.5235i$	1.1974	0.3514

In Table5.6, the small signal stability analysis results of the DFIG-WTs with K_i are given. It can also be concluded that the minimum damping performance can be achieved against different power grid strengths.

Table 5.6: Oscillation mode 2 of a 4M11B system with DFIG-WTs equipped H_∞ based robust damping controller participating in system frequency support under different grid strength

SCR	Eigenvalues	f(Hz)	ζ
5	$-2.3608 \pm 12.0966i$	1.9252	0.1915
4	$-2.2685 \pm 11.4315i$	1.8194	0.1947
3.07	$-2.1082 \pm 10.5870i$	1.6850	0.1953
2.1	$-2.0790 \pm 9.1130i$	1.4504	0.2224
1.4	$-2.1175 \pm 7.5726i$	1.2052	0.2693

As shown in both tables, both robust damping controllers can maintain the minimum damping ratio of the oscillation mode 2 against power grid strength variation. Thus, the system oscillation can be well damped and system stability is ensured. In addition, it can also be found that the K_m can provide better damping performance than K_i when the power grid is very weak, which is better to be used in DFIG-WTs connecting to a weak power grid.

Table5.7 shows the small signal stability analysis results when K_m is used against different K_{P-pll}. By comparing the results in Table5.7, it can be found that the oscillation mode can be well damped against different PLL parameters.

Table 5.7: Oscillation mode 2 of a 4M11B system with DFIG-WTs equipped H_2/H_∞ based robust damping controller participating in system frequency support under different K_{P-pll}

(K_{P-pll},K_{I-pll})	Eigenvalues	f(Hz)	ζ
(15,100)	$-4.9852 \pm 7.5718i$	1.2051	0.5499
(20,100)	$-4.2642 \pm 7.5874i$	1.2076	0.4899
(25,100)	$-3.6852 \pm 7.5537i$	1.2022	0.4385
(30,100)	$-2.2973 \pm 7.5357i$	1.1995	0.3914
(35,100)	$-2.8242 \pm 7.5235i$	1.1974	0.3514

Table5.8 shows the small signal stability analysis results of oscillation mode 2 when K_i is used. By comparing the damping ratio of the oscillation mode 2, it can be found that the robust damping controller can ensure the satisfactory damping performance as required.

Table 5.8: Oscillation mode 2 of a 4M11B system with DFIG-WTs equipped H_∞ based robust damping controller participating in system frequency support under different K_{P-pll}

(K_{P-pll},K_{I-pll})	Eigenvalues	f(Hz)	ζ
(15,100)	$-2.3300 \pm 7.4668i$	1.1884	0.2979
(20,100)	$-2.3104 \pm 7.4758i$	1.1898	0.2953
(25,100)	$-2.2784 \pm 7.4876i$	1.1917	0.2911
(30,100)	$-2.2203 \pm 7.5100i$	1.1953	0.2835
(35,100)	$-2.1175 \pm 7.5726i$	1.2052	0.2693

According to the results given in Table5.7 and 5.8, it can also be concluded that both K_m and K_i can ensure the minimum damping performance against different PLL parameters. Thus, the system oscillation can be well damped when the different PLL parameters are used. It can also be noted that the damping ratio of oscillation mode 2 when K_m is used is higher than using K_i. This indicates that the K_m is better to be used to damp the oscillation mode 2 when PLL parameters are large.

Simulation results

Simulation results are also provided to show the damping performance of the robust controllers. An oscillation is triggered by adding a load disturbance on bus 9 at 1s and cleared at 1.05s. The nominal operating point is selected by setting $K_{P-pll} = 35$, $K_{P-pll} = 100$ under $SCR = 1.4$. Fig.5.9 shows the frequency response under the nominal operating point.

In Fig.5.10, the frequency response under a load disturbance is shown where a strong grid connection is set and SCR equals to 5. By comparing Fig.5.9 and Fig.5.10, it can be found that both robust damping controllers can provide robust damping performance against different power grid strength, while K_m designed based on H_2/H_∞ control approach can provide better transient performance than K_i especially for connecting to a weak grid.

Fig.5.11 shows the frequency response when the PLL parameter K_{P-pll} is decreased to 15. By comparing Fig.5.9 and Fig.5.11, it can also be found that both robust damping controllers can provide robust damping performance to the oscilla-

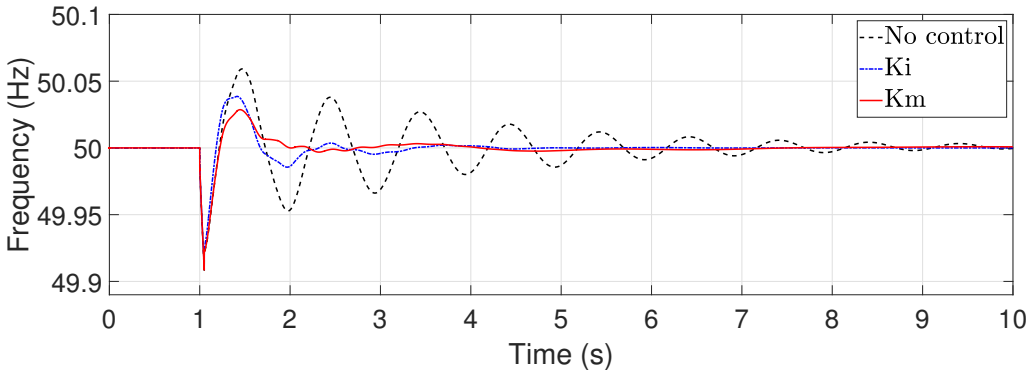

Figure 5.9: Frequency response of a DFIG-WT under nominal operating point in a 4M11B system

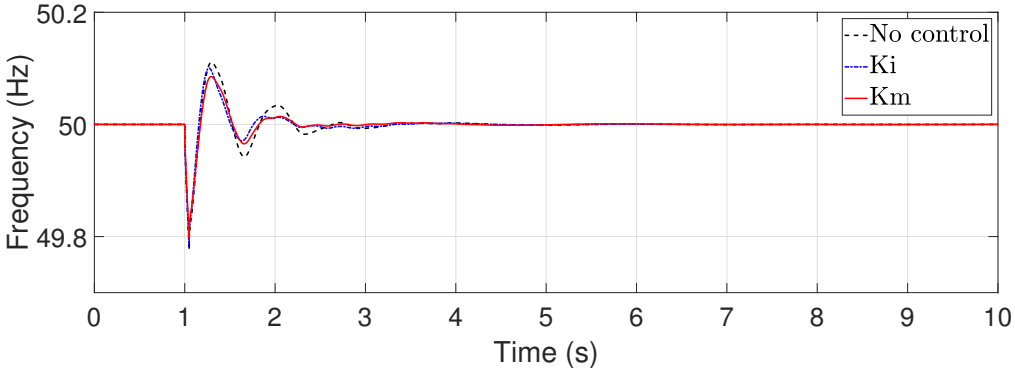

Figure 5.10: Frequency response of a DFIG-WT connecting to a strong grid in a 4M11B system

tion mode. Meanwhile, the transient performance of K_m is better than K_i.

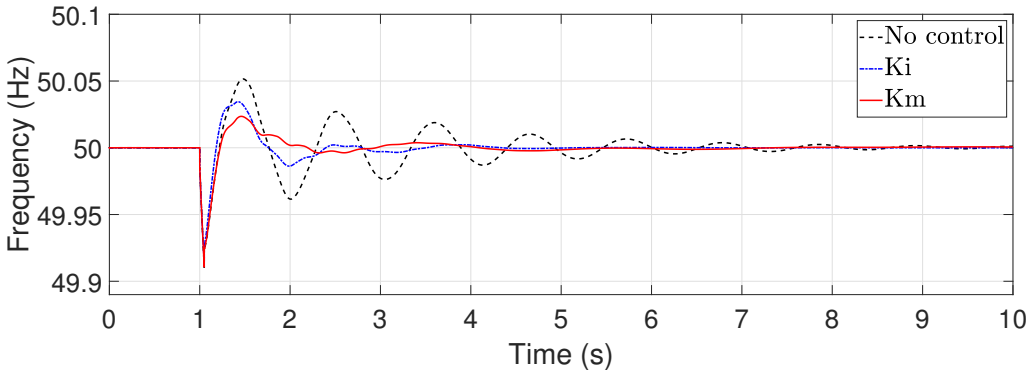

Figure 5.11: Frequency response of a DFIG-WT with $K_{P-pll} = 15$ in a 4M11B system

Moreover, the robustness is also verified by changing the fault added to the system. A new fault is applied by cutting one line between bus 8 and 12 at 1s and cleared at 1.05s. Fig.5.12 shows the frequency response under a new fault. By comparing Fig.5.9 and Fig.5.12, it can be found that both robust damping controllers can provide robust damping performance where the robust damping controller K_m designed based on mixed H_2/H_∞ control approach shows better transient performance than K_i.

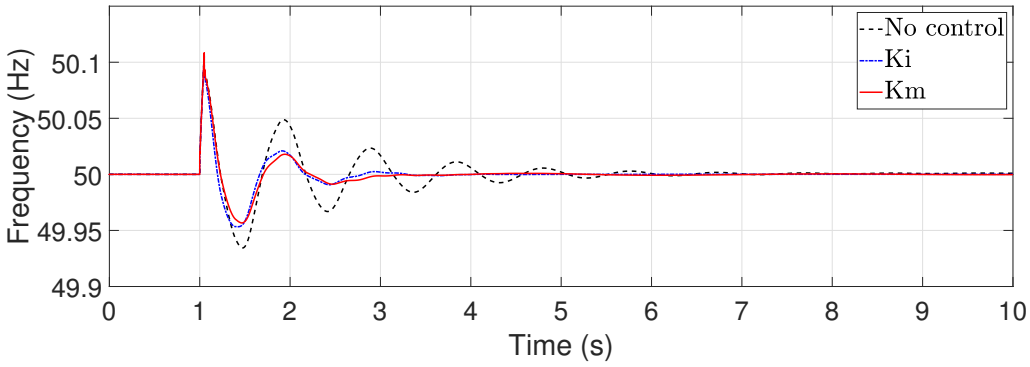

Figure 5.12: Frequency response of a DFIG-WT under a new fault in a 4M11B system

5.5 Case Study II - New England New York 68-bus System

The robust performance of the proposed controller is further verified when DFIG-WTs are connected to a 16M68B system as shown in Fig.5.13, which is the same as the model discussed in Section 2.5.3. The DFIG-WTs are added in a new bus 69 and connected to the bus 31 in Area II. Similar to the case study in a 4M11B system, the DFIG-WT is operated under the rated speed operation where the wind speed is 12 m/s and the rotor speed equals to 1.2 p.u. The power grid strength is determined by the line impedance between bus 31 and 69. All of synchronous generators G1-G16 are equipped with PSSs to damp the local and inter area oscillation modes of the 16M68B system. The detailed parameters of the 16M68B system are given in Appendix B.

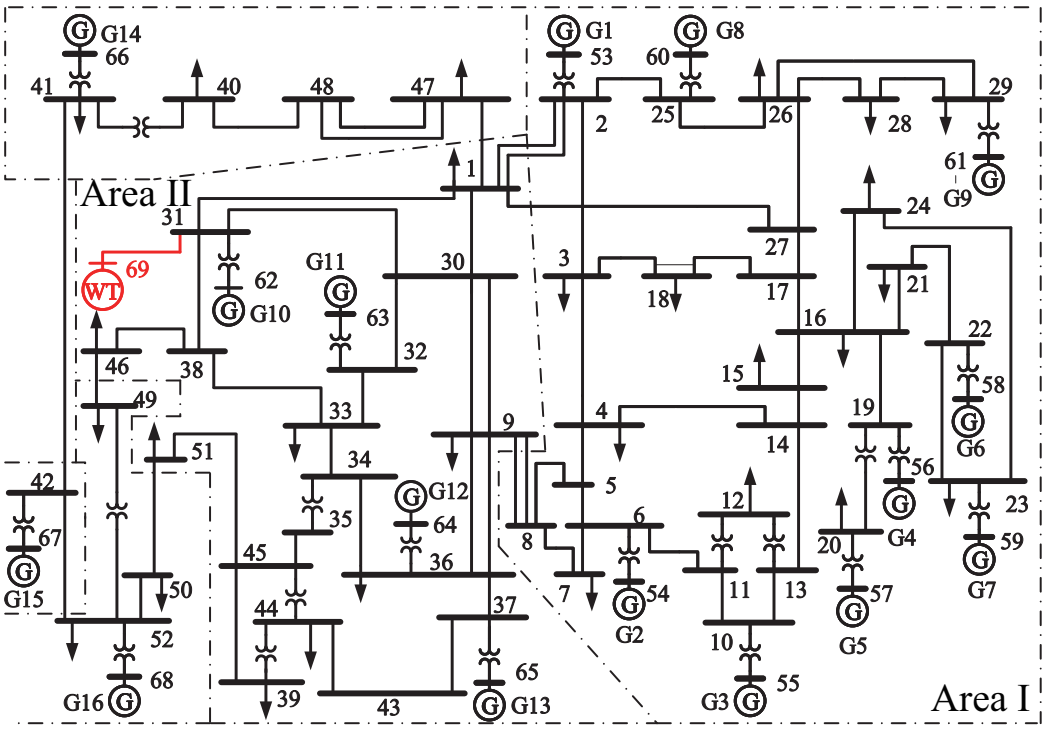

Figure 5.13: New England New York 68-bus system with DFIG-WTs participating in system frequency support [10]

5.5.1 Stability Analysis

Impact of grid strength

Table5.9 shows the small signal stability analysis results of the oscillation mode 2 when the DFIG-WTs contribute to 16M68B system frequency support under different power grid strength. By increasing the line impedance Z_{line} from $0.00975 + j0.0975$ to $0.025 + j0.25$, the SCR is decreased from 5 to 1.94, which represents the power grid strength is varied from strong to weak. By comparing the oscillation frequency and damping ratio of mode 2 given in Table5.9, it can be found that a smaller SCR will cause a smaller oscillation frequency of mode 2, while the damping ratio is reduced for the decrease of SCR. When the power grid strength becomes very weak, i.e. SCR=1.94, the damping ratio of oscillation mode 2 becomes negative which will cause system instability. Hence, it can be summarised that the stability of the DFIG-WTs participating in a 16M68B system frequency support can be greatly affected by the grid strength, where the damping ratio of the PLL and IEC dominated oscillation mode 2 will reduce when the power grid strength decreases.

Table 5.9: Oscillation mode 2 of a 16M68B system with DFIG-WTs participating in system frequency support under different grid strength

SCR	Eigenvalues	f(Hz)	ζ
5	$-1.2476 \pm 10.4070i$	1.6563	0.1190
4.21	$-1.0952 \pm 9.3068i$	1.4812	0.1169
3.88	$-0.9632 \pm 8.4573i$	1.3460	0.1132
2.58	$-0.2342 \pm 7.0263i$	1.1183	0.0333
1.94	$0.2584 \pm 5.3494i$	0.8514	-0.0483

Impact of PLL parameters

Small signal stability analysis results of the oscillation mode 2 when the DFIG-WTs contribute to 16M68B system frequency support under different PLL parameters are also given to show the impact of PLL parameters on the system stability. The power grid strength is chosen as a very weak grid, where $SCR = 1.94$. Table5.10

shows the small signal stability analysis results of a 16M68B system with DFIG-WTs under different K_{P-pll}. When the K_{P-pll} increases from 15 to 35, the oscillation frequency of mode 2 increases, while the damping ratio decreases. Hence, it can be summarised that PLL parameters can also affect the system stability of DFIG-WT participating in a 16M68B system frequency support. The damping ratio of the PLL and IEC dominated oscillation mode 2 is deteriorated with larger PLL parameters.

Table 5.10: Oscillation mode 2 of a 16M68B system with DFIG-WTs participating in system frequency support under different K_{P-pll}

(K_{P-pll},K_{I-pll})	Eigenvalues	f(Hz)	ζ
(15,100)	$-0.0015 \pm 4.2985i$	0.6841	0.0003
(20,100)	$0.0153 \pm 4.5651i$	0.7266	-0.0033
(25,100)	$0.0153 \pm 4.5651i$	0.7700	-0.0139
(30,100)	$0.1511 \pm 5.1022i$	0.8120	-0.0296
(35,100)	$0.2584 \pm 5.3494i$	0.8514	-0.0483

Based on the aforementioned finding, it can be concluded that both weak power grid and large PLL parameters will also deteriorate the 16M68B system stability when the DFIG-WTs contributing to system frequency support. Thus, to ensure system stability of DFIG-WTs with frequency support capabilities against different parameters and system operating points, a robust damping controller is highly required.

5.5.2 Controller Design

Similar to the case study on a 4M11B system, a mixed H_2/H_∞ output feedback control based robust damping controller is designed for DFIG-WTs contributing to the frequency support in a 16M68B system. The full order of a 16M68B system with DFIG-WTs is 223, which is reduced to a 11th order model for controller design through the Schur balanced model reduction approach. The frequency response of a full order and reduced order of system is shown in Fig.5.14. It can be found that a 11th reduced order model can maintain the system performance in the interested

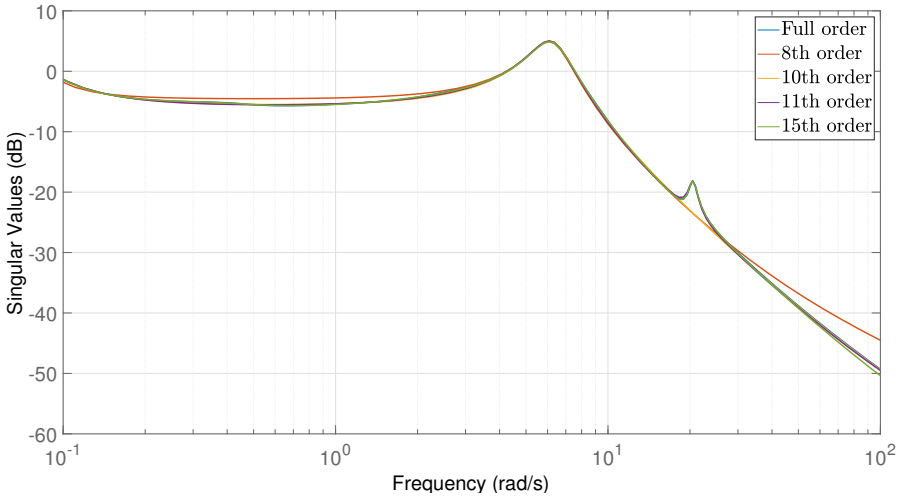

Figure 5.14: Singular values of the full order and reduced order of a 16M68B system with DFIG-WTs model

frequency range. The weighting functions are given as follows:

$$W_1(s) = \frac{50}{s+50}, W_2(s) = \frac{0.005s}{s+60}, W_2(s) = \frac{s}{s+30} \tag{5.5.1}$$

Using '$hinfmix$' function in the LMI Control Toolbox of MATLAB, the robust damping controller can designed. The order of the designed controller was further reduced to a 9th order using the Schur balanced model reduction approach again. The designed mixed H_2/H_∞ based robust damping controller for a 16M68B system, which is denoted as K_m for simplicity, is given as follows:

$$H_{K_m}(s) = \frac{N_m(s)}{D_m(s)} \tag{5.5.2}$$

$$\begin{aligned} N_m(s) =& 2.2393 \times 10^5 s^8 + 8.4030 \times 10^7 s^7 + 1.9124 \times 10^9 s^6 \\ & - 2.3167 \times 10^{10} s^5 - 3.0728 \times 10^9 s^4 - 1.4578 \times 10^8 s^3 \\ & - 6.8728 \times 10^6 s^2 - 2.2933 \times 10^5 s - 8.9947 \times 10^8 \end{aligned} \tag{5.5.3}$$

$$\begin{aligned} D_m(s) =& s^9 + 8.6225 \times 10^5 s^8 + 3.2066 \times 10^8 s^7 + 6.7621 \times 10^9 s^6 \\ & + 3.9879 \times 10^{10} s^5 + 9.8371 \times 10^9 s^4 + 7.5951 \times 10^8 s^3 \\ & + 3.5724 \times 10^7 s^2 + 2.7697 \times 10^5 s - 1.1426 \times 10^{-6} \end{aligned} \tag{5.5.4}$$

The implementation of the designed robust damping controller in the DFIG-WTs connected to a 16M68B system is the same as shown in Fig.5.6.

Similarly, the single objective robust damping controller based on H_∞ mixed-sensitivity approach is designed to maintain stability when the DFIG-WT contributes to a 16M68B system frequency support. The weighting functions for controller design are chosen as,

$$W_1(s) = \frac{30}{s+30}, W_2(s) = \frac{10s}{s+100} \tag{5.5.5}$$

The designed controller which is denoted as K_i for simplicity is given as follows:

$$H_{K_i}(s) = \frac{N_i(s)}{D_i(s)} \tag{5.5.6}$$

$$\begin{aligned} N_i(s) =& 3.4957 \times 10^6 s^9 + 3.9208 \times 10^8 s^8 - 1.6120 \times 10^9 s^7 \\ & - 1.1301 \times 10^{10} s^6 - 1.1585 \times 10^{10} s^5 - 1.4297 \times 10^8 s^4 \\ & + 2.4584 \times 10^7 s^3 - 3.4056 \times 10^5 s^2 - 1.8863 \times 10^4 s \\ & - 1.2561 \times 10^{-6} \end{aligned} \tag{5.5.7}$$

$$\begin{aligned} D_i(s) =& s^{10} + 1.0469 \times 10^7 s^9 + 6.4975 \times 10^8 s^8 + 7.1887 \times 10^9 s^7 \\ & + 2.0794 \times 10^{10} s^6 + 1.7486 \times 10^{10} s^5 + 3.4618 \times 10^9 s^4 \\ & + 3.2898 \times 10^8 s^3 + 1.3086 \times 10^7 s^2 + 1.5281 \times 10^5 s \\ & + 3.3191 \times 10^{-5} \end{aligned} \tag{5.5.8}$$

5.5.3 Performance Evaluation

Small signal stability analysis results

Table5.11 shows the small signal stability analysis results when K_m is used. By comparing the results obtained, it can be found that K_m can provide robust damping performance of the oscillation mode 2 against different power grid strengths. The reason for the damping ratio at $SCR = 5$ is below 0.15 is because the controller is designed based on the reduced order system. Under certain operating conditions, the damping ratios may be less than 0.15. However, it can still ensure the oscillation is damped within 10s.

Table 5.11: Oscillation mode 2 of a 16M68B system with DFIG-WTs equipped H_2/H_∞ based robust damping controller participating in system frequency support under different grid strength

SCR	Eigenvalues	f(Hz)	ζ
5	$-1.4015 \pm 10.5521i$	1.6794	0.1317
4.21	$-1.4368 \pm 9.1178i$	1.4511	0.1557
3.88	$-1.3296 \pm 8.3298i$	1.3257	0.1576
2.58	$-1.1208 \pm 6.9589i$	1.1075	0.1590
1.94	$-1.9852 \pm 4.5600i$	0.7257	0.3992

Furthermore, the small signal stability analysis results of the DFIG-WTs with K_i connected in a 16M68B system are also obtained and shown in Table5.12. It can also be found that the robust damping performance is achieved under different power grid strengths.

Table 5.12: Oscillation mode 2 of a 16M68B system with DFIG-WTs equipped H_∞ based robust damping controller participating in system frequency support under different grid strength

SCR	Eigenvalues	f(Hz)	ζ
5	$-1.4785 \pm 10.5461i$	1.6785	0.1388
4.21	$-1.4503 \pm 9.1156i$	1.4508	0.1571
3.88	$-1.3842 \pm 8.2608i$	1.3147	0.1653
2.58	$-1.2809 \pm 6.8403i$	1.0887	0.1841
1.94	$-1.2864 \pm 4.2187i$	0.6714	0.2917

According to the small signal stability analysis results given in both tables, it can be summarised that both robust damping controllers can provide robust damping performance on the oscillation mode 2 against power grid strength variation. Thus, the 16M68B system stability with DFIG-WTs contributing to system frequency support can be ensured. Furthermore, it can also be seen that the damping performance provided by K_m is better than K_i in the very weak grid strength. This shows that the K_m is more effective when DFIG-WTs with frequency support capability are connected to a weak power grid.

For different K_{P-pll}, the small signal stability analysis results of oscillation

mode 2 when the DFIG-WTs equipped with K_m contributing to a 16M68B system frequency support are given in Table5.13. By comparing the damping ratio shown in Table5.13, it can be found that the oscillation mode 2 can be well damped against different PLL parameters.

Table 5.13: Oscillation mode 2 of a 16M68B system with DFIG-WTs equipped H_2/H_∞ based robust damping controller participating in system frequency support under different K_{P-pll}

(K_{P-pll},K_{I-pll})	Eigenvalues	f(Hz)	ζ
(15,100)	$-5.5983 \pm 4.6732i$	0.7438	0.7677
(20,100)	$-4.8238 \pm 4.6973i$	0.7476	0.7164
(25,100)	$-4.1263 \pm 4.4513i$	0.7084	0.6798
(30,100)	$-3.1496 \pm 4.0018i$	0.6369	0.6185
(35,100)	$-1.9852 \pm 4.5600i$	0.7257	0.3992

In addition, the small signal stability analysis results of oscillation mode 2 when DFIG-WTs equipped with K_i are shown in Table5.14. By comparing the damping ratios of the oscillation mode 2, it can also be found that K_i can ensure the satisfactory damping performance as required.

Table 5.14: Oscillation mode 2 of a 16M68B system with DFIG-WTs equipped H_∞ based robust damping controller participating in system frequency support under different K_{P-pll}

(K_{P-pll},K_{I-pll})	Eigenvalues	f(Hz)	ζ
(15,100)	$-6.4104 \pm 4.3290i$	0.6890	0.8287
(20,100)	$-5.3954 \pm 4.4034i$	0.7008	0.7747
(25,100)	$-4.9869 \pm 47783i$	0.7605	0.7220
(30,100)	$-4.4393 \pm 4.4842i$	0.7137	0.7035
(35,100)	$-1.2864 \pm 4.2187i$	0.6714	0.2917

Based on the small signal stability analysis results given in both Table5.13 and 5.14, it can also be summarised that both K_m and K_i can provide robust damping performance against different PLL parameters when DFIG-WTs contribute to a 16M68B system frequency support. Thus, system stability can be ensured when

different PLL parameters are used. It can also be noted that the damping ratio of oscillation mode 2 for large PLL parameters when K_m is used is higher than using K_i. This indicates that K_m can provide better damping performance especially when the PLL parameters are large.

Simulation results

Simulation results of DFIG-WT participating in the 16M68B system frequency support are also provided to show the damping performance of the robust controllers. An oscillation is triggered by adding a load disturbance on bus 7 at 1s and cleared at 1.1s. The nominal operating point is selected by setting $K_{P-pll} = 35$, $K_{P-pll} = 100$ under $SCR = 1.94$. Fig.5.15 shows the frequency response under the nominal operating point. Comparing the simulation results in Fig.5.15, it can be concluded that both K_m and K_i can provide robust damping performance which is consistent to the small signal stability analysis results. The oscillation can be well damped in 8s. It can also be found that when DFIG-WTs are equipped with K_m, the transient performance is better than K_i due to the H_2 performance is considered in the controller design which is more suitable to suppress the time domain transient performance.

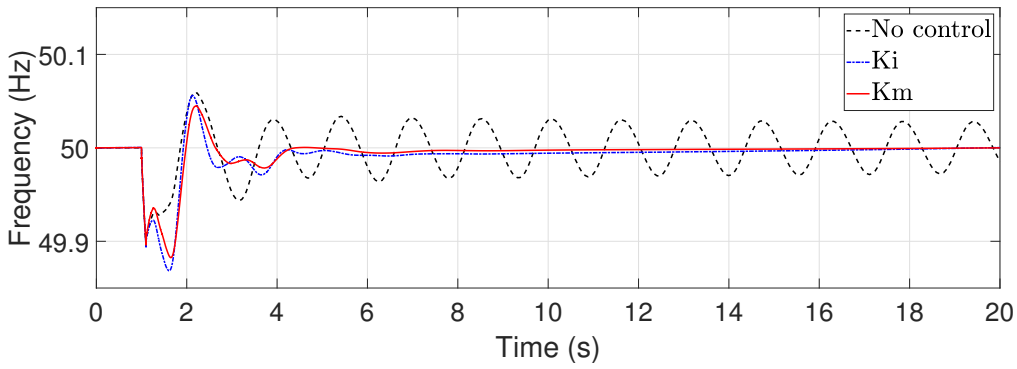

Figure 5.15: Frequency response of a DFIG-WT under nominal operating point in a 16M68B system

To test the robust damping performance under different power grid strength, simulation results under a strong grid connection are given and shown in Fig.5.16, where SCR equals to 5. By comparing the simulation results in Fig.5.15 and Fig.5.16, it

can be concluded that both K_m and K_i can provide robust damping performance against different power grid strength, while K_m designed based on H_2/H_∞ control approach can provide better transient performance than K_i.

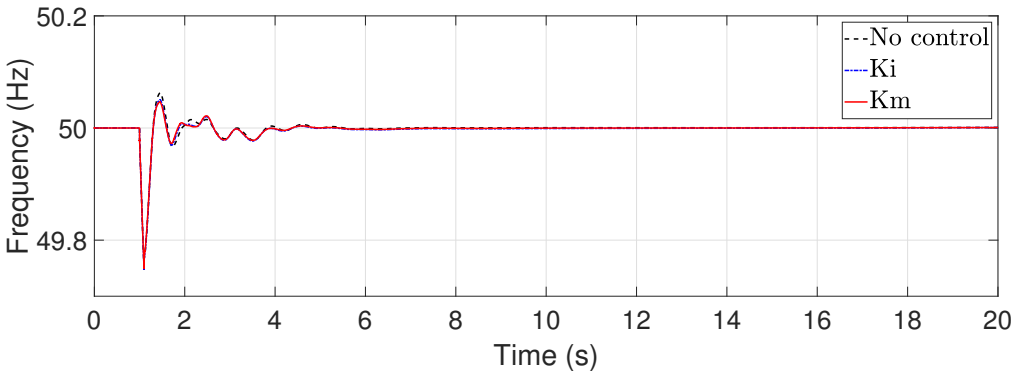

Figure 5.16: Frequency response of a DFIG-WT connecting to a strong grid in a 16M68B system

The robustness can also be tested by changing the PLL parameter K_{P-pll}. Fig.5.17 shows the frequency response when K_{P-pll} is decreased to 15. By comparing Fig.5.15 and Fig.5.17, it can also be found that both K_m and K_i can provide robust damping performance to ensure system stability. Meanwhile, the transient performance with K_m is better than K_i.

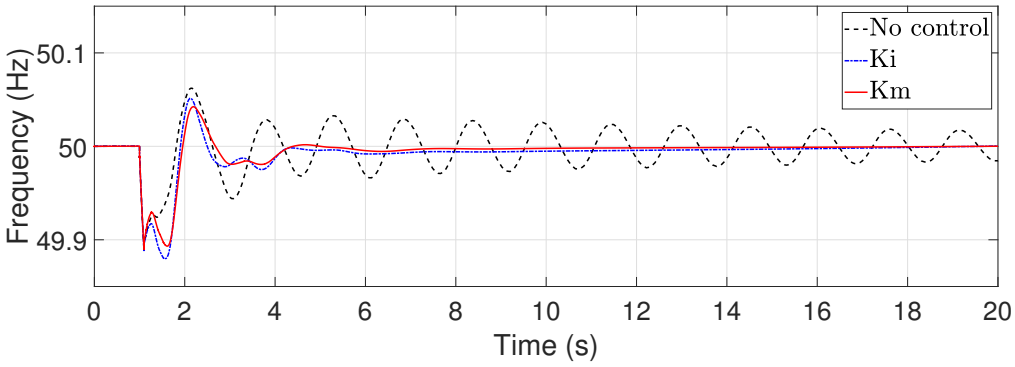

Figure 5.17: Frequency response of a DFIG-WT with $K_{P-pll} = 15$ in a 16M68B system

Moreover, the robustness is tested by changing the external fault applied to the system. A new load disturbance is applied at bus 47 at 1s and cleared at 1.1s.

Fig.5.18 shows the frequency response under a new fault at bus 47. Comparing the simulation results given in Fig.5.15 and Fig.5.18, it can be concluded that both K_m and K_i can provide robust damping performance under different external disturbances where the robust damping controller K_m designed based on mixed H_2/H_∞ control approach shows better transient performance than K_i.

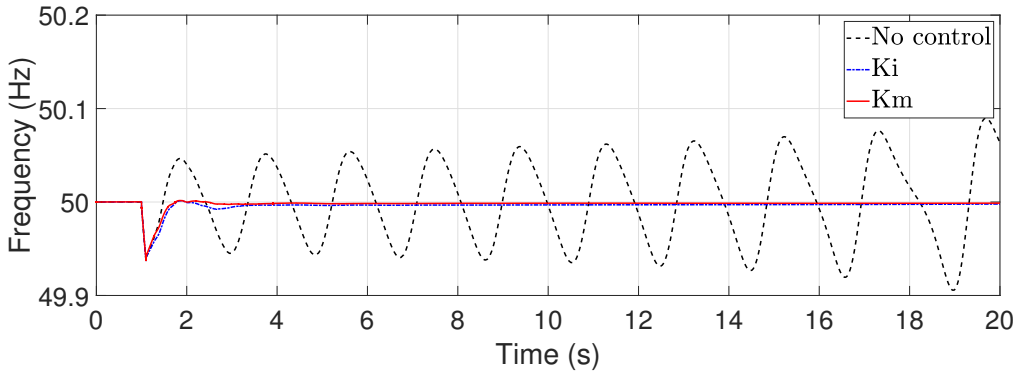

Figure 5.18: Frequency response of a DFIG-WT under a new fault in a 16M68B system

5.6 Conclusion

As the PCC frequency of DFIG-WTs participating in system frequency support is obtained by the PLL, the impact of the PLL on system stability is important to be investigated. In this chapter, a poorly damped oscillation mode which is dominated by both PLL and IEC is found. Through analysis, it can be found that large PLL parameters and weak power grid strength will lead to very poor damping ratio of the oscillation mode and deteriorate system stability. Thus, a mixed H_2/H_∞ output feedback control approach is used to design the damping controller and compare with the single objective H_∞ mixed-sensitivity based damping controller. Case studies are obtained when the DFIG-WTs contribute to the frequency support in a 4M11B system and a 16M68B system. Both small signal stability analysis results and simulation results are obtained to verify the performance. It can be found that both robust damping controllers can achieve the minimum damping requirement, while the H_2/H_∞ based damping controller gives a better damping performance in

the weak power grid and large PLL parameters. Moreover, the transient performance of H_2/H_∞ based damping controller is better as shown in the simulation results. This is due to the fact that the multi-objective synthesis control approach can achieve both H_2 and H_∞ performance, where the H_2 performance can suppress the random disturbances more effectively.

Chapter 6

Conclusions and Future Work

This chapter summarises the results obtained in this thesis. Moreover, suggestions for future research are also provided.

6.1 Conclusions

As the wind turbine generators are widely deployed in the modern power system, the effective system inertia is decreased significantly. This is due to the fact that the wind turbine generators are connected to the grid through the power electronics, which decoupled them from the power grid and thus which provide zero inertia. To improve the system frequency response performance, TSOs have asked the wind power plants to contribute to frequency support. This thesis has studied the impact of the DFIG-WT with inertia emulation control capability on system stability and proposes robust controllers to ensure a stable operation considering the inevitable uncertainties in parameters, time-varying operating points and external disturbances. The main conclusions are presented as follows.

In Chapter 2, the effect of an IEC on the system stability of DFIG-WT contributing to system frequency support is firstly investigated. It has been found that after adding an IEC, a new poorly damped oscillation mode is introduced which deteriorates system stability. A RDC is proposed which can provide robust damping performance on the new oscillation mode when DFIG-WTs participate in system fre-

quency support. H_∞ mixed-sensitivity control approach is used to design the RDC. The robust damping performance of the designed RDC is verified and compared to a CDC designed based on the residue approach. Case studies are presented when DFIG-WTs contribute to the frequency support in a SMIB system, a 4M11B system and a 16M68B system under different power grid strength, system power flow, wind power penetration levels and external disturbances. Both small signal stability analysis and simulation results are obtained, which verified that the proposed RDC can provide robust damping performance under different system operating points.

In Chapter 3, a novel robust PD-type controller design approach is proposed based on H_∞ control approach with additional LMI constraints on regional pole placement. An IIEC is designed based on the proposed robust PD-type controller design approach which can provide robust frequency support performance without introducing a poorly damped oscillation mode in the system, such that the need of an additional damping controller is avoided. Case studies are achieved when DFIG-WTs with IIEC contribute to the frequency support of a SMIB system, a 4M11B system and a 16M68B system. Both small signal stability analysis and simulation are carried out to show the effectiveness of the proposed IIEC. With the proposed IIEC, the DFIG-WTs can provide robust frequency support performance comparing to the CIEC and CIEC plus RDC. Simultaneously, the damping ratio of the new introduced oscillation mode is ensured as design, such that the oscillation can be mitigated. Hence, additional damping control loop design can be avoided and the DFIG-WTs participating in the system frequency regulation can be simplified.

In Chapter 4, the impact of the IEC on the wind turbine drive train torsional oscillation mode is investigated. The research shows that the damping performance of torsional oscillation is deteriorated with supplementary IEC. Geometric controllability is calculated to select the torsional oscillation damping controller output. The calculated geometric controllability shows that the reactive power control loop of DFIG-WT has superior damping performance than the active power control loop on mitigating the torsional oscillation. Thus, the proposed RTODC is added to the reactive power control of the DFIG-WT. H_∞ mixed-sensitivity control approach is used to design RTODC to ensure the robust damping ratio of the torsional oscillation

during DFIG-WT contributing to system frequency support. Two case studies are presented based on a 4M11B system and a 16M68B system with DFIG-WTs contributing to system frequency support. The robustness of the proposed RTODC was tested under parameter uncertainties, time-varying system operating points and also different external disturbances. Small signal stability analysis and simulation results verify that the robust damping performance of the proposed RTODC is ensured on torsional oscillation mode comparing to the CIEC and CIEC with CDC+CTODC.

In Chapter 5, when the PCC frequency of DFIG-WTs participating in system frequency support is obtained by the PLL, the impact of the PLL on system stability is investigated. Analysis results show that a PLL and IEC dominated poorly damped oscillation mode is found, while large PLL parameters and weak power grid strength deteriorate the system stability. A mixed H_2/H_∞ output feedback control approach is used to design the damping controller and compare with the single objective H_∞ mixed-sensitivity based damping controller. Both small signal stability analysis results and simulation results are obtained to verify the damping performance in a 4M11B system and a 16M68B system. It can be found that both controllers can achieve the minimum damping requirement, while the H_2/H_∞ based damping controller gives a better transient performance. This is due to the fact that the multi-objective synthesis control approach can achieve both H_2 and H_∞ performance, where H_2 performance can ensure better time domain transient response.

In conclusion, the difference between the controllers designed in Chapter 2 - 5 is compared in terms of control objectives, inputs, outputs and controller design approaches. The control objective of Chapter 2 and 3 is to ensure robust frequency support performance of DFIG-WT without affecting system stability, where the new oscillation mode dominated by an IEC is well-damped. When a PLL is used to measure the PCC frequency during DFIG-WTs participating in system frequency support, the new oscillation mode will be dominated by both a PLL and an IEC. Thus, the control objective of Chapter 5 is to ensure robust system stability considering the impact of both a PLL and an IEC. In addition to the new oscillation mode introduced by an IEC, Chapter 4 designs the controller to ensure robust damping performance of the torsional oscillation mode of the WT drive train, where the tor-

sional oscillation mode is deteriorated during DFIG-WTs participating in system frequency support. According to different control objectives, the inputs and outputs of designed controllers are chosen. The input of a RDC designed in Chapter 2 is the frequency deviation and the output is compensation active power added at the active power control loop of DFIG-WTs. The IIEC designed in Chapter 3 is an integrated controller and the input and output of an IIEC are the same as the IEC, which are the frequency deviation and auxiliary power provided for frequency support respectively. Since the torsional oscillation mode is observed on the WT drive train, the input of the RTODC designed in Chapter 4 is the DFIG rotor speed. The output is selected through calculation on geometric controllability which is the damping power added at the reactive power control loop of a DFIG-WT RSC. When a PLL is considered, the control input of the controller designed in Chapter 5 is the phase angle deviation measured by a PLL to mitigate the impact of a PLL on system stability. The output is chosen to add at the reactive power control loop of a DFIG-WT RSC based on geometric controllability. The controller design approaches used in Chapter 2 and 4 are based on the existing H_∞ mixed-sensitivity control approach widely used in designing power system stabilisers, whereas it has not been designed for WTGs participating in system frequency support. This is similar to the mixed H_2/H_∞ output feedback control approach used in Chapter 5. The IIEC designed in Chapter 3 is based on a novel robust PD-type controller design approach proposed in this chapter which can ensure robust frequency support performance and satisfactory damping performance simultaneously.

6.1.1 Challenges and Limitations

Although the designed controllers in this thesis have achieved robust frequency support performance and damping performance considering the impact of IEC and PLL on the new poorly oscillation mode and torsional oscillation mode, there still exists challenges and limitations of the present work which is addressed as follows.

- The research achieved in this thesis is based on the aggregated several WTGs and these WTGs are connected to the power system at one new bus. However, there will be multiple WTGs connected at different buses of a real power

system. Considering this situation, the coordination control between WTGs at different locations to ensure system stability during frequency support is one of the challenges in the current controller design.

- Another challenge is the control strategy of individual WTGs in a wind farm. The current research is limited to assume the WTGs in a wind farm have similar wind power generation. However, the wind speed of each WTG facing is different based on the locations of WTGs. Moreover, wind turbulence will also affect wind generation. Hence, coordinated control within a wind farm is needed and the designed controllers augmented to each WTGs is challenging.

6.2 Future Work

Based on the research of this thesis, the possible future work is listed as follows:

- The coordination of the IEC and the long-term frequency support. This thesis has investigated the frequency support provided by DFIG-WTs to contribute to the short-term frequency response of the power system. It is valuable to coordinate the proposed IEC with the long-term frequency support control approach, such as AGC.

- IEC design considering torsional oscillation. The wind turbine drive train model can be expanded to a multi-mass drive-train model to study the torsional oscillation. In addition, it is worth to design a novel IEC which will not deteriorate the drive-train torsional oscillation.

- PLL parameters tuning approach. This thesis has investigated that the large PLL parameters will lead to system instability, it is worth to adaptively tune PLL parameters to ensure the system stability during inertia emulation, where the constraints on the wind turbine generator frequency support performance and system stability will be considered in the parameters tuning.

- Hardware verification. Although simulation can verify the performance of designed controllers, it is necessary to conduct hardware experiments to test

their performance in real systems. In real systems, the designed controllers need to receive and send the control signals in their control processes. At this time, the time delay is unavoidable and this is hard to predict in the simulation. In addition, noises also exist in different equipment used in experiments to measure signals and observe the performance. The impact of noises on the controller performance during frequency support needs to be verified through hardware experiments. Moreover, assumptions of the model are made during the simulation and these model uncertainties can only occur during hardware experiments. Through hardware experiments, the robustness of proposed controllers in dealing with model uncertainties can be effectively verified. Based on the above discussion, hardware verification should be an important part of the future work. The proposed IIEC and damping controllers can be verified by the 2 kW DFIG-WT test platform in the laboratory. In the test platform, the LabVolt module 8013-A is employed as a DFIG [181]. The wind turbine is emulated by a LabVolt 8540 module which acts as a prime mover and integrates to the 2kW DFIG. The Labvolt 8540 enables the selection on speed and torque control of wind turbine, which is achieved through a Mitsubishi FR-A700 frequency inverter connected to a host PC. The control of DFIG is achieved by two LabVolt 8557 modules PWM VSCs which represent the RSC and GSC. The stator terminal of DFIG is connected to a $415V$ $50Hz$ three phase wall power socket via a three-phase Variac. A OPAL-RT OP4500 real-time simulator is used to implement control algorithms. For the DFIG-WTs contributing to the frequency support in the multi-machine power systems, the performance of the robust damping controllers can be verified through the dSPACE hardware-in-loop test platform in the laboratory. DS1104 board of dSPACE is used to implement and simulate the designed controllers while DS1006 board is used to simulate the multi-machine power systems.

- The proposed IIEC and RDCs can also be extended to apply to the other inverted-coupled renewable energies, such as permanent-magnet synchronous generator based wind turbines and solar PV plants.

References

[1] Renewables 2021 global status report. https://www.ren21.net/, 2021. Accessed: 15 June 2021.

[2] J. Maand Z. Song, Y. Zhang, Y. Zhao, and J. S. Thorp. Robust stochastic stability analysis method of dfig integration on power system considering virtual inertia control. *IEEE Trans. Power Syst.*, 32(5):4069–4079, 2017.

[3] F. M. Gonzalez-Longatt. Effects of the synthetic inertia from wind power on the total system inertia: simulation study. In *2012 2nd International Symposium On Environment Friendly Energies And Applications*, pages 389–395, 2012.

[4] P. Kunder. *Power System Stability and Control*. New York: McGraw-Hill, 1994.

[5] The grid code, issue 4 revision 13. http://www.nationalgrid.com/uk/, 2012. Accessed: 7 June 2012.

[6] Eirgrid grid code version 4.0. http://www.eirgrid.com, 2013. Accessed: 26 April 2013.

[7] Z. Wu, W. Gao, T. Gao, W. Yan, H. Zhang, S. Yan, and X. Wang. State-of-the-art review on frequency response of wind power plants in power systems. *J. Mod. Power Syst. Clean Energy*, 6(1):1–16, 2018.

[8] G. C. Tarnowski, P. C. Kjar, P. E. Sorensen, and J. Ostergaard. Variable speed wind turbines capability for temporary over-production. In *2009 IEEE Power Energy Society General Meeting*, pages 1–7, 2009.

[9] Y. Wang, J. Meng, X. Zhang, and L. Xu. Control of pmsg-based wind turbines for system inertial response and power oscillation damping. *IEEE Trans. Sustain. Energy*, 6(2):565–574, 2015.

[10] B. Pal and B. Chaudhuri. *Robust Control in Power Systems*. Springer, 2005.

[11] M. Rahimi. Dynamic performance assessment of dfig-based wind turbines: A review. *Renewable and Sustainable Energy Reviews*, 37:852–866, Sep 2014.

[12] M. Debouza and A. Al-Durra. Grid ancillary services from doubly fed induction generator-based wind energy conversion system: A review. *IEEE Access*, 7:7067–7081, 2019.

[13] IRENA. *REthinking energy 2017*. [Online]. Available at:https://www.https://www.irena.org/, January 2017.

[14] Roadmap for a renewable energy future. `https://www.https://www.irena.org/`, 2016. Accessed: March 2016.

[15] EIA. *Installed electricity capacity*. [Online]. Available at:https://www.eia.gov/international/data/world, 2020.

[16] Erdiwansyah et al. A critical review of the integration of renewable energy sources with various technologies. *Protection and Control of Modern Power Systems*, 6(3):1–18, 2021.

[17] Energy trends. `https://assets.publishing.service.gov.uk/`, 2021. Accessed: 29 June 2021.

[18] Z. A. Obaid, L. M. Cipcigan, L. Abrahim, and M. T. Muhssin. Frequency control of future power systems: reviewing and evaluating challenges and new control methods. *J. Mod. Power Syst. Clean Energy*, 7(1):9–25, 2019.

[19] North American Electric Reliability corporation. Fast frequency response concepts and bulk power system reliability needs. *White paper*, pages 1–29, 2020.

[20] H Bevrani, H. Golpîra, A. R. Messina, N. Hatziargyriou, F. Milano, and T. Ise. Power system frequency control: An updated review of current solutions and new challenges. *Electric Power Systems Research*, 194:1–11, 2021.

[21] M. Shouran, F. Anayi, and M. Packianather. A state-of-the-art review on lfc strategies in conventional and modern power systems. In *2021 International Conference on Advance Computing and Innovative Technologies in Engineering (ICACITE)*, pages 268–277, 2021.

[22] H. Bevrani, M. Watanabe, and Y. Mitani. *Power System Monitoring and Control*. IEEE-Wiley, 2014.

[23] H. E. Lokay and V. Burtnyk. Application of underfrequency relays for automatic load shedding. *IEEE Trans. Power App. Syst.*, PAS-87(3):776–783, 1968.

[24] M. M. Chowdhury, M. E. Haque, M. Aktarujjaman, M. Negnevitsky, and A. Gargoom. Grid integration impacts and energy storage systems for wind energy applications — a review. In *2011 IEEE Power and Energy Society General Meeting*, pages 1–8, 2011.

[25] D. Gautam, V. Vittal, and T. Harbour. Impact of increased penetration of dfig-based wind turbine generators on transient and small signal stability of power systems. *IEEE Trans. Power Syst.*, 24(3):1426–1434, 2009.

[26] C. Han, A. Q. Huang, M. E. Baran, S. Bhattacharya, W. Litzenberger, L. Anderson, A. L. Johnson, and A. A. Edris. Statcom impact study on the integration of a large wind farm into a weak loop power system. *IEEE Trans. Energy Convers.*, 23(1):226–233, 2008.

[27] D.M. Logan, J.S. Baylor, D. Cotcher, and D. Krauss. Communicating the value of dispatchability for non-utility generation projects. *IEEE Trans. Power Syst.*, 10(3):1408–1413, 1995.

[28] A. Miller, Muljadi, and D.S. Zinger. A variable speed wind turbine power control. *IEEE Trans. Energy Convers.*, 12(2):181–186, 1997.

[29] A. Mullane and M. O'Malley. The inertial response of induction-machine-based wind turbines. *IEEE Trans. Power Syst.*, 20(3):1496–1503, 2005.

[30] F. Díaz-González, M. Hau, A. Sumper, and O. Gomis-Bellmunt. Participation of wind power plants in system frequency control: Review of grid code requirements and control methods. *Renew. Sust. Energy Rev.*, 34:551–564, 2014.

[31] ENTSO-E, commission regulation. `http://www.entsoe.eu`, 2017. Accessed: 24 November 2017.

[32] D.N. Kosterev and C.W. Taylor andW.A. Mittelstadt. Model validation for the august 10, 1996 wscc system outage. *IEEE Trans. Power Syst.*, 14(3):967–979, 1999.

[33] G. Tsourakis and B. M. Nomikosand C. D. Vournas. Contribution of doubly fed wind generators to oscillation damping. *IEEE Trans. Energy Convers.*, 24(3):783–791, 2009.

[34] M. Garmroodi, D. J. Hill, G. Verbič, and J. Ma. Impact of tie-line power on inter-area modes with increased penetration of wind power. *IEEE Trans. Power Syst.*, 31(4):3051–3059, 2016.

[35] H. Geng, X. Xi, L. Liu, G. Yang, and J. Ma. Hybrid modulated active damping control for dfig-based wind farm participating in frequency response. *IEEE Trans. Energy Convers.*, 32(3):1220–1230, Sep. 2017.

[36] J. Ying, X. Yuan, J. Hu, and W. He. Impact of inertia control of dfig-based wt on electromechanical oscillation damping of sg. *IEEE Trans. Power Syst.*, 33(3):3450–3459, 2018.

[37] R. G. D. Almeida and L. J. A. Pecas. Participation of doubly fed induction wind generators in system frequency regulation. *IEEE Trans. Power Syst.*, 22(3):944–950, 2007.

[38] X. Wang, Y. Song, and M. Irving. *Modern Power Systems Analysis*. Springer, 2003.

[39] P. Du and J. Matevosyan. Forecast system inertia condition and its impact to integrate more renewables. *IEEE Trans. Smart Grid*, 9(2):1531–1533, 2018.

[40] T. Chen, J. Guo, B. Chaudhuri, and S. Y. Hui. Virtual inertia from smart loads. *IEEE Trans. Smart Grid*, 11(5):4311–4320, 2020.

[41] Shuthakini Pulendran and Joseph Euzebe Tate. Energy storage system control for prevention of transient under-frequency load shedding. *IEEE Trans. Smart Grid*, 8(2):927–936, 2017.

[42] Hydro-Quebec TransEnergie. Transmission provider technical requirements for the connection of power plants to the hydro-quebec transmission system. `http://www.hydroquebec.com/transenergie/fr/commerce/pdf/exigence_raccordementfev09en.ndf`, 2009.

[43] S. Bernard, D. Beaulieu, and G. Trudel. Hydro-quebec grid code for wind farm interconnection. In *IEEE Power Engineering Society General Meeting, 2005*, pages 1248–1252 Vol. 2, 2005.

[44] Feasibility of fast frequency response obligations of new generators. `https://www.aemc.gov.au`, 2017. Accessed: 8 June 2017.

[45] J. Brisebois and N. Aubut. Wind farm inertia emulation to fulfill hydro-québec's specific need. In *2011 IEEE Power and Energy Society General Meeting*, pages 1–7, 2011.

[46] Transmission provider technical requirements for the connection of power plants to the hydro-quebec transmission system. `http://publicsde.regie-energie.qc.ca/projets/208/DocPrj/R-3830-2012-B-0044-DemAmend-PieceRev-2013_11_29.pdf`, 2013. Accessed: November 2013.

[47] L. Ruttledge and D. Flynn. Emulated inertial response from wind turbines: Gain scheduling and resource coordination. *IEEE Trans. Power Syst.*, 31(5):3747–3755, 2016.

[48] Z. Zhang, Y. Sun, J. Lin, and G. Li. Coordinated frequency regulation by doubly fed induction generator-based wind power plants. *IET Renew. Power Gener.*, 6(1):38–47, Jan 2012.

[49] M. Hwang, E. Muljadi, J. W. Park, P. Sørensen, and Y. C. Kang. Dynamic droop–based inertial control of a doubly-fed induction generator. *IEEE Trans. Sustain. Energy*, 7(3):924–933, 2016.

[50] J. V. Vyver, J. D. M. D. Kooning, B. Meersman, L. Vandevelde, and T. L. Vandoorn. Droop control as an alternative inertial response strategy for the synthetic inertia on wind turbines. *IEEE Trans. Power Syst.*, 31(2):1129–1138, 2016.

[51] Graham Stein. Frequency response technical sub-group report. *National grid*, 1:1–34, 2011.

[52] P. K. Keung, P. Li, H. Banakar, and B. T. Ooi. Kinetic energy of wind-turbine generators for system frequency support. *IEEE Trans. Power Syst.*, 24(1):279–287, 2009.

[53] L. Chang-Chien, W. Lin, and Y. Yin. Enhancing frequency response control by dfigs in the high wind penetrated power systems. *IEEE Trans. Power Syst.*, 26(2):710–718, 2011.

[54] Y. Wang, G. Delille, H. Bayem, X. Guillaud, and B. Francois. High wind power penetration in isolated power systems—assessment of wind inertial and primary frequency responses. *IEEE Trans. Power Syst.*, 28(3):2412–2420, 2013.

[55] Y. Xue and N. Tai. Review of contribution to frequency control through variable speed wind turbine. *Renew Energy*, 36(6):1671–1677, 2011.

[56] Z. Wu, W. Gao, J. Wang, and S. Gu. A coordinated primary frequency regulation from permanent magnet synchronous wind turbine generation. In *2012 IEEE Power Electronics and Machines in Wind Applications*, pages 1–6, 2012.

[57] X. Zhu, Y. Wang, L. Xu, X. Zhang, and H. Li. Virtual inertia control of dfig-based wind turbines for dynamic grid frequency support. In *IET Conference on Renewable Power Generation (RPG 2011)*, pages 1–6, 2011.

[58] A. Teninge, C. Jecu, D. Roye, S. Bacha, J. Duval, and R. Belhomme. Contribution to frequency control through wind turbine inertial energy storage. *IET Renew. Power Gener.*, 3(3):358–370, 2009.

[59] M. Kang, K. Kim, E. Muljadi, J. Park, and Y. Kang. Frequency control support of a doubly-fed induction generator based on the torque limit. *IEEE Trans. Power Syst.*, 31(6):4575–4583, 2016.

[60] M. Kang, J. Lee, K. Hur, Y. Choy, and Y. Kang. Stepwise inertial control of a doubly-fed induction generator to prevent a second frequency dip. *J. Electr. Eng. Technol.*, 10(6):2221–2227, 2015.

[61] I. A. Gowaid, A. El-Zawawi, and M. El-Gammal. Improved inertia and frequency support from grid-connected dfig wind farms. In *2011 IEEE/PES Power Systems Conference and Exposition*, pages 1–9, 2011.

[62] Z. Wu, W. Gao, X. Wang, M. Kang, M. Hwang, Y. C. Kang, V. Gevogian, and E. Mulijadi. Improved inertial control for permanent magnet synchronous generator wind turbine generators. *IET Renew. Power Gener.*, 10(9):1366–1373, 2016.

[63] A. Bonfiglio, M. Invernizzi, A. Labella, and R. Procopio. Design and implementation of a variable synthetic inertia controller for wind turbine generators. *IEEE Trans. Power Syst.*, 34(1):754–764, 2019.

[64] X. Peng, W. Yao, C. Yan, J. Wen, and S. Cheng. Two-stage variable proportion coefficient based frequency support of grid-connected dfig-wts. *IEEE Trans. Power Syst.*, 35(2):962–974, 2020.

[65] M. H. Ravanji, C. A. Cañizares, and M. Parniani. Modeling and control of variable speed wind turbine generators for frequency regulation. *IEEE Trans. Sustain. Energy*, 11(2):916–927, 2020.

[66] W. He, X. Yuan, and J. Hu. Inertia provision and estimation of pll-based dfig wind turbines. *IEEE Trans. Power Syst.*, 32(1):510–521, 2017.

[67] S. Wang, J. Hu, and X. Yuan. Virtual synchronous control for grid-connected dfig-based wind turbine. *IEEE J. Emerg. Sel. Top Power Electron.*, 3(4):932–944, 2015.

[68] E. Muljadi, V. Gevorgian, M. Singh, and S. Santoso. Understanding inertial and frequency response of wind power plants. In *2012 IEEE Power Electronics and Machines in Wind Applications*, pages 1–8, 2012.

[69] I. D. Margaris, S. A. Papathanassiou, N. D. Hatziargyriou, A. D. Hansen, and P. Sorensen. Frequency control in autonomous power systems with high wind power penetration. *IEEE Trans. Sustain. Energy*, 3(2):189–199, 2012.

[70] Active power control in siemens wind turbines. `http://www.nrel.gov/electricity/transmission/pdfs/nelson.pdf`, 2016. Accessed: 29 May 2016.

[71] G. C. Tarnowski, P. C. Kjær, S. Dalsgaard, and A. Nyborg. Regulation and frequency response service capability of modern wind power plants. In *IEEE PES General Meeting*, pages 1–8, 2010.

[72] K. D. Vos, S. D. Rijcke, and J. Driesen. Asymmetric reserve power delivered by large wind power plants. *Innovative smart grid technologies*, pages 1–8, 2010.

[73] Y. Z. Sun, Z. S. Zhang, G. J. Li, and J. Lin. Review on frequency control of power systems with wind power penetration. In *2010 International Conference on Power System Technology*, pages 1–8, 2010.

[74] K. V. Vidyanandan and N. Senroy. Primary frequency regulation by deloaded wind turbines using variable droop. *IEEE Trans. Power Syst.*, 28(2):837–846, 2013.

[75] M. Wang-Hansen, R. Josefsson, and H. Mehmedovic. Frequency controlling wind power modeling of control strategies. *IEEE Trans. Sustain. Energy*, 4(4):954–959, 2013.

[76] L. Chang-Chien, C. Hung, and Y. Yin. Dynamic reserve allocation for system contingency by dfig wind farms. *IEEE Trans. Power Syst.*, 23(2):729–736, 2008.

[77] T. Ackermann. *Wind Power in Power Systems*. John Wiley Press, 2012.

[78] H. T. Ma and B. H. Chowdhury. Working towards frequency regulation with wind plants: combined control approaches. *IET Renew. Power Gener.*, 4(4):308–316, 2010.

[79] A. Zertek, G. Verbic, and M. Pantos. A novel strategy for variable-speed wind turbines' participation in primary frequency control. *IEEE Trans. Sustain. Energy*, 3(4):791–799, 2012.

[80] A. Zertek, G. Verbic, and M. Pantos. Optimised control approach for frequency-control contribution of variable speed wind turbines. *IET Renew. Power Gener.*, 6(2):17–23, 2012.

[81] E. Ela, V. Gevorgian, and P. Fleming et al. Active power control from wind power: briding the gaps. *National Renewable Energy Laboratory*, 2014.

[82] J. Morren, S. W. H. de Haan, W. L. Kling, and J. A. Ferreira. Wind turbines emulating inertia and supporting primary frequency control. *IEEE Trans. Power Syst.*, 21(1):433–434, Feb 2006.

[83] V. Gevorgian, Y. Zhang, and E. Ela. Investigating the impacts of wind generation participation in interconnection frequency response. *IEEE Trans. Sustain. Energy*, 6(3):1004–1012, 2015.

[84] E. Ela, V. Gevorgian, A. Tuohy, B. Kirby, M. Milligan, and M. O'Malley. Market designs for the primary frequency response ancillary service—part i: Motivation and design. *IEEE Trans. Power Syst.*, 29(1):421–431, 2014.

[85] L. Ruttledge and D. Flynn. Co-ordination of frequency responsive wind plant in future power system. In *2nd IET renewable power generation conference*, pages 1–4, 2013.

[86] Z. Cao, X. Wang, and J. Tan. Control strategy of large-scale dfig-based wind farm for power grid frequency regulation. In *31st Chinese control conference*, page 6835–6840, 2012.

[87] Mohammadreza Fakhari Moghaddam Arani and Yasser Abdel-Rady I. Mohamed. Analysis and mitigation of undesirable impacts of implementing frequency support controllers in wind power generation. *IEEE Trans. Energy Convers.*, 31(1):174–186, 2016.

[88] M. Kayikci and J. V. Milanovic. Assessing transient response of dfig-based wind plants—the influence of model simplifications and parameters. *IEEE Trans. Power Syst.*, 23(2):545–554, 2008.

[89] M. Kayikci and J. V. Milanovic. Dynamic contribution of dfig-based wind plants to system frequency disturbances. *IEEE Trans. Power Syst.*, 24(2):859–867, 2009.

[90] N. R. Ullah, T. Thiringer, and D. Karlsson. Temporary primary frequency control support by variable speed wind turbines— potential and applications. *IEEE Trans. Power Syst.*, 23(2):601–612, 2008.

[91] J. F. Conroy and R. Watson. Frequency response capability of full converter wind turbine generators in comparison to conventional generation. *IEEE Trans. Power Syst.*, 23(2):649–656, 2008.

[92] J. Licari, C. E. Ugalde-Loo, J. B. Ekanayake, and N. Jenkins. Damping of torsional vibrations in a variable-speed wind turbine. *IEEE Trans. Energy Convers.*, 28(1):172–180, 2013.

[93] A. Buckspan, J. Aho, P. Fleming, Y. Jeong, and L. Pao. Combining droop curve concepts with control systems for wind turbine active power control. In *2012 IEEE Power Electronics and Machines in Wind Applications*, pages 1–8, 2012.

[94] L. Wu and D. G. Infield. Towards an assessment of power system frequency support from wind plant—modeling aggregate inertial response. *IEEE Trans. Power Syst.*, 28(3):2283–2291, 2013.

[95] A. Basit, A. D. Hansen, M. Altin, P. Sorensen, and M. Gamst. Wind power integration into the automatic generation control of power system with large-scale wind power. *J. Eng*, 2014(10):538–545, 2014.

[96] Y. Liu, L. Jiang, Q. H. Wu, and X. Zhou. Frequency control of dfig-based wind power penetrated power systems using switching angle controller and agc. *IEEE Trans. Power Syst.*, 32(2):1553–1567, 2017.

[97] K. Liao, Y. Xu, Y. Wang, and P. Lin. Hybrid control of dfigs for short-term and long-term frequency regulation support in power systems. *IET Renewable Power Gener.*, 13(8):1271–1279, 2019.

[98] L. Yu, R. Li, and L. Xu. Hierarchical control of offshore wind farm connected by parallel diode-rectifier-based hvdc and hvac links. *IET Renewable Power Gener.*, 13(9):1493–1502, 2019.

[99] J. Lee, G. Jang, E. Muljadi, F. Blaabjerg, Z. Chen, and Y. Cheol Kang. Stable short-term frequency support using adaptive gains for a dfig-based wind power plant. *IEEE Trans. Energy Convers.*, 31(3):1068–1079, 2016.

[100] Y. Hu and Y. Wu. Approximation to frequency control capability of a dfig-based wind farm using a simple linear gain droop control. *IEEE Trans. on Ind. Appl.*, 55(3):2300–2309, May 2019.

[101] J. Lee, E. Muljadi, P. Srensen, and Y. C. Kang. Releasable kinetic energy-based inertial control of a dfig wind power plant. *IEEE Trans. Sustain. Energy*, 7(1):279–288, 2016.

[102] M. Garmroodi, G. Verbič, and D. J. Hill. Frequency support from wind turbine generators with a time-variable droop characteristic. *IEEE Trans. Sustain. Energy*, 9(2):676–684, 2018.

[103] T. K. Chau, S. S. Yu, T. L. Fernando, H. H. Iu, and M. Small. A novel control strategy of dfig wind turbines in complex power systems for enhancement of primary frequency response and LFOD. *IEEE Trans. Power Syst.*, 33(2):1811–1823, 2018.

[104] J. Yang, Y. Chen, and Y. Hsu. Small-signal stability analysis and particle swarm optimisation self-tuning frequency control for an islanding system with dfig wind farm. *IET Gener. Transm. Distrib.*, 13(4):563–574, 2019.

[105] I. Horowitz. *Synthesis of Feedback Systems*. Academic Press, 1963.

[106] M. G. Safonov. Origins of robust control: Early history and future speculations. *IFAC Proceedings Volumes*, 45(13):1–8, 2012.

[107] Y. Zhang. *Design of wide-area damping control systems for power system low-frequency inter-area oscillations*. PhD thesis, Washington State University, 2007.

[108] K. Glover. Robust stabilisation of linear mutli-variable system: Relations to approximation. *Int. Journal of Control*, 43(3):741–766, 1986.

[109] R. Fletcher. *Practical Methods of Optimization*. John Wiley Sons, 200.

[110] S.S. Ahmed, L. Chen, and A. Petroianu. Design of suboptimal $h\infty$ excitation controllers. *IEEE Trans. Power Syst.*, 11(1):312–318, 1996.

[111] R. Asgharian. A robust $h\infty$ power system stabilizer with no adverse effect on shaft torsional modes. *IEEE Trans. Energy Convers.*, 9(3):475–481, 1994.

[112] S. Chen and O.P. Malik. $h\infty$ optimisation based power system stabiliser design. *IET Proc. Gener. Transmiss. Distrib.*, 142(2):179–184, 1995.

[113] M. Klein, L.X. Le, G.J. Rogers, S. Farrokhpay, and N.J. Balu. $h\infty$ damping controller design in large power systems. *IEEE Trans. Power Syst.*, 10(1):158–166, 1995.

[114] I. Kamwa, G. Trudel, and L. Gerin-Lajoie. Robust design and coordination of multiple damping controllers using nonlinear constrained optimization. *IEEE Trans. Power Syst.*, 15(3):1084–1092, 2000.

[115] T. C. Yang. Applying $h\infty$ optimisation method to power system stabiliser design part 1: Single-machine infinite-bus systems. *International Journal of Electrical Power Energy Syst.*, 19(1):29–35, 1997.

[116] B. Chaudhuriand B.C. Pal. Robust damping of multiple swing modes employing global stabilizing signals with a tcsc. *IEEE Trans. Power Syst.*, 19(1):499–506, 2004.

[117] M. Chilali, P. Gahinet, and P. Apkarian. Robust pole placement in lmi regions. *IEEE Trans. Automat. Contr.*, 44(12):2257–2270, 1999.

[118] Y. Zhang and A. Bose. Design of wide-area damping controllers for interarea oscillations. *IEEE Trans. Power Syst.*, 23(3):1136–1143, 2008.

[119] W. Yao, L. Jiang, Q. H. Wu, J. Y. Wen, and S. J. Cheng. Delay-dependent stability analysis of the power system with a wide-area damping controller embedded. *IEEE Trans. Power Syst.*, 26(1):233–240, 2011.

[120] Y. Li, C. Rehtanz, S. Ruberg, L. Luo, and Y. Cao. Wide-area robust coordination approach of hvdc and facts controllers for damping multiple interarea oscillations. *IEEE Trans. Power Del.*, 27(3):1096–1105, 2012.

[121] J. Liu, W. Yao, J. Wen, J. Fang, L. Jiang, H. He, and S. Cheng. Impact of power grid strength and pll parameters on stability of grid-connected dfig wind farm. *IEEE Trans. Sustain. Energy*, 11(1):545–557, 2020.

[122] C. Scherer, P. Gahinet, and M. Chilali. Multiobjective output-feedback control via lmi optimization. *IEEE Trans. Automat. Contr.*, 42(7):896–911, 1997.

[123] L. Ba, W. Yao, and L. Jiang. Robust damping controller for dfig-based wind turbine with frequency response. In *2019 IEEE Sustainable Power and Energy Conference (iSPEC)*, pages 2205–2210, 2019.

[124] X. Xi, H. Geng, G. Yang, S. Li, and F. Gao. Torsional oscillation damping control for dfig-based wind farm participating in power system frequency regulation. *IEEE Trans. Ind. Appl.*, 54(4):3687–3701, 2018.

[125] M. F. M. Arani and Y. A. I. Mohamed. Analysis and damping of mechanical resonance of wind power generators contributing to frequency regulation. *IEEE Trans. Power Syst.*, 32(4):3195–3204, 2017.

[126] X. Zhang, W. He, and J. Hu. Impact of inertia control of dfig-based wt on torsional vibration in drivetrain. *IEEE Trans. Sustain. Energy*, 11(4):2525–2534, 2020.

[127] M. A. Mohammed Manaz and Chan-Nan Lu. Design of resonance damper for wind energy conversion system providing frequency support service to low inertia power systems. *IEEE Transactions on Power Systems*, 35(6):4297–4306, 2020.

[128] G. P. Prajapat, N. Senroy, and I. N. Kar. Stability enhancement of dfig-based wind turbine system through linear quadratic regulator. *IET Gener. Transm. Distrib.*, 12(6):1331–1338, Jan 2018.

[129] F. Blaabjerg and K. Ma. Wind energy systems. *Proceedings of the IEEE*, 105(11):2116–2131, 2017.

[130] D. Sun, L. Sun, F. Wu, L. Zhang, W. Geng, J. Peng, and F. Liu. Research on frequency inertia response control strategy of scess-dfig system considering variable wind speed. *The Journal of Engineering*, 2019(16):2995–3001, 2019.

[131] W. Yao, L. Jiang, J. Wen, Q. H. Wu, and S. Cheng. Wide-area damping controller of facts devices for inter-area oscillations considering communication time delays. *IEEE Trans. Power Syst.*, 29(1):318–329, 2014.

[132] J. M. Carrasco, L. G. Franquelo, J. T. Bialasiewicz, E. Galvan, R. C. PortilloGuisado, M. A. M. Prats, J. I. Leon, and N. Moreno-Alfonso. Power-electronic systems for the grid integration of renewable energy sources: A survey. *IEEE Trans. Ind. Electron.*, 53(4):1002–1016, June 2006.

[133] Vladislav Akhmatov. *Induction Generators for Wind Power*. Multi-Science Publishing Company, Ltd, 2005.

[134] L. Yang, Z. Xu, J. Østergaard, Z. Y. Dong, K. P. Wong, and X. Ma. Oscillatory stability and eigenvalue sensitivity analysis of a dfig wind turbine system. *IEEE Trans. Energy Convers.*, 26(1):328–339, 2011.

[135] J. Ekanayake, L. Holdsworth, and N. Jenkins. Comparison of 5th order and 3rd order machine models for doubly fed induction generator (dfig) wind turbines. *Elect. Power Syst. Res.*, 67(3):207–215, 2003.

[136] K. Shi, X. Yin, L. Jiang, Y. Liu, Y. Hu, and H. Wen. Perturbation estimation based nonlinear adaptive power decoupling control for dfig wind turbine. *IEEE Trans. Power Electron.*, 35(1):319–333, 2020.

[137] M. G. Safonov and R. Y. Chiang. A schur method for balanced-truncation model reduction. *IEEE Transactions on Automat. Control*, 34(7):729–733, 1989.

[138] N. Yang, Q. Liu, and J. D. McCalley. Tcsc controller design for damping interarea oscillations. *IEEE Trans. Power Syst.*, 13(4):1304–1310, 1998.

[139] E.Z. Zhou. Functional sensitivity concept and its application to power system damping analysis. *IEEE Trans. Power Syst.*, 9(1):518–524, 1994.

[140] H. Holttinenand R. Hirvonen. *Wind Power in Power Systems*. John Wiley & Sons, Ltd, 2005.

[141] G. Rogers. *Power System Oscillations*. Norwell, MA:Kluwer, 2000.

[142] Y. Liu, L. Jiang, J. S. Smith, and Q. H. Wu. Primary frequency control of dfig-wts using bang-bang phase angle controller. *IET Gener. Transm. Distrib.*, 12(11):2670–2678, 2018.

[143] M. Hwang, E. Muljadi, G. Jang, and Y. C. Kang. Disturbance-adaptive short-term frequency support of a dfig associated with the variable gain based on the rocof and rotor speed. *IEEE Trans. Power Syst.*, 32(3):1873–1881, 2017.

[144] H. Ye, W. Pei, and Z. Qi. Analytical modeling of inertial and droop responses from a wind farm for short-term frequency regulation in power systems. *IEEE Trans.Power Syst.*, 31(5):3414–3423, 2016.

[145] Y. Wu, W. Yang, Y. Hu, and P. Q. Dzung. Frequency regulation at a wind farm using time-varying inertia and droop controls. *IEEE Trans. Ind. Appl.*, 55(1):213–224, 2019.

[146] M. Toulabi, A. S. Dobakhshari, and A. M. Ranjbar. An adaptive feedback linearization approach to inertial frequency response of wind turbines. *IEEE Trans. Sustain. Energy*, 8(3):916–926, 2017.

[147] P. Kou, D. Liang, L. Yu, and L. Gao. Nonlinear model predictive control of wind farm for system frequency support. *IEEE Trans. Power Syst.*, 34(5):3547–3561, 2019.

[148] T. Surinkaew and I. Ngamroo. Coordinated robust control of dfig wind turbine and pss for stabilization of power oscillations considering system uncertainties. *IEEE Trans. Sustain. Energy*, 5(3):823–833, 2014.

[149] Y. J. Isbeih, M. S. E. Moursi, W. Xiao, and E. Saadany. h_∞ mixed-sensitivity robust control design for damping low-frequency oscillations with dfig wind power generation. *IET Gener. Transm. Distrib.*, 13(19):4274–4286, 2019.

[150] F. Teng and G. Strbac. Assessment of the role and value of frequency response support from wind plants. *IEEE Trans. Sustain. Energy*, 7(2):586–595, 2016.

[151] S. Xu and J. Lam. *Robust Control and Filtering of Singular Systems*. Springer, 2006.

[152] C. Zhang, L. Jiang, Q. H. Wu, Y. He, and M. Wu. Delay-dependent robust load frequency control for time delay power systems. *IEEE Trans. Power Syst.*, 28(3):2192–2201, 2013.

[153] M. Chilali and P. Gahinet. h_∞ design with pole placement constraints: an lmi approach. *IEEE Transactions on Automatic Control*, 41(3):358–367, 1996.

[154] P. S. Rao and I. Sen. Robust pole placement stabilizer design using linear matrix inequalities. *IEEE Transactions on Power Systems*, 15(1):313–319, 2000.

[155] S. Ghosh, S. Kamalasadan, N. Senroy, and J. Enslin. Doubly fed induction generator (dfig)-based wind farm control framework for primary frequency and inertial response application. *IEEE Trans. Power Syst.*, 31(3):1861–1871, 2016.

[156] ENTSO-E. Policy 1: Load-frequency control and performance. `https://www.entsoe.eu`. Accessed: 2018.

[157] Y. Fu, Y. Wang, and X. Zhang. Integrated wind turbine controller with virtual inertia and primary frequency responses for grid dynamic frequency support. *IET Renew. Power Gener.*, 11(8):1129–1137, 2017.

[158] G. Ramtharan, J. B. Ekanayake, and N. Jenkins. Frequency support from doubly fed induction generator wind turbines. *IET Renew. Power Gener.*, 1(1):3–9, 2007.

[159] M. Tsili and S. Papathanassiou. Review of grid code technical requirement for wind farms. *IET Renew. Power Gener.*, pages 1–25, 2009.

[160] D. Wang, X. Gao, K. Meng, J. Qiu, L. L. Lai, and S. Gao. Utilisation of kinetic energy from wind turbine for grid connections: a review paper. *IET Renew. Power Gener.*, 12(6):615–624, 2018.

[161] S. Faulstich, B. Hahn, and P. J. Tavner. Wind turbine downtime and its importance for offshore deployment. *Wind Eng.*, 14(3):327–337, 2011.

[162] G. Mandic, A. Nasiri, E. Muljadi, and F. Oyague. Active torque control for gearbox load reduction in a variable-speed wind turbine. *IEEE Trans. Ind. Appl.*, 48(6):2424–2432, 2012.

[163] V. Akhmatov. Variable-speed wind turbines with doubly-fed induction generators, part i: Modelling in dynamic simulation tools. *Wind Eng.*, 26:171–188, 2002.

[164] I. P. Girsang, J. S. Dhupia, E. Muljadi, M. Singh, and J. Jonkman. Modeling and control to mitigate resonant load in variable-speed wind turbine drivetrain. *IEEE J. Emerg. Sel. Topics Power Electron.*, 1(4):277–286, 2013.

[165] F. Fateh, W. N. White, and D. Gruenbacher. Torsional vibrations mitigation in the drivetrain of dfig-based grid-connected wind turbine. *IEEE Trans. Ind. Appl.*, 53(6):5760–5767, 2017.

[166] A. Heniche and I. Kamwa. Assessment of two methods to select wide-area signals for power system damping control. *IEEE Trans. Power Syst.*, 23(2):572–581, 2008.

[167] H. M. A. Hamdan and A. M. A. Hamdan. On the coupling measures between modes and state variables and subsynchronous resonance. *Elect. Power Syst. Res.*, 13(3):165–171, 1987.

[168] S. Skogestad and I. Postlethwaite. *Multivariable Feedback Control:Analysis and Design*. Wiley, 2005.

[169] Y. Zhou, D. D. Nguyen, P. C. Kjær, and S. Saylors. Connecting wind power plant with weak grid - challenges and solutions. In *2013 IEEE Power Energy Society General Meeting*, pages 1–7, 2013.

[170] J. Hu, B. Wang, W. Wang, H. Tang, Y. Chi, and Q. Hu. Small signal dynamics of dfig-based wind turbines during riding through symmetrical faults in weak ac grid. *IEEE Transactions on Energy Conversion*, 32(2):720–730, 2017.

[171] C. Gao, H. Liu, H. Jiang, Y. Li, and X. Tang. Research on the sub-synchronous oscillation in wind power connected to series compensated power system and its influencing factors. *CES TRANSACTIONS ON ELECTRICAL MACHINES AND SYSTEMS*, 1(3):334–340, Sep 2017.

[172] B. C. Pal and F. Mei. Modelling adequacy of the doubly fed induction generator for small-signal stability studies in power systems. *IET Renew. Power Gener.*, 2(3):181–190, Mar 2008.

[173] Y. Song and F. Blaabjerg. Overview of dfig-based wind power system resonances under weak networks. *IEEE Transactions on Power Electronics*, 32(6):4370–4394, 2017.

[174] X. Xi, H. Geng, and G. Yang. Enhanced model of the doubly fed induction generator-based wind farm for small-signal stability studies of weak power system. *IET Renew. Power Gener.*, 8(7):765–774, Jul 2014.

[175] Y. Song and F. Blaabjerg. Analysis of middle frequency resonance in dfig system considering phase-locked loop. *IEEE Transactions on Power Electronics*, 33(1):343–356, 2018.

[176] Ö. Göksu, R. Teodorescu, C. L. Bak, F. Iov, and P. C. Kjær. Instability of wind turbine converters during current injection to low voltage grid faults and pll frequency based stability solution. *IEEE Trans. Power Syst.*, 29(4):1683–1691, 2014.

[177] J. Z. Zhou, H. Ding, S. Fan, Y. Zhang, and A. M. Gole. Impact of short-circuit ratio and phase-locked-loop parameters on the small-signal behavior of a vsc-hvdc converter. *IEEE Trans. Power Del.*, 29(5):2287–2296, 2014.

[178] Cigre. *Connection of Wind Farms to Weak AC Networks*. Cigre, 2016.

[179] CIGRE. *Guide For Planning DC Links Terminating AC System Locations Having Low Short Circuit Capacities*. document CIGRE WG BI4.07, IEEE WGI5.05.05, 1997.

[180] M. Abdelrahem, C. M. Hackl, and R. Kennel. Finite position set-phase locked loop for sensorless control of direct-driven permanent-magnet synchronous generators. *IEEE Trans. Power Electron.*, 33(4):3097–3105, 2018.

[181] Labvolt Festo. *2 kW DFIG Training System*. 2021.

Appendix A

Two-area Four-machine Power System Parameters

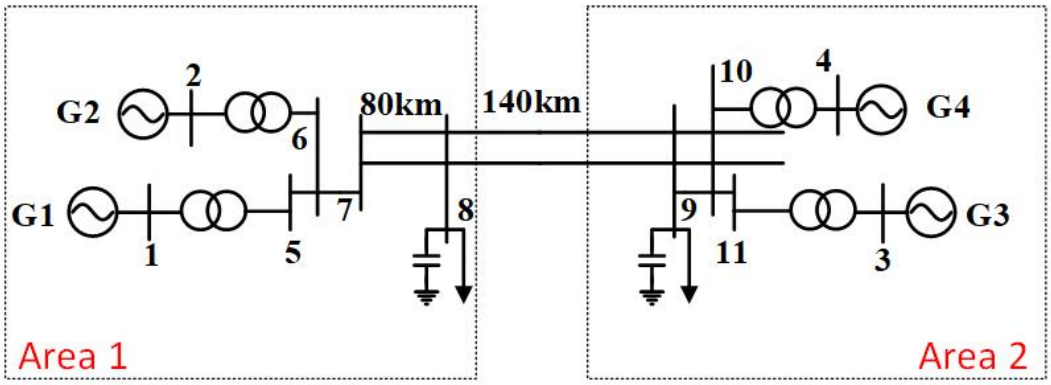

Figure A.1: A 4M11B system

As shown in Fig. A.1, the studied 4M11B system is based on the two-area system given in [4], which consists of two areas and are connected by two parallel transmission lines. Each area includes two synchronous generator units, where the rating is 900 MVA and 20kV. Synchronous generator parameters of G1 - G4 are given in per unit based on the MVA and kV as follows:

$X_d = 1.8$	$X_q = 1.7$	$X'_d = 0.3$
$X'_q = 0.55$	$X''_d = 0.25$	$X''_q = 0.25$
$T'_{d0} = 8.0$ s	$T'_{q0} = 0.4$ s	$T''_{d0} = 0.03$ s
$T''_{q0} = 0.05$ s	$H = 6.5$ (for G1 and G2)	$H = 6.175$(for G3 and G4)

The step-up transformer has the impedance $0 + j0.15$ in per unit which is based on the 900 MVA and 20/230 kV.

The nominal voltage of the transmission system is 230kV. The transmission line parameters are given in per unit based on 100 MVA, 230 kV as follows:

$$r = 0.0001\text{pu/km} \quad x_L = 0.001\text{pu/km} \quad b_C = 0.00175\text{pu/km}$$

The nominal operating condition of this system transmit 400MW from area 1 to area 2, the generators G1-G4 are operated as follows:

$$\begin{aligned}
&\text{G1:} \quad P = 700\text{MW}, \quad Q = 185\text{MVAr}, \quad E_t = 1.03\angle 20.2^\circ \\
&\text{G2:} \quad P = 700\text{MW}, \quad Q = 235\text{MVAr}, \quad E_t = 1.01\angle 10.5^\circ \\
&\text{G3:} \quad P = 719\text{MW}, \quad Q = 176\text{MVAr}, \quad E_t = 1.03\angle -6.8^\circ \\
&\text{G4:} \quad P = 700\text{MW}, \quad Q = 202\text{MVAr}, \quad E_t = 1.01\angle -17.0^\circ
\end{aligned}$$

The loads and reactive power compensation by the shunt capacitors at buses 8 and 9 are given are given as follows:

$$\begin{aligned}
&\text{Bus 7:} \quad P_L = 967\text{MW}, \quad Q_L = 100\text{MVAr}, \quad Q_C = 200\text{MVAr} \\
&\text{Bus 9:} \quad P_L = 1,767\text{MW}, \quad Q_L = 100\text{MVAr}, \quad Q_C = 350\text{MVAr}
\end{aligned}$$

Appendix B

New England New York 68-Bus Power System Parameters

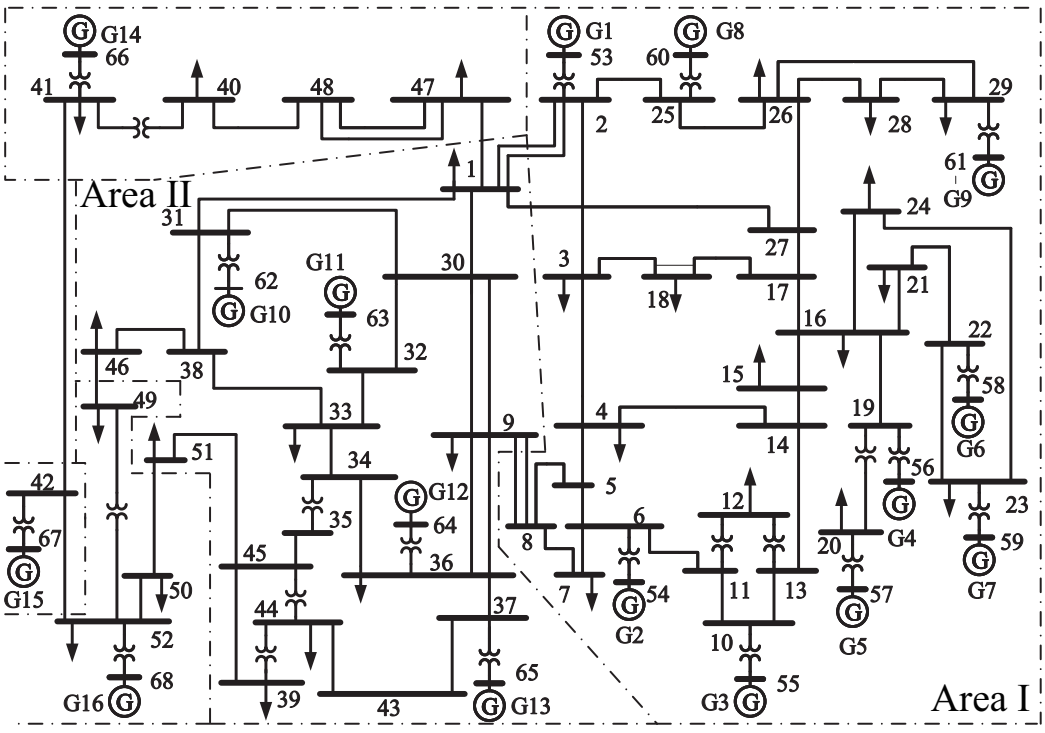

Figure B.1: A 16M68B system

As shown in Fig. B.1, the studied 16M68B system is based on the 16-machine 5-area system given in [10]. The machine bus data, load bus data, machine data, load

Table B.1: Machine bus data

Bus number	Voltage (pu)	Power Generation (pu)
1	1.0450	2.50
2	0.9800	5.45
3	0.9830	6.50
4	0.9970	6.32
5	1.0110	5.05
6	1.0500	7.00
7	1.0630	5.60
8	1.0300	5.40
9	1.0250	8.00
10	1.0100	5.00
11	1.0000	10.00
12	1.0156	13.50
13	1.0110	35.91
14	1.0000	17.85
15	1.0000	10.00
16	1.0000	40.00

data, DC excitation system data, static excitation system and PSS data are given as follows:

Table B.2: Load bus data

Bus number	P_L (pu)	Q_L (pu)
17	60.0000	3.0000
18	24.7000	1.2300
19	0.0000	0.0000
20	6.8000	1.0300
21	2.7400	1.1500
22	0.0000	0.0000
23	2.4800	0.8500
24	3.0900	-0.9200
25	2.2400	0.4700
26	1.3900	0.1700
27	2.8100	0.7600
28	2.0600	0.2800
29	2.8400	0.2700
30	0.0000	0.0000
31	0.0000	0.0000
32	0.0000	0.0000
33	1.1200	0.0000
34	0.0000	0.0000
35	0.0000	0.0000
36	1.0200	-0.1946
37	0.0000	0.0000
38	0.0000	0.0000
39	2.6700	0.1260
40	0.6563	0.2353
41	10.0000	2.5000
42	11.5000	2.5000
43	0.0000	0.0000
44	2.6755	0.2100
45	1.5070	0.2850

Table B.3: Load bus data (Continued)

Bus number	P_L (pu)	Q_L (pu)
46	1.5070	2.2850
47	2.0312	0.3259
48	2.4120	0.0220
49	1.6400	0.2900
50	1.0000	-1.4700
51	3.3700	-1.2200
52	1.5800	0.3000
53	2.5270	1.1856
54	0.0000	0.0000
55	3.2200	0.0200
56	2.0000	0.7360
57	0.0000	0.0000
58	0.0000	0.0000
59	2.3400	0.8400
60	2.0880	0.7080
61	1.0400	0.0000
62	0.0000	0.0000
63	0.0000	0.0000
64	0.0900	0.8800
65	0.0000	0.0000
66	0.0000	0.0000
67	3.20	1.5300
68	3.29	0.32

Table B.4: Line data

From	To	Resistance (pu)	Reactance (pu)	Line charging (pu)	Tap ratio
54	1	0.0000	0.0181	0.0000	1.0250
58	2	0.0000	0.0250	0.0000	1.0700
62	3	0.0000	0.0200	0.0000	1.0700
19	4	0.0007	0.0142	0.0000	1.0700
20	5	0.0009	0.0180	0.0000	1.0090
22	6	0.0000	0.0143	0.0000	1.0250
23	7	0.0005	0.0272	0.0000	0.0000
25	8	0.0006	0.0232	0.0000	1.0250
29	9	0.0008	0.0156	0.0000	1.0250
31	10	0.0000	0.0260	0.0000	1.0400
32	11	0.0000	0.0130	0.0000	1.0400
36	12	0.0000	0.0075	0.0000	1.0400
17	13	0.0000	0.0033	0.0000	1.0400
41	14	0.0000	0.0015	0.0000	1.0000
42	15	0.0000	0.0015	0.0000	1.0000
18	16	0.0000	0.0030	0.0000	1.0000
36	17	0.0005	0.0045	0.3200	0.0000
49	18	0.0076	0.1141	1.1600	0.0000
68	19	0.0016	0.0195	0.3040	0.0000
19	20	0.0007	0.0138	0.0000	1.0600
68	21	0.0008	0.0135	0.2548	0.0000
21	22	0.0008	0.0140	0.2565	0.0000
22	23	0.0006	0.0096	0.1846	0.0000
23	24	0.0022	0.0350	0.3610	0.0000
68	24	0.0003	0.0059	0.0680	0.0000
54	25	0.0070	0.0086	0.1460	0.0000
25	26	0.0032	0.0323	0.5310	0.0000
37	27	0.0013	0.0173	0.3216	0.0000
26	27	0.0014	0.0147	0.2396	0.0000

Table B.5: Line data (Continued)

From	To	Resistance (pu)	Reactance (pu)	Line charging (pu)	Tap ratio
26	28	0.0043	0.0474	0.7802	0.0000
26	29	0.0057	0.0625	1.0290	0.0000
28	29	0.0014	0.0151	0.2490	0.0000
53	30	0.0008	0.0074	0.4800	0.0000
61	30	0.0019	0.0183	0.2900	0.0000
61	30	0.0019	0.0183	0.2900	0.0000
30	31	0.0013	0.0187	0.3330	0.0000
53	31	0.0016	0.0163	0.2500	0.0000
30	32	0.0024	0.0288	0.4880	0.0000
32	33	0.0008	0.0099	0.1680	0.0000
33	34	0.0011	0.0157	0.2020	0.0000
35	34	0.0001	0.0074	0.0000	0.9460
34	36	0.0033	0.0111	1.4500	0.0000
61	36	0.0022	0.0196	0.3400	0.0000
61	36	0.0022	0.0196	0.3400	0.0000
68	37	0.0007	0.0089	0.1342	0.0000
31	38	0.0011	0.0147	0.2470	0.0000
33	38	0.0036	0.0444	0.6930	0.0000
41	40	0.0060	0.0840	3.1500	0.0000
48	40	0.0020	0.0220	1.2800	0.0000
42	41	0.0040	0.0600	2.2500	0.0000
18	42	0.0040	0.0600	2.2500	0.0000
17	43	0.0005	0.0276	0.0000	0.0000
39	44	0.0000	0.0411	0.0000	0.0000
43	44	0.0001	0.0011	0.0000	0.0000
35	45	0.0007	0.0175	1.3900	0.0000
39	45	0.0000	0.0839	0.0000	0.0000
44	45	0.0025	0.0730	0.0000	0.0000
38	46	0.0022	0.0284	0.4300	0.0000

Table B.6: Line data (Continued)

From	To	Resistance (pu)	Reactance (pu)	Line charging (pu)	Tap ratio
53	47	0.0013	0.0188	1.3100	0.0000
47	48	0.0025	0.0268	0.4000	0.0000
47	48	0.0025	0.0268	0.4000	0.0000
46	49	0.0018	0.0274	0.2700	0.0000
45	51	0.0004	0.0105	0.7200	0.0000
50	51	0.0009	0.0221	1.6200	0.0000
37	52	0.0007	0.0082	0.1319	0.0000
55	52	0.0011	0.0133	0.2138	0.0000
53	54	0.0035	0.0411	0.6987	0.0000
54	55	0.0013	0.0151	0.2572	0.0000
55	56	0.0013	0.0213	0.2214	0.0000
56	57	0.0008	0.0128	0.1342	0.0000
57	58	0.0002	0.0026	0.0434	0.0000
58	59	0.0006	0.0092	0.1130	0.0000
57	60	0.0008	0.0112	0.1476	0.0000
59	60	0.0004	0.0046	0.0780	0.0000
60	61	0.0023	0.0363	0.3804	0.0000
58	63	0.0007	0.0082	0.1389	0.0000
62	63	0.0004	0.0043	0.0729	0.0000
64	63	0.0016	0.0435	0.0000	1.0600
62	65	0.0004	0.0043	0.0729	0.0000
64	65	0.0016	0.0435	0.0000	1.0600
56	66	0.0008	0.0129	0.1382	0.0000
65	66	0.0009	0.0101	0.1723	0.0000
66	67	0.0018	0.0217	0.3660	0.0000
67	68	0.0009	0.0094	0.1710	0.0000
53	27	0.0320	0.3200	0.4100	1.0000
69	18	0.0006	0.0144	1.0300	0.0000
50	69	0.0006	0.0144	1.0300	0.0000

Table B.7: Machine data

Bus	Base (MVA)	X_{ls} (pu)	R_s (pu)	X_d (pu)	$X_d^{'}$ (pu)	$X_d^{''}$ (pu)	$T_{d0}^{'}$ (s)	$T_{d0}^{''}$ (s)
1	100	0.0125	0.0	0.1000	0.0310	0.0250	10.2	0.05
2	100	0.0350	0.0	0.2950	0.0697	0.0500	6.56	0.05
3	100	0.0304	0.0	0.2495	0.0531	0.0450	5.7	0.05
4	100	0.0295	0.0	0.2620	0.0436	0.0350	5.69	0.05
5	100	0.0270	0.0	0.3300	0.0660	0.0500	5.4	0.05
6	100	0.0224	0.0	0.2540	0.0500	0.0400	7.3	0.05
7	100	0.0322	0.0	0.2950	0.0490	0.0400	5.66	0.05
8	100	0.0280	0.0	0.2900	0.0570	0.0450	6.7	0.05
9	100	0.0298	0.0	0.2106	0.0570	0.0450	4.79	0.05
10	100	0.0199	0.0	0.1690	0.0457	0.0400	9.37	0.05
11	100	0.0103	0.0	0.1280	0.0180	0.0120	4.1	0.05
12	100	0.0220	0.0	0.1010	0.0310	0.0250	7.4	0.05
13	200	0.0030	0.0	0.0296	0.0055	0.0040	5.9	0.05
14	100	0.0017	0.0	0.0180	0.00285	0.0023	4.1	0.05
15	100	0.0017	0.0	0.0180	0.00285	0.0023	4.1	0.05
16	200	0.0041	0.0	0.0356	0.0071	0.0055	7.8	0.05

Table B.8: Machine data (Continued)

Bus	X_q (pu)	$X_q{}'$ (pu)	$X_q{}''$ (pu)	$T_{q0}{}'$ (s)	$T_{q0}{}''$ (s)	H (s)	D
1	0.0690	0.0280	0.0250	1.5	0.0350	42.0	4.0
2	0.2820	0.0600	0.0500	1.5	0.0350	30.2	9.75
3	0.2370	0.0500	0.0450	1.5	0.0350	35.8	10
4	0.2580	0.0400	0.0350	1.5	0.0350	28.6	10
5	0.3100	0.0600	0.0500	0.44	0.0350	26.0	3
6	0.2410	0.0450	0.0400	0.4	0.0350	34.8	10
7	0.2920	0.0450	0.0400	1.5	0.0350	26.4	8
8	0.2800	0.0500	0.0450	0.41	0.0350	24.3	9
9	0.2050	0.0500	0.0450	1.96	0.0350	34.5	14
10	0.1150	0.0450	0.0400	1.5	0.0350	31	5.56
11	0.1230	0.0150	0.0120	1.5	0.0350	28.2	13.6
12	0.0950	0.0280	0.0250	1.5	0.0350	92.3	13.5
13	0.0286	0.0050	0.0040	1.5	0.0350	248	33
14	0.0173	0.0025	0.0023	1.5	0.0350	300	100
15	0.0173	0.0025	0.0023	1.5	0.0350	300	100
16	0.0334	0.0060	0.0055	1.5	0.0350	225	50

Table B.9: DC excitation system data

Machine no.	T_r (s)	K_A	T_A (s)	V_{rmax} (pu)	V_{rmin} (pu)	K_E (s)	T_E	A_{ex}	B_{ex}
1	0.01	40	0.02	10	-10	1	0.785	0.07	0.91
2	0.01	40	0.02	10	-10	1	0.785	0.07	0.91
3	0.01	40	0.02	10	-10	1	0.785	0.07	0.91
4	0.01	40	0.02	10	-10	1	0.785	0.07	0.91
5	0.01	40	0.02	10	-10	1	0.785	0.07	0.91
6	0.01	40	0.02	10	-10	1	0.785	0.07	0.91
7	0.01	40	0.02	10	-10	1	0.785	0.07	0.91
8	0.01	40	0.02	10	-10	1	0.785	0.07	0.91

Table B.10: Static excitation system and PSS data

Machine no.	K_a	V_{rmax} (pu)	V_{rmin} (pu)	K_{pss}	T_1 (s)	T_2 (s)	T_3 (s)	T_4 (s)
1	200	9	-9	20	0.05	0.02	3	5.4
2	200	9	-9	20	0.05	0.02	3	5.4
3	200	9	-9	20	0.05	0.02	3	5.4
4	200	9	-9	20	0.05	0.02	3	5.4
5	200	9	-9	20	0.05	0.02	3	5.4
6	200	9	-9	20	0.05	0.02	3	5.4
7	200	9	-9	20	0.05	0.02	3	5.4
8	200	9	-9	20	0.05	0.02	3	5.4
9	200	9	-9	20	0.05	0.02	3	5.4
10	200	9	-9	20	0.05	0.02	3	5.4
11	200	9	-9	20	0.05	0.02	3	5.4
12	200	9	-9	20	0.05	0.02	3	5.4
13	200	9	-9	20	0.05	0.02	3	5.4
14	200	9	-9	20	0.05	0.02	3	5.4
15	200	9	-9	20	0.05	0.02	3	5.4
16	200	9	-9	20	0.05	0.02	3	5.4

Appendix C

Small Signal Stability Analysis

The small signal stability analysis is used to study power system stability under a small disturbance. The Lyapunov linearised method is used for power system small signal stability analysis. It can be supposed that the local stability of the nonlinear system around the equilibrium point can be obtained from the stability of its linear approximation. The steps of analysing power system small signal stability can be concluded in the following,

1. The steady state operation points of the power system are calculated.
2. The differential-algebraic equations of power system nonlinear dynamics is linearised for achieving linearised differential algebraic equations [38].
3. The system state matrix $\mathbf{A}$ will be obtained from linearised differential algebraic equations and power system stability will be evaluated by examining the real part of $\mathbf{A}$ eigenvalues.

Following the analysing methods shown above, the small signal stability analysis of the model is achieved by the following steps. Firstly, the steady state operation points of the system are calculated in the initialisation code. Secondly, DFIG model built in Section 2.2 will be linearised and the linearised DFIG system can be described by using equation (C.0.1)

$$\Delta x^* = A\Delta x + B\Delta u \tag{C.0.1}$$

Thirdly, the eigenvalues of matrix $\mathbf{A}$ and as well as left and right eigenvectors can be calculated. The left and right eigenvectors matrix are normalised and it can be found that equation (C.0.2) [38] is hold.

$$\mathbf{X}_L\mathbf{X}_R = \mathbf{I} \tag{C.0.2}$$

The oscillation modes of power system are studied based on the complex conjugate eigenvalue pairs of matrix $\mathbf{A}$. Each complex conjugate pairs represents an oscillation mode, its general form can be described in (C.0.3). Thus, the oscillation frequency can be calculated using (C.0.4) and damping ratio can be calculated using (C.0.5) [38].

$$\lambda = \sigma \pm j\omega \tag{C.0.3}$$

$$f = \frac{\omega}{2\pi} \tag{C.0.4}$$

$$\zeta = \frac{-\sigma}{\sqrt{\sigma^2 + \omega^2}} \tag{C.0.5}$$

In addition, participation factor is calculated and normalised to find the dominated states of a oscillation mode. Equation (C.0.6) is used to calculated the participation factor.

$$p_{ki} = \frac{|v_{ki}|\,|u_{ki}|}{\sum_{k=1}^{n} |v_{ki}|\,|u_{ki}|} \tag{C.0.6}$$

where n is the state variable numbers, p_{ki} is used to measure the participation factor of the ith mode and kth state variable, v_{ki} is the kth element of the ith right eigenvector of matrix A, and u_{ki} is the kth element of the ith left eigenvector of matrix A [38].